

ACTIVATING SINGLE-WALLED CARBON NANOTUBES FOR HYDROGEN ADSORPTION

Milton R. Smith, Edward W. Bittner, and Bradley C. Bockrath

National Energy Technology Laboratory
US Department of Energy
PO Box 10940
Pittsburgh, PA 15236

Introduction

Single-walled carbon nanotubes have attracted considerable attention as candidates for hydrogen storage materials. Several reviews of this rapidly growing area have appeared.¹⁻³ Of particular note are various reports of considerable amounts of hydrogen taken up at 80 EC⁴, room temperature⁵, and even higher temperatures⁶. Numerous theoretical simulations have also been made. For example, adsorption isotherms have been calculated based on simulated tube arrays as a function of the diameter of the tubes, the structure of the tube bundles, and the interaction potential between hydrogen and the tube walls.⁷ Although the potential of nanotubes has been explored and discussed, it is still not clear what the ideal structure might be for optimal hydrogen storage. Chemical activation is one option for improving adsorption characteristics. Although it has a long history of application in carbon chemistry, its potential for use with the recently synthesized carbon nano-structures is just beginning to become evident.^{8,9}

In the work described below, we have used a tapered element oscillating mass analyzer to obtain isotherms for hydrogen adsorption at 25 EC and up to 700 psia for various samples of single-walled carbon nanotubes. A simple means of activating purified or as prepared nanotubes based on partial oxidation with CO₂ has been found. This activation leads to an increase in the amount of excess hydrogen adsorbed at 25 EC and 700 psia from 0.3-0.4 wt % up to nearly 1.2 wt%.

Experimental

A block diagram of the apparatus including the TEOM Series 1500 Pulse Mass Analyzer (Rupprecht and Patashnick) is given in Fig. 1.

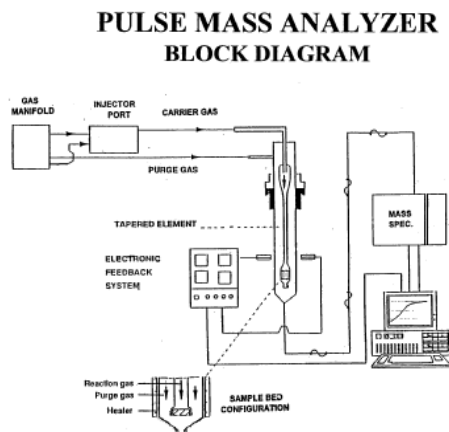


Figure 1. Block Diagram of the Rupprecht and Patashnick PMA 1500 and Associated Hardware

The PMA 1500 is a mass measuring device that employs a tapered glass element that is stimulated to vibrate at its natural frequency. The element consists of a hollow glass tube with a cylindrical sample bed, diameter 4 mm, height 6 mm, at one end. Samples were packed

into the bed between “Astro quartz” wool plugs. Hydrogen was used in both purge and reactant gas streams.

Changes in the mass of the sample bed are related to changes in the frequency of oscillation of the tapered element by equation 1.

$$\bullet m = k/(1/f_1^2 - 1/f_2^2) \quad (1)$$

Isotherms were generated by subtracting the value of the mass change found with the empty reactor from the corresponding value found with the packed reactor for each step in pressure. Typically, a 30 to 50 mg sample was packed into the bed, flushed with dry helium or nitrogen, and heated to 200 EC for 2 or more hours. After cooling to 25 EC, the gas was switched to hydrogen and measurements of pressure vs. mass were made using a program that increased pressure in 7 steps to 700 psia, holding pressure constant for 20 minutes after each increment. The pressure was decreased after 20 minutes at the maximum, usually by the same format of 100 psi steps and 20 minute intervals. The reported isotherms are a combination of both pressurization and depressurization data. Individual points are based on accumulated data from 2-12 complete cycles, except isotherm C in Figure 4, which is based on one cycle. The standard deviations about points derived from 12 repetitions ranged from 0.024 – 0.034 wt%.

Nanotubes were purchased from Tubes @ Rice in two grades, “Raw Material Grade” and “Purified Grade”.

Activation was accomplished by mild oxidation. Samples (50-75 mg) were placed in a 20 cm long by 12mm ID Vicor tube and heated in a tube furnace. A stream of Ar or He at 5 cc/min was used to flush out air, then CO₂ was added at 5 cc/min (total flow 10 cc/min). The sample was then heated to ca 600 EC until CO evolution was no longer evident. The samples were cooled under inert gas flow.

Results

Two isotherms for a sample of “Raw Material” tubes from Rice are shown in Fig 2. The upper curve (A) was taken

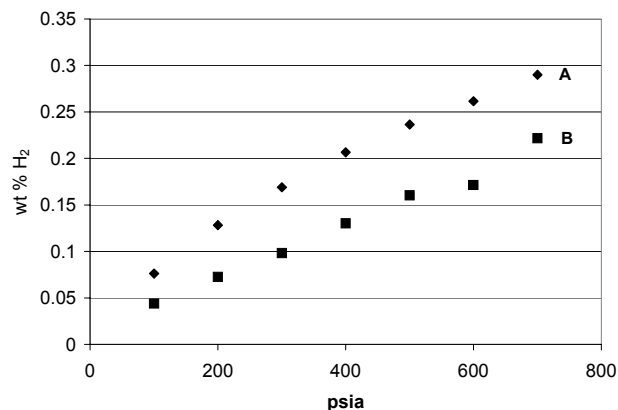


Figure 2. Hydrogen Isotherms for “Raw Material” Rice Nanotubes. After treatment at A., 200° C and B., 700° C

after the sample had been heated *in situ* to 200 EC under a flow of helium, then cooled before the isotherm experiment was begun. The lower curve (B) was obtained in a subsequent experiment after the sample had been heated in a similar manner to 700 EC. Pyrolysis at 700 EC reduced the affinity of the sample for hydrogen by a significant amount. The effect of pyrolysis on the sample was tracked by monitoring the exit gases by the in-line mass spectrometer throughout the course of heating. Hydrogen, methane, and carbon

oxides were detected as the temperature increased. After the sample had returned to 25 EC, the PMA measured a weight loss of 13.2 mg, or 23.2% of the sample weight. (Data in Fig. 2 have been corrected for loss of sample weight to allow direct comparison of the two data sets on the basis of actual sample weight.)

“Purified” nanotubes have undergone oxidation by reflux in 2.6 M nitric acid for 12 hours.⁸ The oxidation selectively removes amorphous carbon, leaving behind a greater proportion of nanotubes in the sample. The four isotherms in Fig. 3 compare the results obtained after different treatments were applied to the same sample. It may be seen that heating to 700 EC, milling, and a second pyrolysis step had modest effects on the isotherms. In general, the magnitude of hydrogen adsorption with purified tubes is similar to that found for the raw material, but in contrast, pyrolysis of the purified material at 700EC slightly increases the hydrogen storage capacity.

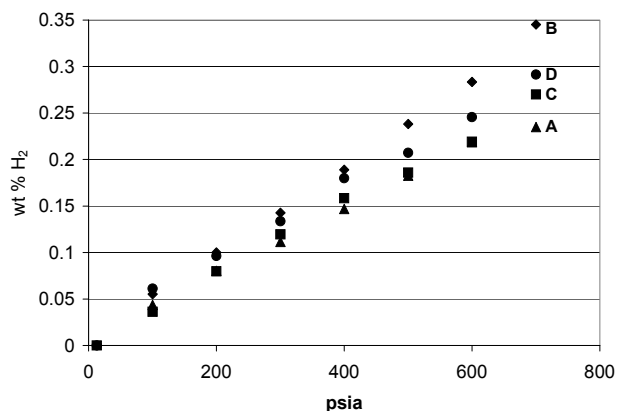


Figure 3. Comparison of Adsorption Isotherms of Hydrogen on Purified Rice Tubes: A. Sample Treated at 200 EC in He atm. B. Sample (A) Treated at 700 EC in He atm. C. Sample (B) after removal and milling in air. D. Sample (C) Treated at 700 EC in H₂ atm.

Activation of the nanotube samples took place in two steps. First partial oxidation was carried out under a stream of CO₂ at about 600 EC. A marked improvement in the amount of hydrogen adsorbed was obtained for both the raw material and the purified tubes (Fig. 4, Curves A and C). The second step was heating the oxidized tubes to 700 EC in the pulse mass analyzer. This induced further weight loss. For example, the oxidized raw material lost an additional 20% when pyrolyzed under H₂ at 700 EC. The total effect of the two steps is a significant increase in hydrogen storage capacity (Fig. 4, Curves B and D). Values of 1.16 wt % (Purified) and 1.2 wt % (Raw Material) were reached at 700 psia.

The changes in hydrogen adsorption characteristics are associated with losses in sample weight. The oxidative procedure removes about 37 % of the purified nanotube sample. Comparison of TGA data taken before and after shows that the fraction removed was significantly less resistant to oxidation by either CO₂ or O₂ than the remainder. Examination by TEM shows that the rope-like structures are left intact. In the case of the raw material, about 21% of the weight is removed during CO₂ oxidation. The difference in CO₂ reactivity in this sample is not so clearly defined as in the Purified tubes. Pyrolysis under hydrogen at 700EC of the oxidized raw material causes an additional 20% weight loss. Ultimately the two materials exhibit similar isotherms after both activation steps were executed.

The highest pressure investigated here was dictated by the upper limit of the instrument. It is clear that more hydrogen would be adsorbed at higher pressures and that the highest values given here do not represent the upper limit. The marked improvement found in our initial attempts indicates that activation of a given sample of nanotubes is a viable option for improving its hydrogen storage characteristics that warrants further exploration.

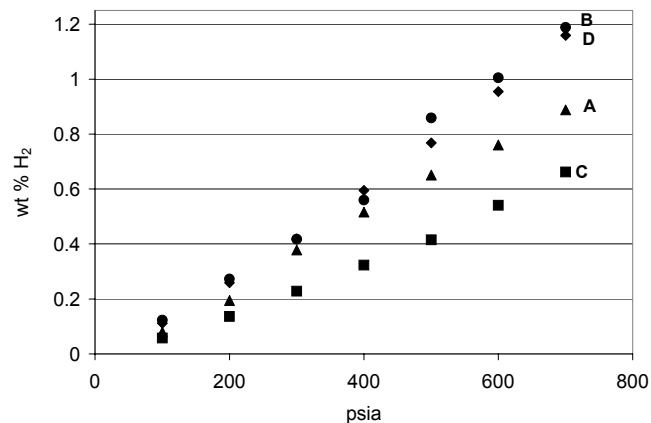


Figure 4. Adsorption Isotherms: Hydrogen on A. “Raw Material” Rice SWCNT after CO₂ Oxidation; B. Sample (A) after 700 EC in H₂; C. Purified Rice Nanotubes after CO₂ Oxidation; D. Sample Similar to (C) after 700 EC in He.

Acknowledgment. Dr. J. Karl Johnson has provided insightful discussions on hydrogen storage. MRS and EWB are Oak Ridge Institute for Science and Education Faculty Research Associates at NETL.

Disclaimer. Reference in this work to any specific commercial product is to facilitate understanding and does not necessarily imply endorsement by the United States Department of Energy.

References

1. Dresselhaus, M.S.; Williams, K.A.; Eklund, P.C. *MRS Bulletin* **1999**, 24(11), 45-50.
2. Dillon, A.C.; Heben, M. J. *Appl. Phys. A* **2001**, 72, 133-142.
3. Cheng, H.-M.; Yang, Q.-H.; Liu, C.; *Carbon*, **2001**, 39, 1447-1454.
4. Ye, Y.; Ahn, C.C.; Witham, C.; Fultz, B.; Liu J.; Rinzler, A.G.; Colbert, D.; Smith K.A.; Smalley, R.E. *App. Phys. Letts.* **1999**, 74, 2307-2309.
5. Liu, C.; Fan, Y.Y.; Liu, M.; Cong, H.T.; Cheng, H.M.; Dresselhaus, M.S. *Science* **1999**, 286, 1127-1129.
6. Dillon, A.C.; Jones, K.M.; Bekkedahl, T.A.; Kiang, C.H.; Bethune, D.S.; Heben, M.J. *Nature* **1997**, 386, 377-379.
7. Wang, Q.; Johnson J.K. *J. Phys. Chem. B* **1999**, 103, 4809-4813.
8. Kuznetsova, A.; Yates, J.T. Jr.; Simonyan, V.V.; Johnson, K.J.; Huffman, C.B.; Smalley, R.E. *J. Chem. Phys.* **2001**, 115, 6691-6698.
9. Tsang, S.C.; Chen, Y.K.; Harris, P.J.F.; Green, M.L.H. *Nature* **1994**, 372,159-162.
10. Rinzler, A.G.; Liu, J.; Dai, H.; Nikolaev, P.; Huffman, C.B.; Rodriguez-Macias, F.; Boul, P.J.; Lu, A.H.; Heymann, D.; Colbert, D.T.; Lee, R.S.; Fischer, J.E.; Rao, A.M.; Eklund, P.C.; Smalley, R.E. *Appl. Phys. A* **1998**, 67, 29-37.

ADVANCED FUEL PROCESSING CATALYSTS FOR THE STEAM REFORMING OF METHANE

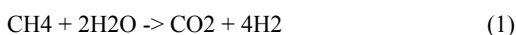
Ronald Silver and Christina Geras

HydrogenSource, 60 Bidwell Road, South Windsor, CT 06074

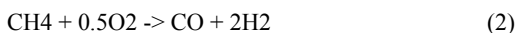
Introduction

Fuel processing is the first stage in a fuel cell power plant. It is used to extract hydrogen from hydrocarbon fuels which can then be fed to a cell stack. The first step in fuel processing utilizes a reformer reactor. Three types of reformers are generally available: catalytic steam reformers (CSR), autothermal reformers (ATR) and catalytic partial oxidizers (CPO).

Catalytic steam reformers are generally considered to be the largest of the reformer reactors. The large reactor size also tends to make it more costly and harder to start up than other reformers. The primary reaction is endothermic, so the process requires heat input. The big benefit of catalytic steam reforming is that it is very efficient, producing 4 hydrogen molecules per methane as indicated in equation (1).

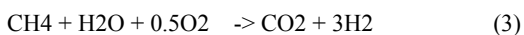


Catalytic partial oxidizers are at the other end of the spectrum, with the smallest reactors, the least costly and the easiest to start up. The primary reaction in this process is exothermic, so the process produces excess heat that must be managed. The biggest drawback of catalytic partial oxidation is its efficiency, as it only produces 2 hydrogen molecules per methane as indicated in equation (2).



The relatively large amount of CO that these reactors produce requires a relatively larger CO clean up section for the fuel processor.

Autothermal reformers are a combination of the two previously described processes. They tend to be intermediate in size, cost, start up and efficiency to the two alternatives. The exothermic reaction in this process produces just enough heat to support the endothermic one. A typical autothermal reforming reaction is shown in equation (3).



This paper will focus on new catalysts for steam reforming, as its higher efficiency may outweigh other considerations in certain applications. Steam reforming may be especially appropriate in industrial applications where long-term costs can exceed initial expenditures.

Experimental

A test was developed to evaluate catalysts for steam reforming applications on a laboratory scale reactor. The reactor consisted of three sections of 25 mm diameter steel tube, each section heated with heating tape and insulated. Methane and water were introduced into the first section and heated and mixed over inert support to form a hot steam and fuel mixture. The second section served to further mix the reactants. The third reactor section held the catalyst samples, which could consist of pellets, washcoated honeycomb monoliths or washcoated foams. The hot gas mixture would react over the sample and the conversion was measured using a gas chromatograph with a TCD detector.

Typical catalysts for catalytic steam reforming are Ni based. Each test of Ni catalyst began with a reduction of the catalyst sample in 1000 cm³/min H₂ and 1500 cm³/min N₂ at 509°C average bed

temperature. The catalyst was cooled down to the first test temperature and CH₄, H₂O and H₂ were fed into the reactor. CH₄ conversion was measured at a series of different temperatures and compared to the conversion expected at equilibrium at the same temperature. A pseudo kinetic rate was defined as being proportional to the gas volumetric space velocity times the reciprocal of the difference between equilibrium and actual conversion. By plotting the reaction constant, *k*, against the reciprocal of the temperature at each data point, an Arrhenius plot was constructed for each catalyst sample.

Approach

It was desired to eliminate the need for catalyst reduction by switching to advanced precious metal (PM) based formulations. These advanced PM catalysts were proprietary formulations supplied by various vendors. Because of this exact compositions are not available. The PM catalysts were evaluated using the same screening test used to evaluate Ni catalyst, except that the PM samples were not reduced prior to the start of the test. The goal was to identify a PM with activity for steam reforming similar to that of the best Ni based formulation. An example of the results is shown in Figure 1, which compares PM Sample B vs. a commercial Ni catalyst.

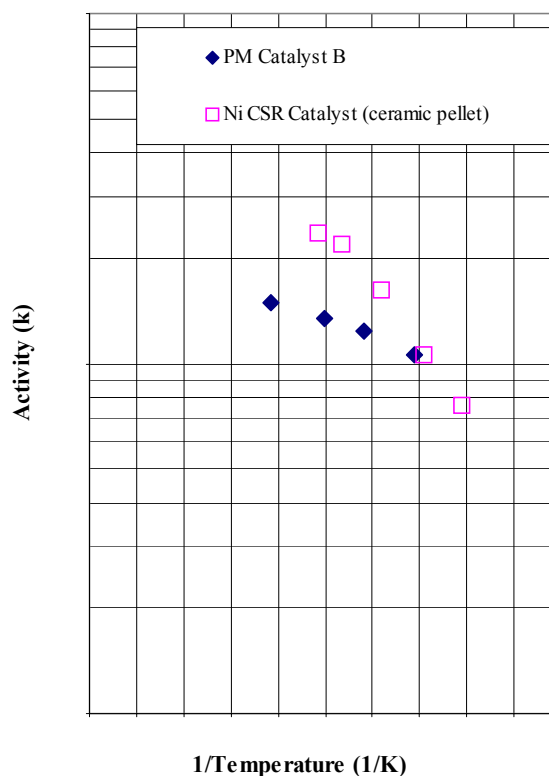


Figure 1. Reformer catalyst activity test results (example).

In this case, PM Catalyst B would be expected to have similar activity to the Ni catalyst at lower temperatures. The flatter profile of the PM sample indicates its energy of activation may be somewhat less than that of the Ni sample.

Similar experiments were run with other PM catalysts allowing a comparison of Ni versus PM, as well as a comparison of PM catalyst on several types of supports. Based on these comparisons, conclusions were drawn about the suitability of these PM formulations for steam reforming applications.

ANALYSIS OF A NON-RECYCLING HYDRIDE SYSTEM FOR POWERED WHEELCHAIRS

Edward G. Skolnik, Christina Y. TerMaath

Energetics, Inc.
901 D Street, SW, Suite 100
Washington, DC 20024

Introduction

The power wheelchair market reported 93,467 power wheelchair users and 63,636 scooter users in 1996 (1), and the market continues to grow. The current source of power for these devices is wet or gel/sealed lead-acid batteries. These batteries have several disadvantages, creating an incentive for the investigation of a different type of power supply. The batteries are heavy, consume a significant volume in the wheelchair, and require recharging to replenish the power supply. Maintenance is also an issue, particularly with the wet lead-acid batteries.

A proton exchange membrane (PEM) fuel cell using hydrogen stored in sodium hydride was analyzed for its ability to be used as a power supply in wheelchairs. Sodium hydride releases the hydrogen upon reaction with water. Processes have been developed using metal hydrides that evolve hydrogen upon contact with water, but generally prove costly when one includes the cost of regenerating the hydride from the byproduct hydroxide. This analysis chooses a niche market- the power wheelchair market- where recycling would not be necessary. Because the hydride is not recycled, a major cost in the use of hydrides is avoided.

This analysis focuses solely on the power source of the wheelchair, ignoring all costs of the wheelchair itself. As the conventional power source, batteries were researched to determine the type, size, weight, and cost of typical wheelchair batteries. Information about PEM fuel cells and sodium hydride was also gathered to determine these parameters for a PEM fuel cell/sodium hydride power system. The two systems are compared on the basis of user convenience and yearly cost over a ten-year lifetime.

Current Wheelchair Power Systems

Battery Specifications. Wheelchairs are currently powered by wet (flooded) or gel/sealed lead-acid batteries. Gel/sealed lead-acid batteries are considered to be safer because the electrolyte will not spill and cause damage as can the electrolyte in wet lead-acid batteries. For this reason, only gel/sealed lead-acid batteries are approved for air travel (2). Gel/sealed batteries also require less maintenance; however, they are more expensive and provide less energy than a wet lead-acid battery of the same size. These specifications cause some people to purchase both types of batteries in order to have a set for travel and a set for every day use (3).

There are four standard groups of wheelchair batteries that are used for wheelchairs. According to MKBattery.com, they range from 23-63 lbs and 288-850 in³. All the batteries are 12 volts. A powered wheelchair normally requires 24 volts, so two batteries are required and they are sold in sets of two. The cost ranges from around \$150-\$450 per set. The specifications provide battery capacities for a total discharge, but actually discharging a battery to this extent would damage it. MK Battery recommends using a 50% depth of discharge for best performance, so the actual amp hours that would be obtained from each battery is half of the listed value. Unless specified otherwise, a 50% depth of discharge (DOD) is assumed for all calculations in this analysis.

It was found that "manufacturers typically recommend gel-cell batteries over wet-cell batteries due to environmental and maintenance concerns with wet-cell batteries" (2), so the gel/sealed

MK Batteries are the focus of this analysis. Within this type of lead-acid battery, the group 22NF and group 24 batteries were chosen for further analysis because they offer a middle range, applicable to most wheelchair users.

Total System. The capital cost is simply the cost of the battery charger. The batteries are expected to last one year on average (3, 4), so the costs of the batteries and recharging are added to create the yearly operating costs.

Hydride/Fuel Cell Wheelchair Power Systems

This alternative wheelchair power system involves the use of a PEM fuel cell for the power device and sodium hydride as the fuel source. Upon reaction with water, hydrogen is released, which would then be supplied to the fuel cell for conversion into power. Other than electricity, the fuel cell reaction products are sodium hydroxide and water. The sodium hydroxide could be collected and sold. The water could also be easily collected and disposed of or recycled. This system was chosen for consideration because of its smaller size and weight relative to batteries. Decreasing these parameters would create a higher energy storage capacity and decrease the burden of a heavy and obstructive load on the wheelchair.

Sodium Hydride. Sodium hydride would be used as the source of hydrogen for the fuel cell. Sodium hydride is currently a specialty chemical with a current price of \$6.15/lb (\$13.53/kg), according to Chemical Market Reporter. This creates a cost of \$162/kg of hydrogen. If sodium hydride is used to fuel power wheelchairs, a larger market would be developed and that could bring down the cost. An estimation of the bare cost to produce sodium hydride can be used to estimate a larger production/lower cost case. The conventional process for sodium hydride manufacture involves electrolyzing sodium chloride and then sparging hydrogen gas through a bath of the molten sodium metal. The costs for this process create an estimated sodium hydride cost of \$3.41/kg (5). This estimation provides a much lower cost for sodium hydride, making the cost of hydrogen \$41/kg. The price does not account for packaging or sales profits, but provides a number for a general, lower cost scenario for sodium hydride.

In order to directly compare the sodium hydride to the battery, the amount of energy provided by each must be equal; therefore, the amount of sodium hydride necessary to provide the same amount of energy as a battery must be calculated. The amount of hydrogen can be estimated using its lower heating value and a fuel cell efficiency of 50%. The quantity of sodium hydride needed to provide this amount of hydrogen can then be calculated.

PEM Fuel Cell. The size of the PEM fuel cell can be estimated by first considering the amount of instantaneous power used by a wheelchair. This is estimated by calculating the kinetic energy needed to move a 170 lb person, 100 lb wheelchair, 2 lbs of sodium hydride, and a 4 lb fuel cell at a speed of 5 miles/hour (84 Wh). Considering the fact that this does not account for friction or uphill operation, and some people will weigh more and want to go faster (to go 7 miles/hour, 156 Wh would be needed), a 160 W PEM fuel cell was chosen for evaluation.

Sale of Sodium Hydride. The by-product of the reaction of sodium hydride with water is sodium hydroxide, which is a useful chemical and could be sold to recover some of the cost of the sodium hydride. Since we consider the wheelchair application to be a niche market, we do not feel that the amount of NaOH produced would be enough to affect the market price. The selling price of sodium hydroxide is estimated at \$0.42/kg (6).

Total System. When the system is considered as a whole, it is apparent that the size and weight of the fuel cell, when compared to batteries, decrease the net cost of the fuel supply. The total weight of

the system (fuel cell plus hydride and water) is less than 3 kg, which is significantly lighter than the batteries (around 34 kg). The significant decrease in weight translates into less energy required to power the wheelchair. So the PEM fuel cell/hydride system would actually provide the user with a longer range than a battery system with the same energy. The amounts and costs of sodium hydride were calculated with consideration for the decreased system weight and the sale of sodium hydroxide.

The economic feasibility of the system depends largely on the cost of the fuel cell, which for smaller fuel cells such as this could be estimated at \$10/W (7). The system is not very realistic if the price of the PEM fuel cell stays at \$16,000, but a mass production cost of \$1600 would be reasonable considering the benefits that would be gained from a significantly smaller and lighter power system. The size and weight of the fuel cell/hydride system is less than a quarter of the battery system size and weight. The fuel cell/hydride system is also very flexible since the energy storage is a separate component and can be easily increased or decreased simply through the amount of hydride. A user could easily obtain much longer ranges that would be difficult to reach using lead-acid batteries.

Battery vs. Fuel Cell Power System

A comparison of the two wheelchair power supplies is performed by directly comparing the parameters of each system and evaluating the costs over a ten-year lifetime (Table 1). This allows the capital costs to be considered on a yearly basis. A ten-year lifetime is assumed for both the fuel cell and the battery charger, creating yearly costs of \$160 and \$25, respectively. Because the battery charger cost is not a significant amount and is not always an additional purchase, it is eliminated from these calculations.

Table 1. Power System Comparison over a Ten-Year Lifetime-Very Active User

Parameter	22NF or Equivalent Performance	
	Battery System	Fuel Cell System
Volume	954 in ³	129 in ³
Weight	34.1 kg	2.21 kg
Yearly Cost	\$284.60	\$1891 (current) \$507 (future market)

Parameter	Group 24 or Equivalent Performance	
	Battery System	Fuel Cell System
Volume	1368 in ³	145 in ³
Weight	48.6 kg	2.53 kg
Yearly Cost	\$358.62	\$2777 (current) \$682 (future market)

These calculations assume that the user consumes the maximum battery capacity (50% DOD) all 365 days a year. This is a profile for an extremely active user. Some very active users may require more than one set of batteries to fit their needs, doubling the yearly cost and making the fuel cell system a more competitive choice. Other users will require a less consistent and diminished amount of energy. Because the batteries would still deteriorate after one year even with less use (8), the battery costs remain the same for this type of user while the sodium hydride costs would greatly decrease (Table 2).

Although the fuel cell system costs are still higher than the battery costs, the decreased costs of the sodium hydride lessened the yearly costs of the fuel cell system by a considerable amount. The fuel cell system yearly cost is very dependent on the amount and cost of sodium hydride.

Table 2. Power System Comparison over a Ten-Year Lifetime-Less Active User

Parameter	22NF or Equivalent Performance	
	Battery System	Fuel Cell System
Volume	954 in ³	122 in ³
Weight	34.1 kg	2.04 kg
Yearly Cost	\$284.60	\$1025 (current) \$334 (future market)

Parameter	Group 24 or Equivalent Performance	
	Battery System	Fuel Cell System
Volume	1368 in ³	135 in ³
Weight	48.6 kg	2.27 kg
Yearly Cost	\$358.62	\$1469 (current) \$421 (future market)

Wheelchair users have a variety of lifestyles and it is clear that the benefits of a fuel cell system would weigh against the costs very differently for different users. For example, a user with an average daily energy consumption that was low but still needed a few days of long ranges would be a perfect customer of a fuel cell/hydride system. The flexibility of the system would allow the user to supply themselves with a large amount of energy on those long-range days while requiring small purchases of sodium hydride on a majority of the days. If forced to use batteries, this same user would need to purchase and carry the largest battery for just those few very active days. The users who would be inclined to stick with the conventional battery power supply would be those users that manage to get the most out of their battery. These users would have consistent daily energy needs that match the capacity of the battery sizes available. For some users, the battery sizes available are simply not large enough for all their needs. These users may wish to purchase a fuel cell/hydride system even at very high costs.

The fuel cell/sodium hydride system is capable of fulfilling the needs of users not satisfied with the conventional battery system and can compete with the battery system for certain types of power wheelchair users. If the price of sodium hydride should drop due to a larger market, the cost difference would become small and the advantages of this alternative system would make it very attractive to all wheelchair users.

References

- (1) "Proceedings for the Stakeholder Forum on Wheeled Mobility", Rehabilitation Engineering Research Center on Technology Transfer (T2RERC). November 1999.
- (2) DiGiovine, C.; Cooper, R. "Battery Power & You: How to Choose", SpinLife.com. January 2000.
- (3) Medsupport FSF International. "Wheelchair Preventive Maintenance", Medsupport FSF Newsletter. June/July 1999.
- (4) Rowan, E.J. "Batteries & Chargers", Wheelchair Services of the Eastern Paralyzed Veterans Association (www.epva.org/wheelchair). 2001.
- (5) DiPietro, P.; Skolnik, E. "Analysis of the Sodium Hydride-based Hydrogen Storage System being developed by PowerBall Technologies, LLC". October 1999. Appears in *Proceedings of the 2000 Hydrogen Program Review* (www.doe.gov/hydrogen/docs/28890toc.html).
- (6) *Chemical Market Reporter*, April 9, 2001.
- (7) Wilson, M., Los Alamos National Laboratory. Personal Communication. 2001.
- (8) Porter, S.L. "Battery Questions Answered", Wheelchair Sales & Service, Inc. 2001.

Analysis of Fuel Choices for Fuel Cell Vehicles

Johannes Thijssen and Stephen Lasher

Arthur D. Little, Inc.
Acorn Park
Cambridge MA, 02140

Introduction

The DOE Office of Transportation Technologies has been supporting the development of polymer electrolyte membrane fuel cells (PEMFC) for transportation applications. A study was commissioned by DOE to assess the potential impact of various fuel choices for fuel cell vehicles; comparing the feasibility, efficiency, economy, and safety of direct hydrogen fuel cell vehicles (FCVs) with on-board reforming. Excerpts from that study are presented here.

Approach

Arthur D. Little has developed detailed well-to-wheel performance and cost calculations for FCVs taking into account technology options, system integration and efficiencies, hybridization, vehicle weight, and drive cycle. To the extent possible, we have taken advantage of Argonne National Lab's GREET model, and updated its fuel chain assumptions (especially for hydrogen) with original analysis where necessary. We also incorporated a more thorough analysis of FCV performance over the drivecycle, based on a detailed assessment of FCV powertrain weights and turn-down characteristics. Additionally, we determined fuel and vehicle ownership costs based on detailed hydrogen fueling station cost analysis and bottom-up fuel cell component cost analysis.

Each of the options analyzed and shown in this report represent future established markets for fuels and vehicles, not early market penetration of the technologies. This means that for the purpose of the analyses, we made assumptions that are consistent with established markets, i.e. established fuel infrastructure and vehicles produced in high volumes. The assumptions are also consistent with projected cost and performance scenarios for 2010.

Results

The powertrain efficiency assumptions (i.e. performance curves) for FCVs are presented in Figure 1 with a comparison to a conventional internal combustion engine (ICE). The performance curves are constructed from the sum of the fuel cell, parasitic power, and reformer (when present) efficiencies at full to part load. The fuel cell efficiencies are constructed from our kinetic analysis of reformat and direct hydrogen fuel cells based on current data and projected scenarios of future performance¹. The analysis includes the effect of low pressure at part load and high temperature membrane operation. The single cell voltage at full power is selected to be 0.8 V for high efficiency and consistency with previous DOE analyses². The single cell voltage operating point is higher at part load. The parasitic power calculations are based on the DOE goals for compressor/expander module performance and our own thermodynamic analysis for direct hydrogen and reformer-based systems. The reformer efficiencies are based on in-house thermodynamic and kinetic analyses. We assumed future

improvements in reformer turn-down and/or operating strategies that will allow a turn-down of 20:1.

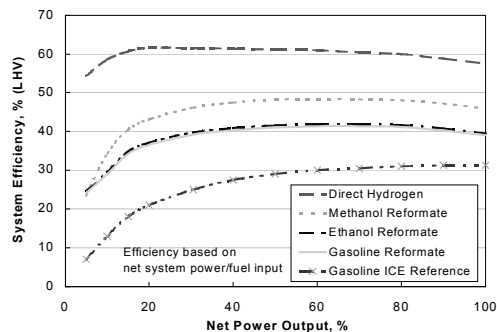


Figure 1. Fuel cell vehicle powertrain efficiency assumptions

Preliminary well-to-wheel energy use results for conventional ICE vehicles (ICEV), hybrid electric vehicles (HEV), and FCVs can be found in Figure 2. FCV results are based on aggressive technology improvements compared with the current technology status. These improvements would occur if existing multi-year R&D programs were successful in achieving their technical targets within reasonable bounds, and if the system integration were optimized to take advantage of the improvements in basic stack and fuel processor technology. The most significant improvement in fundamental technology assumed here was the availability of high temperature membranes.

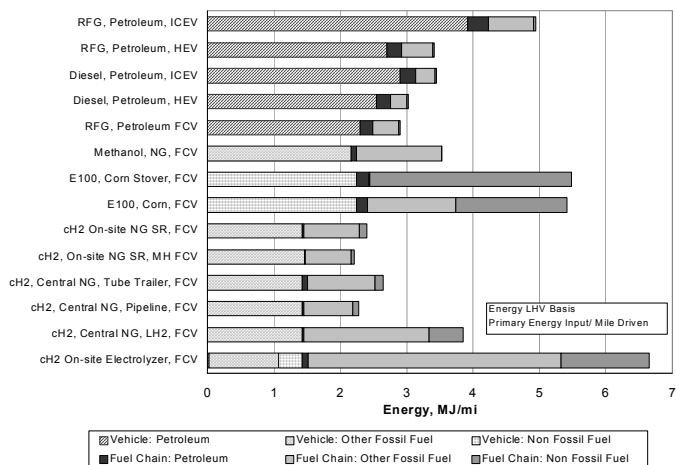


Figure 2. Well-to-wheel energy use for various vehicle and fuel choices

The reformulated gasoline (RFG) and ethanol (E100) FCVs are assumed to be PEMFCs with autothermal reformers (ATR) for hydrogen generation. The methanol FCV uses a low temperature steam reformer (SR) to generate hydrogen while the compressed hydrogen (cH₂) for the direct hydrogen FCVs is produced off-board. Energy inputs for corn stover and corn based E100 production are partially allocated to other coproducts.

The central production cH₂ options include central steam reformer (SR) production from natural gas (NG) with tube trailer, pipeline, or liquid (LH₂) delivery to a hydrogen fueling station. The local cH₂ production options include local SR production from NG and local electrolyzer production from the U.S. average power plant mix. All cH₂ FCV options assume high-pressure on-site storage (3600 psia on-site storage to 5000 psia on-board the vehicle) except

¹ Carlson, E.J. "Cost Analysis of Fuel Cell System for Transportation – Pathways to Low Cost", 2001 Final Report, prepared for DOE, to be published in 2002

² Carlson, E.J.; Thijssen, H.J. "Cost Analysis of Fuel Cell Stacks/Systems", 2001 Annual Progress Report - Fuel Cells for Transportation; DOE, OTT; pp. 40-43.

the metal hydride (MH) FCV option which assumes low-pressure on-site storage (100 psia on-site and on-board storage).

Fuel price estimates for hydrogen are shown in Figure 3 compared to gasoline. "Central Plant" cost includes the central production costs and "Fuel Station" cost includes transportation from the central plant (when applicable), capital, operation and maintenance, and energy costs of the local fueling station. All central plant options assume 50 miles transportation distance to the local fueling station. Costs include margins but exclude taxes.

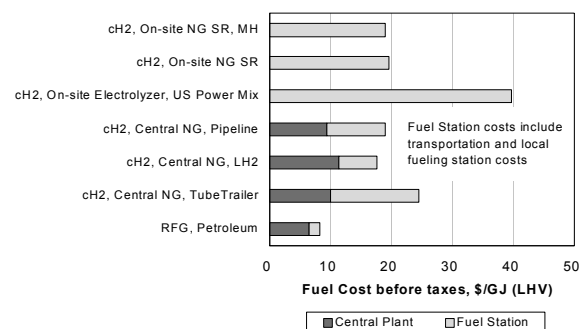


Figure 3. Comparison of hydrogen and gasoline costs

Hydrogen fueling station capital costs are based on detailed vendor quotes for equipment, which have been adjusted for higher production volumes (100 units/year). The natural gas and electricity costs for the local fueling stations are assumed to be \$5/MMBtu and \$0.07/kWh, respectively, based on the 2010 EIA commercial rate projections. All fueling stations assume 690 kg/day hydrogen capacity (~300 vehicles/day) integrated into existing gasoline fueling stations.

Figure 4 shows vehicle ownership costs on a \$/year basis, assuming a 5 year finance period. FCV costs are based on stretch goals for fuel cell system performance and assume high automotive production volume (500,000 units/year) manufacturing. ICEV costs are based on conventional vehicles. All vehicles assume the same mid-sized vehicle platform with 350 mile range except for the Battery Electric Vehicle (EV), which has only a 120 mile range. Fuel costs are estimated based on calculated vehicle fuel economies and estimated 2010 fuel prices before taxes. The fuel price for hydrogen vehicles assumes \$20/GJ. O&M costs have not been analyzed in detail and are assumed to be essentially the same for all vehicles.

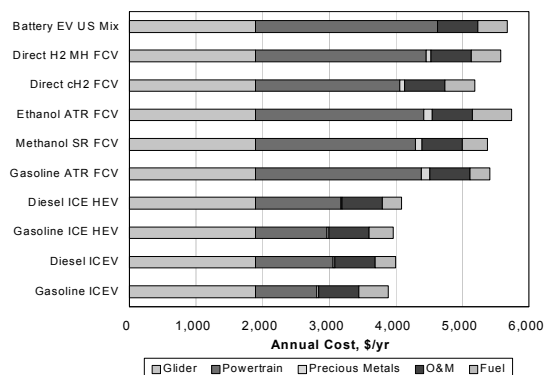


Figure 4. Vehicle ownership costs for various vehicle and fuel choices

Conclusions

Fuel cell vehicles are expected to be able to achieve the lowest well-to-wheel energy consumption, provided efficient fuel chains are used. However, substantial additional technology breakthroughs will

be required to achieve FCV cost competitiveness with ICEVs. Fuel economy and cost results are based on aggressive technology goals for hydrogen storage, fuel cell, and reformer power density, cost, and performance.

Energy Use. Part load efficiency is a major contributor to overall tank-to-wheel energy use because the vehicle spends most of its time at part load. Reformer based powertrains have much lower efficiency at part load due to heat losses and other inefficiencies in the reformer. High turn-down or other operating strategies that improve the minimum load efficiency are essential to the performance of reformer-based vehicles.

Direct hydrogen FCVs carrying compressed hydrogen produced from natural gas can offer well-to-wheel energy consumption of approximately half of conventional gasoline-fueled vehicles: an unparalleled well-to-wheel efficiency. This high efficiency is due to excellent turn-down performance, resulting in very high (~80 mpg) vehicle fuel economy. It is also necessary to have thermally well-integrated hydrogen production facilities and modest transportation distances (< 50 miles) for centralized production.

Gasoline-fueled FCVs (with on-board reformer) are expected to achieve a 40% lower well-to-wheel energy consumption than conventional vehicles. The use of methanol in fuel cell vehicles leads to a considerably higher well-to-wheel energy consumption, despite the high vehicle efficiency, due to the significant losses incurred in fuel production. However, the use of methanol simplifies on-board fuel processing. The inefficiency of ethanol production leads to well-to-wheel primary energy consumption for ethanol FCVs slightly above that of conventional vehicles. Primary fossil fuel consumption is of course strongly reduced.

Diesel HEVs can also approach a 40% reduction in well-to-wheel energy consumption over conventional vehicles (as the gasoline-fueled FCVs). Electrolyzer-based hydrogen production has high energy consumption due to the relative inefficiency of power generation, resulting in a well-to-wheel energy consumption higher than that of conventional vehicles.

Cost. The most economical hydrogen fuel chains are expected to be two to three times more expensive than gasoline, on a \$/GJ basis. Hydrogen capital costs are four to seven times more expensive than gasoline capital costs (including local and central plant capital). Transportation and distribution costs (including local compression and storage at the fueling station) are far higher than those for gasoline. Electrolyzer-based production is costly with EIA energy price projections. Scenarios for load shifting and power price reductions were not analyzed here.

Even including the technology improvements over current technology, FCVs are expected to add several thousand dollars to conventional ICE powertrain cost. Powertrain costs for direct-hydrogen FCVs are lower than those of systems with on-board reformers because: fuel processors add cost and weight, fuel cell stacks operating on reformate are larger due to reformate quality effects, and the heavier reformate system results in additional vehicle power requirements. Direct hydrogen FCV cost could be further reduced if cost were optimized such that efficiency dropped to provide equal well-to-wheel primary energy consumption to gasoline FCVs.

Higher vehicle costs for gasoline reformer based FCVs make them more expensive despite fuel cost savings. However, some alternative fuels, especially hydrogen, will require significant upfront investment, representing a risk to both vehicle manufacture and fuel provider stakeholders. Dealing with this risk represents a formidable barrier to the use of hydrogen for FCVs.

Acknowledgement. This work was supported by the Office of Advanced Automotive Technologies, U.S. Department of Energy, under contract DE-FC04-02AL67602.

Catalyst Development for the Reforming Process of Liquid Hydrocarbons

Christina R. Manns, Heather A. Elsen, and Charles E. Taylor

U.S. Department of Energy
National Energy Technology Laboratory
P.O. Box 10940
Pittsburgh, PA 15236-0940

Introduction

Fuel cells are fast becoming a desirable source of electricity to power automobiles and light-duty trucks. They are currently used in some small stationary applications and have the potential to power residential and commercial buildings. Fuel cells, powered by hydrogen, have the potential to be the cleanest and most efficient source of electricity for use by the automotive industry. Our goal is to develop a process that will use a liquid hydrocarbon fuel as the hydrogen source in an on-board fuel cell. A problem in current reforming processes is the quantity of carbon monoxide (CO) produced. Carbon monoxide acts as a poison upon contact with the proton exchange membrane (PEM) fuel cell (Pt based) catalyst. The objective of our research is to reduce the quantity of carbon monoxide produced during reforming to near-zero levels.

Published investigations [1] have indicated that copper-based catalysts may be the optimum catalyst for use in the reforming of liquid hydrocarbons, such as methanol and petroleum-based fuels. Our earlier investigations of a selective copper-based catalyst and various modifications agree with these scientific studies and experiments. However, our initial studies were done using only methanol as a feed, while other studies have used water and methanol as a feed with a ratio between 1.0 and 1.3. In fact, our system demonstrated higher methanol conversion over an extended period of time than what was recorded in other experimental studies and research [2]. This led us to our current investigative studies, which involve using water and methanol with a volume ratio of 1.0. Our studies have indicated that methanol conversion is approximately the same as that reported in the literature [1], however, we observed higher hydrogen yields.

Experimental

The catalysts were prepared by sequential precipitation. 4.62 g $Zr(NO_3)_2O$, 1.50 g $Al(NO_3)_3 \cdot 9H_2O$, and 1.53 g $Y(NO_3)_3 \cdot 6H_2O$ were dissolved in 125 ml distilled water. The solution was heated in a 1500 ml beaker to about 70°C on a hot plate with magnetic stirring for 10 minutes. 33.34 g $Cu(NO_3)_2 \cdot 3H_2O$ in 250 ml distilled water was added dropwise to the solution while a pH of 7 was maintained using Na_2CO_3 solution. A pH meter was used to monitor pH while adjustments were made by adding the Na_2CO_3 with a dropper as needed. After approximately 20 minutes, 10.14 g $Zn(NO_3)_2 \cdot 6H_2O$ in 125 ml distilled water was added dropwise over a 15 minute interval to the solution. The pH was maintained at 7 using the same Na_2CO_3 solution. The product was recovered by filtration using a Büchner funnel and aspirator. The product was washed three times with distilled water. The sample was dried at 120°C over night followed by calcination in air at 350°C for 6 hours.

All reactions were conducted in a 0.5 inch od x 0.375 inch id (1.27 cm od x 0.95 cm id) x 10 inch (25.4 cm) 304 stainless steel reactor. The inside wall of the reactor was coated with Restek Corporation's SilcoSteel® coating. The catalyst was supported in the reactor between quartz-wool plugs and the reactor was operated in an up-flow configuration. A gold-plated thermocouple in the center of the catalyst bed was used to control the temperature of reaction to $\pm 0.5^\circ C$. Brooks proportional ratio mass-flow controllers were used to feed the gases to the reactor. An Isco high-pressure syringe pump controlled feeds of liquids to the reactor. The feeds were preheated to approximately 130°C prior to entering the reactor and the products of reaction were heated to approximately 150°C between the exit of the reactor and the cold trap, which was maintained at $-4^\circ C$.

Reaction conditions were as follows: 1.0000 grams of catalyst were placed in the reactor supported between deactivated-quartz wool plugs such that the tip of the thermocouple was located in the middle of the catalyst bed. The reactor was purged with helium at 5 mL/min for at least 2 hours. The temperature of the reactor was increased to either 150 or 255 °C. Methanol flow was begun, at a weight hourly space velocity of 1 hr^{-1} , after the catalyst had reached the desired temperature.

Products of reaction were directly sampled and analyzed by an online dual-column gas chromatograph (GC). The GC, a Hewlett-Packard 5890 Series II, was equipped with a 6 ft x 0.125 od 80/100 Porapak Q and a 20 ft x 0.125 od 60/80 Molecular Sieve 5A (both obtained from Supelco). The GC was held at a constant temperature of 100°C during elution. Argon was used as the carrier gas having an average linear velocity, at 30°C, of 30 mL/min for the Molecular Sieve column and 50 mL/min for the Porapak Q column. The Molecular sieve column was used to separate the light gaseous products while the Porapak Q column was used to identify unreacted liquid hydrocarbons. Both columns were equipped with back-flushing capability. Dual thermal conductivity detectors (TCD's) were employed to detect the separated components.

Results and Discussion

Reforming of methanol was done using methanol only and then using methanol and water with a 1:1 volume basis. Reforming of methanol only was run at various reaction temperatures. Table I list the data from a series of those methanol-reforming reactions.

TABLE I Results of Methanol Reforming Reactions

Catalyst	Temp. (°C)	CH ₃ OH Conversion	H ₂ (%)	CO ₂ (%)	CO (%)
Cu/Zn/Zr/Al/Y*	150	21.2	8.9	91.1	0.0
Cu/Zn/Zr/Al/Y*	255	72.2	91.1	8.9	0.0
Cu/Zn/Zr/Al/Y**	255	49.1	77.6	16.6	5.8
Cu/Zn/Ce/on α -Al ₂ O ₃	255	85.1	47.2	22.5	29.3
Cu/Zr/ on α -Al ₂ O ₃	255	80.9	53.5	40.6	5.9
Cu/Zn/Zr/ on α -Al ₂ O ₃	255	90.5	45.5	35.2	19.3

* 69/17/10/2/2 mole percent. ** 8/2/64/13/13 mole percent.

As is shown in Table I, methanol conversion increases with reaction temperature. For the Cu/Zn/Zr/Al/Y 69/17/10/2/2 mole

percent) catalyst at 150°C, methanol conversion was approximately 21%. The majority of product detected by the GC was carbon dioxide. When the reaction temperature was increased to 255°C, conversion of methanol increased initially to 80%. The product selectivity also increased, with hydrogen comprising approximately half of the detected product.

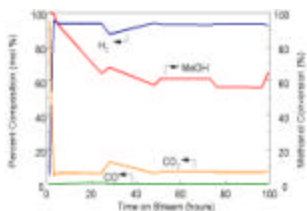


Figure 1 Results of methanol conversion over Cu/Zn/Zr/Al/Y catalyst as a function of time.

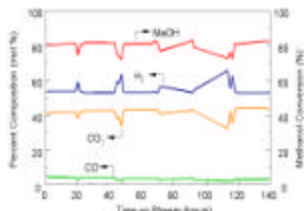


Figure 2 Results of methanol Cu/Zr on α -Al₂O₃ catalyst as a function of time.

Figure 1 shows an extended conversion run for the Cu/Zn/Zr/Al/Y (69/17/10/2/2 mole percent) catalyst. As is shown in Figure 1, conversion of methanol at 255°C decreased with time on stream. This is due to coke formation during the reaction.

When compared to the literature values [1], our catalyst gave similar results. Conversion of methanol was low at 150°C and increased with increasing temperature. Conversions of methanol at 250°C were greater than 50% in both cases. Differences arise when the product slate is examined. Our catalyst produced larger quantities of carbon dioxide than those reported in the literature.

Of importance is that carbon monoxide was not detected at either reaction temperature in our investigation or in the literature with the Cu/Zn/Zr/Al/Y catalyst.

Figure 2 shows an extended conversion run for the Cu/Zr on α -Al₂O₃ (7/3/90 mole percent) catalyst. As is shown in Figure 2, conversion of methanol at 255°C is relatively stable with time on stream as are the products produced. This catalyst did exhibit CO production at 255°C, however coking was much less than that observed with the Cu/Zn/Zr/Al/Y catalyst.

The same group of catalysts was run using a 1:1 volume methanol/water feed and a reaction temperature of 250°C. The results of reactions of methanol and water are listed in Table II. As is shown in Table II, conversion of methanol for all the catalysts except the low surface area Cu/Zn/Zr/Al/Y were greater than 99%. Product selectivity for the experiments using water and methanol as a co-feed exhibited lower carbon monoxide levels than the experiments with methanol alone..

Figure 3 shows an extended conversion run for a 1:1 methanol/water reaction over the Cu/Zn/Zr/ on α -Al₂O₃ (12/2.5/2.5/83 mole percent) catalyst. As is shown in Figure 3, conversion of methanol at 255°C remains constant with time on stream. Of importance is that carbon monoxide was almost nonexistent at either reaction temperature in our investigation with the Cu/Zn/Zr/ on α -Al₂O₃ catalyst. Note that carbon monoxide was not observed in the methanol/water reactions when it was observed for the methanol only reactions.

When using methanol and water as a co-feed and the higher temperature of 250°C, methanol conversions increased by another 50%.

TABLE II Results of Methanol/Water Reforming Reactions

Catalyst	Temp (°C)	CH ₃ OH Conversion	H ₂ (%)	CO ₂ (%)	CO (%)
Cu/Zn/Zr/Al/Y*	250	100	59.0	35.8	4.3
Cu/Zn/Zr/Al/Y**	250	21.2	7.9	4.8	0.0
Cu/Zn/Ce/ on α -Al ₂ O ₃	250	99.0	57.6	38.5	3.7
Cu/Zr/ on α -Al ₂ O ₃	250	99.4	43.2	30.4	1.1
Cu/Zn/Zr/ on α -Al ₂ O ₃	250	99.7	60.9	38.0	0.98

* 69/17/10/2/2 mole percent. ** 8/2/64/13/13 mole percent.

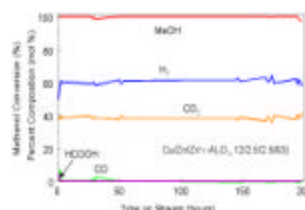


Figure 3 Results of methanol/water conversion over Cu/Zn/Zr on α -Al₂O₃ catalyst as a function of time.

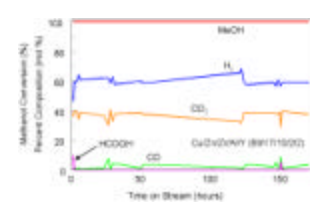


Figure 4 Results of methanol/water conversion over Cu/Zn/Zr/Al/Y catalyst as a function of time.

Figure 4 shows an extended conversion run for a 1:1 methanol/water reaction over the Cu/Zn/Zr/Al/Y (69/17/10/2/2 mole percent) catalyst. As is shown in Figure 4, conversion of methanol at 255°C is relatively stable with time on stream as are the products produced. This catalyst did exhibit CO production at 255°C, however coking was not observed.

Table III Catalyst Surface Area

Catalyst Composition (mole %)	Surface Area (as prepared) (m ² /gm)	Surface Area (after reaction) (m ² /gm)	Surface Area (after reaction w/H ₂ O) (m ² /gm)
Cu/Zn/Zr/Al/Y 69/17/10/2/2	92	55	57
Cu/Zn/Zr/Al/Y 8/2/64/13/13	21	16	
Cu/Zr/ α -Al ₂ O ₃ 12/5/83	200	188	
Cu/Zn/Zr/ α -Al ₂ O ₃ 12/2.5/2.5/83	198	187	186
Cu/Zn/Ce/ α -Al ₂ O ₃ 12/2.5/2.5/83	194	195	194

Table III shows the surface area of the catalyst as prepared, after 150 of reaction with methanol reforming, and after 150 hours of

methanol/water reforming. As is shown in Table III, both catalyst preparations of Cu/Zn/Zr/Al/Y exhibit a loss of surface area after reaction due to coking. The three catalysts supported on γ -Al₂O₃ retain more than 90% of their as prepared surface area. These catalysts were also the most stable of all the catalysts that we tested.

Conclusions

We have synthesized several catalysts that are capable of reforming methanol at moderate temperatures. The main products of reaction are hydrogen and carbon dioxide. Our results agree well with those reported in the literature [1]. We observed higher selectivity of H₂ with our catalysts without the need for the water-gas shift reaction. However, by employing the WGS reaction we detect a decrease in the selectivity of CO and CO₂. A direct correlation between the catalyst's surface area, methanol conversion, and catalyst stability is also observed.

Acknowledgement.

The authors would like to acknowledge the technical assistance of Richard R. Anderson, Bret Howard, Edward P. Ladner, and Dirk D. Link.

Disclaimer

Reference in this report to any specific commercial product, process, or service is to facilitate understanding and does not necessarily imply its endorsement or favoring by the United States Department of Energy.

References

1. Breen, J.P. and Ross, J.R.H. *Catal. Today* 1999, 51, 521.
2. Taylor, C.E. and Manns, C.R. *Preprints of the Fuels Division* 2001, 46(2), 652.

Catalytic Hydrogen Production for Small Portable Power Applications

Jianli Hu, Yong Wang, Cathy Chin, Daniel Palo, Jamie Holladay, Robert Rozmiarek, Robert Dagle, James Cao, Ed Baker

Pacific Northwest National Laboratory, Richland, WA 99352, USA

Introduction

Recent global energy shortages and more stringent emission regulations have stimulated research and development in fuel cell applications. A fuel processor is a critical technology for the deployment of a polymer-electrolyte membrane (PEM) fuel cell for on-board and stationary applications. Typically, a fuel processor produces a hydrogen rich stream from hydrocarbon feeds through a multi-step process (fuel vaporizer, reformer, and CO clean-up). Optimal integration of these various processes is key to the design of efficient fuel processors. Fuel cell based portable power devices offer significant advantages over current battery technologies in terms of power density. Developers of remote portable power devices are facing the challenges of supplying on-board hydrogen to the fuel cell for extended periods of operation[1,2]. As part of the development of a highly efficiency on-board 0.1-50 W_e fuel processor for portable applications, PNNL has investigated the steam reforming of methanol with various catalyst systems under high throughput conditions. Under steam reforming conditions, current PNNL catalysts produce mainly CO₂ and H₂ along with minimal amount of CO. The concentration of CO in the product stream has been found to be lower than reported for the well-studied commercial Cu based catalyst[3]. A hydrogen rich stream with low CO content is highly desired since the electrocatalyst at the fuel cell anode is extremely sensitive to CO poisoning at the operating temperature of PEM fuel cells. Catalytic CO reduction processes are being developed to reduce CO concentration to levels acceptable by PEM fuel cells.

Experimental

Catalyst screening tests were carried out in a 4 mm I.D. quartz tube reactor. Approximately 0.200g of catalyst was loaded between two layers of quartz wool inside the reactor. A thermocouple was placed in the middle of the catalyst bed. A premixed 1:1wt % methanol-water feed was introduced into the reactor by using a syringe pump. The feed rate was adjusted such that the reaction was conducted under 100 ms contact time, which is equivalent to a standard GHSV of 36000 h⁻¹. Prior to entering the reactor, the feed was fully vaporized through a vaporizer, operated at 200 °C. Prior to activity testings, the catalysts were reduced *in-situ* under 10 % H₂/N₂ at 350 °C. A glass condenser at 0°C was used to separate liquid products from gaseous products. The product gases, CO, CO₂, and H₂, were separated using MS-5A and PPQ chromatographic columns, and analyzed on-line by means of a Hewlett Packard Micro GC (Model Q30L) equipped with a TCD

After catalyst screening tests, steam reforming catalysts were structured and integrated into micro channel reactor. The structured engineered catalysts were tested in micro channel reactor over a temperature range of 250°C to 450°C. Distilled de-ionized water was added to the fuel to make a mixture with the desired molar ratio of steam to carbon. The first test was to determine an optimal steam to carbon ratio for methanol processing. The catalysts were tested over a range of molar steam to carbon ratio from 3:1 to pure methanol, and a contact time of approximately 100 ms, except for the flow of pure

methanol. Figure 1 shows the schematic flow diagram of testing devices.

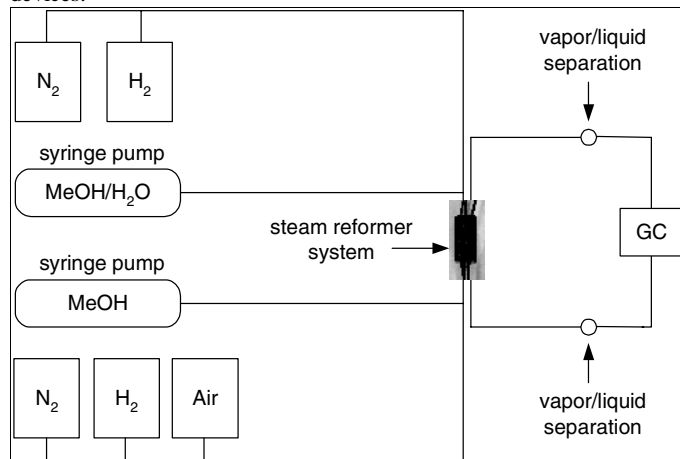


Figure 1. Testing equipment schematic

Results and Discussion

Performance of Methanol Steam Reforming Catalysts

Conventionally, methanol steam reforming is conducted in fixed-bed reactors using Cu/Zn/Al catalyst. The throughput varies from 1-5 second contact time (GHSV between 720-3600 h⁻¹). In micro channel reactors, throughput is increased to sub-second contact time (GHSV>36000h⁻¹). In order to achieve high energy density, the efficiency of the reformer must be high. As shown in Figure 2, methanol steam reforming tests were conducted at different contact times. As expected, with an increase in contact time, the temperature required to achieve >99% conversion also decreased. The advantage of operating at lower temperature and longer contact time can be lower methane formation, longer catalyst life and minimum insulation. However, the desired reactor volume is relatively larger due to relatively low throughput. In micro reactor design, the balance between operating temperature and contact time is one of the major design criteria.

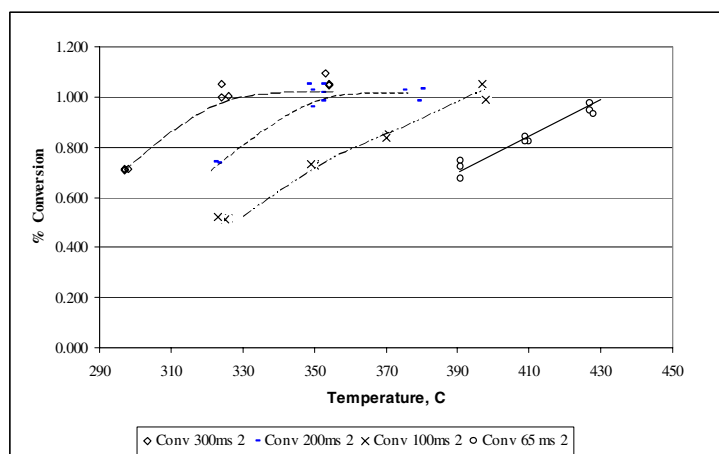


Figure 2. Effect of contact time on methanol reforming

Since the portable power devices are designed to operate for extended periods of time, catalyst deactivation should be taken into consideration. In the past few years, PNNL has developed several steam reforming catalyst systems with very minimum deactivation rates. Catalyst can be operated for about few hundred hours without major deactivation.

Steam Reforming of Different Hydrocarbon Fuels

Different hydrocarbon can be steam reformed at different temperatures, and sometimes this may require different catalyst compositions. Compared with other hydrocarbons, steam reforming of methanol can occur at relatively low temperature and low steam to carbon ratio. High conversion of about 100% can be reached at 300 °C, ambient pressure and 100 ms contact time. Hydrogen productivity is at least 6 times higher than that reported in the literature for other catalysts under the same conditions.

Table 1. Fuel processor feed energy density (hydrocarbon + water)

Fuel	Steam to Carbon Ratio	Energy kW _t -hr/L	Energy kW _t -hr/kg	Catalyst Performance Temperature (°C)
Methanol	1	2.81	3.29	300-400
n-Butane	2	2.57	3.11	450-650
n-Octane (gasoline)	2	2.67	2.99	550-750

Catalyst Performance in Micro Channel Demonstration Device

Currently at PNNL, portable high-energy density power supply devices are being developed. These power supply devices (once coupled to appropriately sized fuel cells) will provide more extended operating times and efficiencies for microelectronic devices than conventional battery technologies[5,6]. Recently, an integrated methanol fuel reformer system has been designed and built. Initial testing of the engineered fuel reformer system resulted in the production of 200 mW_t of hydrogen at a high efficiency of 9% utilizing methanol as fuel. The reformat stream was composed of hydrogen (73-74%), with 25-26% carbon dioxide and less than 1% carbon monoxide. The device very nearly approached the ideal conversion ratio of 3 moles hydrogen produced per mole of methanol reacted. A complete system would consist of liquid and gas delivery systems, valves, packaging, and integration with a fuel cell.

Carbon Monoxide Reduction

We have successfully reduced CO concentration in reformat to less than 0.6%, but this is still above the limit required by a PEM fuel cell. Options for CO clean-up including preferential oxidation, methanation and use of hydrogen membrane are considered. We are able to reduce CO to the level acceptable by certain type of PEM fuel cells.

Conclusions

Steam reforming catalysts have been developed and integrated into micro channel reactors for high efficiency portable power devices. The integrated system can be operated at GHSV greater than 36000 h⁻¹ to achieve high power density. The integrated reforming and CO clean-

up processes allow us to develop a light portable power systems for remote operation purposes.

Acknowledgement

This work was supported in part by Defense Advanced Research Projects Agency contract # DABT63-99-C-0039. Their support is gratefully acknowledged.

References

- Holladay, J.D., P. Humble, J. Harb, R. LaFollette, L. Salmon, R. Barksdale, and B. Anderson. "Ni/Zn and Li-ion Rechargeable Microbatteries for Use with MEMS Devices." *The 195th Meeting of the Electrochemical Society, Inc.*, Seattle WA, USA, The Electrochemical Society, 1999.
- Koeneman, P.B., I.J. Busch-Vishniac, and K.L. Wood. "Feasibility of Micro Power Supplies for MEMS." *Journal of Microelectromechanical Systems* 6 (4) pp. 355-362. 1997.
- Hu, J., Wang, Y., VanDerwiell, D., Chin, Y-C., Palo, D., Rozmiarek, R., Dagle, R., Cao, C., Holladay, J., Baker, E.G. "Development of Fuel Processor Catalyst for Portable Power Applications." *Chem. Eng J.*, submitted July 2001.
- Tonkovich, A.Y., J.L. Zilka, M.J. Lamont, Y. Wang, R.S. Wegeng. "Microchannel Reactors for Fuel Processing Applications. I. Water Gas Shift Reactor." *Chem Eng Sci.* 54, pp. 2947-2951, 1999.
- Palo, D.R., J.D. Holladay, E.O. Jones, R.T. Rozmiarek, C. Guzman, Y. Wang, Hu, J., Dagle, R.A. Baker, E.G. "Fuel Processor Development for a Soldier-Portable Fuel Cell System." *IMRET 5 2001 International Conference on Microreaction Technology*, Strasbourg, France, 2001.
- Jones, E.O., J. Holladay, Perry, S., Orth, R., Rozmiarek, R., Hu, J., Phelps, M., Guzman, C. "Sub-Watt Power Using an Integrated Fuel Processor and Fuel Cell." *IMRET 5 2001 International Conference on Microreaction Technology*, Strasbourg, France, 2001.

CATALYTIC PRODUCTION OF HYDROGEN GAS BY METHANOL REFORMING

Erdogan Gulari, and J. Chris Brown

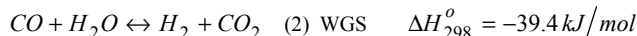
Department of Chemical Engineering
University of Michigan
2300 Hayward St.
Ann Arbor, MI 48109

Introduction

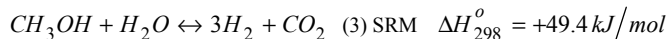
Recently, there has been a big move forward to find alternative methods to the current propulsion system in automobiles. These alternative methods need to preserve oil and provide more environmentally friendly exhaust than the current internal combustion system. One such, potentially viable alternative, is the use of PEM fuel cell system. Fuel cells turn hydrogen gas into useful electric power with an efficiency that is not limited by thermodynamics. Due to current infrastructure and safety concerns, hydrogen gas cannot be stored on-board. It is proposed that hydrogen be produced on-board as needed from liquid hydrocarbons. Methanol reforming is a proposed method of producing hydrogen gas on-board. This method has a couple of advantages: unlike oil, liquid methanol can be readily produced from biomass, it is easily adaptable to current infrastructure, it is easily transported and stored, and finally it has more hydrogen density than hydrogen gas.^{1,2} The methanol must be converted to hydrogen gas without the production of harmful gases such as CO, because they deactivate the PEM fuel cells. There are three main reactions that extract H₂ from methanol. The first reaction is decomposition of pure methanol.



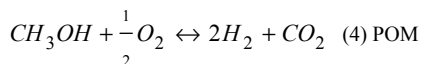
There are two issues concerning this reaction. The first is this is an endothermic reaction, thus heat must be provided to sustain the reaction. Second, the carbon monoxide is harmful to the fuel cells, so some downstream processing must be done to eliminate the CO. This can be done with the water-gas shift reaction.



The next method of producing H₂ gas from methanol is the steam reforming of methanol. This involves the sum of reactions 1 & 2 combined into one step as given in eq. 3:



This reaction is also endothermic and requires heat. However, steam reforming also produces some CO as a byproduct. The last major reaction is partial oxidation of methanol (POM). It proceeds as follows:



$$\Delta H_{298}^{\circ} = -192.2 \text{ kJ/mol}$$

This reaction is exothermic and can provide heat to the SRM and DEC reactions.^{3,4}

Experimental

Catalyst Preparation. Various formulations of Pd/CeO₂-Al₂O₃ and Pt/CeO₂-Al₂O₃ catalyst were prepared for testing. The Al₂O₃ supported catalysts were made by either conventional impregnation or sol-gel techniques. The CeO₂/Al₂O₃ was always made by sol-gel and was used as a support for the impregnated metal. It was prepared

as follows; The aluminum isopropoxide was added to a beaker of water at 80°C. After 30 minutes of stirring, nitric acid was added. This will result in a fibrillar sol. Cerium (III) oxide was added to the sol at room temperature and then the mixture is mixed and aged until gelation occurred. The gel was then dried overnight at 100°C. The resulting sol-gel was then crushed and sieved at 100 mesh. Next the required amounts of Pt (from H₂PtCl₆) or Pd (from Pd(NO₃)₂) was impregnated in the CeO₂/Al₂O₃. A few catalysts, such as Pt/Al₂O₃ were made by the single step sol-gel process (i.e. the metal precursor was incorporated into the gel). In this case, the Pt or Pd precursor was added immediately after the Ce in the sol-gel process, instead of impregnation at the end. All catalysts were dried at 373 K for 24 hrs, and calcined at 773 K for another 24 hrs. The catalysts were reduced under the conditions of: 20/80 hydrogen/helium 100 ml/min gas at 573 K.

Activity testing. The reforming of methanol was conducted using an ordinary, vertical fixed bed reactor under atmospheric pressure. A Pyrex glass tube was used as the bed. The system was charged with 60 mg of catalyst. The catalyst was held in place by a glass wool plug. The reactions took place at temperatures ranging from 433-673 K. The thermocouple tip was positioned to touch the top of the catalyst. The liquid, either pure methanol or a water-methanol mixture, was vaporized and then combined with the carrier gas, helium. The total flow rate ranged from 43,000-120,000 ml⁻¹ h⁻¹ g-cat⁻¹. The products were then separated by a HP 5710A GC with a Carbosphere 80/100 10 ft. column. The products were analyzed using a thermal conductivity detector.

Results and Discussion

Catalytic activity for methanol decomposition. Each catalyst was tested at a space velocity of 43,000 ml⁻¹ h⁻¹ g-cat⁻¹ with 14% methanol and 86% helium. The methanol conversion graphs are shown in Figures 1 & 2. The 2 wt.% Pt/Al₂O₃ sol-gel performed the worst with a 100% conversion occurring at 405°C. The presence of CeO₂ has a significant effect. The 2 % Pt-5% CeO₂/Al₂O₃ exhibited much better activity with the conversion near 100% happening around 360°C.

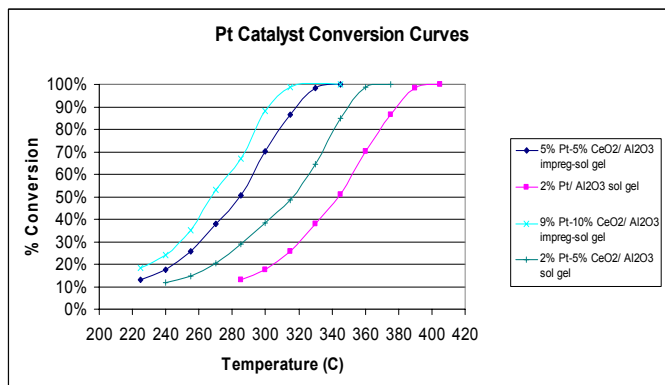


Figure 1. The decomposition curves for the Pt-based catalyst

A higher loading of Pt also has a positive effect on lowering the maximum conversion temperature. The 5% Pt catalyst performed better than the 2% while the 9% Pt catalyst was the best. The palladium catalysts performed similarly.

The 10% Pd-10%CeO₂/Al₂O₃ prepared by impregnation/sol-gel (315°C 99.8% conv.) showed higher activity than the 5% Pd-10% CeO₂/Al₂O₃ prepared by imp/sol-gel(330°C 100% conv). The preparation techniques had little effect on the 5% Pd-10% CeO₂/Al₂O₃. An imp/sol-gel and a single step sol-gel catalyst of the same formulations were made and they behave similar under the

decomposition reaction. They both reached maximum conversion at 330°C. There is also very little activity difference between the Pd

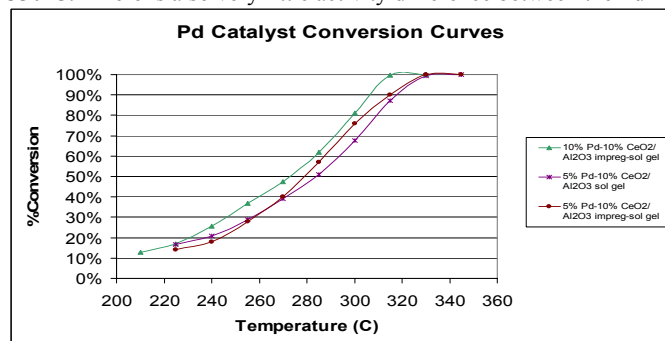


Figure 2. Decomposition curves for the Pd-based catalyst.

and the Pt catalyst. Their complete conversion temperatures are roughly the same for comparable formulations. For all of the catalysts tested the selectivity to H_2 is very high. It is over 98.3 % except for the 2% Pt/ Al_2O_3 sol-gel which produces a selectivity of 91.8%.

Catalytic activity for steam reforming of methanol. The steam reforming of methanol was tested next. Two formulations of catalyst were tested; the 9% Pt-10% CeO_2/Al_2O_3 and the 5% Pd-10% CeO_2/Al_2O_3 both impregnation. The system was run under the condition of $115,000\text{ ml}^{-1}\text{ h}^{-1}\text{ g-cat}^{-1}$ with 50% helium. The rest of the feed was made of water and the methanol. The ratio of water to methanol ranged from 1:1 and 2:1. Since the steam reforming is a combination of the decomposition followed by the water-gas shift reactions, the results will be presented in that manner. The conversion rate for the DEC and WGS will be expressed. For the Pd-based catalyst, the water seems to have very little effect on the complete conversion temperature. The curves are very similar and reach 100% conversion around 330°C. This is comparable for the no water case. For the second reaction, WGS, the conversion curves appear much different. There is no measurable steam-reforming or WGS occurring.

In the case for the Pt based catalyst, the conversion curves appear a bit different. The water does have an effect on the 100% conversion temperature. The presence of water definitely lowers that temperature. Without water the temperature is 315°C, while for the systems with water the 100% conversion temperature is approximately 290°C. The conversion curves for all the experiments containing water look virtually identical, so the amount of water seems to have little effect on the methanol conversion rates. In Figure 3, the conversions for the water-gas shift reactions are displayed. The conversion is based on the initial amount of

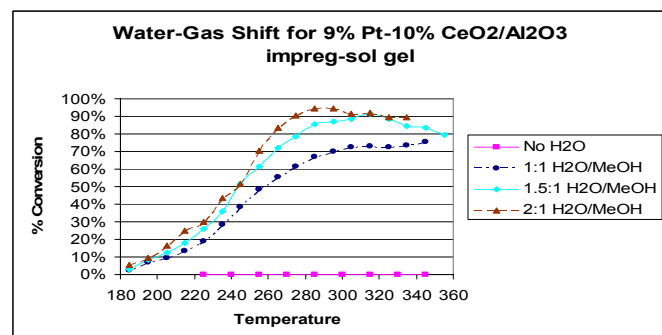


Figure 3. Water-Gas shift or SRM conversion for the Pt-catalyst

methanol. The maximum conversion depends on the amount of water initially. The 1:1 ratio reaches a maximum conversion of 75%, whereas the 1.5:1 has a maximum conversion of 92% and the 2:1 ratio has a maximum of 95%. The temperature at which the maximum conversion occurs also depends on the initial amount of water. The higher the amount of water, the lower the temperature of which the maximum conversion occur. For the 2:1 case, this temperature is 285°C, while for 1:1 case it is 345°C. The 1.5:1 case falls in between with a temperature of 315°C. The water also has an effect on the selectivity of CO_2 produced. The selectivity to CO_2 is higher for higher water to MeOH ratios. The selectivity reaches above 90% for the 1.5 and 2 $H_2O:MeOH$ ratios and the began to level out at around 93% at temperature above 290°C.

Catalytic Activity in the Presence of Oxygen. In this set of experiments, the conditions were similar to SRM experiments except different amounts of oxygen were added. The only catalyst used is the 9% Pt-10% CeO_2/Al_2O_3 catalyst. The conditions were the same as the reaction for 1.5:1 $H_2O:MeOH$ runs except the appropriate amount of oxygen was added. The maximum conversion temperature is affected by the amount of oxygen present at the beginning. The 20% and 32% O_2 runs had the lowest temperature at 255°C and no O_2 had the highest at 315°C. The 6% and 10% fell in between at 305°C and 295°C, respectively. They all reached a maximum conversion of 100%.

The oxygen also had an effect on the WGS reaction. The maximum conversion is affected by the amount of oxygen present. This can be seen in Figure 4. The 32% O_2 reached the highest maximum

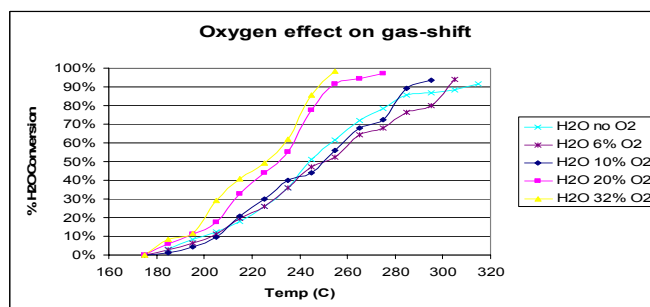


Figure 4. POX of methanol for Pt-based catalyst

conversion at 99%, while the run without oxygen reached a maximum 92%. It seems that the more oxygen present, the higher the conversion. This is not exactly true for 6% and 10% runs. The 6% and 10%, both, have a maximum conversion of 94%. The biggest effect oxygen has on the WGS reaction is at the temperature at which this maximum temperature occurs. This temperature is 255°C for the 32% O_2 , which is the lowest such temperature. The no O_2 run produced the highest such temperature at 315°C. The others three fall in between this two runs. They follow the trend of the higher the oxygen content, the lower the maximum conversion temperature. The more oxygen present, the higher the selectivity to CO_2 . At 20 and 32% O_2 , the selectivity reaches very near 100% and levels out at this level for higher temperatures. In contrast, when there is no water present the maximum selectivity of CO_2 reaches 92%.

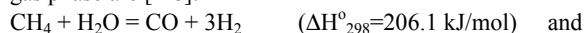
References

- (1) S. Velu, K. Suzuki, T. Osaki, *Chem. Commun.*, **1999**, 23, 2341.
- (2) T. Takahashi, M. Inoue, T. Kai, *Appl. Catal. A-Gen.*, **2001**, 218 1-2, 189.
- (3) L. Alejo, R. Lago, M. A. Pena, J. L. G. Fierro, *Appl. Catal. A-Gen.*, **1997**, 162 1-2, 281.
- (4) H. Jan, I. S. Kim, H. S. Choi, *J. Power Sources*, **2000**, 86 1-2, 223.

CATALYTIC REACTOR CONFIGURATIONS FOR HYDROGEN GENERATION AND INLINE FUEL CELL OPERATION

*Savvas Vasileiadis and Zoe Ziaka
ZiVaTech Institute, 15549 Dearborn Street,
North Hills, CA 91343-32, USA*

Introduction - Processor Description. Utilization of improved reactors and reaction systems for hydrogen production and delivery in the fuel cell is of high importance for the optimized operation of the cell. Both low and high temperature fuel cells use hydrogen as fuel in anode to produce electricity via electrochemical molecular hydrogen oxidation or decomposition reactions. We have reported on improved catalytic permreactors using inorganic membranes for in-situ hydrogen and hydrogen-carbon oxide mixtures separation and delivery in the cell [1-4]. We have examined methane steam reforming combined with water gas shift and paraffinic hydrocarbon dehydrogenation reactions from a kinetic, catalytic and process synthesis point of view [1-4]. Catalysis studies are underway to produce improved catalysts with minimal deactivation. Nickel based catalysts are our starting point due to their low cost and strong performance measures (constant activity on stream for variable feedstocks). The main reactions occurring in gas phase are [1-8]:



Current work is on improved process and reactor configurations for hydrogen fuel delivery in the interconnected cell. Variable composition feedstocks rich in methane are considered. Current designs utilize improved permselective and catalytic materials with different properties for achieving final desired product composition, purity and throughput. The proposed systems are applied to produce hydrogen based fuel mixtures for continuous, reliable fuel-cells operation or direct hydrogen enhanced combustion. Specifically, this initial communication reports on single reactors, multifunctional reactors, and reaction-separation systems -including systems of permreactors and permeators- for hydrocarbon to hydrogen conversion. Exit hydrogen mixtures are used to continuously power fuel cells. Part of the product reformed gas can be used in consecutive chemical synthesis applications; as example part of a H_2 , CO , CO_2 rich product is used for alternative methanol synthesis [1-4]. We present and analyze new processes for steam hydrocarbon reforming and water gas shift reactions including work in experimental design, operation, and best parameter selection and optimization of such systems for specific fuel cell applications. The proposed processes are of increased significance in the area of clean power generation with enhanced pollution minimization. This includes reduction in CO_2 emissions from hydrocarbon reforming plants via CO_2 conversion in consecutive synthesis or recycling routes; also reduction of NO_x emissions due to clean power generation from the fuel cell. There are unique characteristics of the examined operational systems to perform multiple tasks; among others to utilize equilibrium shift principles in hydrocarbon conversion and hydrogen yield through the removal of selective permeative gases out of the conversion zone and utilization of byproduct gases as chemical synthesis blocks [1,2,3]. Similar multifunctional operational systems including permreactors and permeators, or other operation type

reactor-separator networks are suited for environmentally benign and energy efficient higher hydrocarbon reforming. Objective of similar studies is integrated process development for the fuel cell power industry, with increased processing capacity, efficacy, separation, and further utilization of primary and secondary hydrocarbon feedstocks and their produced byproducts. Reduction in carbon deposition propensity is an excess requirement for such reforming, especially in view of converting higher hydrocarbons into hydrogen rich exit mixtures. Nickel and nickel based catalysts enriched with earth type metals such as Ca, K, and La are again the starting research point for constant activity continuous operations. Advanced materials in microporous or dense phase can be used as activated structure hydrogen or hydrogen-carbon oxide receptors and transmitters in above operations to recover hydrogen and hydrogen-carbon oxide mixtures directly out of the reactor or from the post reacted exit streams. These include metals, ceramics, high temperature polymers, special types of carbon based and composite materials [1]. Dense type materials are better candidates than microporous ones. The rejected hydrocarbons and/or CO streams from the following membrane permeator or separator can be recycled into the inlet of the reformer/gas shift reactor for increasing the process efficiency via the utilization of the unreacted materials. Product mixtures of H_2 and CO_2 from the permeate stream can be used directly as anode feed gas into an adjacent molten carbonate fuel cell unit [4]. Similarly, separated product mixtures of H_2 and CO can be used directly as anode feed gas into an adjacent solid oxide fuel cell unit [1-4]. In several reactor-catalyst instances the main reactor operates at high enough conversions and produces hydrogen rich mixtures for direct use in the fuel cell, thereby eliminating the need for the downstream separator and associated costs.

Results and discussion. Related modeling of such multifunctional reactors and systems for the aforementioned applications is under way to describe their function, operational range, yield and capacity. The models used, simulate relevant acquired data and predict conditions for best multifunctional reactor and process operation by variation of key intrinsic parameters [1,3,5,7,9]. The proposed efficient reactor/processor systems configurations and their specific fuel cell-power generation applications seek to perform multiple unit operations within a single or integrated type module which makes them advanced in comparison with up to now proposed and utilized conventional and permeable type of reactors [1,2,5-9]. They project a promising advancing technology for primary and secondary hydrocarbon to hydrogen upgrading reactors for use in continuous (inline) fuel cell processes. The described positive technical aspects/effects are fortified in view of the environmental and economic benefits that these processes possess especially in connection with directly powering fuel cell stacks. In the Figures below we present some comparative modeling analysis of the described reforming processors for continuous fuel cell operation. Fig.1 shows the required methane feed rate in the reformer, for various types of fuel cells of constant 100kW output power and variable cell efficiencies for two types of reaction systems. A single reactor of 90% conversion with a single inlet and outlet, and a reactor-permeator cascade of 60% conversion with CH_4 and CO recycling in the feed are compared. Hydrogen is produced by the combined methane steam reforming and water gas shift reactions in both cases and assumed to be fed clean in the fuel cells. It is characteristic that an increase in fuel cell efficiency (such as use of a higher efficiency SOFC or MCFC

cell) lowers the methane requirement in the reactor necessary for powering the consecutive fuel cell. Fig.2 shows the total rate of hydrogen consumption by the fuel cell for various efficiency fuel cells. A double reaction scheme is considered in the feed reactor as in Fig.1 which powers a constant 100 kW fuel cell by use of the produced hydrogen. It is characteristic that the hydrogen requirement for high temperature fuel cells is about half the one required for lower efficiency cells. Thus, use of a smaller reformer or lower methane flowrates are required for the high temperature fuel cells, which in turn results into smaller overall installation costs. Fig.3 finally, plots the output power produced by a high temperature fuel cell (constant 60% efficiency) interconnected with the reformer for different reforming reaction and feed conditions. A jump from 500 to 700°C in reformer temperature increases by three fold the cell power output (kW) for all feed conditions.

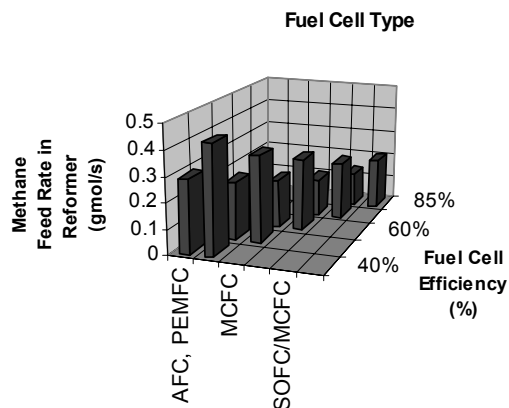


Fig.1: Methane feed rate (gmol/s) vs Fuel cell efficiency (%), 100kW units, Steam reforming+WGS, 2 cases: Single Reformer (lower bars, 90% total conversion), and Reformer+Permeator (higher bars, 60% total conversion)

Acknowledgements: DOE support for this project is gratefully acknowledged by the authors.

References: (1) Vasileiadis, S., Ziaka, Z., Environmentally benign hydrocarbon processing applications of single and integrated permreactors, in Reaction Engineering for Pollution Prevention, Elsevier Sci., 2000; pp.247-304. (2) Vasileiadis, S., Ziaka, Z., Alternative generation of H₂, CO and H₂, CO₂ mixtures from steam, carbon dioxide reforming of methane and the water gas shift with permeable (membrane) reactors, Chem. Eng. Comm., **1999**, 176, 247. (3) Ziaka, Z., Vasileiadis, S., Reactor-membrane permeator cascade for enhanced production and recovery of H₂ and CO₂ from the catalytic methane-steam reforming reaction, Chem. Eng. Comm., **1996**, 156, 161. (4) Ziaka, Z., Vasileiadis, S., Reactor-membrane permeator process for hydrocarbon reforming and the water gas shift reactions, USP#6,090,312, **2000**. (5) Xu, J., Froment, G.F., Methane steam reforming, methanation and water-gas shift: I. Intrinsic Kinetics, AIChE J., **1989**, 35, 1, 88. (6) Van Hook, J.P., Catal. Rev. Sci. Eng., **1980**, 21, 1, 1. (7) Murray, A.P., Snyder, T.S., Ind. Eng. Chem. Process Des. Dev. **1985**, 24, 286. (8) Rostrup-Nielsen, J.R., J. Catal., **1984**, 85, 31. (9) Shao, X., Xu, S., Govind, R., AIChE Symp. Ser., **1989**, 268, 85.

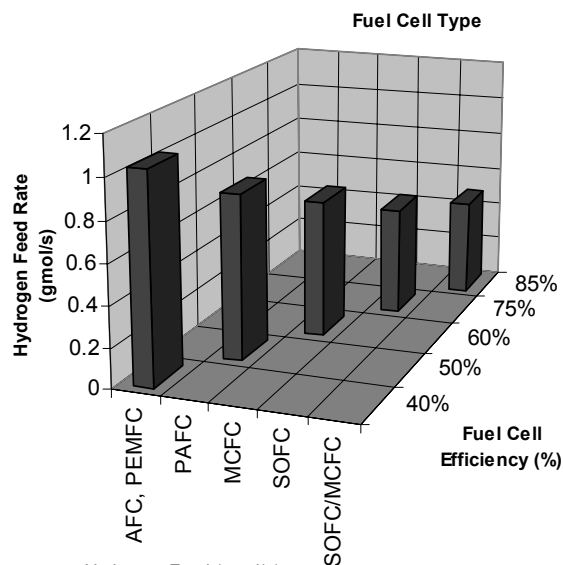


Fig.2: Hydrogen Feed (gmol/s) vs Fuel Cell Efficiency (%), 100kW units, Steam Reforming plus WGS

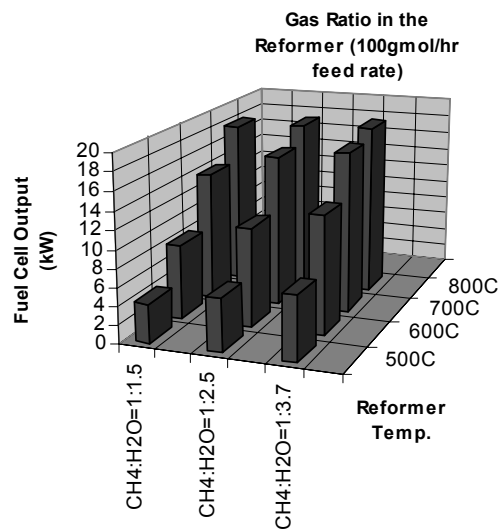


Fig.3: Fuel cell power vs reforming conditions, 60% fuel cell efficiency at equilibrium gas composition (2 reactions in reformer: CH₄-H₂O reforming &WGS)

COMPACT FUEL PROCESSORS FOR PEM FUEL CELLS

A.S. Chellappa¹, M.R. Powell², M. Fountain², C. J. Call¹, N. A. Godshall³

¹ MesoSystems Technology, Inc. 2425 Ridgecrest Dr. SE,
Albuquerque, NM 87108

² MesoSystems Technology, Inc. 1021 N. Kellogg St., Kennewick
WA 99336

³ MesoFuel, Inc. 2425 Ridgecrest Dr. SE, Albuquerque, NM 87108

Introduction

Recent improvements in the design and manufacture of PEM fuel cells have increased interest in their use as a replacement for batteries and other, larger power supplies (e.g., internal combustion engines). Although PEM fuel cells represent a relatively mature technology (they have been around since 1839), they have yet to receive widespread commercial or military use primarily due to the non-availability of reliable, convenient, and compact hydrogen sources. Several approaches have been identified for hydrogen generation and/or storage. These include hydrocarbon and methanol fuel reforming, hydrogen absorption into metal hydrides, hydrogen-generating chemical reactions, and ammonia decomposition (Blomen and Mugerwa, 1993; Bloomfield et al., 1995). We have developed a compact ammonia-processing MesoChannelTM reactor system that generates hydrogen at a rate sufficient to meet the requirements for a 50 W PEM fuel cell. More recently, we have extended the capabilities of our hydrogen generator to process C₁ to C₄ hydrocarbon fuels. A summary of our work on compact fuel processors is the subject of this paper.

Hydrogen from methane

Compact hydrocarbon-based hydrogen generators are needed to power a wide range of portable applications. Our target was to produce hydrogen at a rate sufficient to power a 20 W PEM fuel cell to satisfy the requirements of our subcontract to the Research Triangle Institute under the Defense Advanced Research Projects Agency (DARPA) Palm Power Program. The hydrocarbons to be evaluated under this project include butane and JP-8. Since steam reforming of these higher hydrocarbons proceeds through the reformation of methane, we decided to first evaluate the steam reforming of methane using our MesoChannelTM reactor. The hydraulic diameters of the channel in these reactors were in the 0.5 to 1.5 mm range as opposed to the micron sized channels that are typically adopted in micro reactors.

Methane (C.P. grade) and other gases such as hydrogen (commercial grade) for pretreatment of the catalysts were metered through Brooks 5850E mass flow controllers. Distilled water was vaporized at 180 to 250 C. Methane and the steam generated in a vaporizer were contacted downstream of the vaporizer and were then routed through a preheater. The steam-hydrocarbon mixture was heated to within 50 C of the desired reaction temperature in the preheater. The reaction temperature was typically in the 550 C to 625 C range. Temperatures were measured using Inconel-clad 1/16 inch OD type K thermocouples. The gas mixture exiting the preheater was routed into the MesoChannelTM reactor. The gases exiting from the reactor passed through a back pressure regulator and into a condenser to remove any unreacted water, and the dry gas mixture was vented or combusted before venting. The flow rate of the dry product gas was monitored continuously. A portion of the dry gas was routed to a gas chromatograph (Shimadzu GC 17A)

for analysis. The gas chromatograph was equipped with a flame ionization detector, a methanator and a thermal conductivity detector. The carbon balance was found to be within 3%.

Figure 1 shows the hydrogen production rate observed while operating in the 600 to 625 C range and at residence times of less than 0.4 s.

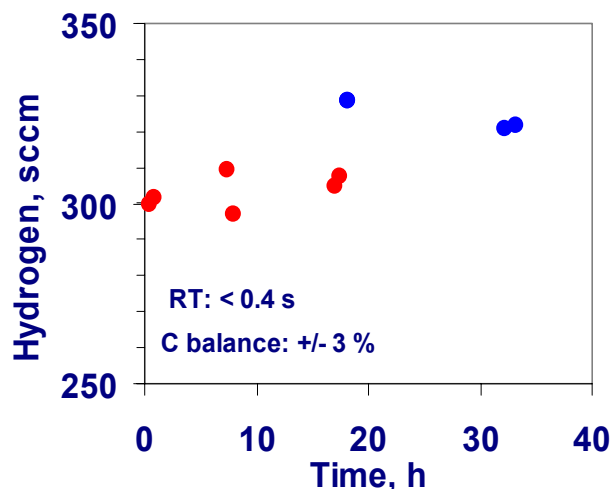


Figure 1. Hydrogen generation-steam reforming of methane. 600 C (red), 625 C (blue).

As can be seen, excellent catalyst stability was observed for over 30 h. The methane conversion during this period was about 53 % (equilibrium conversion at 625 C, S/C ratio of 1 is about 85%). As shown in Figure 2, the product stream contained only about 5% CO during this period.

Our next efforts will target the integration of hydrogen separation schemes into the reactor. The reactor will be modified to accommodate a combustor that is in close proximity to the reformer (similar to our ammonia cracker system that is discussed below). Unreacted methane and/or hydrocarbons will be combusted to drive the reforming of hydrocarbons.

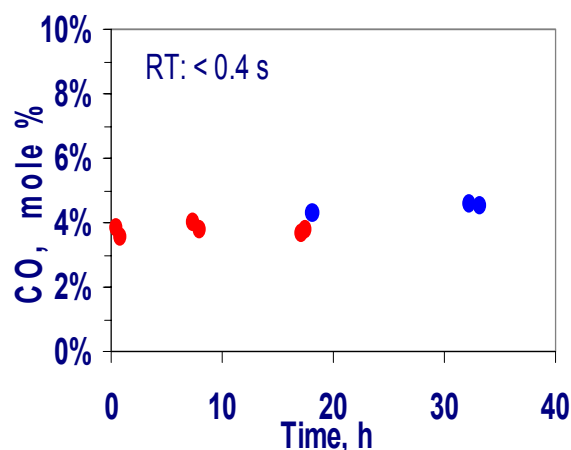


Figure 2. CO content in the product gas (dry basis). 600 C (red), 625 C (blue).

Hydrogen from ammonia

Ammonia decomposition for PEM fuel cell applications has received relatively less attention because of ammonia's toxicity and foul odor, and because it is not economical for power production except in remote, low-power applications (Appleby and Foulkes 1989). Of greater significance is the fact that trace ammonia needs to be effectively removed before the product stream is fed to the PEM fuel cell. However, ammonia is an attractive source because the usable hydrogen per kilogram of fuel is relatively high (Figure 3), particularly when the weight of water needed for hydrocarbon steam reforming is taken into account. Stoichiometric steam/fuel ratios were assumed in Figure 3.

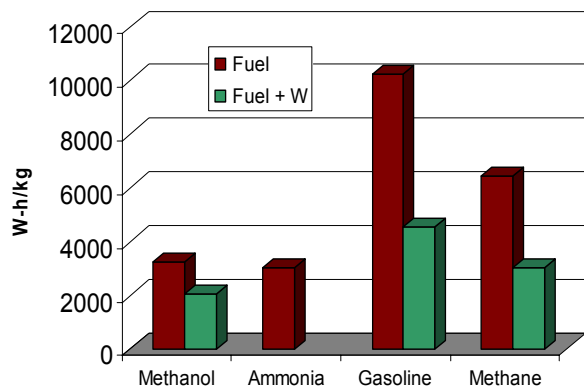


Figure 3. Comparison of fuels: Energy density.

Ammonia decomposition was conducted in MesoChannelTM reactors. The reactor volume and weight was typically less than 4 cc and less than 140 g, respectively. The reactor is integrated with a heat exchange system in an elegant and rugged fashion that is suitable for field use. Our current prototype produces hydrogen at a rate sufficient to generate 50 W of electrical power from a fuel cell, providing up to 1000 W-h of energy. The prototype, which is named MAC-50 (MesoSystems Ammonia Cracker), has the options of either providing heat by hydrocarbon combustion (typically butane) or by combusting ammonia itself. The combustor contains a versatile catalyst-coated substrate that also allows for quick start-up.

The MAC-50 system includes the following design features that serve to minimize size and weight:

- MesoChannelTM reactor architecture to minimize heat and mass-transfer limitations so reactor sizing is driven by the catalyst's intrinsic kinetics and is thereby minimized
- Use of a high-activity noble metal catalyst to keep reactor volume small
- Lightweight, recuperative heat exchanger to improve the system thermal efficiency and reduce the quantity of fuel that must be burned to maintain the reactor at temperature
- Lightweight, ultra-low-thermal-conductivity insulation to reduce heat loss to ambient without significantly increasing the system size
- Butane/propane and/or ammonia combustion for rapid reactor startup and to provide heat during steady-state operation.

Figure 4 shows the performance of our catalyst for ammonia decomposition over a 300 h testing period. This duration also includes 6 thermal cycles between room temperature and 600 C. As can be seen, the catalyst showed excellent activity and stability over this period.

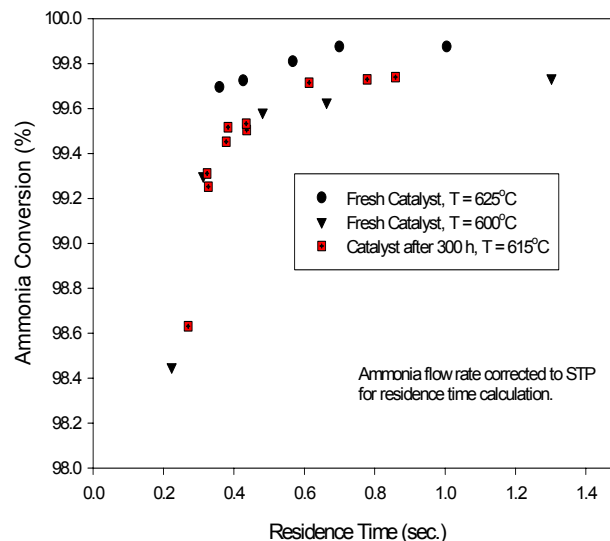


Figure 4. Stability of catalysts to ammonia cracking.

A photograph of the MAC-50 prototype is shown in Figure 5. The prototype includes the reactor, recuperators, and an adsorbent column. High-temperature vacuum insulation is used to limit the heat loss to the surroundings to less than a 2 W at 600C. The system mass is about 820 grams, not including the ammonia. The 0.8-liter ammonia storage tank will hold up to 480 grams of anhydrous ammonia, which will yield about 1150 W-h of energy from a fuel cell (assuming 17 W-h per gram of hydrogen). Roughly 20% of the ammonia is consumed in the combustor and 80% is fed to the decomposition reactor. Including the mass of the ammonia, this prototype produces hydrogen with an apparent energy density of about $1150/(820+480) = 885$ W-h/kg.



Figure 5. MAC-50 Prototype.

The product typically contains about 2000 ppm of residual ammonia. Since ammonia is harmful to PEM fuel cell performance, the residual ammonia is completely removed using a proprietary high capacity carbon adsorbent. A typical breakthrough curve of the adsorbent that was obtained while using 0.7 SLPM of air containing 1000 ppm ammonia is shown in Figure 6. The adsorbent (30 g used for the test in Figure 6) has a capacity of about 9 to 10 wt.-% and as a result, the MAC-50 prototype needs only about 30 g of adsorbent for a 1000 W-h duty. To put this in perspective, the capacity of commercial adsorbents is in the 2 to 4 wt% range.

We are now in the process of field testing the MAC-50 prototype after integrating it with a PEM fuel cell. Based on the results of these tests, a control system will be designed and incorporated that would allow for quick start-up and shut-down as well as load following capabilities.

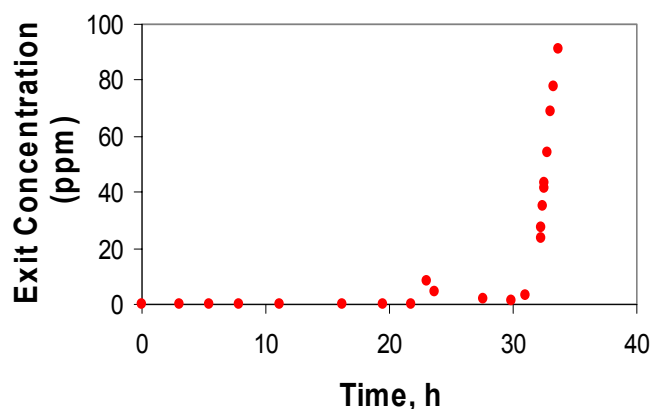


Figure 6. High performance ammonia adsorbents: Breakthrough curves.

Acknowledgement. This work was partly funded by the US Army Research Office under Contract DAAD19-01-C-0002 and by the Research Triangle Institute under contract 1-81U-8152 .

References

1. Appleby, A.J., and F.R. Foulkes. 1989. Fuel Cell Handbook. Van Nostrand Reinhold, New York.
2. Blomen, L., and M.N. Mugerwa. *Fuel Cell Systems*. Plenum Press, New York, 1993.
3. Bloomfield, D.P., V.J. Bloomfield, P.D. Grosjean, and J.W. Kelland. *Mobile Electric Power*. Analytic Power Corp., NTIS Report ADA296709, 1995.

COMPACT REFORMING SYSTEMS FOR ON-SITE HYDROGEN GENERATION

Michael S. Hsu

Ztek Corporation
300 West Cummings Park
Woburn, MA 01801

Market for Hydrogen Reforming

The Bush Administration's recent creation of Freedom Cooperative Automotive Research (FCAR) represents a profound policy shift in automotive research. Rather than committing to improve the efficiency of the traditional combustion engine, the Federal Government had embraced hydrogen fuel cell powered automobiles as the best way to reduce the country's overwhelming dependence on foreign oil and to control tailpipe emissions.

The State of California has mandated that Zero Emission Vehicles (ZEVs) be 10% of all new vehicles sold by 2003. Based on the number of vehicles sold annually in California, this means that at least 200,000 ZEVs will be sold each year in that state. Maine, Massachusetts, New York and Vermont have adopted California's standard.

According to our estimates, the use of hydrogen as a fuel source will initially require about 500 hydrogen filling stations in California alone. That number is expected to grow to 2,000 stations by 2010. There is therefore a significant opportunity for Ztek to establish a key role in this market.

Currently, there is no existing infrastructure for the bulk delivery of hydrogen for retail distribution. Even if economically competitive, the development of such an infrastructure will require significant technological advancement, billions of dollars in new investment and disruption to suppliers and consumers.

Ztek Corporation has fully developed a product that is capable of delivering hydrogen to the consumers who choose hydrogen-powered vehicles. This product uses the existing gasoline supply infrastructure and offers the capability to sequester carbon dioxide, providing the means of a totally emission free vehicle energy supply. It can assure the continued existence of the corner gas station and provide hydrogen services that grow proportionally to demand, leaving the existing experience of consumers uninterrupted as the new hydrogen economy emerges.

The storage of hydrogen on-site following reforming will require significant amounts of electricity. Ultimately, integrating the reformer with Ztek's SOFC system will supply electricity in addition to the production of hydrogen, providing station owners a complete power and energy solution with unsurpassed efficiency.

Existing Hydrogen Generation Capabilities and Their Drawbacks

Currently, it is possible to generate hydrogen by reforming processes in both a remote central production facility and on-site at fleet operation, existing automobile or truck service stations. To date there is no delivery infrastructure for central production facilities. Hydrogen production can also be performed by electrolysis using utility grid power. This comes with substantial cost, while also burdening the electric power infrastructure. Hydrogen production

using electrolysis with renewal resources such as wind or solar has the natural limitation in its capacity and availability. Moreover, conventional systems are not provisioned for CO₂ emission control. The continued release of CO₂ greenhouse gases at the fuel production and electric generation stations offsets the benefits achieved from using ZEVs. The above costs and corresponding emissions are counter-productive to the savings achieved from the use of zero/low emission vehicles.

The Ztek Solution

Ztek's system can produce hydrogen from multiple fuel sources such as natural gas, gasoline, methanol, and diesel. The company has worked diligently to ready a product that can produce hydrogen from these easily transportable and readily available fuels. Ztek's emphasis on small component design and a highly efficient reforming method with a total thermal integration (TTI) for processing waste gas makes the unit compact and cost effective. Other commercially available hydrogen producing plants are much larger for the same level of hydrogen output and efficiency. Ztek estimates that its production cost per unit will be economically viable for the street corner service station owners.

In Ztek's low emission system under current testing, liquid fuels and water are vaporized in the reforming process to produce a hydrogen rich gas. Some of the hydrogen atoms in the vaporized water separate from oxygen bond and double the hydrogen output of the reformer. This process is commonly referred to as steam reforming. Thermal energy for the endothermic steam reforming reaction is provided by waste streams, and is transferred by radiation and/or convection in a unique and thermally efficient design. Ztek's primary product, the solid oxide fuel cell, will provide energy for reforming. It can also satisfy the heavy electrical usage of the station (**Figure 1**).

The Ztek Advantage

The Ztek commercial hydrogen reformer will convert natural gas or gasoline to hydrogen at 85% efficiency, meaning that 85% of the energy contained in the reformer fuel will be converted into useful hydrogen. This efficiency is many times greater than hydrogen produced by the alternative method of electrolysis.

California and many other states have adopted regulations that require automobile manufacturers to offer an increasing number of low and zero-emissions vehicles over the next several years. The Ztek reformer is "low emission ready" because its hydrogen has a high level of purity and the ZES itself has extremely low levels of SO_x and NO_x. The reformer will also enable true zero-emissions vehicles by allowing for the separation and sequestration of carbon dioxide, the only by-product of its gasoline to hydrogen conversion.

In order to ensure the widespread acceptance of hydrogen fuel cell vehicles, we believe it is imperative that the existing customer experience is preserved as much as possible. By providing hydrogen through existing gasoline filling stations, the customer experience will remain largely unchanged and the acceptance of hydrogen-powered automobiles will be seamless.

Other manufacturers of hydrogen reformers have been unable to fully develop commercial size reformers that are small enough to be integrated into existing filling stations. Existing sites in California use a reformer that produces 4200 scfh per hour, is over 40 feet long, 8 feet wide and 8 feet high. The Ztek Model ZES commercial

reformer will produce 4000 scfh of hydrogen but will be only 10 feet long, 10 feet high and 10 feet wide. As a result, it will be much less problematic to integrate into gasoline fueling stations and will give owners superior flexibility in their hydrogen supply.

Acknowledgments. The Ztek Planar Solid Oxide Fuel Cell Technology has been developed with the support of the Tennessee Valley Authority, the Electric Power Research Institute, TNP Enterprises, Inc., MCN Energy Group, Huntsville Utilities, the U.S. Department of Defense and the U.S. Department of Energy.



Figure 1. Ztek 25 kW SOFC System with Hydrogen Reformer

COMPARISON OF HYDROGEN STORAGE TECHNOLOGIES: A FOCUS ON ENERGY REQUIRED FOR HYDROGEN INPUT

Monterey R. Gardiner and Andrew Burke

Institute of Transportation Studies
One Shields Ave.
University of California, Davis, CA 94539

Introduction

Why focus on hydrogen as a fuel? Fuel cell vehicles (FCVs) are rapidly approaching commercialization. Honda will be the first to market here in the US, with plans to offer a small number of passenger FCVs for fleet applications next year (2003). DaimlerChrysler and Ford will follow shortly with plans to offer a limited number of vehicles in 2004. With the rapid approach of FCVs, more detail is needed with respect to near term options for hydrogen storage. Hydrogen for a direct hydrogen fuel cell vehicle (DHFCV) is seen as both the near term and long term fuel choice for auto manufacturers and society as a whole. Due to challenges of storing hydrogen onboard vehicles, two midterm fuel solutions have been suggested. They are methanol or a specially designed hydrocarbon. However, in the near term compressed hydrogen gas (CHG) and liquid hydrogen (LH₂) are the most mature methods of onboard storage. However, other options exist such as metal hydrides and sodium borohydride.

The purpose of this paper is to add to and consolidate information about the range of onboard hydrogen storage options. There are journals and papers with informative graphs of wt% or vol% hydrogen stored or their respective pairs specific energy storage density by weight and volume, however updated information is required for the comparison. A base line of 5 kgs of hydrogen is chosen as the amount of hydrogen to be stored to facilitate the comparison. This is the amount of hydrogen required to attain a FCV range comparable to an ICE vehicle. The value was calculated with the UC Davis fuel cell vehicle model using a combined FUDs and HIWY driving cycle.¹

In order to expand upon and update available information regarding hydrogen storage options, energy required to store the hydrogen needs to be taken into consideration. A detailed look at the required energy to store the hydrogen will allow one to put into perspective the energy cost between 10 kpsi CHG and a possible metal hydride for example. With the option of home refueling as a partial solution to the "infrastructure problem", the most cost effective and convenient storage method still needs to be determined. This paper will assist in that process. The following calculations are a first approximation at determining the energy required to store hydrogen for four different onboard storage technologies: LH₂, CHG, metal hydrides, and sodium borohydride.

Calculations

Liquid Hydrogen. The energy cost for this storage method is one of the most difficult to approximate due to the multiple steps required to liquefy hydrogen, therefore I will outline the method for determining the ideal work for the liquefaction of hydrogen which, is relatively straight forward. However, I will also provide the liquefaction energy based on the nitrogen pre-cooled Linde process, which uses liquid nitrogen to first cool the hydrogen. Liquid hydrogen requires a temperature of 20 K. At this temperature almost all the hydrogen has a para-hydrogen electron configuration. At room temperature 25% of the hydrogen is para-hydrogen and 75% is ortho-hydrogen. The conversion is an exothermic reaction and releases a significant amount of heat (527 kJ/kg).² The conversion is

very slow, but can be done much faster using a catalyst. The theoretical process for ideal liquefaction uses a reversible expansion to reduce the energy required for liquefaction. It consists of an isothermal compressor, followed by an isentropic expansion to cool the gas and produce a liquid.³ The following values of entropy, enthalpy, pressure and temperature are used to calculate the ideal work per kilogram to liquefy hydrogen.⁴

$$S_1 = 15.472 \frac{\text{cal}}{\text{gm} \cdot \text{K}} \quad h_1 = 1003 \frac{\text{cal}}{\text{gm}} \quad P_1 = 1 \text{ atm} \quad T_1 = 300\text{K}$$

$$S_2 = 4.35 \frac{\text{cal}}{\text{gm} \cdot \text{K}} \quad T_2 = 300\text{K}$$

$$S_3 = 4.35 \frac{\text{cal}}{\text{gm} \cdot \text{K}} \quad h_3 = 70 \frac{\text{cal}}{\text{gm}} \quad P_3 = 1 \text{ atm} \quad T_3 = 20\text{K}$$

$$w = T_1(S_1 - S_2) - (h_1 - h_2) \quad w = 2.795 \frac{\text{kW} \cdot \text{hr}}{\text{kg}}$$

The ideal work required to liquefy hydrogen is 2.795kWh/kg, while the work calculated for the nitrogen pre-cooled liquefaction of hydrogen is 19.839kWh/kg.⁵ At 5kg this is 99.195kWh.

Compressed Hydrogen Gas: 3500 psi, 5000 psi, 10000 psi. The energy to compress the hydrogen can be found in a similar manner. The example shown is for 3500 psi.

$$S_1 = 15.472 \frac{\text{cal}}{\text{gm} \cdot \text{K}} \quad h_1 = 1003 \frac{\text{cal}}{\text{gm}} \quad P_1 = 1 \text{ atm} \quad T_1 = 300\text{K}$$

$$S_2 = 4.35 \frac{\text{cal}}{\text{gm} \cdot \text{K}} \quad h_2 = 1033 \frac{\text{cal}}{\text{gm}} \quad P_2 = 238 \text{ atm} \quad T_1 = 300\text{K}$$

$$w = T_1(S_1 - S_2) - (h_1 - h_2) \quad w = 1.931 \frac{\text{kW} \cdot \text{hr}}{\text{kg}}$$

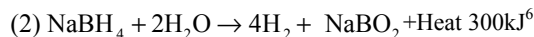
Table 1. Compression Energy

	3500 PSI	5000 PSI	10000 PSI
kWhr/kg	1.93	2.08	2.39
KWhr at 5kg	9.66	10.38	11.95

Table one clearly shows, the energy required to compress hydrogen gas, starting at an initial pressure of 1 atm and the energy for 5 kilograms.

Metal Hydrides. The work required to store hydrogen in a metal hydride depends on the type of hydride and how quickly it needs to be done. Typically hydrogen is supplied a little over atmospheric pressure to the metal alloy. The process is slightly exothermic. For large systems, cooling may be needed. When all the metal has reacted the pressure will begin to rise. The hydrogen is stored at a relatively low pressure, ~30 psi. To discharge the gas, slight heat needs to be added, however sufficient waste heat is available from the fuel cell. Little to no energy is required for hydrogen gas input to metal hydrides.

Sodium Borohydride. NaBH₄ in aqueous solution produces 4 moles of hydrogen when passed over a catalyst.



Two moles of hydrogen come from the sodium borohydride and two moles of hydrogen come from the water. Therefore, the energy calculation only needs to be done for 2.5kgs of hydrogen. The process for making sodium borohydride involves reacting boric acid with methanol to produce tri-methyl borate, which is then reacted with sodium hydride at elevated temperatures. The product of equation (2) is essentially sodium tetraborate, more commonly known as Borax. We can use the exothermic heat as a very rough

estimate for the absolute minimum energy required to change the sodium meta-borate back into sodium borohydride. The energy required, is 300 kJ per eight grams of hydrogen. This is equivalent to 10.48kWhr/kg of hydrogen. 5kgs of hydrogen requires 52.08 kWhrs, assuming an ideally reversible reaction.

Results

The energy calculated for the liquefaction of 5 kgs of hydrogen is 99.195kWh, which is a little bit high. A rule of thumb is that the energy it takes to liquefy the hydrogen is equal to the energy in 30% of the total amount of hydrogen liquefied. Using the upper heating value of hydrogen, 142MJ/kg, the energy for liquefaction should be about 65 kWhr for 5kgs of hydrogen. However, the energy to liquefy the hydrogen is much higher than the energy required to compress the hydrogen, which is ~12kWhr at 10000 psi for 5kgs of hydrogen. The energy for the sodium borohydride is similar to the energy for LH₂ at 52.08kWhr for 5 kgs. This number still needs to be verified, with data from the actual process. Metal hydrides have no energy requirements and look like the best option, when only considering the "energy input" metric. Two more common metrics of hydrogen storage technologies are specific storage density by weight (wt%) and specific storage density by volume (vol%). It is important to clarify if these numbers are for the material or the entire storage system. The following numbers are for storage systems.

Table 2. Weight and Volume % for Storage Systems

Technology	Wt%	Vol %
Liquid Hydrogen	7.50	0.03
CHG 5000 PSI	6.67	0.02
CHG 10000 PSI	6.00	0.03
Low Temp MH	5.45	0.06
Sodium Borohydride	4.50	0.02

Table two shows the comparison of total system weight and total system volume for the different storage technologies.

Discussion

The energy to store hydrogen is just one variable among many for deciding which storage option is best. There are many advantages and disadvantages for each option that need to be considered. The main advantage/disadvantage that people tend to take into account is cost of the storage material or technology and secondly, the relative safety of a particular technology. Sodium borohydride is very inert and no hydrogen is released without the addition of a catalyst. In addition, the raw material is relatively inexpensive. Another advantage, which may be minor, is the fact that the gas from the sodium borohydride is already humidified to a certain extent, because of the exothermic reaction and half the hydrogen is coming from the water. The largest challenge facing this technology is finding an economical way to recycle and charge the sodium borohydride. Right now, metal hydrides are still quite expensive for the material itself, and they need a certain amount of thermal management, which makes the storage system relatively complex. However, the material does not have any serious safety issues. Liquid hydrogen, is one of the more mature technologies, however, a tank can not be kept full longer than 30 days due to boil off issues. Compressed hydrogen offers the simplest delivery system of the hydrogen gas to the fuel cell, though it does need to be humidified. The high pressure tanks are also relatively expensive. Auto manufactures are concerned about the public's receptiveness to high pressure tanks. In reality, the different options will be chosen depending on the particular niche they are most suited for.

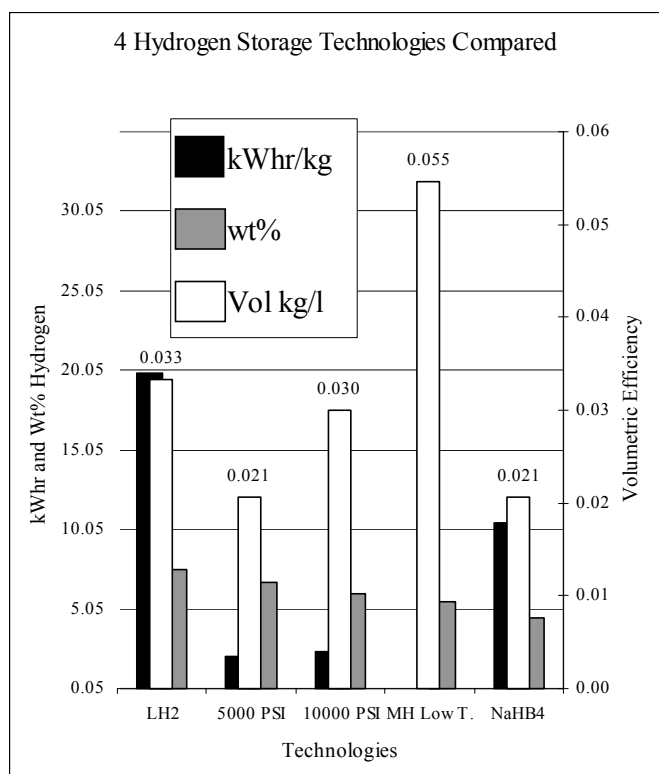


Figure 1. Comparison of kWhr/kg of hydrogen, total system weight and total system volume for four different storage technologies.

Conclusion

Figure one shows how difficult the decision is, to choose between the four technologies. By system weight % LH₂ is best. When looking at volumetric efficiency, metal hydrides are the best option. As far as energy to store the hydrides, metal hydrides are also the best option. However, two main factors are missing from this chart, cost of the system and the relative safety of the systems or public perception of the that safety. These two unknown factors will have a large impact on the best choice and will likely depend on the particular application the storage will be used in.

References

- (1) Gardiner, M., Cunningham, J., Moore R.M., *Society of Automotive Engineers, Future Transportation Technology Conference*, **2001**, 2001-01-2531, p. 4.
- (2) Noganow, L.S. "Hydrogen." *McGraw-Hill Encyclopedia of Science & Technology*. 7th edition. Vol. 8. New York: McGraw-Hill; **1992**; pp. 581-588.
- (3) Timmerhaus, C.; Flynn, T.M. *Cryogenic Engineering*. Plenum Press: New York: **1989**.
- (4) McCarty, D.R, "Hydrogen Technological Survey-Thermophysical Properties", Cryogenics Div, Inst. for Basic Stds. Nat. Bureau of Stds, Boulder CO. Sci. and Tech. Info. Office, Washington, DC **1975**
- (5) Amos, W.A., *Costs of Storing and Transporting Hydrogen*, NREL/TP-570-25106 **1998**; p. C-5
- (6) S. Amendola et al, "A safe, portable, hydrogen gas generator using aqueous borohydride solution and Ru catalyst", *Int. J. Hydrogen Energy* **25** **2000**; p.969-975

CONCENTRATING DILUTE HYDROGEN STREAMS WITH A METAL HYDRIDE BASED PRESSURE SWING ADSORPTION PROCESS

Karen D. Daniel and James A. Ritter

Department of Chemical Engineering
Swearingen Engineering Center
University of South Carolina
Columbia, SC 29208, USA

Introduction

Conventional PSA cycles¹, which are designed for the most part to produce a very pure light product via stripping reflux²⁻⁴, are limited to the high to low pressure ratio when it comes to enriching the heavy component⁵. In reality the enrichment of the heavy component is far below the pressure ratio due to the dilution effect of the purge gas that is used to regenerate the column for the ensuing cycle and the fact that the adsorption isotherm of the heavy component is typically a favorable Langmuir isotherm which gives rise to a simple spreading wave during desorption. Clearly, it would be desirable to not only produce a very high purity light product, but also a heavy product enriched at least to the pressure ratio. A novel PSA cycle is introduced here for that purpose.

This PSA process combines a conventional PSA cycle with an adsorbate-adsorbent system that exhibits an unfavorable Langmuir isotherm. An example is H₂ adsorption by a metal hydride adsorbent. An isothermal equilibrium theory model⁵⁻⁷ is used to analyze this PSA cycle because it establishes the periodic state directly and analytically, and it gives the upper thermodynamic limit for an equilibrium-based separation. It also establishes the feasibility of a separation. A brief overview of the assumptions associated with and equilibrium theory analysis is given, along with an example for the concentration of H₂ from a dilute feed stream using a metal hydride adsorbent.

Mathematical Model

Equilibrium theory accounts for mass conservation but ignores transport phenomena such as mass transfer resistance, and generally results in analytical solutions of the governing material balance equations⁷. The assumptions associated with equilibrium theory include: instantaneous local equilibrium between the fluid phase and adsorbed phase, isothermal operation, no axial dispersion, and no axial pressure drop. Since the feed consists of very low mole fractions of H₂ in an inert carrier gas, the fluid-phase velocity is assumed to be constant throughout the column. Fluid-phase accumulation of H₂ is negligible, due to the large partition ratio between the solid phase and the bulk phase. Another important assumption is frozen adsorbed and fluid phases during pressurization and blowdown. This assumption simplifies the PSA cycle to a two-step process consisting of only feed and purge steps^{5,6,8}. The frozen solid-phase approximation also requires the feed mole fraction to be less than the inverse of the pressure ratio of the cycle⁷.

A rigorous equilibrium theory analysis in terms of wave theory is beyond the scope of this short communication. Nevertheless, there are two cases that can be analyzed, one with and one without breakthrough of hydrogen into the light product. The more complicated case is when there is breakthrough. When there is no breakthrough of H₂ into the light product, both the feed and purge steps consist of only simple waves. With unfavorable isotherms, lower concentrations travel faster and will therefore penetrate the farthest down the column during the feed step. The subsequent purge step will consist of a self-sharpening simple wave, meaning that the

slope of the concentration profile will gradually get steeper as it travels back towards the feed end of the column. When the volumetric purge-to-feed ratio is unity, a shock of the fullest strength (vertical concentration profile) develops just at the bed inlet at the end of the purge step. The bed profiles at the end of the feed and purge steps for this simpler case are shown in **Figure 1**.

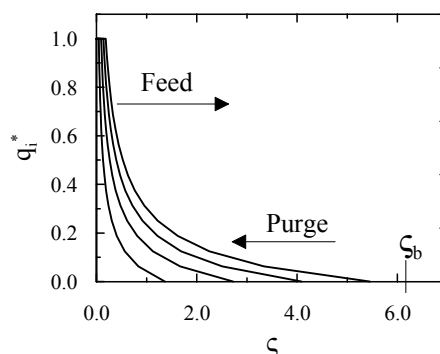


Figure 1. Bed profiles at different times during the feed and purge steps at the periodic state for the no breakthrough case.

The recovery of the heavy product is defined as the ratio of the change in the amount of H₂ in the solid-phase over the purge step to the amount of H₂ in the solid-phase after the first feed step⁷. Since each purge step results in complete clean up, the recovery of the heavy product is 100%. The recovery of the light product is defined as the ratio of the difference between the moles of carrier gas used during the feed and the purge steps to the moles of carrier gas used in the feed step. The light product impurity is defined as the ratio of the number of moles of H₂ to the total number of moles in the light product. When there is no breakthrough of H₂, the light product will be 100% pure. The purity of the heavy product is defined as the ratio of the number of moles of H₂ to the total number of moles in the heavy product. The enrichment of the heavy product is the ratio of the mole fraction of H₂ in the heavy product during the purge to the mole fraction of H₂ in the feed.⁷ This enrichment of the heavy product simply equals the high-to-low pressure ratio. When breakthrough of H₂ occurs in the light product, the purge step will involve both a self-sharpening simple wave and a shock wave. At the beginning of the purge step, a shock wave will form instantaneously. Since the shock wave travels faster than the simple wave on the left, it will gradually consume the simple wave while being decelerated. Once the shock wave has completely consumed the simple wave a shock wave of the fullest strength will exist. From this point on the shock wave will propagate towards the feed end of the column with a constant velocity. If the purge step ends before the shock wave reaches the end of the column, a square heel will be left in the column as an initial condition for the subsequent purge step. **Figure 2** shows bed profiles at different times during the feed and purge steps at the periodic state. Notice the vertical profile at the end of the bed, indicating breakthrough occurred up to this concentration. Also, notice the heel that remains in the bed at the end of the purge step. This heel does not exist when there is not breakthrough as it is pushed back exactly to the feed end of the bed as shown in **Figure 1**.

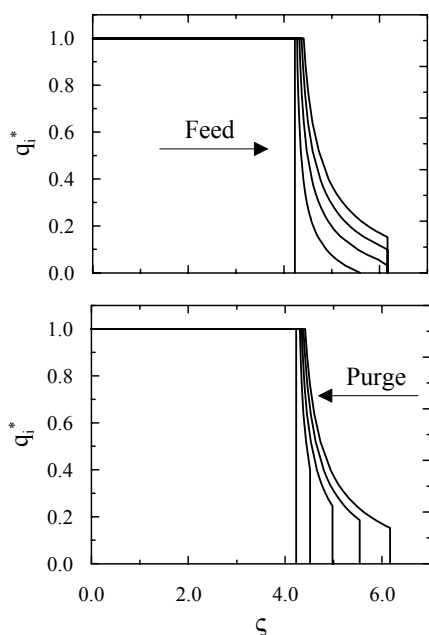


Figure 2. Bed profiles at different times during the feed and purge steps at the periodic state for the breakthrough case.

The process performance parameters are derived in a similar manner as when there is no breakthrough. All the same definitions apply, but in this case the recovery of the heavy product will not be 100%, since some H_2 is lost in the light product during the feed step. This recovery simply becomes equal to the purge to feed ratio, γ . The definition of the recovery of the light product is the same as when there is no breakthrough, except now γ does not equal to unity so the expression becomes one minus the ratio of the purge to feed ratio to the pressure ratio. The light product impurity is found by determining the average H_2 concentration of the light product, which is the feed concentration times one minus the purge to feed ratio. The purity and enrichment of the heavy product are the same as for the case with no breakthrough.

Design Study

A brief design study is carried out here with the H_2 - $MmNi_{4.2}Al_{0.8}$ metal hydride system at 308 K¹² to show the feasibility of a stripping reflux PSA process for concentrating dilute systems that exhibit an unfavorable Langmuir isotherm. The isotherm is shown in **Figure 3**, with the Langmuir model fit only to the unfavorable section. This system is unique because only H_2 adsorbs on the metal hydride, which makes all other components like CO_2 , CH_4 , etc the light inert components. In this study, a 5% H_2 mole fraction in the feed (y_f) and a 1% H_2 (y_{LP}) maximum light product impurity are imposed. A y_f of 5% limits the pressure ratio to less than 20; and to stay on the concave portion of the adsorption isotherm, the high (feed) pressure is limited to 29.6 atm. The pressure ratio was thus set at 19, which results in a low pressure of 1.56 atm.

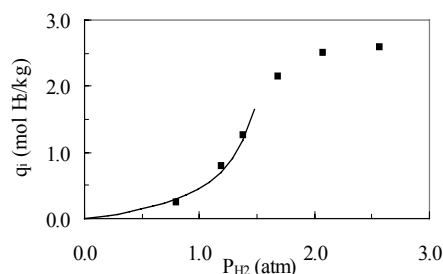


Figure 3. H_2 - $MmNi_{4.2}Al_{0.8}$ adsorption isotherm at 308 K. Points: experimental data. Solid line: Langmuir correlation.

Other process conditions are specified in **Table 1**, where v_f is the feed velocity, V_f is the feed volumetric flow rate, L_b is the bed length, d_b is the bed diameter, and t_f is the feed cycle time (which is equal to the purge cycle time). With these conditions set, the remaining process conditions and performance indicators can be calculated. To reach a periodic state when there is no breakthrough, γ must be 1. The only restriction on γ when there is breakthrough is that it is less than 1, so $\gamma = 0.8$ was chosen for the case with breakthrough. Now, the recovery, purity, and enrichment can be calculated. The results of these calculations are summarized in **Table 2**.

Table 1. Operating Conditions and Parameters for the Design Study

y_f	---	0.05
v_f	m/s	0.10
V_f	m ³ STP/min	44.5
ρ_b	kg/m ³	2000
L_b	m	6.00
d_b	m	0.60
P_H	atm	29.6
P_L	atm	1.56
T	K	308
t_f	s	550
y_{LP}	---	0.01

Table 2. Calculated Process Parameters and Performance Indicators

	Units	w/o BT	w/BT
R	---	5.45	5.45
ζ_a	---	0.00	4.23
γ	---	1.00	0.80
L	m	0.97	0.97
E	---	19.0	19.0
L_b/d_b	---	10.0	10.0
Rec _{HP}	%	100	80.0
Rec _{LP}	%	94.7	95.8
$y_{H2,LP}$	---	0.00	0.01
$y_{H2,HP}$	---	0.95	0.95

The results of the no breakthrough design study show that a 5% H₂ stream can be enriched 19 times with a recovery of 100%. This can be achieved while producing a 100% pure light component with a recovery of 94.7%. The columns are also reasonably sized. For the breakthrough case with 1% H₂ allowed in the light product, although the light component recovery increases, the H₂ recovery decreases significantly to 80%, which outweighs the beneficial effects associated with breakthrough. Nevertheless, these design results are quite remarkable. Although in actual practice the performance will be diminished due to heat effects, this analysis shows that high heavy component enrichments may still be achieved.

Conclusions

The equilibrium theory analysis carried out here showed that it is possible to achieve high enrichments and recoveries of the heavy product with a simple two-step PSA process using an adsorbate-adsorbent that exhibits an unfavorable Langmuir isotherm. The resulting analytical expressions (not given) can be used for feasibility studies, and designing and developing heavy component upgrade systems as shown here with a brief design study using the H₂-MmNi_{4.2}Al_{0.8} metal hydride system that included the effects of H₂ breakthrough into the light product.

Acknowledgements. Funding provided by the Westvaco Charleston Research Center, the SRP at the University of Texas at Austin, and the NSF GK-12 Program through award DGE-008642 is greatly appreciated.

References

1. Skarstrom, C.W. *Ann. N.Y. Acad. Sci.* **1959**, 72, 751.
2. Ruthven, D.M. *Principles of Adsorption and Adsorption Processes*; John Wiley & Sons: New York, 1984.
3. Yang, R.T. *Gas Separation by Adsorption Processes*; Imperial College Press: London, 1997.
4. Ruthven, D.M.; Farooq, S.; Knaebel, K.S. *Pressure Swing Adsorption*; VCH Publishers: New York, 1994.
5. Liu, Y.; Subramanian, D.; Ritter, J.A. *Stud. Surf. Sci. Catal.* **1998**, 120, 213.
6. LeVan, M.D. *Ind. Eng. Chem. Res.* **1995**, 34, 2655.
7. Subramanian, D.; Ritter, J.A. *Chem. Eng. Sci.* **1997**, 52, 3147.
8. Ritter, J.A.; Yang, R.T. *Ind. Eng. Chem. Res.* **1991**, 30, 1023.
9. Daniel, K.D.; Ritter, J.A. *Ind. Eng. Chem. Res.*, submitted 2001.
10. DeVault, D. *J. Amer. Chem. Soc.* **1943**, 65, 532.
11. Ritter, J.A.; Yang, R.T. *Chem. Eng. Sci.* **1991**, 46, 563.
12. Mongole, M.N.; Balasubramaniam, R. *Int. J. Hydrogen Energy.* **2000**, 25, 55.

Density Functional Theory Studies of Hydrogen Diffusion in CuPd Alloys

Preeti Kamakoti* and David S. Sholl*[†]

*Dept. of Chemical Engineering, Carnegie Mellon University,
Pittsburgh, PA 15213, USA

[†]National Energy Technology Laboratory, Pittsburgh,
PA 15236, USA

Introduction

Nonporous membranes made from Pd and Pd alloys have been extensively studied because of their ability to be highly selective for hydrogen separations¹. The effectiveness of these membranes for permeation of hydrogen relies on the dissociation of molecular hydrogen at the membrane surface, the solubility of atomic hydrogen in interstitial sites of the metal, and rapid diffusive transport of atomic hydrogen through between interstitial sites. In applications involving separation of hydrogen from mixed gas streams, the poisoning of metal membrane surfaces by non-hydrogen species can be a severe problem.

Several recent studies have suggested that membranes made from alloys of Cu and Pd may have favorable properties²⁻⁴. One potential complication with using CuPd alloys is that multiple bulk phases are observed as the Cu content is varied⁵. At temperatures lower than 600 °C, a broad region of the CuPd phase diagram including all alloys with greater than 60 at.% Pd exist as a disordered fcc phase (often referred to as the α phase). For a substantial range of compositions centered about 40 at.% Pd, however, the stable phase in the same temperature range is an ordered bcc phase (the β phase). Separating the regions where the fcc and bcc phases are stable is a region where both phases are observed, depending on the sample preparation method. For temperatures below 500 °C, alloys with 50 at.% Pd fall in this two phase region. Above 600 °C, only the disordered fcc phase is observed.

One reason that the CuPd phases described above are interesting in terms of membrane applications is that several studies have suggested that the diffusion rate of atomic hydrogen in bcc CuPd alloys is substantially faster than the same quantity in either fcc CuPd alloys or pure Pd. Experiments by Piper indicated that the diffusivity of H in bcc CuPd is almost two orders of magnitude faster than the diffusivity in fcc CuPd alloys at room temperature⁶. Piper estimated that the activation energy for H diffusion in the bcc phase is 0.035 eV. Subsequent experiments by Zetkin *et al.* for deuterium diffusion gave similar conclusions^{7,8}. Studies of practical alloy membranes by Roa *et al.* recently indicated that bcc CuPd membranes exhibit higher fluxes than comparable fcc CuPd membranes³.

We have used plane wave Density Functional Theory (DFT) to examine the binding sites, diffusion pathways, and diffusion activation energies for H diffusion in pure Pd and CuPd alloys with ~50 at.% Pd. At this alloy composition, both fcc and bcc phases can exist, so we separately considered fcc and bcc CuPd. Our results provide a useful basis for developing an accurate model of H diffusion rates in CuPd alloys over a broad range of compositions.

Computational Methods

All calculations were performed using plane wave DFT within the Generalized Gradient Approximation (GGA) as implemented in the Vienna *ab initio* Software Package^{9,10}. These calculations examine materials of infinite spatial extent by using supercells with periodic boundary conditions in all three principal directions. Pure fcc Pd and ordered bcc CuPd (50 at.% Pd) were studied using computational supercells containing 27 and 16 atoms respectively. A randomly ordered fcc CuPd system (51.9 at.% Pd) was examined

using a supercell containing 14 Pd atoms and 13 Cu atoms. All calculations below referring to interstitial H were performed by inserting a single H atom into these supercells, corresponding to dilute loadings of interstitial H. The geometry relaxations performed for each material are described in our results section below. Geometry relaxations were terminated when residual forces on all unconstrained atoms were less than 0.03 eV/Å. The Monkhorst-Pack scheme for generating *k*-points was used and all calculations used an energy cutoff of 17.18 Ry.

Zero point energy (ZPE) corrections can be substantial for light species such as H. At each H binding site, we approximated the Hessian matrix for the Born-Oppenheimer potential energy surface using finite difference approximations. The Hessian was then used to find the normal modes of H at each binding site and ZPE corrections were made by assuming a harmonic potential in the neighborhood of the local minima. ZPE corrections at the transition states discussed below were computed in the same manner. For all of the transition states discussed below, normal mode analysis for a mobile H atom in the presence of constrained metal atoms yielded two real and one imaginary frequency, as required.

Results and Discussion

We first discuss interstitial H in pure Pd. All DFT calculations for pure Pd used a 4×4×4 *k*-point mesh. Full geometry relaxations, including the supercell volume, were performed both with and without the presence of an interstitial H. Both the lattice constant calculated for pure Pd (3.95 Å) and the lattice expansion induced by H at this loading (0.5 %) are in excellent agreement with experimental results. Our calculations confirm the well-known fact that H sits in the octahedral sites in this fcc lattice. Our calculations give a binding energy of 3.47 eV for atomic H. This binding energy is reduced to 3.38 eV after accounting for ZPE corrections. These ZPE corrections are very similar in magnitude to previously reported values^{11,12}.

To estimate the diffusion activation energy for H in pure Pd, we fixed the metal atoms in the geometry found to minimize the total energy when H sits at an octahedral site. We then computed the energy of an interstitial H at a series of points along a straight line path between two octahedral sites. As expected, the maximum energy along this path lies symmetrically between the two octahedral sites. Without ZPE corrections, the activation energy required to traverse this path is 0.39 eV. When ZPE corrections at the energy minimum and the approximate transition state are included, this energy difference increases to 0.49 eV. The activation energy is increased by the ZPE corrections because the two vibrational frequencies at the transition state are substantially higher than the three degenerate vibrational frequencies for H in an octahedral site. This estimated diffusion activation energy is somewhat higher than the activation barrier observed experimentally (0.23 eV)¹¹. Some of this discrepancy may be accounted for by noting that the diffusion activation energy of H in Pd decreases as the concentration of interstitial H is increased¹².

DFT calculations for ordered bcc CuPd were performed in a similar manner to our pure Pd calculations. All calculations used a 4×4×4 *k*-mesh. Volume and geometry relaxations for bcc CuPd with no interstitial H gave a lattice constant of 3.03 Å, in excellent agreement with the experimental value for a 47 at.% Pd bcc alloy (2.97 Å)¹³. Volume and geometry relaxations for the same system including one interstitial H show that H preferentially binds in the tetrahedral sites of the alloy. The ZPE corrected binding energy for atomic H in this material is 3.26 eV. Thus, the binding energy of H is only slightly lower in this bcc CuPd alloy than in pure Pd. The activation energy required for H to diffuse between two adjacent tetrahedral sites was determined in a manner similar to that used for

pure Pd. Metal atoms were fixed in their optimized geometry in the presence of a H atom at a tetrahedral site and the energy of moving an H atom in a straight line path through a Cu₂Pd face between tetrahedral sites was subsequently computed. The energy difference between the minimum energy site and the estimated transition state determined in this way is only 0.07 eV. Including ZPE corrections at both the minimum and the transition state reduces this activation energy to 0.03 eV. The striking observation that the diffusion activation energy for H in bcc CuPd is roughly an order of magnitude smaller than in pure fcc Pd strongly supports the experimental results cited above that show H diffusion to be much faster in bcc CuPd than in pure Pd. Although we have not yet computed the analogous diffusion barrier for motion through a Cu₂Pd₂ face between tetrahedral sites, we note that it is possible to diffuse arbitrary distances through this bcc structure passing through only Cu₂Pd faces, so the barrier given above provides an upper limit on the diffusion activation energy to net diffusion in this ordered alloy.

Describing the binding and diffusion of H in fcc CuPd is more complex than in the two materials discussed above because of the disordered nature of this alloy. Our calculations for fcc CuPd with 51.9 at.% Pd were performed with a 2×2×2 *k*-mesh. The cell volume and geometry of the alloy was optimized with no H present and no further relaxations of metal atoms were performed when interstitial H was included in the supercell. Similar calculations performed for pure Pd indicated that lattice relaxations due to interstitial H gave only small corrections to H binding and activation energies. The lattice parameter of the fcc CuPd system was found to be 3.83 Å, in excellent agreement with the experimentally observed 3.77 Å at the same composition¹³. Our calculations indicate that H binds in octahedral sites in fcc CuPd, as it does in pure Pd. The H binding energy increases monotonically as the Pd content of the octahedral metal atoms surrounding the H atom increases. Specifically, we find binding energies of 3.05, 3.15, 3.23, and 3.26 eV in Cu₅Pd, Cu₄Pd₂, Cu₃Pd₃, and Cu₂Pd₄ octahedra respectively. These values do not include ZPE corrections, which are likely to be similar to those for pure Pd. These results indicate that the binding energies of interstitial H in fcc CuPd are quite similar to those in pure Pd and in bcc CuPd. It is worth noting that bcc CuPd alloys with compositions other than 50 at.% Pd also exhibit random disorder, so these alloys will also exhibit a variety of H binding energies, unlike the ordered bcc alloy considered above.

Because of the large number of energetically distinct binding sites in randomly ordered fcc CuPd, there is a plethora of distinct diffusion activation energies for H atoms hopping between adjacent octahedral sites. To examine these activation energies in a preliminary manner, we focused on a single transition between two adjacent Cu₃Pd₃ octahedral sites in our supercell. The transition state was estimated by placing the H atom at the centroid of a triangular face shared by the two octahedra through which the diffusion path passes. The resulting activation energy is 0.42 eV without ZPE corrections. As in pure Pd, including ZPE corrections raises the activation energies somewhat, in this case to 0.48 eV respectively.

The disordered nature of the fcc CuPd alloy means that in addition to the distribution of binding energies described above, there are multiple inter-site hopping barriers. Determining the net activation energy for H diffusion in fcc CuPd requires a more comprehensive survey of inter-site hopping energies, together with a dynamic theory of H diffusion in this heterogeneous lattice¹⁴. We can note, however, that the activation energies given above are likely to be underestimates of the activation energies for hopping from the most strongly binding sites (i.e. Pd₆ and CuPd₅ octahedra) to less strongly bound sites. Since net diffusion of H in fcc CuPd will be dominated by the rate at which H can escape from the most strongly binding sites, the activation energy for net H diffusion is likely to be

considerably larger than the two barriers listed above. That is, the activation energy for H diffusion in fcc CuPd with ~50 at.% Pd is much larger than the activation energy for H diffusion in bcc CuPd with the same composition. Our current work is focused on providing a more quantitative basis for this comparison.

Conclusions

We have used plane wave DFT to examine the binding and diffusion of interstitial H in pure Pd and CuPd alloys with ~50 at.% Pd. In agreement with experimental results, we find that the diffusion activation energy of H in ordered bcc CuPd is much lower than the same quantity in either pure Pd or randomly substituted fcc CuPd alloys. Since the diffusion activation energies of interstitial H can vary in a complex way with alloy crystal structure and composition¹⁴, our results suggest that plane wave DFT can provide a useful computational tool for achieving a quantitative understanding of H diffusion in technologically relevant alloys as functions of these crucial parameters.

Acknowledgement. DSS is an ORISE Faculty Fellow at NETL and an Alfred P. Sloan fellow. Computations were performed at the Pittsburgh Supercomputer Center and on a computer cluster in the CMU Chemical Engineering Department supported by the NSF and Intel. We thank J. D. Way for helpful discussions.

References

- (1) Edlund, D.; Friesen, D.; Johnson, B.; Pledger, W. *Gas Purification and Separation* **1994**, 8, 131-136.
- (2) Roa, F.; Way, J. D.; McCormick, R. L.; Paglieri, S. *Chemical Engineering Journal* **2002**, in press.
- (3) Roa, F.; Block, M. J.; Way, J. D. *Desalination*, submitted.
- (4) Nam, S.-E.; Lee, K.-H. *Journal of Membrane Science* **2001**, 192, 177-185.
- (5) Hansen, M. *Constitution of Binary Alloys*; McGraw-Hill: New York, 1958.
- (6) Piper, J. *Journal of Applied Physics* **1966**, 37, 715-721.
- (7) Zetkin, A. S.; Kagan, G. Y.; Levin, Y. S. *Phys. Met. Metall.* **1987**, 64, 130-134.
- (8) Zetkin, A. S.; Kagan, G. E.; Varakshin, A. N.; Levin, E. S. *Sov. Phys. Solid State* **1992**, 34, 83-85.
- (9) Kresse, G.; Hafner, J. *Physical Review B* **1993**, 48, 13115.
- (10) Kresse, G.; Furthmüller, J. *Comput. Mat. Sci.* **1996**, 6, 15.
- (11) Volkl, J.; Alefield, G. In *Hydrogen in Metals I*; Alefield, G., Volkl, J., Eds.; Springer-Verlag: Berlin, 1978; Vol. 28, pp 321-348.
- (12) Elasseer, C.; Ho, K. M.; Chan, C. T.; Fahnle, M. *J. Phys. Condens. Matter* **1992**, 4, 5207-5226.
- (13) Pearson, W. B. *A Handbook of Lattice Spacings and Structures of Metals and Alloys*; Macmillan: New York, 1958.
- (14) Brouwer, R. C.; Salomons, E.; Griessen, R. *Physical Review B* **1988**, 38, 10217-10226.

DEVELOPING HIGH-TEMPERATURE, CO TOLERANT POLYMER ELECTROLYTE MEMBRANE FUEL CELLS

S. Tulyani^a, K.T. Adjemian^b, L. Krishnan^b, C. Yang^c, S. Srinivasan^c,
A.B. Bocarsly^b, J.B. Benziger^a

Department of Chemical Engineering^a
Department of Chemistry^b
Center for Energy and Environmental Studies^c
Princeton University, Princeton, NJ 08544

Introduction

High temperature operation of polymer electrolyte membrane fuel cells is desirable to allow for operation using reformed hydrocarbon fuels which contain CO impurities. Elevated temperatures also improve fuel cell performance by improving reaction kinetics. However higher temperatures introduce greater challenges in maintaining hydration in the membrane and membrane-electrode interface which are necessary to allow for proton conductivity. Modification of the membrane and electrode interface by the impregnation of mesoscopic metal oxide particles has been found to allow for improved fuel cell performance at elevated temperatures. The structure and properties of these modified membranes are being studied through a combination of water uptake and conductivity experiments as well as small-angle x-ray scattering analysis.

Experimental

Modified Membrane Preparation. The membranes were pretreated to remove impurities. After pretreatment, the membranes were placed in a 2:1 by volume mixture of methanol and water for a few minutes. The membranes were then submerged in a 3:2 by volume mixture of tetraethoxysilane and methanol for a period of time depending on the desired silicon oxide content. The membranes were then dried at 100°C and treated again to remove impurities. Recast silicon oxide membranes were produced by mixing commercial 5%Nafion solution with isopropanol and a siloxane polymer solution. After formation, the recast membranes were also treated to remove impurities.

Active Layer Modification. The silica sol was prepared by mixing 2 ml TEOS (Tetraethoxy silane), 4.7 ml distilled water and 100 μ l of 0.1 M HCl for 3 hours. Electrodes (E-TEK ELAT double sided, 20% Pt on C, 0.4 mg/cm²) are prepared by brushing 0.6 mg/cm² Nafion solution (5 % by wt) and required amount of the silica sol depending on the wt % of silica needed on the electrodes. Nafion 115 was used as the membrane. MEAs were prepared by hot pressing the electrodes and the membrane at 130°C for 1 min without pressure and applying 1 metric ton pressure for 1 minute.

Water Uptake and Conductivity Measurements. A barometric sorption vessel (400 cm³) was constructed and used to quantify water uptake of a membrane sample[1]. The dry membrane is placed within the sorption vessel held at a given temperature and known quantity of water is introduced into the vessel through a septum. The membrane water uptake can be calculated by using a pressure transducer to determine the difference between the expected vapor pressure and actual vapor pressure. The conductivity is measured on the membrane in the longitudinal (in-plane) direction by an AC impedance spectroscopy two probe method using a PAR 273A potentiostat/galvanostat and a 5210 lock-in amplifier[2].

SAXS Analysis. The Cu-K α x-rays were generated by a Philips XRG-3000 sealed tube generator source. The beam was slit collimated and the scattering was detected by an Anton-Paar compact Kratky camera equipped with a Braun OED-50M detector. Empty beam scattering, sample transmittance, and detector response were corrected for in the data analysis. The data reduction and desmearing procedures used are described in detail by Register [3].

Results and Discussion

Fuel Cell Data. Introducing metal oxides into the membrane and the active electrocatalyst layer have been shown to improve fuel cell performance at elevated temperatures as shown in **Figures 1 and 2**.

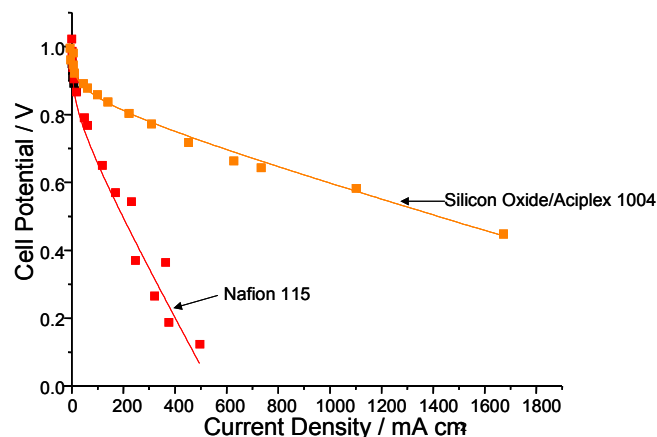


Figure 1. Cell Potential versus current density at a fuel cell temperature of 130°C.

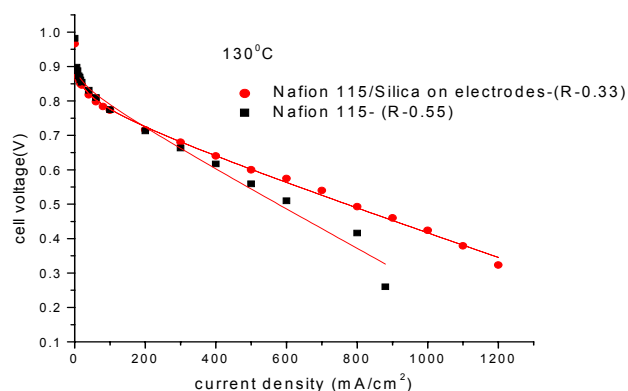


Figure 2. Performance curves of PEMFC with cell temperature 130°C at 3 atm

Membranes containing silicon oxide lead to significant improvements of fuel cell performance at 130°C as can be seen in **Figure 1**. In the modification of the electrode membrane interface it was found that 6% by weight of silica provided the best results. Higher silica concentrations led to mass transport problems.

Water Uptake and Conductivity Results. The comparison between the Nafion and Nafion composite membrane shows higher uptake by the composite membrane around a relative humidity of 65% as shown in **Figure 3**.

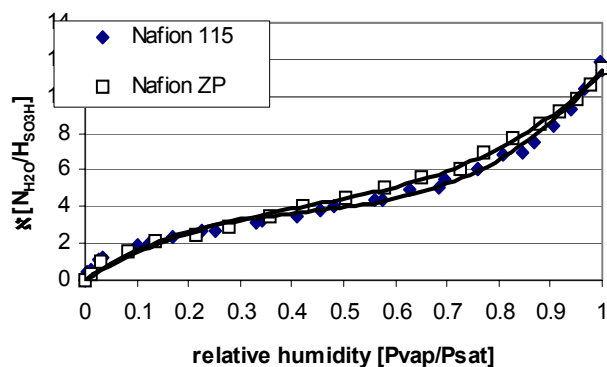


Figure 3. Nafion 115 and Nafion Zirconium Phosphate membrane water content vs relative humidity at 80°C.

As the water content of the membrane increases, the conductivity of the membrane rises exponentially as shown in **Figure 4**.

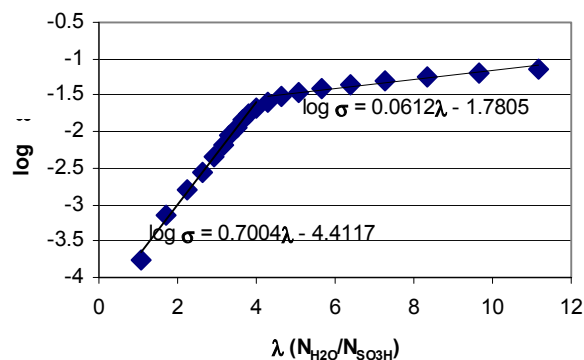


Figure 4. Membrane conductivity variation with water content for Nafion 115 membrane.

The semilog plot in shows two distinct regions of exponential conductivity increase with increasing water content. At low water content, conductivity increases rapidly as the membrane water increases. For a hydration state greater than 4 waters per sulfonate group, conductivity increases less with additional water.

SAXS Results. From the SAXS analysis, it was found that the Bragg spacing which represents the distance between ionic clusters increased with increasing water content in all cases as shown in **Figure 5**.

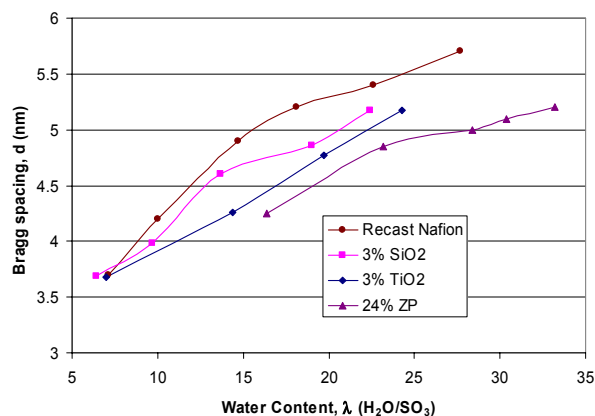


Figure 5. Comparison of Bragg spacing of composite membranes with pure Nafion at different levels of hydration

For a given water content, the Bragg spacing was lower for the composite membranes than for the control membrane. This indicates that the presence of the inorganic compound may inhibit the agglomeration of the ionic clusters to the extent that occurs in pure Nafion. Further experiments are in progress to find out how the characteristics of each compound effect the behavior of the composite membranes as they uptake water. This SAXS study provides information on the structural changes of the membrane during the uptake of water in the presence of inorganic compounds.

The reason that the inclusion of small amounts of metal oxide in the membrane and active layer lead to improved fuel cell performance is uncertain. It is believed that the improvement in fuel cell operation is due to a combination of effects including higher water uptake, improved conductivity and more, smaller ionic clusters.

References

- (1) Mikaye, N.; Wainwright, J. S.; and Savinell, J. *J. Electrochem. Soc.*, **2001**, 148 (8), A898.
- (2) Yang, C.; Costamanga, P.; Srinivasan, S.; Benziger, J.B.; and Bocarsly, A.B. *J. Power Sources*, **2001**, 103, 1.
- (3) Register, R.A. and Bell, T.R. *J. Polym. Sci., Part B: Polym. Phys.*, **1992**, 30(6), 569.

DEVELOPMENT OF A REVERSIBLE HYDROGEN STORAGE MATERIAL FROM METAL DOPED SODIUM ALUMINUM HYDRIDE

J. A. Ritter¹, R. A. Riggelman¹, A. D. Ebner¹, and R. Zidan²

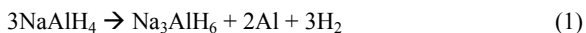
¹Department of Chemical Engineering
University of South Carolina
Columbia, SC 29208 USA

²Westinghouse Savannah River Company
Savannah River Technology Center
Aiken, SC 29804 USA

Introduction

Chemical and metal hydrides have been investigated as materials of predilection for hydrogen storage;¹⁻⁶ efforts have also explored the use of activated carbon and carbon nanotubes. Chemical hydrides, such as NaAlH₄ and LiAlH₄, are promising materials in this regard because of their high concentration of useful hydrogen (5.6 and 7.9 wt%, respectively), which is typically much higher than most metal hydrides (0.5–2.0 wt %) and carbon materials (0.5–1.0 %). Also, the costs and the hydrogen dissociation energies of these materials are sufficiently small to warrant further investigation.

At standard conditions, the dehydrogenation of NaAlH₄ is thermodynamically favorable, but it is kinetically slow and takes place at temperatures well above 200°C in a two-step process involving the following reactions:¹⁻⁴



Bogdanovic and Schwickardi¹ found that the hydrogen dissociation temperature in NaAlH₄ could be lowered by about 50°C when catalyzed with at least 2 mol% of titanium, consequently improving the kinetics and the conditions for reversibility. Zidan and other investigators³⁻⁵ discovered later that a further lowering of the dehydrogenation temperature was highly dependent on the doping and homogenization procedures. Zidan et al.³⁻⁴ also found that zirconium when mixed with titanium improved the dehydrogenation reversibility of NaAlH₄ over Ti alone.

The present study is an update of the on-going effort to lower the hydrogen desorption temperature of catalyzed NaAlH₄. In this regard, the search for new and better catalysts, other than the traditional Ti and Zr catalysts, is underway. The effect of two new metals, Fe and Va, as well as combinations of these with Ti and Zr on the hydrogen desorption kinetics is shown. Note that the samples utilized in this study were doped manually only using a mortar and pestle in tetrahydrofuran; nevertheless, it was assumed that the relative effect of a catalyst or combination of catalysts was not going to be affected. Thermogravimetric measurements were carried out on both catalyzed and uncatalyzed NaAlH₄ to determine the initial dehydrogenation temperature and the temperature at which the maximum rate of dehydrogenation occurs.

Experimental

Ti(BuO)₄ (Aldrich, 97%), Zr(PrO)₄ (Aldrich, 70%), Fe(EtO)₃ (Gelest) and Bis(cyclopentadienyl)Va (Aldrich) were used as precursors for the catalysts. Each of these precursors was diluted into 100 mM solutions using THF (Aldrich, 99.9%) as a solvent. The NaAlH₄ (Fluka) was purchased as a 1.0 M solution in THF; the THF was completely removed by drying at 55 °C overnight. The dried NaAlH₄ was mixed with a predetermined amount of catalyst solution

to produce a doped sample in the desired concentration. Samples containing a single catalyst or a combination of them with concentrations varying from 0.25 to 8 mol% were all prepared in this manner. The THF evaporated while the NaAlH₄ and the catalyst were mixed manually for about 30 minutes using a mortar and pestle, or until the samples were completely dry. The above procedures were carried out in a N₂-laden glove box free of oxygen and moisture.

A DSC7 Perkin-Elmer thermogravimetric analyzer (TGA) was used for to determine the hydrogen desorption kinetics at atmospheric pressure. This instrument was located in another glove box under nitrogen atmosphere to prevent any exposure of the samples to air and moisture. Samples were heated to 300°C at a ramping rate of 5°C/min under 1 atm of He, using an initial 15 minute delay to ensure an environment of pure He. Approximately 10 mg of sample was used in the TGA analyses.

Results and Discussion

Figure 1 shows the TGA results for a series of single and multiple metal catalyzed NaAlH₄. Note that since all the samples were evaluated as prepared, weight losses larger than the maximum expected for NaAlH₄ were observed; however, this was only a consequence of the organic precursors still being present in the samples. Except for the pure Fe and Va catalysts, all the samples exhibited an initiation of the weight loss at about 150°C. The pure Fe and Va catalysts exhibited initial weight losses at approximately 180°C. Table 1 summarizes the effect of the catalyst and its concentration on the initial dehydrogenation temperature. In general, the samples containing Ti exhibited the best behavior. However, it was particularly interesting to observe the synergistic behavior with the Fe-Ti mixed catalyst system, which performed better than either Fe or Ti alone; it also performed better than the Zr-Ti mixed catalyst system that has been studied previously,³⁻⁴ despite the fact that the sample catalyzed only with Zr performed better than the sample catalyzed only with Fe. It is also observed that post-washing with THF and drying after preparation of the sample did not cause any significant effect on the desorption behavior of the sample.

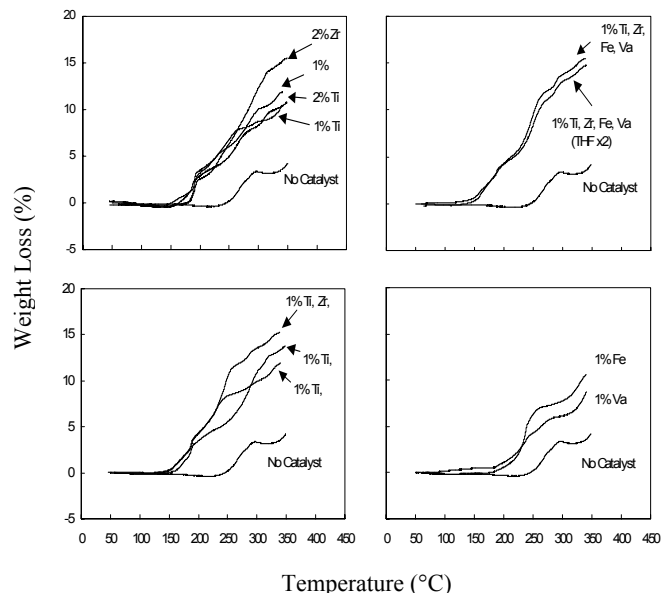


Figure 1. Thermogravimetric analyses of NaAlH₄ doped with varying amounts of single and multiple metal catalysts.

Figure 2 shows the differential TGA results for the same series of single and multiple metal catalyzed NaAlH₄. With the exemption of the samples containing Fe and Va alone, all the samples had a maximum rate of weight loss at about 180 °C, which coincided with the melting point of the chemical hydride. Samples containing pure Fe and Va catalysts had maximum weight losses at approximately 220°C. In contrast, the uncatalyzed NaAlH₄ exhibited maximum weight losses at temperatures between 250 and 270°C. The valleys observed at the higher temperatures for these samples were believed to be mainly due to the decomposition and/or desorption of the organic precursors.

These preliminary results were quite exciting in that they demonstrated very clearly the positive effect of doping NaAlH₄ with a transition metal. However, they tend to generate more questions than answers. Why does the NaAlH₄ doped with single and mixed metal catalysts appear to reach a threshold dehydrogenation temperature of around 140 to 150 °C, essentially independent of the type of metal? What is the role of the metal dopant? Is it a surface catalytic mechanism or is it a mechanism that alters the molecular framework of the NaAlH₄? Will reversibility, i.e., hydrogenation, be as insensitive to the metal catalyst as dehydrogenation? Answers to these questions are currently being sought with more experimentation.

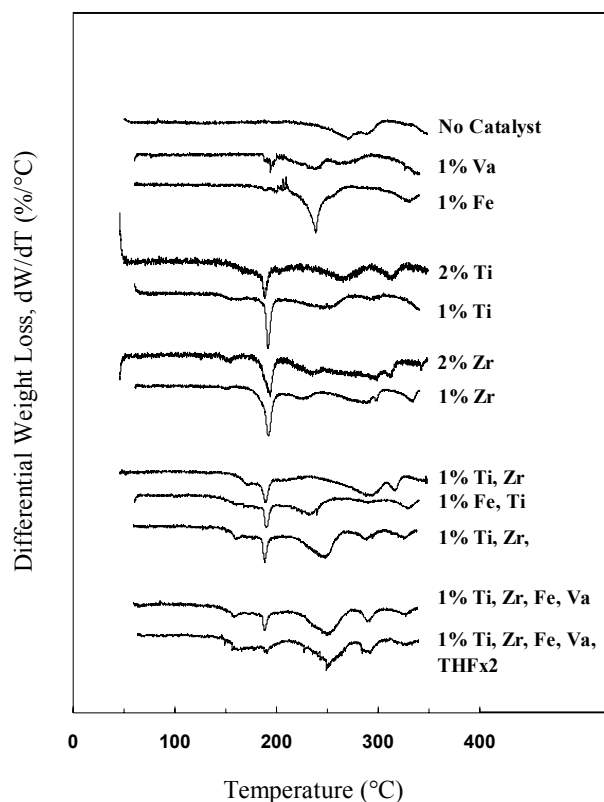


Figure 2. Differential thermogravimetric analyses of NaAlH₄ doped with varying amounts of single and multiple metal catalysts.

Conclusions

In an ongoing effort to reduce the kinetic limitations of the dehydrogenation of sodium aluminum hydrides (NaAlH₄) the addition of different transition metal catalysts (Ti, Zr, Fe and Va) in various concentrations and combinations have been investigated using thermogravimetric analysis (TGA). The TGA results revealed that Ti and Zr doped systems had their effective hydrogen desorption

temperature lowered by approximately 85°C, while systems with only Fe or Va had their effective desorption temperature lowered by about 55°C. The systems with the lowest desorption temperature (in order of performance) were Ti-Fe, Ti-Zr-Fe and Ti in 1-1, 1-1-1 and 1 mol%, respectively; although with only slight differences among them. Overall, these results continue to prove that doping NaAlH₄ with transition metals improves the dehydrogenation kinetics.

Additional studies are under way to determine the effect of those catalysts on the hydrogenation conditions of NaAlH₄. The study is also aimed at determining the effect of high energy balling milling on the performance of the catalyzed samples investigated here. This overall effort will involve optimizing the conditions (temperature and pressure) needed for cycling, thereby making a more viable reversible hydrogen storage material for transportation applications.

Table 1. Effect of the Catalyst and Its Concentration on the Initial Dehydrogenation Temperature of NaAlH₄

Catalyst	Initial Dehydrogenation T (°C)	Catalyst	Initial Dehydrogenation T (°C)
No Catalyst	240	1% Va	189
2% Zr	152	1% Ti, Zr, Fe, Va	150
1% Zr	152	1% Ti, Zr, Fe, Va (THF x 2)	152
2% Ti	155	1% Ti, Zr, Fe	145
1% Ti	149	1% Ti, Zr	158
1% Fe	180	1% Ti, Fe	142

Acknowledgements

Financial support provided by SCUREF/WSRC/DOE under contract WEST052, KG09725-O, and the National Reconnaissance Office under contract NRO-00-C-0134 is greatly appreciated.

References

1. B. Bogdanovic, M. Schwickardi, J. Alloys Comp. 253 (1997) 1.
2. B. Bogdanovic, R. A. Brand, A. Marjanovic, M. Schwickardi, J. Tölle, J. Alloys Comp. 302 (2000) 36.
3. R. A. Zidan, S. Takara, A. G. Hee C. M. Jensen, J Alloys Comp. 285 (1999) 119.
4. C. M. Jensen, R. Zidan, N. Mariels, A. Hee, C. Hagen, Inter. J. Hydrogen Energy 24 (1999) 461.
5. C. M. Jensen, K. J. Gross, Appl. Phys. A: Mat. Sci. Proc. 72 (2001) 213.
6. K. J. Gross, S. Guthrie, S. Takara, G. Thomas, J. Alloys Comp. 297 (2000) 270.

Distributed Hydrogen by Rapid Solar-thermal Dissociation of Methane

Alan W. Weimer¹, Jaimee K. Dahl¹, Karen J. Buechler¹, Allan Lewandowski², Carl Bingham³, Pamela Spath², and Wade A. Amos²

(1) Department of Chemical Engineering, University of Colorado, Boulder, CO 80309-0424, Fax: 303-492-4341, alan.weimer@colorado.edu, (2) Thermal Group, National Renewable Energy Laboratory, (3) NREL

ABSTRACT

A solar-thermal process is being developed for the benign dissociation of natural gas. The process takes advantage of rapid reaction rates at high reaction temperatures near 2000 K. The reactor is a vertical transport reactor and is comprised of multiple concentric tubes. An outer quartz protection tube allows concentrated sunlight to pass through while an inner porous graphite tube provides for a gaseous hydrogen "fluid-wall" that prevents the build-up of carbon black along the inside wall. Single pass methane conversions of 75% have been achieved for residence times less than 100 milliseconds. Various process options being considered for development include distributed hydrogen for a "fleet" service station or to supply hydrogen to a semi-conductor facility in the desert SW. Another variation of the process is for a small utility where produced carbon black supplies a carbon conversion fuel cell while hydrogen supplements natural gas flowing to a conventional turbine. The produced carbon black is amorphous and nanosized with a surface area approaching 100 m²/gram.

INTRODUCTION

The environmental consequences of providing energy will continue to increase as the demand for energy increases throughout the world. The environmental impacts, such as increased carbon dioxide emissions, will be significant and cleaner methods of producing energy will have to be developed. Consequently, new economical and environmentally benign methods for synthesizing hydrogen on-site (distributed) are desperately needed. The ideal process would generate hydrogen in an easily purified form without generating carbon dioxide. One such process is the ultra-high temperature (near 2000 K) thermal dissociation of natural gas to hydrogen and carbon black. While the hydrogen is used to fill fuel cell vehicles or supply hydrogen users, the carbon black produced can displace current carbon black production, thus saving the energy and pollution associated with conventional carbon black production. The carbon black can also be used to supply carbon fuel cells, which are an efficient source of energy. A schematic of a distributed on-site hydrogen facility is shown in Figure 1.

Natural gas from an existing natural gas line can be used for the feed. The natural gas passes through a hydrogenator and then a ZnO bed to remove mercaptans and hydrogen sulfide from the stream. Purified natural gas is then fed vertically down through the inner porous graphite tube where it is rapidly dissociated to hydrogen and carbon black. The exiting stream of hydrogen, carbon black, and un-reacted natural gas passes through a jacketed cooling zone where it is cooled prior to being fed to a baghouse filter. Carbon black is separated in the baghouse and the hydrogen/natural gas mixture is then flowed through a pressure swing adsorber (PSA) where the hydrogen is purified. Incompletely converted natural gas is recycled to the solar-thermal reactor.

Some of the produced hydrogen is recycled and used to pad the annular region between the quartz and solid graphite tube, thus,

preventing oxidation of the outer graphite tube. Additional recycled hydrogen enters the annular region between the solid and porous graphite tubes and flows radially inward between the two tubes, thus, providing a fluid-wall that prevents deposition of carbon black on the inside wall of the reaction tube. The bulk of the product purified hydrogen is compressed and stored in a high pressure hydrogen storage tank. If additional hydrogen above that required for fueling fuel cell vehicles is produced, it may be fed to a hydrogen pipeline or to a PEM fuel cell for electrical power generation that can be supplied back to the grid.

The produced carbon black contains no ash and will be of high purity. It can be sold into the carbon black market or fed to a carbon conversion fuel cell for additional electrical power generation. The lack of ash makes the carbon black a very desirable feed stock for carbon conversion fuel cells.

EXPERIMENTAL

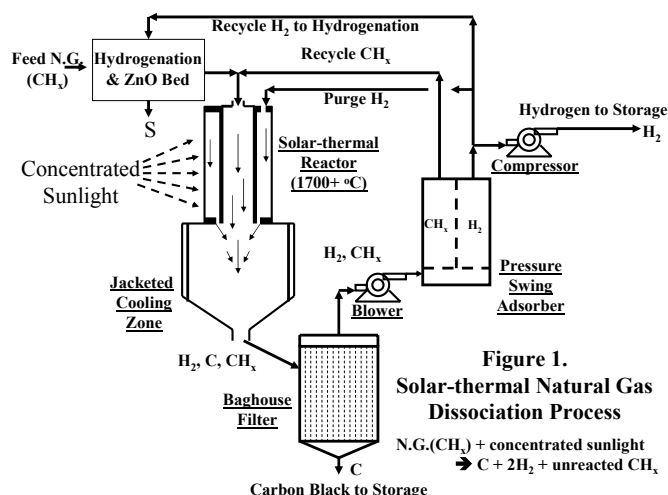


Figure 1.
Solar-thermal Natural Gas
Dissociation Process

The High Flux Solar Furnace (HFSF) facility at the National Renewable Energy Laboratory in Golden, Colorado is being used for this research. The HFSF uses a series of mirrors that concentrate sunlight to a focused beam at maximum power levels of 10 kW into an approximate diameter of 10 cm. A 74% efficient secondary concentrator distributes 7.4 kW of energy circumferentially around a 2.4 cm diameter x 9.4 cm long graphite reaction tube. The graphite tube is surrounded by a 5.1 cm diameter quartz protection tube. The quartz walled reactor is operated as a cold wall process, because the beam is delivered directly on target to the graphite. The control of solar radiation (on/off) is almost instantaneous. A pyrometer is used to measure the temperature of the graphite tube in the vertical center of the hot zone. In addition, a gas chromatograph/mass spectrometer is located downstream of the reactor to obtain in-line composition. The fine carbon black particles produced during the reaction are collected on a downstream filter. A photograph of the installed and operating reactor is shown in Figure 2.

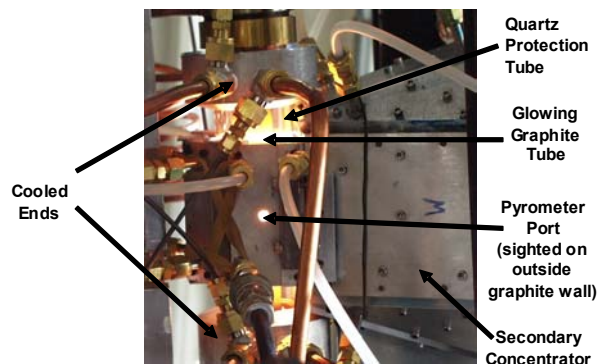


Figure 2. Reactor Tube Close-up On-sun

RESULTS AND DISCUSSION

Initial experimental studies with this reactor configuration are underway and have revealed extremely positive results. The process gas stream easily reaches temperatures greater than 1900 K with residence times less than 0.1 seconds. The effect of reactor temperature and residence time on reactor conversion is shown in Figure 3.

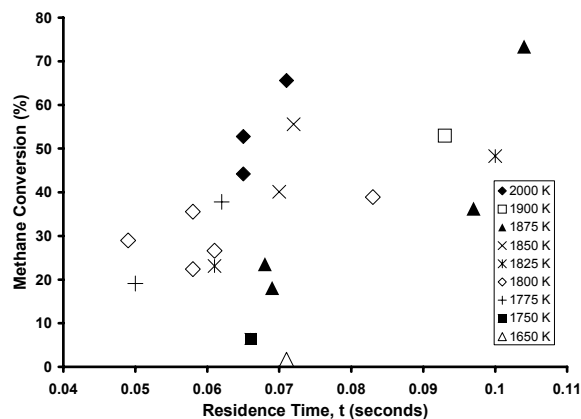


Figure 3. Effect of Temperature and Residence Time on Conversion

CONCLUSIONS

A solar-thermal aerosol flow reactor has been designed to dissociate methane to hydrogen and carbon black. High temperatures (greater than 1900 K) and short residence times (less than 0.1 seconds) are easily achievable using this reactor configuration. High single-pass conversions have been obtained. This process offers a promising method for producing distributed hydrogen to power fuel cell vehicles or supply hydrogen users in an environmentally benign manner.

Acknowledgement. The authors thank the DOE Hydrogen Program, the University of Colorado, and cost sharing companies (BP, Chevron-Phillips, Chevron-Texaco, EPRI, General Motors, Harper International, Pinnacle-West, PlugPower, Siemens) for financially supporting this work under Grants DE-FC36-99GO10454, DE-PS36-99GO10383. In addition, we thank the U.S. Department of Education for support through the Graduate Assistantships in Areas of National Need (GAANN) program.

FLUIDIZABLE CATALYSTS FOR HYDROGEN PRODUCTION FROM STEAM REFORMING BIOMASS PYROLYSIS PRODUCTS

Richard French, Kimberly. Magrini-Bair, Stefan Czernik,
Yves Parent, Marc Ritland and Esteban Chornet

National Renewable Energy Laboratory, 1617 Cole Boulevard,
Golden, Colorado 80401

Introduction

Previous work established that biomass pyrolysis oil could be steam-reformed to generate hydrogen using fixed-bed commercial catalysts.¹ These catalysts generally contain Ni, K, Ca, and Mg on alumina-based supports. The fixed-bed experiments showed that the carbohydrate-derived fraction of poplar pyrolysis oil could be almost stoichiometrically converted to hydrogen. However, process performance decreased with time because of char and coke deposition on the catalyst surface and in the bed itself thus limiting the reforming cycle to two or three hours. This cycle was even shorter when whole bio-oil or polymeric biomass-derived liquids (hemicellulose-rich fraction from biomass steam fractionation process) were used as feedstocks for hydrogen production.

Process performance was significantly improved by using a fluidized catalyst bed for reforming whole bio-oil and its fractions.²⁻³ The fluidized bed configuration, which provides better contact between the reactants and the catalyst, significantly extended time-on-stream. The reforming experiments conducted to date in the fluidized bed system with the carbohydrate-derived fraction of pyrolysis oils have shown promising results. The fluidized catalyst shows a slow decrease in activity with time, which we have shown can be reversed by catalyst regeneration, either on- or off-stream.

The mechanical strength of the fluidized catalyst is a significant process issue that must be addressed. We have been using commercial reforming catalysts that are designed and used for fixed-bed applications. We made a fluidizable catalyst material by grinding the pelletized commercial catalysts and by screening out the desired particle size fraction. These particles show good catalytic activity but poor physical strength. The high attrition rate of the particles results in excessive losses of catalyst solids from the reactor. Such losses are not acceptable for an industrial process. We have identified and evaluated inexpensive commercial supports of required mechanical strength and attrition resistance for the fluid bed system. We prepared and tested several catalysts, made with these supports and containing NiO and/or MgO and K₂O, for attrition resistance and activity. The results of these tests are reported.

Experimental

We pursued several routes to finding a fluidizable catalyst support that could withstand reforming conditions for extended operation. The simplest approach was to determine if the commercial catalyst support we had been using could be improved for fluidization use. A company with expertise in powder agglomeration and compaction looked at improving mechanical strength through grinding, the addition of various binders, and subsequent compaction of the resultant materials. Such processing did not improve mechanical strength of the commercial material. We then looked for other commercially available materials of reasonable cost that could have the required mechanical strength for fluidization. Grinding media provided required mechanical strength though surface areas generally were too low to provide a reasonable catalyst support. We identified an alumina manufacturer (CoorsTek Ceramics) that had readily available materials with the required properties. They were also able to tailor the

properties of these aluminas to our requirements for particle size, surface area, and attrition resistance with readily available processes.

The supports were evaluated for attrition resistance in a 2" fluidized bed reactor for 48 hours. Simulated reforming conditions were: 850°C, 2.5g/min fluidizing steam and 2.5g/min liquid water injected into the 250g-support bed with nitrogen. Weight losses of these materials were measured after exposure to these conditions and are reported as %loss per day.

The best of the initial support materials, alpha alumina particles of 90-99% purity, were used to prepare several simple Ni-based catalysts to evaluate reforming activity first with methanol and then with aqueous pyrolysis oil extract in a fluidized reactor. Actual reforming conditions were similar with 2.5 g/min of either methanol or aqueous extracted pyrolysis oil replacing water from the attrition tests. The catalysts contained from 0.1-1.0 wt% MgO, 1.0-9.0 wt% NiO and 0.1-0.5 wt% K₂O. In general, Mg is used to stabilize Ni crystallite size and K to reduce coke deposition on the catalyst surface. All catalysts were prepared by addition of aqueous solutions of Ni, Mg, and K nitrate salts to the alumina supports to incipient wetness. The catalysts were calcined at 650°C in air to convert the metal salts to oxides. The goal of the preliminary tests was evaluating catalyst activity and determining attrition losses from use during reforming.

Results and Discussion

Results of the attrition resistance tests are summarized in Table 1. Both commercial catalysts were used for 48 hours of pyrolysis oil reforming and losses ranged from 28-33% of the original catalyst charge. The corundum material and most of the alumina samples exhibited acceptable attrition resistance after 48 hours of simulated reforming. Alumina samples 6 and 7 (90 and 99% alumina) had the best combination of attrition resistance and surface area. A Ni-based catalyst prepared from alumina-6 was used for 48 hours of methanol reforming. Sieve analysis showed minimal change in distribution after use. After sieving, this same catalyst was used for reforming pyrolysis oil for 48 h. Attrition losses were similar to the methanol experiment (<0.5% per day).

Table 1. Attrition Tests in Two-Inch Reactor

Catalyst	In	Out	% Loss	Surface Area (m ² /g)
Commercial Ni Cat. 1	292.7	208.7	28.7	8.8
Commercial Ni Cat. 2	250.2	167.1	33.2	n/a
Corundum	250.0	249.9	0.4	0.03
Alumina-1	250.3	248.9	0.6	0.02
Alumina-2	250.1	219.5	12.2	0.07
Alumina-3	250.0	248.5	0.6	0.27
Alumina-4	92.5	89.5	3.0	2.7
Alumina-5	117.6	64.7	45.0	4.9
Alumina-6 ¹	251.4	248.8	1.0	0.2
Alumina-7	298.9	299.6	-0.2	1.4

¹ with Ni after 48 hrs of methanol reforming

Composition and performance data for reforming catalysts based on the CoorsTek aluminas (supports 6-7, 90 and 99% Al₂O₃) are shown in Table 2. We used the CO₂/CO ratio to measure selectivity for water-gas shift and coke gasification and the H₂/CH₄ ratio to measure reforming selectivity. The selectivity ratios were calculated by averaging concentrations from the first 3 hours of reaction for all catalysts and from 20-23 hours for commercial catalyst-1 and NREL-prepared catalysts 1 and 5.

Our first catalyst (NREL-1) contained 3% Ni and 1% Mg on 90% alumina with 0.2 m²/g surface area. During the first three hours

of use, this catalyst had shift/gasification activity comparable to the industrial catalyst but reforming ability was reduced. Performance during the 20-23 hour period showed that carbon to gas conversion activity and hydrogen yield were significantly reduced compared to the commercial material, though reforming activity stabilized. This result suggests that potassium is necessary to stabilize water-gas shift and coke gasification activity. The second NREL material contained 9% Ni on 99% alumina and all three performance measures were reduced compared to the commercial material. We then decided to scale the proportion of additives to the industrial catalyst composition based on available surface area of our supports. Preparations 3-4 are identical and use 90% alumina as the support. Catalysts 3 and 4, which were used for only 6 hours, show improved shift, gasification and reforming activity for the first 3 hours but activity slowly declined during the last 3 hours of use. Reproducibility was good for these two identical preparations. Catalyst 5 was prepared on the higher surface area support (99% Al₂O₃, 1.0 m²/g). Catalyst 5, run for 24 hours and containing more Ni and Mg, has comparable shift/gasification and reforming activity as the commercial catalyst.

Table 2. Reforming Catalyst Performance

Catalyst	Ni (wt%)	Mg (wt%)	K (wt%)	Support	CO ₂ /CO	H ₂ /CH ₄	H ₂ Yield ²
Comm.1	19	5.0	8.0	Mix ¹	4.0	594	90
Comm.1 ³	19	5.0	8.0	Mix ¹	4.1	39.6	91
NREL-1	3.0	----	1.0	90% al.	4.5	232	91
NREL-1 ³	3.0	----	1.0	90% al.	0.7	26.3	69
NREL-2	9.0	----	----	99% al.	3.2	23.2	87
NREL-3	1.5	0.1	0.1	90% al.	6.6	937	86
NREL-4	1.5	0.1	0.1	90% al.	7.7	665	88
NREL-5	2.0	0.2	0.1	99% al.	5.1	593	92
NREL-5 ³	2.0	0.2	0.1	99% al.	4.5	28.3	91

All catalysts: CO₂/CO, H₂/CH₄, and H₂ yield calculated from 0-3 hrs of reforming.

¹ Kaolin, Portland cement

² H₂ yield reported as H₂ actual/H₂ theoretical

³ CO₂/CO, H₂/CH₄, and H₂ yield calculated from 20-23 hrs of reforming.

Conclusions

Most of the alumina materials tested exhibited improved attrition resistance under steam reforming conditions compared to that of commercial fluidized reforming catalysts though surface areas are about an order of magnitude less. The best support materials were Coorstek 90 and 99% alumina particles (300-400 μ m) with surface areas of 0.2-1.0 m²/g. Attrition losses for these materials were less than 0.5 wt% per day. Catalysts (3-5) show increased shift/gasification activity and significantly improved reforming ability compared to the industrial material for the first 3 hours of reaction. From 20-23 hours, we observed a reduction in shift/gasification activity for both the NREL and commercial catalysts. Catalyst 5 had comparable performance to the commercial catalyst during 24 hours on stream: both shift and gasification activity were slightly better and reforming activity moderately reduced. With these promising results, additional work is being performed to optimize these fluidizable catalysts for long-term, stable hydrogen production from pyrolysis liquids.

References

- (1) Wang, D.; Czernik, S.; and Chornet, E. *Energy and Fuels*, **1998**, 12, 19.
- (2) Czernik, S., French, R.; Feik, C.; Chornet, E., In *Progress in Thermochemical Biomass Conversion*, Bridgwater, A.V., Ed. London: Blackwell Science Ltd., **2001**, 1577-1585.
- (3) Czernik, S., French, R., Feik, C., and Chornet, E., in *Advances in Hydrogen Energy*, C. E. Gregoire-Padro and F. Lau Eds., Kluwer Academic, New York, **2000**, 87-92.

H₂/CO ELECTROOXIDATION ON PT ANODE IN PEM FUEL CELL

Jingxin Zhang, and Ravindra Datta

Fuel Cell Center and Department of Chemical Engineering,
Worcester Polytechnic Institute
Worcester, MA 01609

Introduction

Hydrogen is the ideal fuel for PEM fuel cell, producing high power density at low temperatures. However, due to the difficulty in storage and distribution of hydrogen gas, liquid fuels will be processed on board to generate hydrogen rich gas as anode feed stream for PEM fuel cell intended for vehicular applications. Inevitably, there will be 10~100 ppm CO in the reformat gas even after the CO cleaning steps, such as water gas shift reaction (WGS) and preferential oxidation (PrOx). The presence of CO even at this low level is a serious concern as it affects performance dramatically by acting as a poison for anode catalyst.

The performance loss in PEM fuel cell anode due to CO surface poisoning has been evaluated quantitatively by Springer *et al.*^{1,2}. They proposed a kinetic model for the anode reaction, i.e., simultaneous hydrogen and CO electrooxidation on Pt catalyst. In our recent work³, we have reported a significant effect of anode flow rate on fuel cell performance. An anode model was provided which can quantitatively explain why the anode overpotential increases with anode flow rate. It does so by accounting for CO balance in anode chamber including terms for flow in, flow out and electrocatalytic oxidation. The model thus predicts that the anode CO concentration is a function of anode flow rate.

In this work, we present our recent experimental results on anode CO concentration as a function of anode flow rate, which confirms our early hypothesis. The experimental results are compared with our previous model prediction. Further, two plausible hydrogen electrooxidation mechanisms⁴, i.e., the Tafel-Volmer and Heyrovsky-Volmer mechanisms, are compared in the simulation. The Tafel-Volmer mechanism gives a better fit of the experimental data in the reasonable range of parameter values.

Experimental

The complete experimental details are provided in our previous work³. A summary is given here. Gas diffusion electrodes loaded with 20%(w/o) Pt/C at a metal loading of 0.4 mg/cm², were purchased from E-TEK. Nafion[®] 115 proton-exchange membranes (Du Pont, Fayetteville, PA) were used after treatment. The membrane electrode assembly (MEA) was prepared by hot-pressing in a Model C Carver hot press at 130 °C and under a pressure of 4000 lbs for about 2 minutes. The MEA was then incorporated in a 5 cm² single cell from ElectroChem, Inc. (Woburn, MA), and tested in a test station with temperature, pressure, humidity and flow rate control. The current-voltage characteristics were recorded using a HP 6060B DC electronic load, interfaced with a PC using LabView software (National Instruments, Austin, TX).

Anode and cathode gases were humidified through a stainless steel bottle containing water at a desired temperature before being fed into the fuel cell. The total pressure of both anode and cathode was maintained at 30 psig. The flow rates reported in this study are all at the standard state (1 atm and 25 °C) and in units of standard cubic centimeter per min (scc/min). Pre-mixed H₂/108ppm CO was purchased from MG Industries (Morrisville, PA) and was used as anode feed. The anode outlet CO concentration was monitored by a Model 200 IR gas analyzer (California Analytical Instruments, Orange, CA).

Results and Discussion

Figure 1 shows the anode overpotential versus flow rate at 80 °C at various constant current density. It is seen that the anode overpotential first increases with the anode flow rate, and finally levels off to a nearly constant value. These effects of anode flow on anode overpotential were also observed at other temperatures (e.g., 70 °C and 55 °C), different cathode oxygen pressures (e.g., 10 and 20 psig) and using different membranes (e.g., Nafion 112 and 117).

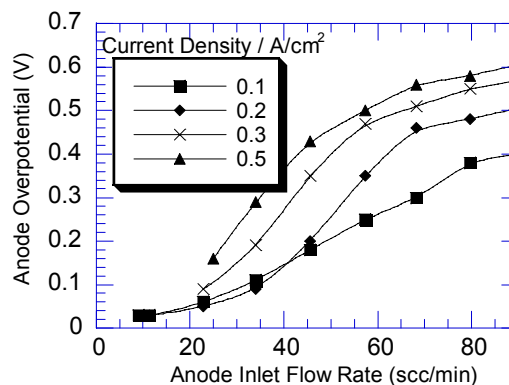
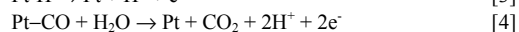


Figure 1. Anode overpotential versus flow rate at various constant current densities. Nafion[®] 115; Cell temperature, 80 °C.

In order to explain and quantify the observed effect of anode flow rate, a model was developed which accounts for the electrooxidation of both H₂ and CO on the Pt anode surface and material balance of different species in the PEM fuel cell anode. The model also incorporates the contribution to CO oxidation by O₂, which permeates through the membrane from the cathode. The interfacial kinetics was taken from the literature². Four general reaction steps are considered on Pt surface, i.e.,



The 5 cm² single cell anode is modeled as an differential reactor, i.e., well-mixed and the concentration of all species are uniform in the anode chamber. Thus, the material balance of CO and H₂ in the anode can be applied at steady state. The simulation results³ using thus developed model have shown that the Pt catalyst surface is largely covered by CO at 80 °C, approaching monolayer. The hydrogen surface coverage decreases with the flow rate due to the increase of CO surface coverage and anode overpotential. The hydrogen surface coverage can be orders of magnitude lower than the CO coverage. Our inventory model reproduces the essential features of the experimental observations and confirms the observed form of dependency of anode overpotential on the flow rate.

The simulation results also shows that the CO content in anode chamber increases with the inlet flow rate, which has not been experimentally observed and reported so far. Recently we set up an on line CO analyzer connected with the fuel cell anode to measure the CO concentration in order to check the validity of the model prediction. The results are shown in Figure 2 and compared with our previous model prediction. It is clear that at a constant current density, the anode outlet CO concentration is a function of anode inlet flow rate. The anode CO concentration increases as the anode

flow rates increase and the data match reasonably well with our model prediction.

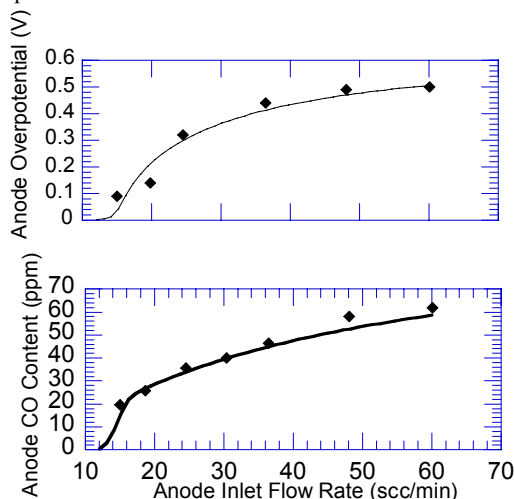
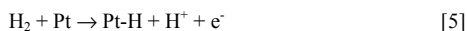


Figure 2. Comparison of model prediction with experimental results. (top) Anode overpotential vs. anode inlet flow rate. (bottom) Anode CO concentration vs. anode inlet flow rate. Anode feed, H₂/100ppm CO. The dots are experimental data and the line is simulation result. Fuel cell conditions: 200 mA/cm², 80 °C and Nafion 115 membrane.

In the model development, H₂ electrooxidation was assumed to follow a Tafel-Volmer mechanism, *i.e.*, two surface catalyst sites are needed for H₂ adsorption(equation [2]). In the literature, there is another reaction path which is also considered plausible for H₂ electrooxidation⁴, *i.e.*, Heyrovsky-Volmer mechanism,



in which a single catalyst site is needed for H₂ adsorption. This step is further followed by Volmer step (equation [3]).

In this work, we compared model results to experimental data using Heyrovsky-Volmer mechanism for H₂ electrooxidation in the simulation. In the first case, it is assumed that the anode overpotential does not affect adsorption/desorption rate, as treated by Igarashi *et al.*⁵, and Springer *et al.*². A typical result is shown in **Figure 3** (top). The results indicate that the model overestimates anode CO concentration and underestimates anode overpotential at a certain anode flow rate. Variation of the parameter values in the reasonable range is also conducted, but the simulation result is not improved appreciably.

Since step [5] is a charge transfer step, adsorption and desorption rate may also depend on anode overpotential. Thus the potential contribution is also considered in the simulation. A typical result is shown in **Figure 3** (bottom). The model prediction still overestimates anode CO concentration and underestimates anode overpotential. Furthermore, variation of the parameter values in the reasonable range does not improve the simulation results as well.

In summary, our simulation work seems to support Tafel-Volmer mechanism as the hydrogen electrooxidation mechanism on Pt anode surface in the presence of CO.

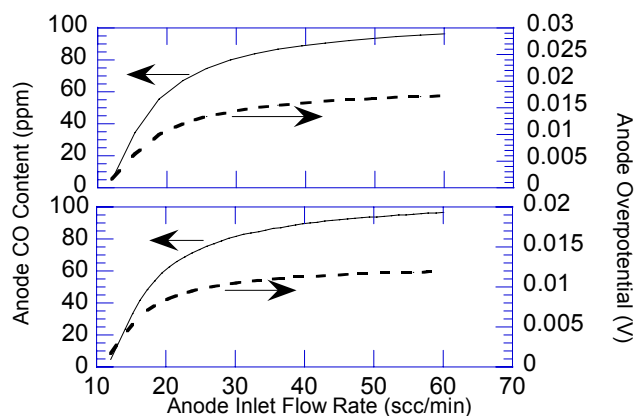


Figure 3. Typical plots of model prediction using Heyrovsky-Volmer mechanism. (Top) Anode overpotential is assumed not to affect the adsorption/desorption rate of H₂. (Bottom) Anode overpotential is assumed to affect the adsorption/desorption rate of H₂. Simulated fuel cell conditions: 200 mA/cm², 80 °C and Nafion 115 membrane.

References

- (1) Springer, T.; Zawodzinski, T.; Gottesfeld, S., *Electrode Materials and Processes for Energy Conversion and Storage IV*, **1997**, 13, 139.
- (2) Springer, T.; Rockward, T.; Zawodzinski, T.; Gottesfeld, S., *J. Electrochem. Soc.*, **2001**, 148, A11.
- (3) Zhang, J.; Thampan, T.; Datta, R., *J. Electrochem. Soc.*, in press.
- (4) Bockris, J.; Mauser, H., *Can. J. Chem.*, **1959**, 37, 475.
- (5) Igarashi, H.; Fujino, T.; Watanabe, M., *J. Electroanal. Chem.*, **1995**, 391, 119.

Highly Efficient Catalyst for Biomass Gasification to Produce Hydrogen and Syngas at Low Temperature

Mohammad Asadullah, Shin-ichi Ito, Kimio Kunimori, and Keiichi Tomishige

Institute of Materials Science, University of Tsukuba, 1-1-1, Tennodai, Tsukuba, Ibaraki 305-8573, Japan, Tel + Fax: +81-298-53-5030

Introduction

The green house gases especially CO₂ and particulate matters, which cause of fear for us and our new generation are mainly coming from fossil fuel burning for energy purpose. To reduce emissions of pollutants and greenhouse gases, the future energy resources should be clean and carbon neutral or carbon balanced between resources and atmosphere.¹⁻⁴ Hydrogen is one of the most promising energy source which offers no emission of particulates and green house gases. However, the traditional method of hydrogen production is the high temperature steam reforming or the partial oxidation of the fossil resources such as methane, light hydrocarbons, naphtha and heavy oils.⁵⁻⁹ To achieve the goal, the sources of hydrogen should be renewable and sustainable, efficient and cost-effective, convenient and safe.^{10,11} Biomass can meet the demand of future energy source since it is renewable and abundantly available everywhere in the world. Hydrogen or syngas can be produced from the gasification of biomass. The traditional process of biomass gasification is problematic because of tar and char formation during the gasification process even at very high temperature. In order to get the higher energy efficiency, when the process is carried out at lower temperature (<1123 K) more tar and char are produced. The catalytic gasification of biomass seems to be promising to reduce tar amount in the product gas even at low temperature, however, the traditional Ni based or dolomite catalysts hardly reduce the tar content in the product gas. These catalysts are suddenly deactivated in the in-bed reaction system due to deposition of carbon on the surface.¹² Highly efficient catalyst and a suitable reactor are necessary to overcome the problems. Here we describe such a process for the cellulose gasification using the Rh/CeO₂/SiO₂ catalyst in a continuous-feeding fluidized-bed reactor at as low as 773 K.

Experimental

A continuous-feeding fluidized-bed reactor was used for cellulose gasification. The operation system is almost the same as previously published¹³. However, the reactor dimension and feeding system have been modified for continuous-feeding gasification system. Here the gasification reactor is a quartz tube with the dimension of 66 cm high and 1.8 cm i.d. with a fluidized-bed section at the middle of the reactor. The cellulose feeder consisted of a glass vessel with a small pore at the bottom of about 0.5 mm diameter, allowing continuous feeding by vibrating the vessel with a vibrator. The vibration rate controlled the feeding rate. Cellulose particles (Merck, particle size 100~160 µm) were transported to the catalyst bed by the flow of N₂ gas through an inner tube of 5 mm i.d. Air and steam were introduced from the bottom of the reactor. Steam was supplied by using a microfeeder. The sample of the product gas was collected from the sampling port by micro syringe and analyzed by Gas chromatograph (GC). The concentration of CO, CO₂, and CH₄ was determined by FID-GC and the concentration of hydrogen was determined by TCD-GC. The amount of char was determined by the

amount of gas (mainly CO₂) formed after stopping the feed of cellulose under the air flowing at the reaction temperature.

CeO₂/SiO₂ was prepared by the incipient wetness method using the aqueous solution of Ce(NH₄)₂(NO₃)₆ and SiO₂ (Aerosil, 380 m²/g). After drying at 393 K for 12 h, the catalyst was calcined at 773 K for 3 h under an air atmosphere. The Rh was loaded on CeO₂/SiO₂ by impregnation of the support with acetone solution of Rh(C₅H₇O₂)₃. The final catalyst was pressed, crushed and sieved to 150-250 µm particle size. Loading amount of CeO₂ is denoted in parenthesis using the weight percent. In each run, 3 g of catalyst was used and pretreated by a hydrogen flow at 773 K for 0.5 h. Composition of the commercial steam reforming catalyst (TOYO CCI, G-91) was 14 wt% Ni, 65-70 wt% Al₂O₃, 10-14 wt% CaO and 1.4-1.8 wt% K₂O. The composition of the dolomite was 21.0 wt% MgO, 30.0 wt% CaO, 0.7 wt% SiO₂, 0.1 wt% Fe₂O₃, and 0.5 wt% Al₂O₃. Before reaction the dolomite was calcined at 773 K for 3 h followed by a hydrogen treatment at 773 K for 0.5 h.

Results and Discussion

In this study, the catalytic and non-catalytic gasification of cellulose were carried out at different temperature in a continuous feeding fluidized-bed reactor. The summation of the formation rate of CO and hydrogen as well as the carbon conversion with respect to various temperatures are shown in Figure 1. The carbon conversion {C-conv = (formation rate of CO + CO₂ + CH₄) / (C-feeding rate in cellulose) × 100} to gas and the formation of H₂ + CO are reasonably increased with increasing temperature in all the reactions. However, these values on Rh/CeO₂/SiO₂ (35) catalyst are much higher than on well known Ni-based catalyst (G-91) and dolomite. The C-conv (26%) and gas formation at lower temperature (823 K) are very low in non-catalytic systems. In this system, combustion reaction mainly proceeded to form CO₂ and H₂O. Although CO was formed slightly, hydrogen was hardly formed in this reaction at 823 K. At higher temperature (1173 K), partial oxidation reaction proceeded and CO was formed remarkably. Maximum 92% carbon converted to gas at this high temperature. The white fume of tar was formed in the non-catalytic system and part of which condensed and deposited in the out flow line. The condensed tar some times blocked the gas flow line and this is one of the problems of non-catalytic gasification of biomass. In the presence of dolomite, the C-conv slightly improved, however, hydrogen formation improved remarkably. The figure shows that the G-91 catalyst worked better with respect to both C-conv and gas formation at low temperature. It gave 79% and 94% C-conv at 823 and 973 K, respectively. Interestingly enough, 86% C-conv was achieved at as low as 773 K and that was achieved to about 100% at 923 K on Rh/CeO₂/SiO₂ (35) catalyst.

Figure 2 shows the C-conv and CO, H₂, CO₂, and CH₄ formation on Rh/CeO₂/SiO₂ (35) (Figure 1a) and G-91 (Figure 1b) catalysts with respect to the time on stream. To investigate the catalyst activity the reactions were carried out until 25 minutes. Within the reaction period, the C-conv to gas and formation of H₂, CO, CH₄, and CO₂ were stable on Rh/CeO₂/SiO₂ (35) (Figure 1a), however, on G-91 (Figure 1b) the C-conv decreased remarkably with time on stream. The rest of the carbon corresponds to the tar and char, which were deposited on the catalyst surface. When the cellulose feeding stopped after 25 min, the deposited carbon slowly converted to mainly CO₂ and this was much higher in the case of G-91 catalyst than that of Rh/CeO₂/SiO₂ (35). The reforming reaction usually proceeds on the clean surface of the catalyst. Since the deposited carbon on G-91 catalyst gradually covered the active sites, the reforming of tar gradually decreased with increasing reaction time and thus the formation of product gases decreased gradually.

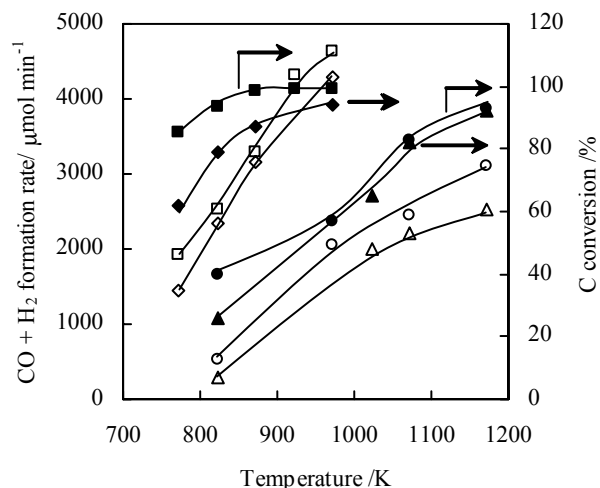


Figure 1. Influence of temperature on the carbon conversion and CO + H₂ formation rate in the cellulose gasification on Rh/CeO₂/SiO₂ (35) (■, Y); G-91 (◆, ◇); dolomite (●, O); and non-catalyst (▲, Δ). Cellulose feeding rate, 85 mg min⁻¹ (C, 3148 μmol min⁻¹; H, 5245 μmol min⁻¹ and O, 2622 μmol min⁻¹); air flow, 51 cm³ min⁻¹ (O₂, 417 μmol min⁻¹); N₂ flow 51 cm³ min⁻¹.

The C-conv as well as the selectivity of H₂ was dramatically improved by the steam addition in the gasification of cellulose on Rh/CeO₂/SiO₂ (35) catalyst. In the absence of steam, 86% C-conv with a less hydrogen was achieved at 773 K, whereas interestingly enough, the 100% C-conv with the higher hydrogen formation was found when the steam with H₂O/C = 0.35 was introduced. Furthermore, the formation of hydrogen and CO₂ expectedly increased with increasing the H₂O/C ratio. The limit of the temperature was 773 K for the complete conversion of cellulose to gas products. No successful report was found for the cellulosic biomass gasification at such a low temperature. This result indicates that the steam directly takes part in the gasification of the tar and char on the highly active catalyst even at low temperatures, and thus complete C-conv was achieved at 773 K. The biomass derived tar can be converted to gas on the Ni-based catalysts in the secondary-bed reactor at above 1073 K;¹⁴ however, in the primary-bed reactor the Ni-based catalysts suddenly deactivated by the carbon deposition,^{15,16} and the similar phenomenon was observed for G-91.

We think that the catalyst is oxidized and it can contribute to the combustion of the tar and char in the lower part of the bed since oxygen is available. In the upper part of the bed it can contribute to the reforming of the tar and char since oxygen is absent. Moreover, the steam directly takes part in the conversion of tar and char to gas as well as the water-gas shift reaction on the catalyst surface. And thus 100% C-conv with high yield of hydrogen even at the low temperature (773 K) becomes possible. Since the catalyst bed is in the fluidized condition, the catalyst particles can interact with the oxygen frequently at the lower part of the reactor. This can contribute to the removal of char with low reactivity by combustion. Methane combustion activity has been tested and it was found that the Rh/CeO₂/SiO₂ (35) catalyst had much higher activity than that of Rh/CeO₂, Rh/SiO₂, and G-91 (Figure 3). Furthermore, the temperature in the fluidized-bed is usually homogeneous. In our fluidized-bed reactor, the temperature difference between the lower and upper parts and also between the out and insides of the reactor was found less significant (only 15 K).

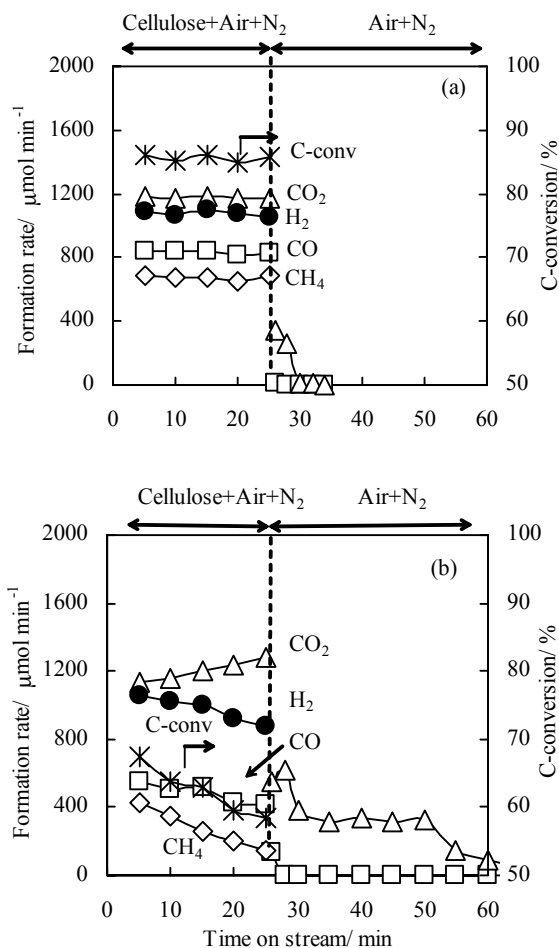


Figure 2. Dependence of time on stream on C-conversion and product distribution of cellulose gasification on (a) Rh/CeO₂/SiO₂ (35) and (b) G-91 at 773 K. Cellulose feeding rate, 85 mg min⁻¹ (C, 3148 μmol min⁻¹; H, 5245 μmol min⁻¹ and O, 2622 μmol min⁻¹); air flow, 51 cm³ min⁻¹ (O₂, 417 μmol min⁻¹); N₂ flow 51 cm³ min⁻¹.

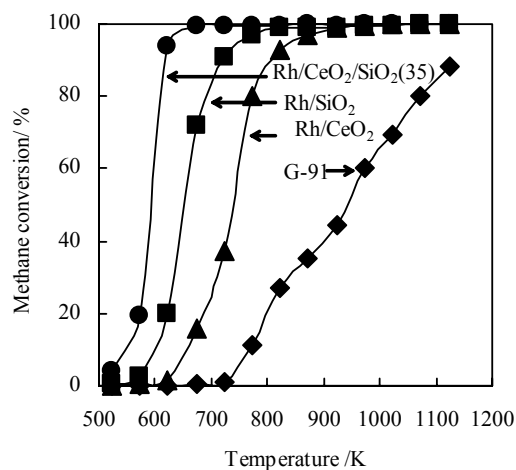


Figure 3. Catalytic activity of various catalyst on methane combustion.

Conclusions

The combination of the Rh/CeO₂/SiO₂ (35) catalyst with the fluidized-bed reactor provided the novel system for the hydrogen and syngas production from biomass at low temperature with a high-energy efficiency. In the fluidized-bed reactor, the catalyst circulates in the oxidizing and reducing atmosphere. Under this situation, the surface of the active site can be kept clear by this in-situ treatment. Therefore our catalytic process is promising in the gasification of biomass with low level of impurities such as wood.

Acknowledgement. This research was supported by the Future Program of Japan Society for the Promotion of Sciences under the Project “Synthesis of Ecological High Quality of Transportation Fuels” (JSPS-RFTF98P01001).

References

1. Ogden, J. M. *Annual Review of Energy and Environment* **1999**, 24, 227.
2. Steinberg, M., *Int. J. Hydrogen Energy* **1999**, 24, 771.
3. Pehr, K.; Sauermann, P.; Traeger, O.; Bracha, M., *Int. J. of Hydrogen Energy* **2001**, 26, 777.
4. Dülger, Z.; Özçelik, K. R., *Int. J. of Hydrogen Energy* **2000**, 25, 895.
5. Pena, M. A.; Gomez, J. P.; Fierro, J. L. G., *Appl. Catal. A: General* **1996**, 144, 7.
6. Armor, J. N., *Appl. Catal. A: General* **1999**, 176, 159.
7. Saito, M., *Shokubai (Catalysis)* **1993**, 35, 485.
8. Kikuchi, E.; Uemiya, S.; Matsuda, T., *Stud. Surf. Sci. Catal.* **1991**, 61, 509.
9. Steinberg, M.; Cheng, C. H., *Int. J. Hydrogen Energy* **1989**, 14, 797.
10. Chum, H. L.; Overend, R. P., *Fuel Proc. Tech.* **2001**, 71, 187.
11. Scarpellini, S.; Romeo, L. M., *Energy Conv. & Management* **1999**, 40, 1661.
12. García, L.; Frence, R.; Czernik, S.; Chornet, E., *Appl. Catal. A: General* **2000**, 201, 225.
13. Asadullah, M.; Tomishige, K.; Fujimoto, K., *Catal. Commun.* **2001**, 2, 63.
14. Corella, J.; Orío, A.; Toledo, J. -M., *Energy Fuel* **1999**, 13, 702.
15. Baker, E. G.; Mudge, L. K.; Brown, M. D., *Ind. Eng. Chem. Res.* **1987**, 26, 1335.
16. García, L.; Salvador, M. L.; Arauzo, J.; Bilbao, R., *Energy Fuel* **1999**, 13, 851.

HYDROGEN AND NANOTUBE PRODUCTION BY CATALYTIC DECOMPOSITION OF ETHANE

Ajay Makkuni, Devadas Panjala, Naresh Shah, and Gerald P. Huffman

University of Kentucky, 533 South Limestone Street, Room 111,
Lexington, KY 40508-4005

Introduction

The demand for hydrogen is expected to increase due to EPA regulations requiring deep desulfurization of petroleum based fuels in refineries and its use in fuel cells in automotive and power generation applications. Traditionally, hydrogen is produced by reforming or partial oxidation of hydrocarbons to produce synthesis gas, followed by the water-gas shift reaction to convert CO to CO₂ and produce more hydrogen, followed by separation procedures. However, further purification steps are required to reduce CO to levels tolerable by the catalysts used in fuel cells. Non-oxidative, catalytic decomposition of hydrocarbons is an alternative, one-step process to produce pure hydrogen.

In our previous study⁽¹⁾, nanoscale, binary Fe-based catalysts supported on high surface area alumina (M-Fe/Al₂O₃, M=Mo, Pd or Ni) were shown to have high activity for the catalytic decomposition of undiluted methane into pure hydrogen and carbon nanotubes. Ethane, a constituent of natural gas and a byproduct of cracking and fractional distillation of petroleum can also serve as a hydrocarbon feed stock to produce pure hydrogen. In this work, the activity of the same binary catalysts for the catalytic cracking of undiluted ethane is investigated.

Experimental Section

Supported catalysts were prepared by first adding an aqueous solution of appropriate catalyst metal salts (Fe(NO₃)₃·9H₂O, (NH₄)₆Mo₇O₂₄·4H₂O, Pd(NO₃)₂·xH₂O and Ni(NO₃)₂·6H₂O) in the desired proportions to a slurry of γ -alumina (150 m²/g) and then precipitating the metal oxyhydroxide on alumina by raising the pH of the slurry with ammonia. The slurry was washed with distilled water, dewatered to form a paste, and extruded. The composition of the binary metal catalysts, M-Fe (M = Mo, Pd or Ni) was 0.5 wt % M and 4.5 wt % Fe with respect to the alumina support.

As described elsewhere,⁽¹⁾ the reactions were carried out in a fixed-bed, plug-flow quartz reactor. Prior to reaction, the catalysts were reduced in flowing hydrogen (50 mL/min) for 2 h at 700 °C. After reduction, the reactor was flushed with an inert gas until the GC showed no residual hydrogen peak (~15 min).

Results and Discussion

The product distributions of thermal and catalytic cracking of ethane using a (0.5%Pd-4.5%Fe)/ γ -Al₂O₃ catalyst are shown in Figures 1 and 2, respectively. It can be seen that the catalytic route leads to increased hydrogen production and a significant decrease in ethane decomposition temperature relative to thermal decomposition. High methane formation at relatively low temperatures (450-500 °C) precedes high hydrogen production, which plateaus at ~650-825 °C. Similar trends were observed for the other bimetallic catalysts (0.5%Ni or Mo-4.5%Fe)/ γ -Al₂O₃. Thermal cracking, on the other hand, produces a significant amount of ethylene compared to catalytic cracking, where it is practically non-existent.

Figure 3 compares the observed hydrogen concentrations as a function of temperature for the different catalysts used, each subjected to a reduction pre-treatment at 700 °C. It is evident that the catalysts lower the temperature of ethane cracking significantly compared to thermal cracking over the alumina support. The three

bimetallic catalysts show similar trends and are all more active for hydrogen production than the monometallic iron catalyst.

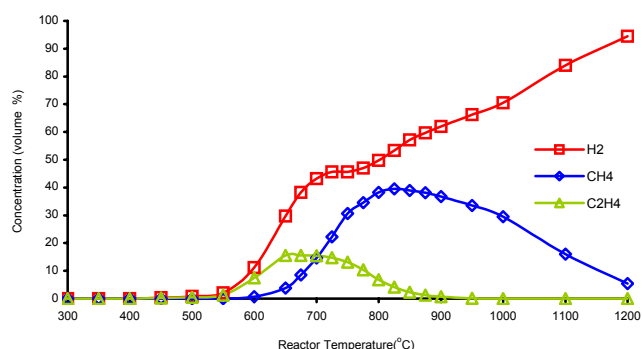


Figure 1. Product distribution of thermal cracking of ethane.

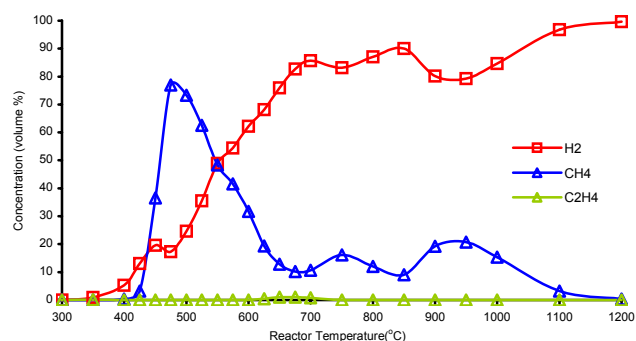


Figure 2. Product distribution of catalytic cracking of ethane, 0.5%Pd4.5%Fe/ γ -Al₂O₃.

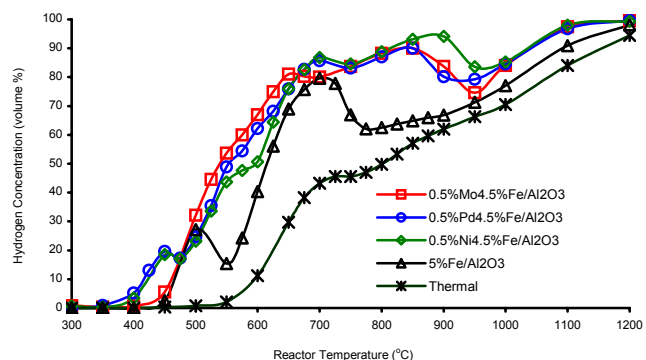


Figure 3. Comparison of hydrogen production by catalytic cracking of ethane with non-catalytic thermal cracking.

Time on stream studies were carried out to determine the loss of activity of the various pre-reduced (at 700 °C) catalysts over time. Figures 4 and 5 show the observed behavior at temperatures of 500 °C and 650 °C. A considerable loss in activity for the iron catalyst is seen at 500 °C within a short period of time (less than an hour). The activities of the Mo-Fe/Al₂O₃ and Ni-Fe/Al₂O₃ catalysts decreases more slowly at 500 °C than the Fe/Al₂O₃ catalyst, while the Pd-Fe/Al₂O₃ catalyst did not exhibit any decrease in activity out to a reaction time of 6 hours. At 650 °C, the iron catalyst shows much

better performance than at 500 °C. The activities of the bimetallic catalysts at 650 °C did not show any appreciable decay out to a reaction time of 4 hours.

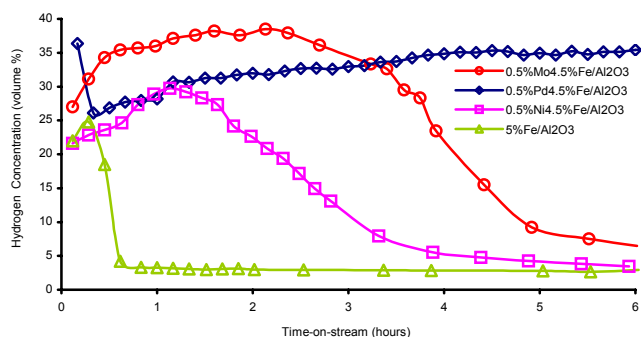


Figure 4. Time-on-Stream at a reactor temperature of 500 °C.

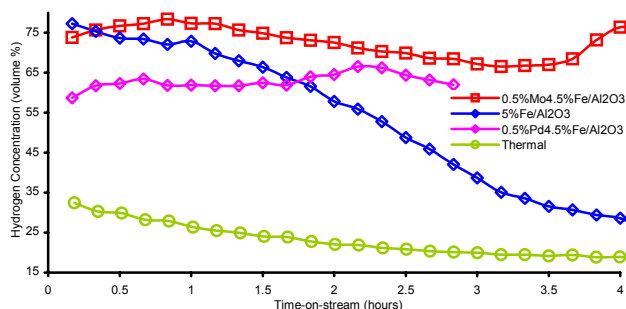


Figure 5. Time-on-Stream at a reactor temperature of 650 °C.

The HRTEM images of multiwalled carbon nanotubes grown by decomposing undiluted ethane over 0.5%Mo4.5%Fe/ γ -Al₂O₃ catalyst are shown in figures 6 and 7. The difference in the forms of the multi-walled carbon nanotubes grown at temperatures of 500 °C and 650 °C is quite interesting. At 500 °C, the multiwalled nanotubes appear to be nested cones stacked over one another, whereas the nanotubes formed at 650 °C were concentric hollow cylinders.

Acknowledgement. This research was supported by the U.S. Department of Energy through both the Office of Fossil Energy (FE) under the National Energy Technology Laboratory (NETL) and the Office of Energy Efficiency and Renewable Energy (EE), under Advanced Automotive Technologies, under contract No. DE-FC26-99FT40540

References

- (1) Shah, N.; Panjala, D.; Huffman G. P. *Energy & Fuels*, **2001**, 15(6), 1528-34.

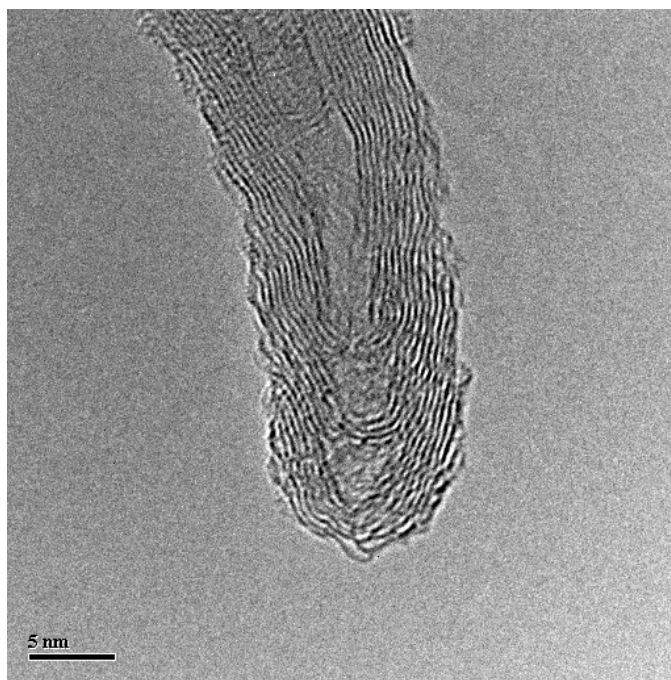


Figure 6. HRTEM image of multiwalled carbon nanotubes grown by decomposing undiluted ethane at 500 °C over 0.5%Mo4.5%Fe/ γ -Al₂O₃ pre-reduced at 700 °C.

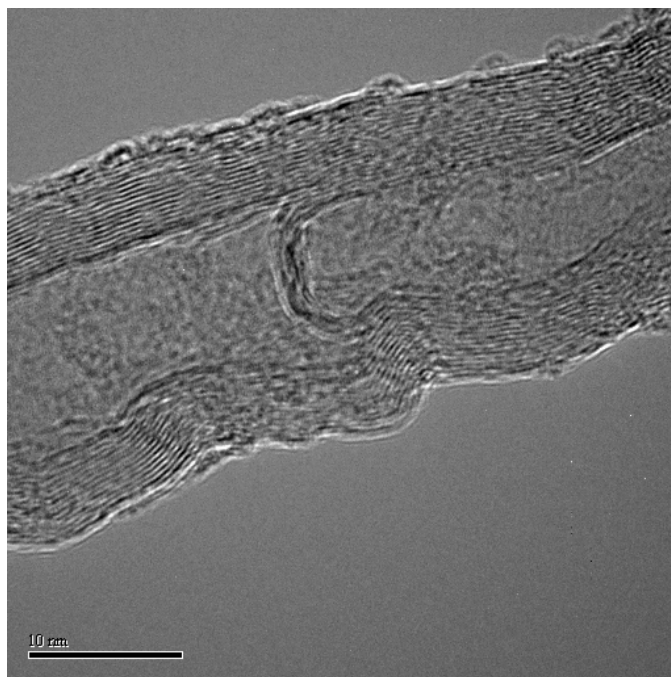


Figure 7. HRTEM image of multiwalled carbon nanotubes grown by decomposing undiluted ethane at 650 °C over 0.5%Mo4.5%Fe/ γ -Al₂O₃ pre-reduced at 700 °C.

HYDROGEN CYCLE EMPLOYING CALCIUM-BROMINE AND ELECTROLYSIS

Richard D. Doctor,¹ Christopher L. Marshall,²
and David C. Wade³

¹Energy Systems Division

²Chemical Technology Division

³Reactor Analysis and Engineering Division

Argonne National Laboratory

9700 South Cass Ave.

Argonne, IL 60439

Introduction

The Secure Transportable Autonomous Reactor (STAR) project is part of the U.S. Department of Energy's (DOE's) Nuclear Energy Research Initiative (NERI) to develop Generation IV nuclear reactors that will supply high-temperature heat at over 800°C. The NERI project goal is to develop an economical, proliferation-resistant, sustainable, nuclear-based energy supply system based on a modular-sized fast reactor that is passively safe and cooled with heavy liquid metal. STAR consists of:

- A combined thermochemical water-splitting cycle to generate hydrogen,
- A steam turbine cycle to generate electricity, and
- An optional capability to produce potable water from brackish or salt water.

However, there has been limited reporting on critical elements of the thermochemical cycle: (1) establishing chemical reaction kinetics and operating pressures and (2) addressing materials issues for hydrogen production. This paper reviews the thermodynamic basis for a three-stage Calcium-Bromine water-splitting cycle based on the University of Tokyo Cycle #3 [UT-3] and discusses the further chemistry work that is required to develop an economical process including modifying UT-3 to incorporate HBr dissociation.

Calcium-Bromine Cycle for Thermochemical Water Splitting

Beginning in the 1960s, interest in thermochemical water-splitting cycles for the large-scale production of hydrogen began to grow. Although many cycles have been published, few have been the subject of rigorous studies based on detailed thermodynamic calculations; fewer yet have undergone laboratory testing to establish kinetics and yields or to develop the chemical and physical properties needed to complete detailed mass and energy balances. The identification of conceptual cycles must then consider secondary environmental releases and special challenges to implementing some cycles (for example, those that employ large volumes of mercury).

Among the cycles that have the highest commercial potential, a recent screening study identified the two leading candidate cycles as Sulfur-Iodine and Calcium-Bromine.¹ The Calcium-Bromine cycle is being investigated by JAERI and has been considered in detailed technical reviews.² At Argonne National Laboratory, we are investigating a variant of this cycle that offers some advantages over the original cycle.³ It is called the "Calcium-Bromine cycle, or Ca-Br cycle," to avoid confusing it with the excellent efforts on the UT-3 cycle.

Thermochemical Considerations for the UT-3 Cycle

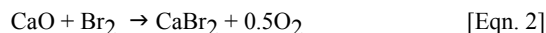
The significant aspects of the thermodynamic operation of the UT-3 cycle can be discussed with reasonable assurance. The developers of the UT-3 process have observed that in this series of reactions, the "...hydrolysis of CaBr₂ is the slowest reaction."⁴

[1] Water splitting with HBr formation (730°C; solid-gas; $\Delta G_T = +50.34$ kcal/gm-mole):



Hence, there is the greatest uncertainty about the practicality of this cycle because of this reaction.

[2] Oxygen formation occurs in an exothermic reaction (550°C; solid-gas; $\Delta G_T = -18.56$ kcal/gm-mole):

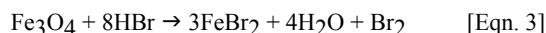


In reviewing this system of reactions, there is a difficulty inherent in the first and second stages [Eqns. 1 and 2]. This difficulty is linked to the significant physical change in dimensions as the calcium cycles between bromide and oxide. The CaO has a cubic structure ($a = 4.81$ Å) that must undergo a dimensional change to accommodate the CaBr₂ orthorhombic structure ($a = 6.58$ Å; $b = 6.87$ Å; $c = 4.34$ Å). This process must then be reversed. As the calcium reactant undergoes this change in dimensions, sintering will occur unless the calcium is carefully dispersed on a suitable support. Recent efforts by Sakurai et al. have considered pellets with the CaO supported on CaTiO₃ at CaO:CaTiO₃ ratios between 0.5 and 2.⁵ Sakurai reported plugging of pore volumes as the cycle is reversed and the CaBr₂ is regenerated. We intend to investigate suitable support structures for the calcium that will tolerate this cycling.

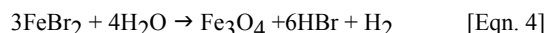
After recovering the HBr, the UT-3 process proposes bromine regeneration at 220°C in a solid-gas reaction followed by heating to regenerate the hydrogen at 650°C at a temperature close to the FeBr₂ melting point of 684°C.

A steam turbine will be used to harvest reject heat (at ~550°C) and will supply the electrical demands for pumping reagents in the water cracking plant, for circulating brine and water in the desalinization plant, and for pressurizing the H₂ and O₂ products for distribution. A desalinization system will be the final heat rejection path from the cascaded thermodynamic cycles.

[3] Bromine regeneration (220°C; solid-gas; $\Delta G_T = 29.470$ kcal/gm-mole; $\Delta H_T = 65.012$ kcal/gm-mole):



[4] Hydrogen formation from FeBr₂ (650°C; solid-gas; $\Delta G_T = 32.178$ kcal/gm-mole; $\Delta H_T = 91.913$ kcal/gm-mole):



The thermodynamics for this reaction system are favorable, and a diagram of the Gibbs free energies for a simplified reaction network appears in **Figure 1**. In this diagram, the last two stages are reduced to the basic process of HBr dissociation.

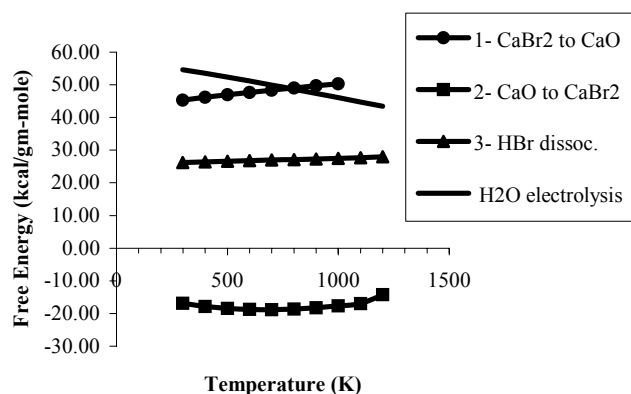
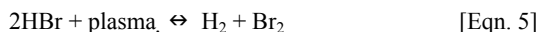


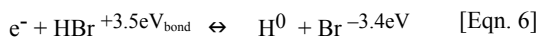
Figure 1. ΔG vs. Temperature ($^{\circ}\text{K}$) for the Calcium-Bromine 3-stage cycle contrasted with water electrolysis shows that the 3rd stage of HBr dissociation has a 48% lower electricity requirement.

The Ca-Br Cycle – a Modified UT-3 Cycle

We propose to employ a *modified* UT-3 cycle – with a single-stage, rather than a two-stage, HBr-dissociation step. Here, the hydrogen formation will employ either commercial HBr electrolysis or the use of a plasma chemistry technique operating near ambient conditions. Process conditions for the plasma-chemical approach are $\sim 100^{\circ}\text{C}$; gas phase; $\Delta G_T = +27.32$ kcal/gm-mole:



The reasons for adopting this strategy can be seen from consideration of the Gibbs free energies for this cycle. This stage takes advantage of power requirements that now are lowered to 48% of those necessary for water electrolysis (where $\Delta G_{T[\text{H}_2\text{O}]} = +56.70$ kcal/gm-mole). Power draws of $\sim 1\text{eV}$ are more realistic for a commercial facility:



Losing the electron to the bromine is economically unacceptable; hence, efforts that began at the Kurchatov Institute (Moscow, Russia) during the 1980s work with plasma-chemical systems so that the products of the dissociation do not recombine. Advances in this technique employing “reverse-vortex flow” have recently been reported.^{6,7} Applying this technique will result in a small draw on the electric power from the system to produce a cold plasma-chemical reaction.

With minor energy recovery in the oxygen-formation stage [Eqn. 2], the calcium-bromine cycle has a 66% ideal efficiency, defined as:⁸

$$\text{Efficiency} - \text{ideal} = \Delta H_{\text{Cycle}} / \Delta G_{\text{Cycle}} * (T_{\text{reactor}} - T_{\text{ambient}}) / T_{\text{reactor}}$$

Practical considerations for the UT-3 cycle suggest an efficiency in the range of 45–49%.⁹

Summary

A Calcium-Bromine thermochemical water-splitting cycle is currently under investigation so that basic process chemistry can be better defined. The thermochemical water-splitting route, in theory, is more efficient than current electrolysis pathways to

hydrogen. However, considerable effort is needed to see whether this promise can be translated into practical operating systems. A 3-stage system employing Calcium-Bromine combined with electrolysis offers a potentially attractive route to the early deployment of this technology. As successful hydrogen producing thermochemical cycles emerge, nuclear power can play a significant role in mitigating climate change and seems the only viable carbon-free route to supplying massive quantities of hydrogen that are needed for the transportation sector.

Acknowledgements. This effort was sponsored by the DOE Nuclear Energy Research Initiative at Argonne National Laboratory under Contract No. W-31-109-Eng-38 with the U.S. Department of Energy. The assistance of M. Serban in preparing this preprint is appreciated.

References

1. Besenbruch, G.E., et al., “High Efficiency Generation of Hydrogen Fuels Using Nuclear Power,” The First Information Exchange Meeting on Nuclear Production of Hydrogen, Paris, France – October 2000, OECD (2001).
2. Tadokoro, Y., O. Sato, “Technical Evaluation of Adiabatic UT-3 Thermochemical Hydrogen Production Process for an Industrial-scale Plant,” JAERI Review 98-22; 10.3 (1998).
3. Wade, D.C., et al., “A Proposed Modular-Sized, Integrated Nuclear and Hydrogen-based Energy Supply/Carrier System,” The First Information Exchange Meeting on Nuclear Production of Hydrogen, Paris, France, October 2000, OECD (2001).
4. Sakurai, M., et al., “Analysis of a reaction mechanism in the UT-3 thermochemical hydrogen production cycle,” *International J. of Hydrogen Energy*, Vol. 21, No. 10, pp. 871–875 (1996).
5. Sakurai, M., et al., “Improvement of Ca-pellet reactivity in the UT-3 Thermochemical Hydrogen Production Cycle,” *International J. of Hydrogen Energy*, Vol. 20, No. 4, pp. 297–301 (April 1995).
6. Gutsol, A.F., and J.A. Bakken, “A New Vortex Method of Plasma Insulation and Explanation of the Ranque Effect,” *J. Physics D: Applied Physics*, Vol. 31, No. 6, 1998, pp. 704–711.
7. Gutsol, A.F., and Kalinnikov, V.T., “Reverse-Flow Swirl Heat Insulation of Plasma and Gas Flame,” *Teplofizika vysokikh temperatur*, Vol. 37, No. 2, 1999, pp. 194–201. (*High Temperature Physics*, Vol. 37, No. 2, 1999, pp. 172–179.)
8. Funk, J.E., and R.M. Reinstrom, “Energy requirements in the production of hydrogen from water,” *Industrial and Engineering Chemistry Process Design and Development*, Vol. 5, No. 3 (July 1966), pp. 336–342.
9. Besenbruch, op. cit.

HYDROGEN FROM WATER: PHOTOCATALYTIC SPLITTING OF WATER WITH VISIBLE LIGHT?

Tom Autrey, Sotiris Xantheas, Liyu, Li, John Linehan, James Franz, Dimitris Katakis, Christiana Mitsopoulou, Zacharias Sofianos, Tom Bitterwolf.

Pacific Northwest National Laboratory
University of Athens
University of Idaho

Introduction

One of the Holy Grails of chemistry is to seek a photo-activated catalyst to split water into H_2 and O_2 using solar spectra.¹ Significant effort has been undertaken by the scientific community to develop a catalyst that can catalytically split water using visible light with limited success.^{2,3,4} However, one exception may be the homogeneous catalyst, tris-[1-(4-methoxyphenyl)-2-phenyl-1,2-ethylenedithiolenic-S,S']tungsten, reported by researchers at the University of Athens.⁵ A unique and highly desirable characteristic of the tris-dithiolene catalyst is its ability to form both hydrogen and oxygen from water without the need to add a consumable (sacrificial) donor.⁶ Water is reduced to hydrogen and oxidized to oxygen in a sequential pathway. The energy storage efficiencies of the tris-dithiolenes have been reported to range between 7-11%, values approaching the economic break point for solar production of hydrogen. While much work has been reported on the stability and efficiency of the various derivatives and isomers of tris-dithiolenes, little is known about the important steps of the mechanism that leads to hydrogen and oxygen formation. To this end, the understanding of the mechanism for the gas formation will assist in the design of the next generation of PCC's with the aim in increasing their efficiency.

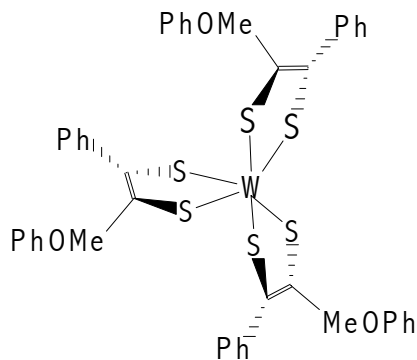


Figure 1. Photocatalyst catalyst (PCC) tris-[1-(4-methoxyphenyl)-2-phenyl-1,2-ethylenedithiolenic-S,S']tungsten

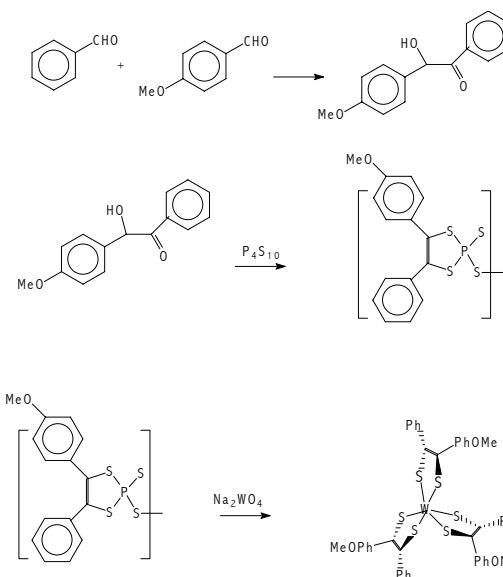
Experimental

Synthesis and purification of PCC tris-[1-(4-methoxyphenyl)-2-phenyl-1,2-ethylenedithiolenic-S,S']tungsten. Synthesis of the PCC requires a three step two-pot procedure, Scheme 1, starting with the mixed benzoin 4-methoxybenzoin prepared according to literature procedures.⁷ The formation of several isomers is feasible, however in practice only 3 isomers are formed under the reaction conditions with 4-methoxybenzoin the major product (80%). Two other isomers, the symmetric benzoin from benzaldehyde and the symmetric benzoin from 4-methoxybenzaldehyde compose the remaining balance of the material. The isomers are not isolated in this step because they are

easier to separate later on a column as the tungsten complexes. The benzoin mixture is placed in a 3-neck round bottom (RB) flask in anhydrous dioxane. Solid P_2S_5 was added to the dioxane solution and the RB was fitted with an argon degas inlet and reflux condenser. On the reflux condenser a hose barb was connected to Tygon tubing emerged in a solution of lead acetate (PbAc). The reaction was brought to reflux and the H_2S generated was purged from the reaction solution and trapped by the PbAc. The reaction mixture was filtered through a Buchner funnel (to remove unreacted P_2S_5) and the resulting dioxane solution containing the thiophosphate ester is used in the next step. To the reaction mixture above was added a sodium tungstate solution (in 1 N HCl). The reaction flask is fitted with bubbler and refluxed under argon for 2.5 hr converting the red thiophosphate ester to a mixture of green tungsten complexes. After cooling to room temperature the reaction mixture was transferred to a separatory funnel and the flask rinsed with toluene and added to separatory funnel. Extraction with toluene yields the tungsten tris-dithiolene complexes. Brine was used to wash the toluene to break up the emulsions formed in the separatory funnel. When the aqueous wash solution no longer turned yellow all tungstate was assumed to be extracted from toluene layer. Rotary-evaporation of toluene provided the tungsten tris-dithiolene complexes for separation on silica column.

A small fraction of the tungsten complex mixture from the toluene extraction was dissolved in toluene and added to the silica column for flash separation of various isomers (eluent 70/30 vol/vol cyclohexane/toluene). The third band to elute from the column is the desired unsymmetrical tungsten complex. Generally two other bands are eluted and some unidentified species sticks to the origin. Rotary evaporation of the first band off the column and a final drying under vacuum provides the desired tris-[1-(4-methoxyphenyl)-2-phenyl-1,2-ethylenedithiolenic-S,S']tungsten complex as a dark green powder. The unsymmetrical complex does not crystallize like the symmetric complexes.⁸

Scheme 1.



Oxygen Measurements. Oxygen evolved during the irradiation of the PCC is measured by chemical trapping with Cr(II). Under the reaction conditions the PCC solution is constantly purged to remove the oxygen that is formed during irradiation. This can complicate gas analysis because as the sample is purged from the reaction mixture

the gases formed from the catalytic splitting of water become diluted. However, if the oxygen is not removed by the in-situ purging the PCC catalyst will be consumed by the O_2 produced. In a typical experiment, the tris-dithiolene tungsten PCC sample (10^{-5} M) and methyl viologen (10^{-3} M) dissolved in a 80/20 v/v acetone/water mixture) is irradiated (>350 nm, 1000 W Xe lamp and continuously purged with acetone saturated nitrogen. The purge gas path is split into two paths with half directed through a control loop composed of double trap containing freshly prepared 0.02 M Cr(II) in 1N HCL and other half of the purge gas is passed through the photolysis sample and before passing through a similar double trap containing the freshly prepared 0.02 M Cr(II).⁹ If any oxygen leaks into the system the control loop will account for this background – non-catalytically generated oxygen. Under the reaction conditions the irradiation of the PCC (>350 nm 1000 W Xe lamp) produced 8.4×10^{-5} moles O_2 in 3.5 hours (or 2 mL O_2 gas). The rate of oxygen produced is ca. $0.16 \mu\text{L } O_2 \text{ s}^{-1}$.

Hydrogen Measurements. An in-situ photoreactor (Ace Glass Reaction assembly 7840) equipped with a Gas Chromatography (Varian microGC with TCD) was used to measure the hydrogen gas evolved during irradiation. The PCC/methylviologen sample as described above is irradiated with visible light (>350 nm) using a 450 W medium pressure mercury vapor lamp. Argon carrier gas is sparged through the reaction vessel to continuously extract the hydrogen formed from irradiation of the PCC. The purge gas is sampled by GC (TC detector) at time intervals by opening and closing a computer control valve. The temperature of the reaction vessel can be controlled with a constant temperature recirculation bath. The experimental data is stored on a PC as chromatographs for H_2 yield analysis.

Results and Discussion

The reports published by the Athens group using the photocatalyst catalyst (PCC) *tris-[1-(4methoxyphenyl)-2-phenyl-1,2-ethylenedithiolenic-S,S'] tungsten* to split water into hydrogen and oxygen gas using visible light and no sacrificial electron donor provide some very seductive observations.

The PCC is stable in the presence of air in the dark, however if the solution is not purged during irradiation the methyl viologen radical cation is formed and the catalyst undergoes decomposition (Figure 2). Current interpretation suggests a ground state complex is formed between the PCC and reversible electron acceptor methylviologen (MV^{2+}), eq. (1). The photo-activated catalyst is believed to be a ground state complex formed between the PCC and methylviologen (MV^{2+}). No apparent absorption change has been observed, but this assumption is based upon the 100-fold excess MV^{2+} used in the experiment. The ground state PCC/ MV^{2+} complex is believed to absorb the visible light and to yield the active catalyst responsible for the observed photodecomposition of water, eq. (2). The active absorption band is centered around 410 nm, with subtle shifts of a few wave numbers depending on the substituents on the dithiolene rings. There are two possible ‘active centers’ on the homogeneous catalyst, the metal or the sulfur atoms on the thiolene ligands. Ultraviolet irradiation destroys the catalyst while long wavelength irradiation gives no observable photochemistry. Some initial spectroscopic investigations¹⁰ suggest that the hydrogen gas is formed on a nanosecond time scale and that it may involve one or maybe two water molecules, eqs. (3) & (4). The oxygen gas may be formed in a subsequent bimolecular reaction leading to the regeneration of the active catalyst, eq. (5). The scheme of the proposed mechanism is as follows where M = the PCC catalyst:

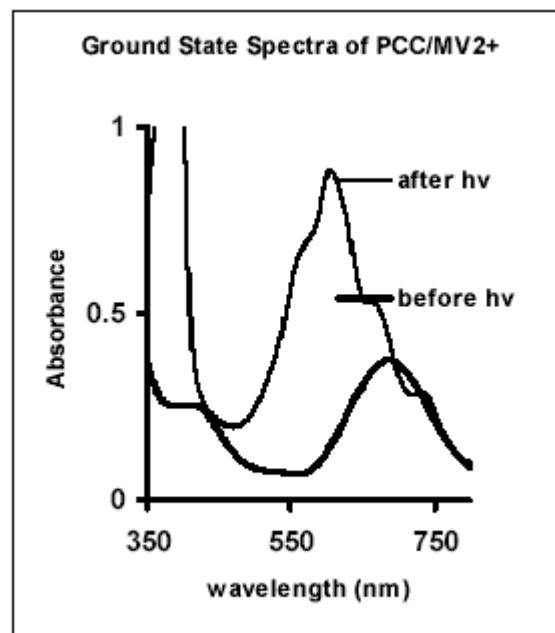
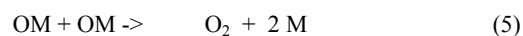
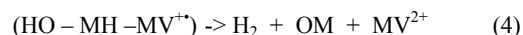
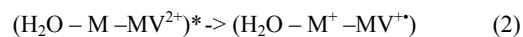
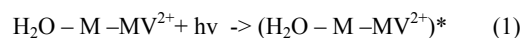


Figure 2. Visible absorption spectra of 10^{-5} M PCC, 10^{-3} M MV^{2+} complex in 80/20 acetone/water before and after irradiation. The absorbance due to the green PCC complex with an absorbance maximum at 686 nm is replaced by the methylviologen radical cation (MV^{+}) complex when the solution is not purged during the irradiation

The chemical trapping oxygen measurements carried out in Athens are convenient for testing a variety of tris dithiolene metal complexes¹¹ or various electron acceptors/relay agents,¹² however, a direct measure of hydrogen gas production is highly desirable. With this goal, a direct measure of hydrogen gas and the constraint of constantly removing the oxygen formed under irradiation, an in-situ photoreactor/detector was designed and assembled in the Environmental Molecular Sciences laboratory at PNNL. The reactor couples a photoreaction vessel with a GC detector. Purge gas is constantly swept the vessel and analyzed with a thermal conductivity detector. Figure 3 shows some preliminary results of our efforts to measure H_2 gas in-situ. The yield of hydrogen increases with irradiation time to a maximum and levels off. However, and most importantly when the light is turn off the H_2 yield drops rapidly to zero. This process was repeated on the subsequent day and the same results were observed, H_2 formation under irradiation – no H_2 when the light is turned off.

While the tungsten tris-dithiolenes may have the potential to provide a cheap alternative source to platinum there are still some technical challenges to overcome to make the PCC catalyst become economically viable. The catalyst is not soluble without a co solvent. While the organic solvent acetone is not consumed it would be far

more desirable to modify the catalyst to be water-soluble. Also the source of water appears to be critical, trace metals, i.e., copper or iron lead to catalyst decomposition under irradiation. These two issues, solubility and trace metal contamination made our initial measurements inconclusive.

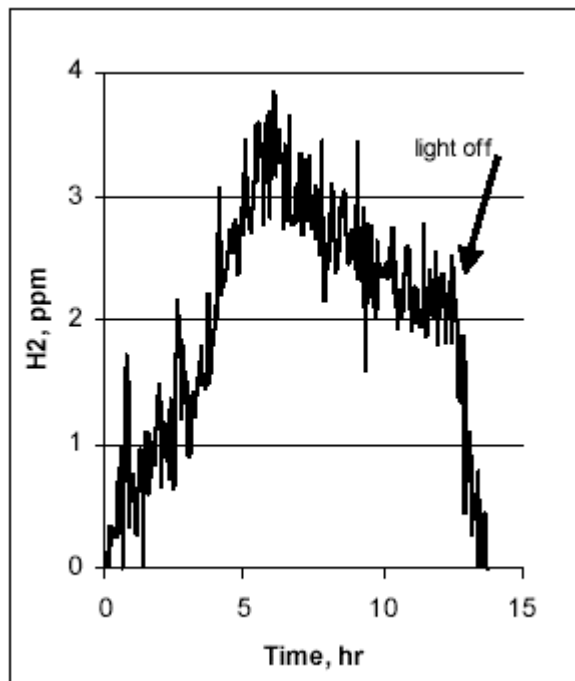


Figure 3. Visible irradiation (>350 nm) of tungsten tris-dithiolene complex/MV²⁺ complex in aqueous acetone solution. Flow rate argon purge gas 30 mL/min. H₂ yield as a function of time measure by GC with a TCD. Light turned off after 12.5 hr irradiation.

Computational Efforts. We have initiated first principles electronic structure calculations on the structures of simply and triply

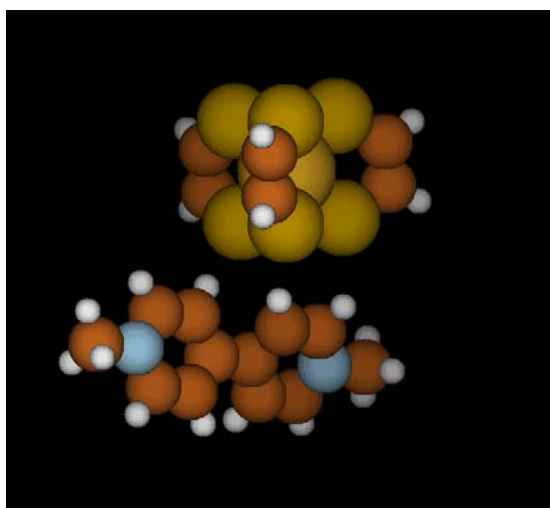


Figure 4. Lowest energy conformation of tris-1,2-ethylene-dithiolenic -S,S'] tungsten methyl viologen complex.

substituted complexes $W(S_2C_2H_2)_2(S_2C_2HPh)$, $W(S_2C_2H_2)_2(S_2C_2HPhOMe)$ and $W(S_2C_2HPhOMe)_3$ as well as the $MV^{2+} \cdots W(S_2C_2H_2)_2$ complex (Figure 4). The calculations were performed at the HF and DFT (B3LYP) levels of theory. Preliminary computational results suggest that the hydrogen may be formed at the sulfur center adjacent to the tungsten metal.

Conclusions

CW Irradiation of the tungsten-tris dithiolene/methylviologen complex with visible light leads to the formation of H₂ gas. Technical issues to overcome are solubility of the catalyst in water or co-solvent and metal impurities that can destroy the tris-dithiolene catalyst. Elucidation of the mechanistic pathways will provide insight into the design of more efficient catalysts. This preliminary work provides a confirmation of the formation of H₂ gas from water from visible light irradiation. The water source must be carefully deionized to remove trace metal elements that lead to catalyst poisoning. Photo-induced electron transport mediated through methyl viologen to yield a mixed valence metal dimer complex intermediate ($M^{n+1} \cdots M^{n-1}$) should be considered as a potential active

H₂ generating species (i.e., $PCC^+ \cdots MV \cdots PCC^-$). The dithiolene ligand is extensively delocalized in 3-dimensions resulting in a nonplanar (3-dimensional) aromaticity that involves the mixing of sigma and pi bonds.¹³ Molecular hydrogen formation either within the dithiolene ligand or at the metal center is possible.

Acknowledgement. Funding for this project was provided by the Energy Science & Technology Directorate's Laboratory Directed Research and Development Program at the Pacific Northwest National Laboratory and the Office of Science, Office of Basic Energy Sciences, Chemical Sciences Division. The hydrogen measurements were performed in the Environmental Molecular Sciences Laboratory, a national scientific user facility sponsored by the Department of Energy's Office of Biological and Environmental Research. TA thanks Dr. Yali Su for designing the in-situ hydrogen apparatus in the EMSL.

References

- ¹ Bard, A.J., Fox, M. A. *Acc. Chem. Res.* **1995**, 28, 141
- ² Amouyal, E. Chpt 8. "Water Splitting: from Molecular to Supramolecular Photochemical Systems," in *Homogeneous Photocatalysis*. Ed. by M. Chanon, John Wiley. **1997**
- ³ Bolton, J.R. *Solar Energy*, **1996**, 57, 37.
- ⁴ Ruttinger, W., Dismukes, G.C. *Chem. Rev.* **1997**, 97, 1.
- ⁵ Katakis, D., Mitsopoulou, C., Vrachnou, E. *J. Photochem. Photobio A* **1994**, 81, 103.
- ⁶ The formation of H₂ from irradiation of a mixed valence metal dimer using a sacrificial donor was recently reported. Heyduk, A.F., Nocera, D.G. *Science*, **2001**, 293, 1639.
- ⁷ Ide, W.S., Buck, J.S. *Organic Reactions* **1948**, 4, 269-301.
- ⁸ Mitsopoulou, C. Konstantatos, J., Katakis, D. *J. Molecul. Cat.* **1991**, 67, 137.
- ⁹ Katakis, D., Mitsopoulou, C., Konstantatos, J. *J. Photochem. Photobio. A. Chem.* **1992**, 68, 375.
- ¹⁰ Humphry-Baker, R., Mitsopoulou, C.A., Katakis, D., Vrachnou, E. *J. Photochem. Photobio A.* **1998**, 114, 137.
- ¹¹ Lyris, E., Argyropoulou, D., Mitsopoulou, C.A., Katakis, D., Vrachou, E. *J. Photochem. Photobio. A.* **1997**, 108, 51.
- ¹² Katakis, D., Mitsopoulou, C.A. *J. Photochem. Photobio. A.* **1994**, 81, 103.
- ¹³ Argyropoulou, D., Lyris, E., Mitsopoulou, C.A., Katakis, D. *J. Chem. Soc. Dalton Trans.* **1997**, 615.

HYDROGEN PERMEABILITY OF TANTALUM-BASED MEMBRANE MATERIALS AT ELEVATED TEMPERATURE AND PRESSURE

K.S. Rothenberger¹, B.H. Howard¹, A.V. Cugini¹, R.M. Enick², F. Bustamante², M.V. Ciocco³, B.D. Morreale³, and R.E. Buxbaum⁴

¹U. S. Department of Energy, National Energy Technology Laboratory (NETL), P.O. Box 10940, Pittsburgh, PA 15236

²NETL Research Associate, University of Pittsburgh

³NETL Support Contractor, Parsons Project Services, Inc.

⁴REB Research and Consulting

Introduction

Literature data indicates that tantalum, with a properly activated surface, may be a suitable component of a hydrogen separation membrane. The solubility of hydrogen in tantalum, based on literature data between 625-944 K and 0-107 kPa [1], was correlated by Steward [2] as (Equation 1):

$$S(H_2/Ta) = 0.132 \exp\left(\frac{4050}{T[K]}\right) \frac{\text{mol}}{\text{m}^3 \text{Pa}^{0.5}} \quad (1)$$

A critical review of diffusion coefficient data from literature was cited by Steward [2] in his review of the permeability of metals as (Equation 2):

$$D(H_2/Ta) = 4.4 * 10^{-8} \exp\left(\frac{-1620}{T[K]}\right) \frac{\text{m}^2}{\text{s}} \quad (2)$$

The product of Equations 1 and 2 was used to estimate the hydrogen permeability of tantalum [2] as (Equation 3):

$$K(H_2/Ta) = 5.8 * 10^{-9} \exp\left(\frac{2430}{T[K]}\right) \frac{\text{mol}}{\text{msPa}^{0.5}} \quad (3)$$

Although the upper temperature limits of the solubility and diffusion coefficient limits are 944 K and 573 K, respectively, graphical representations of this correlation extrapolated to 1000 K can be found in the literature [3,4]. Equation 3 indicates that the permeability of tantalum decreases with increasing temperature because the diffusion coefficient increases with temperature more slowly than the hydrogen solubility decreases.

Direct permeability measurements of palladium-coated tantalum membranes at low to moderate pressure (20-373 kPa) have been reported [3,5]. Permeation experiments were also conducted on bulk tantalum [6], but the results of this internal document were reported in the open literature in terms of diffusion coefficient [7]. The permeability of the tantalum membranes under these conditions was less than the value provided by the extrapolation of the correlation provided in Equation 3 to the temperatures of interest.

The objective of this study was to evaluate the hydrogen permeability and surface behavior of tantalum and palladium-coated tantalum materials under a wide range of temperatures (up to 1173 K) and pressures (up to 2.8 MPa) in order to assess their viability as components in hydrogen separation membranes.

Experimental Section

Membrane Fabrication. Bulk tantalum membranes were fabricated by punching 16 mm diameter disks out of a 1 mm thick, 99.9% pure, tantalum sheet. Tantalum was cleaned using an acid

mixture of 20 vol-% HNO₃, 20 vol-% HF, and 60 vol-% H₂SO₄ in order to remove surface oxides and contaminants before testing and or coating. Tantalum membranes were coated with a thin palladium layer in one of three ways. An electroless plating method, previously described by Buxbaum [3,5,8], was used to deposit a 1-2 micron thick coat of palladium on tantalum at the laboratory of REB Research and Consulting. A sputter coating method, developed at NETL, was used to deposit a thin (average thickness = .04 micron) palladium coating. A modified version of the same method was used to deposit a thicker (average thickness = 1.2 micron) palladium coating. In all cases, both sides of the tantalum disk were coated. Selected membranes were characterized by optical microscopy, scanning electron microscopy (SEM), and x-ray photoelectron spectroscopy (XPS), before and after testing.

Permeability Testing. The hydrogen membrane testing (HMT) unit was designed and constructed at NETL and is described elsewhere [9,10]. The typical membrane unit feed gas consisted of a mixture of 10 percent helium in hydrogen. An argon sweep gas was used to minimize the concentration of hydrogen on the permeate side of the membrane. The hydrogen in the permeate stream was quantified with a gas chromatograph.

Permeability testing was done at temperatures ranging from 623 K to 1173 K. Total feed pressures ranged up to 2.8 MPa from atmospheric. Permeability values were calculated based on a flux analysis that used a hydrogen partial pressure exponent of 0.5 to facilitate comparisons with previous investigators. However, actual best fit measurements of the exponent ranged from 0.21 to 0.83.

Results and Discussion

Bulk Tantalum. A series of bulk tantalum membranes were tested in the temperature range from 873 - 1173 K. The results are shown in Figure 1. Permeability values fell well below that predicted from the extrapolated Steward correlation [2], and were somewhat less than those of Makrides et al [6], which were measured over a smaller temperature range. The temperature dependence of the data was quite scattered, but showed a general trend to higher permeability at increased temperature, in agreement with that recorded by Makrides [5] and Buxbaum [6] and opposite that predicted by Steward [2]. In all cases, equilibration time was relatively slow, with tests taking up to two weeks in duration. In spite of the cleaning procedure used before testing, it appeared that some surface contamination occurred over the course of the long test duration, probably altering the characteristics of the membrane. Tantalum is known to be subject to contamination, particularly via oxidation.

Electroless Plated Tantalum. The electroless plated palladium-coated tantalum membrane was tested for 28 days, the longest single test of any tantalum-based membrane. During this time, it was subjected to the full range of test conditions at temperatures of 623 K, 923 K, and 1173 K, and pressures up to 2.8 MPa. Equilibration times were still quite slow, particularly at the lower temperatures. Permeability values at these three temperatures are shown in Figure 1. The results were approximately an order magnitude below the extrapolated Steward correlation and less than those obtained from the bulk tantalum test. However, the temperature dependence of the permeability was quite linear and nearly parallel to that predicted by Steward, with lower permeability at higher temperature.

The surface of an electroless plated membrane was characterized before and after testing. Prior to testing, surface palladium coverage ranged from 50-80%, with one side showing higher coverage than the other. After testing, the feed side of the membrane was highly eroded, with much evidence of material loss with spalling from the

surface in layers. Generally, no palladium was detected with the

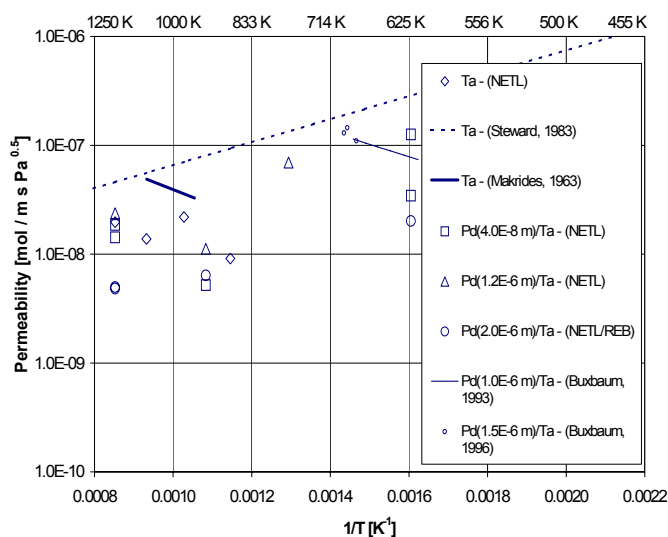


Figure 1. Permeability of tantalum and palladium-coated tantalum.

exception of several small areas near the edges. Tantalum was the primary element detected with varying amounts of oxygen and carbon. The sweep side was also rough and porous with cracking, but without the material loss seen on the feed side. Palladium still covered much of the tantalum surface, with small amounts of carbon and oxygen impurities. Although there is no data available to confirm this, the slow equilibration times of the membrane would seem to indicate that the palladium coating may have been lost early in the testing process.

Sputter Coated Tantalum (Thin Film). A series of four test runs were made using a bulk tantalum disk sputter-coated on each side with a “thin” (average thickness = .04 micron) palladium film. The first two tests were made at 623 K and atmospheric pressure. These runs yielded the two points shown on the right side of Figure 1. One of these points yielded the highest measured permeability of any tantalum-based membrane tested at NETL. Although both points fell slightly below the Steward correlation, they were similar to values recorded on palladium-coated tantalum membranes by Buxbaum [3] in a similar temperature range. For both membranes, attempts to change the test condition resulted in sudden failure. Microscopic examination of the membrane revealed significant cracks in the surface as well as an apparent phase change in the tantalum metal. The formation of a tantalum hydride phase, known to be brittle, is assumed to have occurred. However, as of this writing, it has not yet been experimentally verified. The two other “thin” sputter-coated membranes were tested at 1173 K, and 923 K-1173 K, respectively, with maximum permeability values plotted in Figure 1. Each sample showed an initial rise in flux followed by a longer decay. Characterization of the surface after testing showed no palladium present. It is believed that the decay in measured flux corresponded to a loss of the palladium coating and concomitant increase in surface resistance to hydrogen permeation.

Sputter Coated Tantalum (Thick Film). A series of three test runs were made using a bulk tantalum disk sputter-coated on each side with a “thick” (average thickness = 1.2 micron) palladium film. The goal of these experiments was to see if the palladium film thickness influenced the permeation behavior of the membrane. The three membranes were tested at 773 K, 923 K, and 1173 K, respectively. Test duration varied between 48-94 hours. The

membranes tested at 773 K and 923 K were relatively stable throughout the duration of testing. However the membrane tested at 1173 K showed a slow decay in measured flux beginning almost immediately. The maximum values of permeability are listed in Figure 1. Surprisingly, characterization of the surface after testing showed little palladium present, regardless of the temperature at which testing occurred. Characterization of these membranes is ongoing.

Taken as a group, the permeability values for both the “thin-Pd” and “thick-Pd” sputter coated membranes fall within a range below that predicted by the Steward correlation, and above that recorded for the electroless Pd-plated membrane. The scatter inherent to the data made it difficult to ascertain a distinct temperature dependence of the permeability.

Conclusions

A series of bulk tantalum and palladium-coated bulk tantalum membranes were tested for hydrogen permeability over a temperature range of 623-1173 K, and a pressure range from atmospheric to 2.8 MPa. The measured permeability values fell below that predicted by the extrapolated Steward correlation by as much as one and a half orders of magnitude. The combined effects of diffusion constant reduction at elevated pressure, surface contamination in our continuous high pressure apparatus, and the significant differences between the temperature-pressure conditions of the Steward correlation and our study contributed to this difference. At 623 K, coating of the bulk tantalum metal with a thin palladium film resulted in relatively high hydrogen permeability, but with likely formation of a tantalum hydride phase and failure of the membrane. At 773 K and above, a palladium film coating did not appear to influence the measured hydrogen permeability. Surface characterization performed following testing showed little palladium left on the tantalum surface. However, the palladium film may have at least temporarily protected the tantalum surface from fouling, as the experimental results from the palladium-coated tantalum generally showed both a smaller degree of scatter than that from uncoated bulk tantalum and a quicker response to changes in test conditions.

Acknowledgement. This work was supported by the “Transportation Fuels and Chemicals” and “Gasification Technologies” product lines of the U.S. Department of Energy’s Office of Fossil Energy.

References

- (1) Veleckis, E.; Edwards, R.K. *J. Phys Chem*, **1969**, 73, 683-692.
- (2) Steward, S.A.; “Review of Hydrogen Isotope Permeability Through Metals,” Lawrence Livermore National Laboratory Report UCRL-53441, August 15, 1983.
- (3) Buxbaum, R.E.; Kinney, A.B.; *Ind. Eng. Chem. Res.* **1996**, 35, 530-535.
- (4) Moss, T.S.; Peachey, N.M.; Snow, R.C.; Dye, R.C., *Int’l J. Hydrogen Energy*, **1998**, 23 (2) 99-106.
- (5) Buxbaum, R.E.; Marker, T.L. *J. Membrane Science*, **1993**, 85, 29-38.
- (6) Makrides, A.; Wright, M.; McNeill, R. Final Report for Contract DA-49-189-AMC-136(d); Tyco Lab, Waltham, MA, **1965**.
- (7) Volk, J.; Alefeld, G. In *Diffusion in Solids, Recent Developments*; Nowick, A.S. and Burton, J.J., Eds. Academic Press, New York, NY, 1975, pp. 232-295.
- (8) Buxbaum, R.E.; Hsu, C.Z. U.S. Patent 5,149,429, Sept. 22, 1992.
- (9) Morreale, B.D., *Evaluation of Inorganic, Hydrogen Membranes at Elevated Temperatures and Pressures*, M.S. Thesis, University of Pittsburgh, 2001.
- (10) Rothenberger, K.S.; Cugini, A.V.; Siriwardane, R.V.; Martello, D.V.; Poston, J.A.; Fisher, E.P.; Graham, W.J.; Balachandran, U.; Dorris, S.E. *Prepr. Pap. - Am. Chem. Soc. Div. Fuel Chem. Div., Prepr. Pap.*, **1999**, 44(4), 914-918.

HYDROGEN PRODUCTION BY DIRECT CONTACT PYROLYSIS OF NATURAL GAS

Manuela Serban*, Michele A. Lewis*, Christopher L. Marshall*
and Richard D. Doctor#

*Chemical Technology Division

#Energy Systems Division

Argonne National Laboratory

9700 South Cass Ave.

Argonne, IL 60439

Introduction

Currently petroleum refining is by far the biggest consumer of pure hydrogen, but the major petroleum companies and vehicle manufacturers, are orienting their industry towards a hydrogen economy. Motivations for exploring hydrogen as the leading alternative energy are to assure a future energy supply through a renewable energy source, and to solve global environmental problems through reducing CO₂ emissions, and improving air quality. It is predicted that the world demand for hydrogen will grow by 10 %/yr over the next five years, from the present level of 10-12 billion scf/d.¹

The thermal decomposition of methane has great potential in producing hydrogen without CO₂ emissions and free of CO, but it can hardly be of practical interest unless a thermally efficient process is developed, and unless an efficient way of disposing of the carbon by-product generated during the reaction is designed. We propose here the concept of utilizing the heat generated in the Generation IV nuclear reactors²⁻⁴ to produce hydrogen and carbon from methane or natural gas by direct contact pyrolysis, featuring zero greenhouse gases emission. Methane or natural gas was bubbled through a bed of either low melting point metals, *e.g.*, lead or tin, or through a mechanical mixture of metal and solid media, *e.g.*, silicon carbide. The main advantage of this proposed system is the ease of separation of the generated carbon by-product from the heat transfer media, by buoyancy due to the difference in densities. These experiments lay the groundwork for developing technical expertise in producing pure hydrogen cost-effectively by utilizing the heat energy contained in the liquid metal coolant in the Generation IV nuclear reactors.

Experimental

Reactor Apparatus and Materials. All experiments were conducted in a 1" by 14" 304 stainless steel vertical microreactor. Methane (99.995 % research grade) or natural gas (95 % methane, and 5 % ethane) was fed to the microreactor using mass flow controllers. Typical volumetric flow rates were between 2 and 15 cm³/min. The methane/natural gas was forced to bubble into the heated media through either a 1/4" stainless steel feed tube or through a Mott porous metal filter extending all the way to the bottom of the reactor. The porous metal filter creates small methane bubbles, improving the surface area for effective heat transfer between the gas and the heated media. The heat transfer media, which was either low melting point metals, *e.g.*, lead or tin, a heated solid media, *e.g.*, silicon carbide or alumina, or a mechanical mixture of metal and solid media, was placed in a 1/2" stainless-steel cup, inside the 1" microreactor. The temperature was controlled using four temperature controllers connected to a Thermcraft 4-zone heated furnace. The reaction was run isothermally, at temperatures of 600°C and higher, above the melting points of Pb (MP = 327 °C) or Sn (MP = 232 °C) such that at all times during the reaction the metals were in liquid state. The

effluent gas composition was analyzed continuously using a QMS 200 Mass Spectrometer, which was routinely calibrated over a wide range of compositions with a standard mixture of CH₄, C₂H₆, H₂, and Ar. Mass spectrometer analysis was performed at 30 seconds time intervals, and the average of numerous (frequently several hundreds) measurements was used to characterize the partial pressures of methane or ethane at a given reaction condition. All data reported here are steady-state values. Hydrogen atom balance was checked after each reaction, and the runs with an error bigger than 7% in the hydrogen balance were discarded.

Characterization Methods. SEM/EDS analysis of the carbon samples collected during pyrolysis experiments were performed on a JEOL JSM-6400 Scanning Microscope, while the elemental analysis of carbon was done with a LECO CHN-900 analyzer with combustion at 1000 °C. The instrument detection limits are 0.05 wt% for carbon, and 0.02 wt% for hydrogen. XRD spectra were measured with a Rigaku D/max-2400V diffractometer using Cu K α radiation.

Results and Discussion

In the Generation IV nuclear reactors, a fast neutron spectrum, fissile self-sufficient converter reactor using heavy liquid metal coolant is proposed as the nuclear heat source.⁴ These heavy liquid metal coolants (lead or tin) facilitate reaching the high temperature (~900 °C) required for coupling to a thermo-chemical hydrogen production facility. High temperature gas (He, N₂, CO₂) is used for the heat transport from the nuclear reactor to the thermal cracking unit.⁴ In this study, the choice of Pb and Sn as the heat transfer media for the methane pyrolysis process is independent of their use in the nuclear reactors; they were selected mainly due to their low melting points and absence of carbide formation.

Natural Gas Decomposition over Different Heat Transfer Media. Natural gas was converted selectively to carbon and hydrogen at temperatures ranging from 600 to 900 °C. No other gaseous products besides hydrogen were observed in the effluent stream. **Figure 1** shows a typical result for the thermal decomposition of natural gas bubbled through a 1/4" feed tube into a pool of 4 or 8 inches height of molten Pb, at 750 °C. Methane and ethane conversions increased with decreasing flow rates, and with increasing the heat transfer bed height, or, in other words, with increasing the contact time between the natural gas and the molten metal.

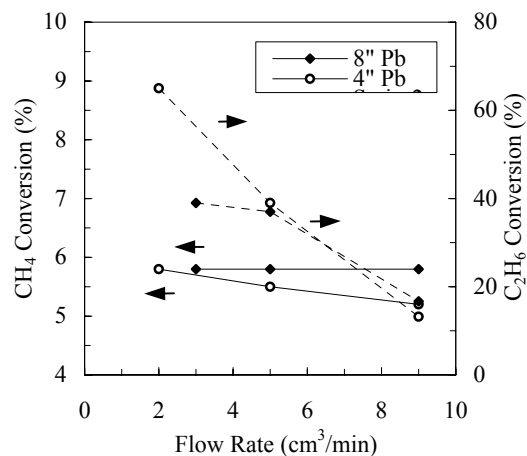


Figure 1. CH₄ and C₂H₆ Conversions in the Natural Gas Pyrolysis over 4" (○) and 8" (◆) of Molten Pb. T = 750 °C.

The rates of methane and ethane conversions and hydrogen formation were found to be approximately in the ratio of 1:2 and 1:3 respectively, thus verifying the reaction stoichiometry.

In order to optimize the process, Mott porous metal filters with two different porosities (0.5 and 2 μm) were used as feed tubes, to minimize the size of the gas bubbles, thus facilitating better heat transfer between the natural gas and the heated media. **Figure 2** depicts a comparison of the hydrogen concentrations (vol %) obtained in the natural gas pyrolysis, bubbled through a range of heat transfer media at 750 °C and different volumetric flow rates. It is apparent that the most efficient systems used for the pyrolysis process are the ones using the Mott porous filters, with almost 80 and 70 vol% H_2 obtained in the conditions of passing natural gas through a bed of 4" Sn + SiC, and Sn respectively. This is comparable to the activity reported for Ni- and Fe- based catalysts⁵, considered to be among the most active catalysts commonly used for the catalytic decomposition of hydrocarbons. Most importantly, the potential ease of separation of carbon by-product from the reaction mixture makes the technique proposed in this paper more advantageous compared to the catalytic process.

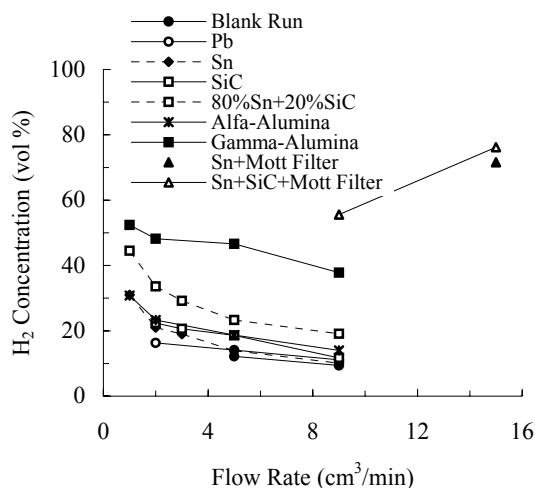


Figure 2. Comparison Between the Concentrations of Hydrogen (vol. %) Produced in the Natural Gas Pyrolysis Bubbled through Different Heat Transfer Media.

Carbon Formation. The carbon by-product generated during the pyrolysis process has a great market potential in both traditional, *i.e.*, rubber industry, plastics, inks, as a reducing reagent for the production of SiC, as a carbon additive/carburizer in the steel industry, as well as in new areas like the carbon/air fuel cell, a process currently under development in Lawrence Livermore National Laboratory.⁶

Figure 3 shows SEM images of the carbon collected after experiments with Pb, and Sn. In the pyrolysis of methane, two forms of carbon are generated, namely, finely divided carbon (soot) (Fig. 3-a,c,d), and pyrocarbon (Fig. 3-b) as solid carbon deposits as a result of surface reactions. Pyrocarbon was found to cover the entire heated section of the reactor, irrespective of the heat transfer media used in the pyrolysis experiments. EDS analysis of sections of the interior cup reactor walls was performed in order to determine the structure and composition of the carbon formed during the pyrolysis reaction. Such an analysis of the top layer of a cross-sectional area of the cup, 4" from the bottom reveals that carbon fibers cover the interior walls (Fig. 3-d).

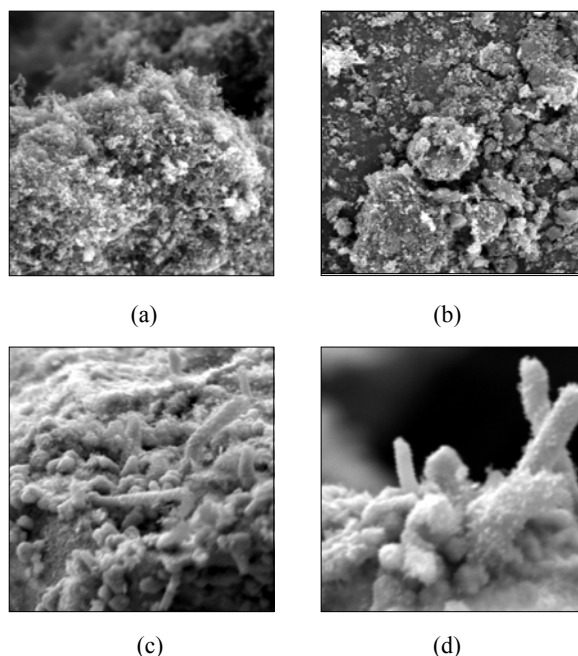


Figure 3. SEM Images of Carbon Samples Collected after Experiments with Pb (a, b), and Sn (c, d).

Elemental analysis of carbon samples generated during the pyrolysis experiments indicate that the C:H atomic ratios (on a molar basis) are within the range 1 C atom per 0.06 H atom for all samples analyzed. This corresponds to the following reaction stoichiometry: $\text{CH}_4 + \text{C}_2\text{H}_6 = 3 [\text{C(H)}_{0.02}] + 4.97 \text{H}_2$. The hydrogen atom balance calculated after each experiment confirms the above reaction stoichiometry. XRD spectra reveals that the carbon by-product is graphitic in nature, with an average particle size of 120 Å. The particle size was calculated using the Scherrer equation.

Acknowledgments

The work was performed using an Argonne LDRD grant under the auspices of the U.S. Department of Energy, under contract number W-31-109-ENG-38.

References

1. Parkinson, G., *Chem. Eng.*, 29-35, Sept. 2001.
2. Lewis, D., and Lewis, M. A., Patent Disclosure ANL IN# 00-070.
3. Marshall, C. L., Lewis, M. A., Leibowitz, L., and Lewis, D., Proceedings of the Nuclear Production of Hydrogen Meeting, Paris, France, October 2-3, 2000.
4. Wade, D. C., Doctor, R. D., Spencer, B. W., Peddicord, K. L., Boardman, C., and Marucci, G., First Information Exchange Meeting, Paris, France, 2-3 October 2000.
5. Muradov, N. Z., *Energy and Fuels*, 12, 41-48, 1998.
6. Cooper, J. F., Cherepy, N., Berry, G., Pasternak, A., Surles, T., and Steinberg, M., Paper No.50, Fall Meeting of the Electrochemical Society, Phoenix AZ, Oct. 2000.

Hydrogen Production via Steam Reforming of Methane with Nonthermal Plasma

Hajime Kabashima and Shigeru Futamura

National Institute of Advanced Industrial Science and Technology,
AIST Tsukuba West, 16-1 Onogawa, Tsukuba, Ibaraki,
305-8569 Japan

Introduction

Steam reforming of methane is an important process to produce hydrogen and/or synthesis gas.^{1,2} Industrially, steam reforming of methane is a process where methane reacts with excessive steam at high temperature (>1100 K) and high pressure (>20 atm) over a Ni-containing catalyst.^{1,3} In this catalytic reforming process, large thermal energy is needed to react methane at high temperature, and 20 - 40 % of the raw material is consumed by combustion owing to the supply of the excessive heat.⁴ Therefore, nonthermal plasma has been applied to methane reforming at lower temperatures with point-to-point type and dielectric barrier discharge plasma reactors for the development of cost-effective processes of hydrogen production.

Nonthermal plasma may provide a useful reaction medium for this reaction because reaction temperature can be kept as low as ambient. The recent reports have shown that reaction temperature can be decreased to 453 K in steam reforming⁵ and ambient temperature in carbon dioxide reforming.^{6,7} With the above-mentioned plasma reactors, however, formation of C₂ hydrocarbons is predominant via methane coupling. Therefore, addition of an excessive oxidizing agent such as steam and carbon dioxide is mandatory to suppress the formation of C₂ hydrocarbons.

We have already reported that a ferroelectric packed-bed reactor (FPR) has shown the higher performance compared with a silent discharge plasma reactor in the hydrogen generation from water.⁸ Nonthermal plasma has a potential for hydrogen-forming reactions such as hydrocarbon reforming and water decomposition, but its scope and limitations have not been clarified yet. It is significant to examine the reaction behavior of methane and steam in nonthermal plasma from the viewpoint of its extended application to diverse chemical processes associated with hydrogen utilization. Also, there have been no reports of the steam reforming of methane at ambient temperature.

In the present work, we have studied the steam reforming of methane for hydrogen formation at ambient temperature in nonthermal plasma, focusing on the effect of plasma-generating methods and the factors governing the reaction efficiencies. A continuous production of hydrogen from methane and steam has been also examined with FPR.

Experimental

FPR and a silent discharge reactor (**SDR**) used in this research were described in detail elsewhere.^{9,10} With **FPR**, gas flow rate ranged from 50 to 500 mL min⁻¹ (residence time 8.9 to 89 s). On the other hand, gas flow rate was fixed at 50 mL min⁻¹ (residence time 3 s) with **SDR**. The both reactors employed AC power supply at 50 Hz and high voltage up to 8.0 kV was applied for both the reactors. No breakdowns occurred during operations within their maximum voltages. Methane balanced with N₂ in a standard gas cylinder was introduced to the reactor through a Teflon tube by adjusting the concentrations of methane and flow rates with sets of mass flow controllers and a gas mixer. Steam was supplied to the reactors by humidifying gas (CH₄ / N₂) in a water-bubbling type device in a thermostatic bath. Steam concentrations were determined by a dew point hygrometer, and its contents were controlled within the range of 0.5 - 2.0 %. The gas streams passed through the entry tube (1/8

inch in diameter) and dispersed into plasma zone as shown in Figure 1. Steam reforming of methane was carried out at room temperature and an atmospheric pressure by using a conventional mass flow reaction system.

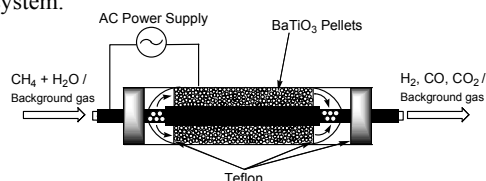


Figure 1. Schematic of ferroelectric pellets packed-bed reactor (FPR).

H₂ and methane were quantified by a TCD-GC with a packed column of Molecular Sieve 13X. CO, CO₂, ethane, ethylene, and acetylene were analyzed by TCD- and FID-GC with a packed column of Porapak Q+N and Molecular Sieve 13X.

Results and Discussion

Definitions of SED, H₂ yield, and CO yield. As a measure of the energy efficiency for **FPR** and **SDR**, specific energy density (SED) will be used later (1), where Power denotes the plug-in power.

$$\text{SED (kJ L}^{-1}\text{)} = \text{Power (kW)} / [\text{Flow rate (L/min)} / 60] \quad (1)$$

H₂ yield and CO yield are defined according to (2).

$$\text{Product yield (mol\%)} = 100 \times [\text{Product amount (mol)}] / [\text{Maximum amount of product evolved from methane (mol)}] \quad (2)$$

Effect of reactor and H₂O concentration on the steam reforming of methane. Table 1 shows the effects of reactor and H₂O concentration on steam reforming of methane in N₂ at 9 kJ L⁻¹ of SED. Gas flow rates of **FPR** and **SDR** were fixed at 100 mL min⁻¹ and 50 mL min⁻¹, respectively. With an increase in H₂O concentration, CH₄ conversion and the yield of C₂ hydrocarbons decrease while that of CO₂ increases irrespective of reactors. With **FPR**, H₂ yield increases with H₂O concentration and a maximum is observed for CO yield. These facts can be ascribed to the occurrence of water-gas shift reaction (CO + H₂O → CO₂ + H₂). As a result, H₂ selectivity exceeds 100 % for the H₂O concentration of 1.5 % and 2.0 %. With **SDR**, CH₄ conversion at the H₂O concentration of 0 % and 2.0 % were 6.5 % and 4.4 %, respectively. Also, the yields of H₂, CO, and CO₂ were much lower than with **FPR** under the same conditions. For methane reforming, **SDR** has shown the lower performance compared with **FPR** as in the case of H₂ generation from water.⁸

Table 1. Effects of reactor and H₂O concentration on steam reforming of methane^{a)}

Reactor	H ₂ O concentration (%)	CH ₄ conversion (mol %)	Yield (mol %) ^{c)}			
			H ₂	CO	CO ₂	C ₂ HCs ^{b)}
FPR	0	36.6	22.2	3.5	0.2	1.3
FPR	1.0	27.6	25.7	14.0	6.9	0.4
FPR	1.5	25.2	26.8	12.6	10.8	0.2
FPR	2.0	22.8	27.1	9.9	12.6	0.1
SDR	0	6.5	2.4	1.3	0.7	0.4
SDR	2.0	4.4	0.7	1.3	1.8	0.1

^{a)} Reaction conditions: methane, 1.0 %; background gas, N₂; SED, 9 kJ L⁻¹.

^{b)} C₂HCs denotes the hydrocarbons such as ethane (C₂H₆), ethylene (C₂H₄), and acetylene (C₂H₂).

^{c)} Product yield (mol%) = 100 × [Product amount (mmol)] / [Maximum amount of product evolved from methane (mmol)]

Since **FPR** and **SDR** have shown the comparable performances in the decomposition of trichloroethylene, bromomethane, and tetrafluoromethane in N_2 ,¹¹ almost the same plasma intensity should be obtained in both the reactors. These facts suggest that water activation is the common rate-determining step for the steam reforming of methane and H_2 generation from water, and that the reaction efficiency highly depends on the plasma-generating method. **SDR**, the point-to-point type of plasma reactor^{6,8} and the dielectric barrier discharge plasma⁷ belong to the same kind of barrier discharge reactor. Our findings clearly show that **FPR** works as a much better reactor for hydrogen-forming reactions than the other three ones.

Steam reforming of methane with FPR. Figure 2 shows that the CH_4 conversion and the yields of H_2 and CO_x gradually increase with an increase in SED in N_2 with **FPR**. When SED was set at 15 kJ L^{-1} , CH_4 conversion, H_2 yield, and CO_x yield were 35.4, 44.4, and 34.9 %, respectively. H_2 selectivity exceeded 100 % at SED higher than 6 kJ L^{-1} . Irrespective of the SED magnitude, almost the same CH_4 conversions and CO_x yields were obtained, i.e., carbon balances were higher than 98 %. In this reaction, no formation of carbon deposits is expected during continuous operations.

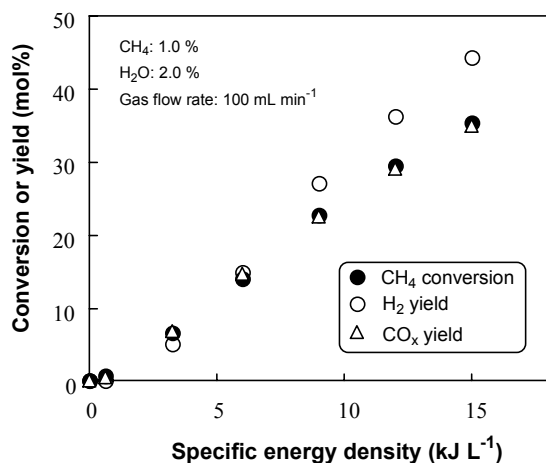


Figure 2. Effect of specific energy density on CH_4 conversion, H_2 yield, and CO_x yield in the steam reforming of methane in N_2 with **FPR**.

Effect of gas flow rate in the steam reforming of methane. The effect of gas flow rate on the yields of H_2 and CO in N_2 with **FPR** was further examined from 50 to 500 mL min^{-1} of gas flow rate under the same condition of Figure 2. With an increase in SED, the yields of H_2 and CO gradually increased at different flow rates. The highest yields of H_2 and CO were 73.4 % and 29.7 %, respectively at 30.0 kJ L^{-1} of SED at 50 mL min^{-1} of gas flow rate. An interesting trend has been observed that higher H_2 yields and CO yields are obtained at higher flow rates, i.e., shorter residence times at fixed SEDs.

Stability of reaction system in continuous synthesis gas production. Figure 3 shows the time profile of the CH_4 conversion, the yields of H_2 and CO , and the selectivities of H_2 , CO , and CO_x in the steam reforming of methane in N_2 with **FPR**. This reaction was carried out at 12 kJ L^{-1} for 10 h under the conditions as the same as for Figure 2. CH_4 conversion and the product selectivities could be kept constant for 10 h. The selectivities of H_2 and CO were 126 % and 58 % on the average, respectively. Therefore, the molar ratio of H_2 to CO was 4.3. Also, CO_x selectivity was almost 100 % for 10 h, i.e., no carbon deposits were formed during the continuous operation.

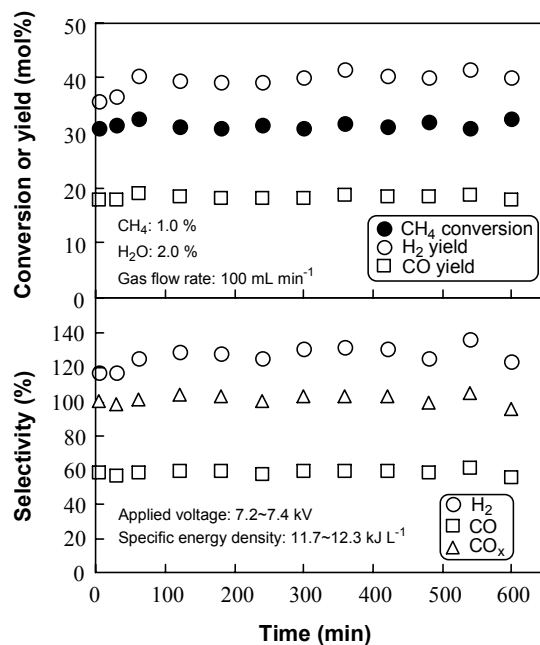


Figure 3. Time profile of the CH_4 conversion, the yields of H_2 and CO , and the selectivities of H_2 , CO , and CO_x in the steam reforming of methane in N_2 with **FPR**.

Conclusions

We have shown here the effects of plasma-generating methods and the factors governing the reaction efficiencies for steam reforming of methane. **FPR** has shown the higher performance compared with **SDR**, suggesting the different electron temperatures in both the reactors at the same input energy densities. For steam reforming of 1 %-methane in N_2 with **FPR**, the optimized water concentration is about 2.0 %. With **FPR**, CO_x selectivity as high as 98 % or higher is constantly obtained under the optimized conditions. This is why this **FPR** can be operated continuously for a long time. For steam reforming of methane at ambient temperature, **FPR** may be one of the best nonthermal plasma reactors.

Acknowledgements

This work was partly supported by the Grants-in-Aid from New Energy and Industrial Technology Development Organization of Japan (NEDO).

References

1. Armor, N. J. *Appl. Catal. A*, **1999**, 176, 159.
2. Pena, A. M.; Gomez, P. J.; Fierro, G. J. *Appl. Catal. A*, **1996**, 144, 7.
3. Solh, E. T.; Jarosch, K.; Lasa, I. H. *Appl. Catal. A*, **2001**, 210, 315.
4. Asaoka, S.; Shimura, M. *Petrotech*, **2001**, 24, 226.
5. Kado, S.; Urasaki, K.; Sekine, Y.; Fujimoto, K. *Chem. Commun.*, **2001**, 415.
6. Yao, L. S.; Okumoto, M.; Nakayama, A.; Suzuki, E. *Energy Fuels*, **2001**, 15, 1295.
7. Zhou, M. L.; Xue, B.; Kogelschatz, U.; Eliasson, B. *Energy Fuels*, **1998**, 12, 1191.
8. Kabashima, H.; Einaga, H.; Futamura, S. *Chem. Lett.*, **2001**, 1314.
9. Futamura, S.; Zhang, A.; Yamamoto, T. *IEEE Trans. Ind. Applicat.*, **2000**, 36(6), 1507.
10. Einaga, E.; Ibusuki, T.; Futamura, S. *IEEE Trans., Ind. Applicat.*, **2001**, 37(5), 1476.
11. Futamura, S.; Einaga, E.; Zhang, A. *IEEE Trans., Ind. Applicat.*, **2001**, 37(4), 978.

HYDROGEN PRODUCTION VIA THERMAL DECOMPOSITION OF METHANE USING A SOLAR REACTOR

Pamela L. Spath, Wade. A. Amos

National Renewable Energy Laboratory
Golden, CO 80401

Introduction

Experimental analysis is being done for hydrogen production via thermal decomposition of methane using a solar reactor. The National Renewable Energy Laboratory (NREL) has analyzed this process for two different applications: (1) for a fueling station and (2) for power production. The fueling station application was examined as a stand-alone system. However, because storage limits the amount of hydrogen production and results in a substantial capital cost, the system was also examined as one that could supply hydrogen to a pipeline network. For the power production scenario, the hydrogen is co-fired in a turbine at a natural gas combined-cycle (NGCC) plant.

Calculation Method

In general, the system for each application is comprised of the same types of equipment, just different sizes and the configuration of each plant is slightly different. The main pieces of equipment include a heliostat field, the solar reactor, a baghouse filter, a pressure swing absorption unit, compression, and storage. Specific information and flow diagrams can be found in a detailed NREL report¹. Material balances for the reactor were obtained from an entrained flow reactor model developed by the University of Colorado². Energy balances were determined using Aspen Plus® and radiant heat loss calculations. The material and energy balances along with hourly solar data from Phoenix, Arizona were used to determine how much hydrogen could be produced by the system.

For a given reactor size, three hydrogen production rates were evaluated by varying the size of the heliostat field. First, the size of the heliostat field was set so that the reactor operating temperature at the highest hourly solar irradiance did not exceed 2,273 K. This temperature was chosen as a practical limit. Next, the heliostat field was doubled, which meant that more hydrogen could be produced at lower light intensities, but at high light intensities, part of the heliostat field must be taken offline to avoid overheating the reactor. Finally, the size of the heliostat field was cut in half. This was done to reduce the capital costs. For the fueling station application, doubling the size of the heliostat field resulted in the lowest cost hydrogen. However, for the power production application the smallest heliostat field was the most economic option.

Results for Stand-Alone Fueling Station Application

Table 1 gives the resulting hydrogen production, storage, and demand amounts for the stand-alone fueling station application. At 4 kg/car, this means that roughly 63, 113, and 188 cars are fueled each day for the different heliostat field sizes. There are many times when the storage capacity is reached and the hydrogen production system must be shutdown. For this reason, only 54%-65% of the total possible hydrogen production was actually produced. Because hydrogen can only be produced during daylight hours, increasing the size of the hydrogen storage did not significantly increase the amount of hydrogen that could be supplied for fuel. The small increase in useable hydrogen did not outweigh the large cost associated with storing the hydrogen.

Table 1. H₂ Production, Storage, and Demand for Stand-Alone

Heliostat size (m ²)	H ₂ produced without storage limit (tonne/yr)	H ₂ storage capacity (kg)	Daily H ₂ demand (kg/day)	H ₂ produced with storage limit (tonne/yr)
2,188	169	800	250	91
4,375	301	1,400	450	164
8,750	416	2,300	750	273

The carbon that is produced from the solar process is assumed to be sold in the carbon black market. The base case uses a carbon black price of \$0.66/kg, which is the price for carbon black in the tire industry³. This is the largest market, accounting for 70% of the worldwide carbon black market. Table 2 gives the cost of hydrogen for the stand-alone fueling station application.

Table 2. Cost of H₂ for Stand-Alone System

Heliostat size (m ²)	Cost of H ₂		Cost to fill fuel tank with 4 kg of H ₂ (\$)
	(\$/GJ)	(\$/kg)	
2,188	\$87	\$12	\$49
4,375	\$73	\$10	\$42
8,750	\$57	\$8	\$32

Note: Fill up cost is without taxes.

Hydrogen storage was the largest capital cost item, accounting for 32% of the total capital for the 8,750 m² heliostat field size. This was followed by the cost of the heliostat field (21%) and hydrogen compression (19%). However, it is important to remember that any competing system (renewable or non-renewable) will also require some amount of storage as well as hydrogen compression for a stand-alone fueling station.

Improving Fueling Station Economics

Several options were examined to increase the productivity of the system in a cost-effective manner for the fueling station application. The following subsections discuss two of those options.

Direct Use or Pipeline. Because of the large costs for storage and compression, along with the fact that the storage limitation prevents maximum hydrogen production, the system was examined as one where the hydrogen could be used directly or sent to a pipeline network. For this scenario, the pipeline was assumed to already be in place, therefore, the expense of the pipeline was not included in the analysis. Table 3 shows the resulting economics for the largest heliostat size. The reduction in the cost of hydrogen is 68% from the stand-alone case.

Table 3. Cost of H₂ for Direct Use or Pipeline System

Heliostat size (m ²)	H ₂ produced from solar process (tonne/yr)	Cost of H ₂	
		(\$/GJ)	(\$/kg)
8,750	416	\$18	\$3

Note: H₂ production is maximized instead of 66% of maximum.

Addition of Small Electric Heater. One other option that was examined to help the productivity of the solar process was adding a small electric heater that can be turned on when the hydrogen supply gets low to provide heat to the solar reactor. Two scenarios using an electric heater were examined: one where the storage is kept constant and the daily demand is increased and one where the demand is kept constant and the hydrogen storage is decreased. Table 4 contains the amounts for production, storage, and demand for both of these scenarios. Even if only 5% of the hydrogen comes from the electric heater, the amount of hydrogen produced from the sun increases from

66% to 88% of the total possible for the constant storage case. For the constant demand case, using the electric heater to account for 5% of the hydrogen production decreased the storage requirements by a factor of 3. See the table below for details. The cost of hydrogen with the supplemental electric heater is considerably less than the stand-alone fueling station case at \$42/GJ and \$46/GJ for the constant storage and constant demand cases, respectively, compared to \$57/GJ.

Table 4. H₂ Production, Storage, and Demand with Supplemental Electric Heater for 8,750 m² Heliostat Field

		constant storage	constant demand
H ₂ storage capacity (kg)		2,300	750
Daily H ₂ demand (kg/day)		1,050	750
H ₂ produced from solar energy input	(tonne/yr)	365	260
	% of total possible from solar	88%	62%
H ₂ produced from electric heater	(tonne/yr)	17	14
	% of total H ₂ produced	4.5%	5.2%

Note: Total possible from solar without storage limit = 416 tonne/yr.

Results for Power Production Application

For the power production application, two options were examined: (1) selling the carbon black and (2) burning the carbon to produce more power. Because of its value, it is more profitable to sell the carbon instead of burning it. However, in order for the electricity produced from the hydrogen to be less than the base electricity production cost of the NGCC plant, the price of the carbon must be greater than \$0.8/kg. Even though the reactor and heliostat field sizes were increased compared to the fueling station application, the amount of power produced from the hydrogen is small compared to the size of the natural gas plant. The electricity generated from the solar process only accounts for about 0.2% to 1.1% of the total output from the power plant. Therefore, even if the power produced from the hydrogen is less than the base power production price, overall, it would not reduce the price of electricity generation from the NGCC power plant. Note also that not all of the power from the hydrogen is renewable because the feedstock to the solar plant is natural gas. Only the heat input from the solar process is renewable. For the scenario where both the hydrogen and carbon are burned, only about 9% of the electricity produced from these feedstocks is renewable (i.e., less than 0.1% of the total output from the power plant).

GWP and Fossil Energy Consumption

The global warming potential and energy balance were examined in a cradle-to-grave manner. Although, the solar process for the fueling station and power production application use natural gas as a feedstock, the net greenhouse gas emissions and overall fossil energy consumption is lower for the solar process than for the conventional fossil system. It was evident that there is a significant environmental benefit from carbon black production via the solar route than from its conventional route. Refer to reference 1 for more details.

Price of Carbon Black

A sensitivity analysis was performed on several variables (carbon selling price, heliostat cost, price of natural gas, and greenhouse gas credit) but the price of the carbon black had the greatest effect on the economics. The specialty markets for carbon black are smaller than the tire industry, but the price of the carbon in

these markets is usually higher because of the more stringent carbon quality specifications. Figure 1 shows the sensitivity in the price of hydrogen for different carbon prices for the fueling station application.

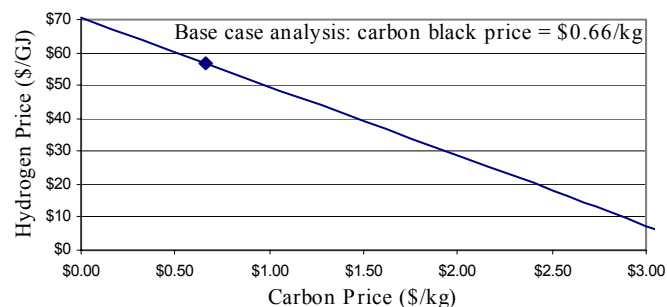


Figure 1. Cost of Hydrogen versus Carbon Price for Stand-Alone Fueling Station Application and Heliostat Size of 8,750 m².

Summary and Conclusions

Because there is no production at night and no production under foggy or cloudy conditions, locating the solar plant in the desert southwest is the most attractive option. The reactor and purification equipment must be sized for peak flow rates, which are a factor of 2.5 to 3.5 greater than the average production rate. This is in comparison to a conventional fossil system, which can be sized to have a continuous production rate to meet demand.

For the fueling station application, hydrogen storage is the largest capital cost item followed by the cost of the heliostat field and compression. However, it is important to remember that any competing system will also require some amount of storage as well as compression. If the hydrogen can be consumed directly or used in another application where storage is eliminated and compression is moderate, then the cost of hydrogen from the system decreases by a factor of three. Adding a small electric heater, which supplies heat to the solar reactor when the hydrogen supply gets low, was a low-cost solution to increasing the productivity of the solar process.

The power production application is able to use the hydrogen directly without storage, but the cost of power from this system is more than the base electricity price of the NGCC power plant for a carbon black price less than \$0.8/kg. Additionally, for this application, because of the value of the carbon, it is more profitable to sell the carbon than burn it and produce more power.

The price of the carbon black has the greatest effect on the economics for both applications. Higher value carbon markets should definitely be pursued. Although, this system uses natural gas as a feedstock, the net greenhouse gas emissions and overall fossil energy consumption is lower for the solar process than for the conventional fossil system.

References

- (1) Spath, P.L.; Amos, W.A. (2002). *Assessment of Natural Gas Splitting with a Concentrating Solar Reactor for Hydrogen Production*. National Renewable Energy Laboratory. Golden, CO. NREL/TP-510-31949.
- (2) Dahl, J.K.; Barocas, V.H.; Clough, D.E.; Weimer, A.W. (2002). Intrinsic kinetics for rapid decomposition of methane in an aerosol flow reactor. *International Journal of Hydrogen Energy*; Vol. 27, Issue 4, pp. 377-386.
- (3) Chemical Marketing Reporter. (2001). Price quote of carbon black, fast extruding (N550). January.

HYDROGEN ADSORPTION IN HCl-TREATED POLYANILINE AND POLYPYRROLE; NEW POTENTIAL HYDROGEN STORAGE MEDIA

Sung June Cho,* Kwang Sup Song, Jong Won Kim, Tae Hwan Kim
and Koyeun Choo

Korea Institute of Energy Research
71-2, Jang-dong, Yusung-gu
Taejeon 305-343, KOREA

Introduction

Hydrogen has attracted a great deal of attention as a clean fuel for mobile and stationary purpose in the future. Of the hydrogen life cycle, the storage using safe and efficient retrieval method is given a priority in research fields. Various hydrogen storage media have been investigated¹⁻⁴, which includes carbon nanotube (CNT), carbon nanofibers, metallic hydride, metal alloy and glass microspheres.

Recent advances on the hydrogen storage technology by CNT, either single-walled (SWNT) and multi-walled (MWNT) have been spurred since the Dillon et al. first reported a significant H₂ adsorption of as prepared soot containing a trace amount of SWNT, 0.1 ~ 0.2 wt% at 133 K.² Chen et al. reported unusual high hydrogen adsorption on alkali-doped CNT, 14 ~ 20 wt%.⁵ Most recently, the alkali-doped CNT was found to adsorb only 2 wt% dry hydrogen at room temperature.⁶ Liu et al. also showed a high hydrogen storage in CNT containing 50 ~ 60 % SWNT, 4.2 wt% if the SWNT is treated with acid cleaning and subsequent vacuum treatment at 773 K.⁷ However, the problem of cost for the CNT production and the low hydrogen storage capacity seems obstacles for the practical application.

Previous studies of CNT-SWNT and B- or N-containing CNT suggests that the tubes exhibit many different structures, which will be either metals or semiconductor.⁸⁻¹¹ We speculate that the metallic character of SWNT which is induced possibly with tangling *p* orbitals of carbon can enhance the hydrogen adsorption. And then organic materials with similar metallic property can also be possible candidates for hydrogen storage media if enough metallic character is present so that it can adsorb hydrogen as noble metal does.

Conducting polymer membranes have been investigated for the separation of binary gas mixtures such as H₂/N₂, O₂/N₂, CO₂/CH₄ etc.¹²⁻¹⁴ The control of the selectivity and permeability can be tailored by creating the permanent morphological in the conjugated polymer system with the repetitive doping, undoping and subsequent redoping. The high selectivity value for H₂/N₂, 3590 through the freestanding films of the conjugated polymer, polyaniline was reported.¹² The molecular sieving mechanism was proposed for the unusually high selectivity of hydrogen in H₂/N₂. The doping, undoping and redoping treatment generated the small micropore, 0.35 nm in diameter that decreased the permeability of larger gases. In addition, the conductivity of the polymer has been claimed to play an indirect role to enhance the selective separation.¹⁵

The unique permanent morphological structure of the polymer by the doping-undoping-redoping process was thus expected to allow the substantial hydrogen storage. In this work, we have explored polyaniline (PANI) and polypyrrole (Ppy), the conducting polymers as a new potential hydrogen storage media.

Experimental

Sample preparation. PANI and Ppy were purchased from Aldrich. Both are inherently conductive polymers with doping. The Ppy was coated as on polyurethane core resin in which the polymer/urethane core resin ratio is four. For the acid treatment, the conducting polymer weighing 500 mg was slurred in 15 ml

hydrochloric acid (Aldrich, 37%) at room temperature for 24 hour. The polymer was then filtered, washed with deionized water thoroughly and dried in oven at 360 K for 24 hour in order to eliminate adsorbed water. The fine powder was made into a self-supporting wafer of 13 mm using an IR press with a pressure of 3000 kg·cm⁻². The pellet was known to be more stable in ambient air than the powder.¹⁶ The pellet was again crushed into 1~2 mm particle for the measurement of hydrogen storage.

Measurement of hydrogen storage. The hydrogen storage capacity of the polymer was measured using an automatic Sievert's type PCT measurement apparatus similar to that Liu et al. used.⁷ A control experiment was carried out to measure the pressure change at 298 K for one hour using an empty sample cell which is immersed in water along the measurement to detect the leakage through the connection, after the evacuation till 10⁻³ Torr and the subsequent charging of 9.3 MPa ultra high purity hydrogen (99.999%). Subsequently, the measurement of hydrogen storage of the polymer weighing ~ 500 mg was performed for 1 hour in the same way as above. The hydrogen storage capacity of the polymer based on the pressure changes has been calibrated with the control data. Between the measurements, the cell containing the polymer was heated up to 473 K to remove the adsorbed gas completely. The measurement of hydrogen adsorption started when the pressure reached 10⁻³ Torr after cooling to room temperature. The hydrogen storage of the known reference materials such as metallic hydrides has been measured using the same apparatus.

Results and Discussion

The hydrogen storage on the Ppy and the PANI increased progressively up to 6 ~ 8 wt% in the repetitive measurement (Fig. 1), corresponding to 80 ~ 100 kg H₂·m⁻³ when the density of the PANI, 1.360 g/cc, was considered. The equilibrium pressure did not reach even for an hour equilibrium time. Liu et al. observed similarly much longer the equilibrium time, typically six hours.⁷ The longer adsorption time might indicate the Knudsen diffusion of the hydrogen into the molecular scale pores, similar to that proposed for the gas separation of polymer membranes.¹⁷ For comparison, the hydrogen storage in metal hydrides and MWNT was compared in Table 1. The hydrogen storage in the metal hydrides was slightly lower the reported value for both AB₅ and AB₂ type.^{18,19}

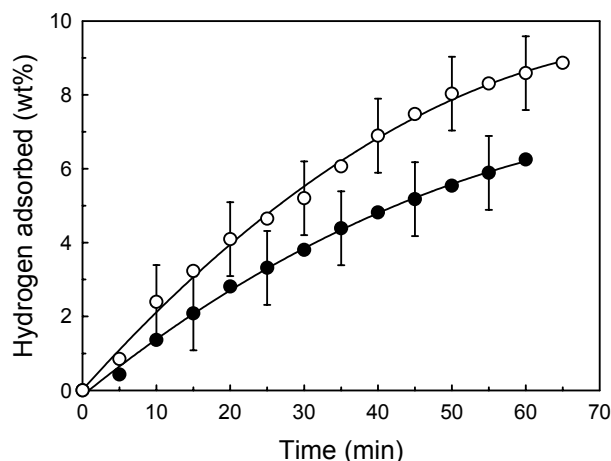


Figure 1. The amount of H₂ in wt % for both (●) the PANI and (○) the Ppy treated with concentrated hydrochloric acid. The measurement was started after evacuation at 473 K and subsequently at room temperature till at least 0.13 Pa.

Table 1. Summary of the hydrogen storage in metal hydrides, multi-walled carbon nanotube and the acid treated conducting polymer measured using the same adsorption apparatus.

Sample	Press. (atm)/ Temp. (K)	wt%
MmNi _{4.7} Al _{0.3}	10 ~ 20/298	1.2
MmNi _{4.8} Al _{0.2}	10 ~ 20/298	1.3
Ti _{0.7} Zr _{0.3} Mn _{1.0} Cr _{0.9} Ni _{0.02} Fe _{0.03}	10 ~ 20/298	2.0
MWNT ^{1,b}	90/298	0.8
HCl-treated PANI ^b	90/298	6.0
HCl-treated Ppy ^b	90/298	8.0

^aSynthesized from the decomposition of CH₄ at 800 ~ 1100 K over the catalysts such as Ni/MgO and Ni/USY. The purification of the obtained CNT was carried out in order to remove amorphous carbon by dissolving the sample in HF solution and then ultra-sonicated. ^bexposed to ~ 90 atm ultra high purity hydrogen (99.999%) for one hour.

The hydrogen storage in the MWNT²⁰ prepared at 800 ~ 1100 K using a catalytic method using Ni catalyst and methane as carbon source was only 0.8 wt% under the same condition. The hydrogen storage in the acid-treated polymer was reproducible within the error of ± 1 wt% during few tens of the adsorption/retrieval cycle in which the desorption of hydrogen was performed 473 K because only about 50% hydrogen was removed at room temperature. However, the weight loss, 0.4 ~ 0.5 wt% detected from the TGA measurement during heating up 473 K may lead to the structural change to alter the hydrogen storage capacity, resulting in the rather large experimental error.

The hydrogen storage can also be varied widely depending on the method of the modification process of the polymer using the concentrated hydrochloric acid, specifically, the exchange or removal level of the dopants, the drying temperature and the rigidity of the polymer backbone.¹⁴ The treatment of the concentrated hydrochloric acid onto the polymer resulted in the replacement of the large organic dopant molecule (OSA) such as camphor sulfonic acid (CSA) and dodecylbenzene sulfonic acid (DBSA) into the smaller dopant, HCl. The morphological change of the polymer texture in the self-supporting wafer observed by SEM suggested that the acid treatment of the PANI induced the formation of micropore or micro-leak desirable for the hydrogen storage or gas separations. As expected, no hydrogen was stored in the polymer without an acid treatment. The combined analysis of the PANI before and after the acid treatment using EDX measurement and elemental analysis showed that 65% of the total organic sulfonic acid was replaced with smaller Cl⁻ dopant while the total dopant level was maintained constant as PANI(OSA)_{0.45} and PANI(OSA)_{0.16}(HCl)_{0.29} before and after the acid treatment, respectively. The molecular scale micropore seems to be generated due to the exchange of the larger dopant molecule, CSA or DBSA into the smaller one if the structure of the polymer backbone was retained to be rigid sufficiently. However, the KA zeolite having small micropore of 0.3 nm was reported to have the hydrogen storage capacity, 9.2 cm³ g⁻¹, which was too low to present competition to metal hydrides, 150 ~ 700 cm³ g⁻¹.²¹ The electronic structure of the polymer seems to play a significant role in hydrogen storage.

The exchange of large organic sulfonic acids into HCl decreased the bulk conductivity significantly from 5 S/cm to 0.4 S/cm for PANI and from 3.1×10^{-3} S/cm to 0.9×10^{-3} S/cm for Ppy, respectively. The XRD intensity of the PANI at $2\theta = 15 \sim 20^\circ$ increased by the acid

treatment, indicating the improvement of the crystallinity. The improved crystallinity might be able to increase or give higher intrinsic metallic properties in the microscopic regions of the polymer, but not bulk conductivity as expected due to the character of the dopant and the poor grain boundary. The conduction process followed the heterogeneous model consisting of ordered crystalline and disordered amorphous regions.^{22,23} The conduction process in the ordered crystalline region of the conducting polymer was so fast that the hopping motion in the disordered amorphous region appears as a limiting mechanism. Thus, the achievable conductivity from the PANI-CSA was claimed to surpass that of copper if the entire charge carrier density in the localized metallic islands containing delocalized carriers participates in the conduction process.²⁴

Summary

The unusual hydrogen storage in the polymer was believed to occur because of the combined effect of the molecular sieving and the conjugated conducting electronic environment in which hydrogen can be stabilized probably due to the metallic character of the conduction band. In near future, the conducting polymer as a new class of hydrogen storage media has to be explored in theoretically and experimentally further to construct the safe, cheap and adsorption/retrieval storage system.

Acknowledgement. SJC thanks for the financial support from the Ministry of Science and Technology, Korea

References

- (1) Ewald, E. *Int. J. Hydrogen Energy*, **1998**, *23*, 803-814.
- (2) Chambers, A.; Park, C.; Baker, R. T.; Rodriguez, N. M. *J. Phys. Chem. B* **1998**, *102*, 4253-4256.
- (3) Dillon, A. C. et al. *Nature* **1997**, *386*, 377-379.
- (4) Buchner, H. et al. Hydrogen and other alternative fuels for air and ground transportation, Wiley: Chichester, UK, 1995.
- (5) Chen, P.; Wu, X.; Lin, J.; Tan, K. L. *Science* **1999**, *285*, 91-93.
- (6) Yang, R. T. *Carbon* **2000**, *38*, 623-626.
- (7) Liu, C. et al. *Science* **1999**, *285*, 1127-1129.
- (8) Odom, T. W. et al. *Nature* **1998**, *391*, 62-64.
- (9) Hsu, W. K. et al. *Chem. Phys. Lett.* **2000**, *323*, 472-479.
- (10) Huang, Y.; Gao, J.; Liu, R. *Synthetic Metals* **2000**, *113*, 251-255.
- (11) Tang, X.-P. et al. *Science* **2000**, *288*, 492-494.
- (12) Anderson, M. R.; Mattes, B. R.; Reiss, H.; Kaner, R. B. *Science* **1991**, *252*, 1412-1415.
- (13) Kaner, R. B. *Nature* **1991**, *352*, 23.
- (14) Gulsen, D.; Hacıoğlu, P.; Toppare, L.; Yilmaz, L. *J. Membr. Sci.* **2001**, *184*, 29-39.
- (15) Reiss, H., Conjugated polymers and related materials: The interconnection of chemical and electronic structure (eds. Salaneck, W. R.; Lundström, I.; Rånby, B., Oxford University Press: New York, 1993, 263-272.
- (16) Rannou, P.; Nechtschein, M. *Synthetic Metals* **1997**, *82*, 755-756.
- (17) Illing, G.; Hellgardt, K.; Wakeman, R. J.; Jungbauer, A., *J. Membr. Sci.* **2001**, *184*, 69-78.
- (18) Liang, G.; Huot, J.; Schulz, R. *J. Alloys and Comps* **2001**, *320*, 133-139.
- (19) Liu, F.-J.; Suda, S.; Sandrock, G. *J. Alloys and Comps* **1996**, *232*, 232-237.
- (20) Cheng, H. M.; Yang, Q. H.; Liu, C. *Carbon* **2001**, *39*, 1447-1454.
- (21) Weitkamp, J.; Fritz, M.; Ernst, S. *Int. J. Hydrogen Energy* **1995**, *20*, 967-970.
- (22) Joo, J. et al. *Phys. Rev. B* **1998**, *57*, 9567-9580.
- (23) Beau, B.; Travers, J. P.; Banka, E. *Synthetic Metals* **1999**, *101*, 772-775.
- (24) Joo, J.; Epstein, A. J.; Prigodin, V. N.; Min, Y.; MacDiarmid, A. G. *Phys. Rev. B, Rapid Commun.* **1994**, *50*, 12226-12229.

KINETIC STUDY OF THE REVERSE WATER GAS SHIFT REACTION IN HIGH-TEMPERATURE, HIGH-PRESSURE HOMOGENEOUS SYSTEMS

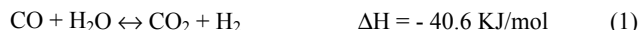
Felipe Bustamante¹, Robert Enick¹, Kurt Rothenberger, Bret Howard, Anthony Cugini, Michael Ciocco² and Bryan Morreale²

U.S. Department of Energy
National Energy Technology Laboratory
P.O. Box 10940, Pittsburgh PA 15236

(1) NETL Research Associate, University of Pittsburgh
feb5@pitt.edu (2) NETL Site Support Contractor, Parsons Project Services Inc.

Introduction

The Water Gas Shift Reaction (WGSR), an important industrial reaction for the production of chemicals and/or hydrogen, is expected to play a key role in the integration of gasification technologies with a H₂ production/recovery unit. The effluent stream of the gasifier, mainly H₂, CO and CO₂ at high pressure (up to 30 atm) and temperature (up to 1000°C), will be directed to the water gas shift reactor along with steam where reaction (1) will take place, increasing the yield of hydrogen.



The WGSR is an exothermic, equilibrium-limited reaction that exhibits decreasing conversion with increasing temperature. Reviews of the catalyzed WGSR at temperatures below 600°C are available in the open literature¹. A catalyst is required under these conditions because of the lower reaction rate at low temperature. There has been renewed interest in the WGSR at extreme temperatures however, because of recent advances in high-temperature materials for hydrogen separation membranes. The permeation of hydrogen through the walls of a membrane reactor enables the attainment of high conversion of CO and steam to hydrogen and carbon dioxide².

Several papers have shown high reaction rates for the high-temperature (>875°C), non-catalytic water gas shift reaction. Graven and Long³ addressed both the forward (CO + H₂ reactants) and the reverse (CO₂ + H₂O reactants) water gas shift reaction in the temperature range 875-1050°C, reporting that the reaction occurs only in the gas phase, i.e. without any heterogeneous contribution. Their experimental results support the chain-reaction mechanism previously proposed. However, some of their results on the reverse WGSR were challenged by two later studies^{4,5}. Tingey⁴ and Kochubei and Moin⁵ found a lower value for the rate constant suggesting experimental errors in the work of Graven and Long due to the presence of traces of oxygen (an homogeneous catalyst) in the gas phase. Tingey studied the reverse water gas shift reaction over an extended temperature range (400-1200°C) and pointed out that at high-temperature (>800°C), the reaction would follow the chain-reaction mechanism but would follow a different mechanism at lower temperature. All of these studies were performed in a highly diluted reaction gas mixture at ambient pressure, without exploring the influence of pressure on the reaction rate and kinetics.

The utility of the high-temperature, non-catalytic WGSR is supported by these previous results showing high reaction rates at extreme temperatures. This report will address the kinetics of the reverse WGSR under conditions not studied previously, namely high-concentration streams, i.e. non-diluted streams, and high-pressures. These conditions are more appropriate to draw conclusions on the application of the WGSR directly to a gasification stream via a

membrane reactor. (The forward water-gas shift reaction will be examined in a subsequent study.)

Experimental

A flow system (CSTR reactor) was used for the kinetic studies. The Hydrogen Membrane Testing unit (HMT-1) at NETL was designed for study the water-gas shift reaction at high-pressure (up to 30 atm), high-temperature (up to 900°C) conditions. The unit has the capability of feeding a gas mixture to a high-pressure, high-temperature reactor composed of quartz or Inconel.

Hydrogen and carbon dioxide were fed by using electronic mass flow controllers. Tubing downstream of the reactor was heat-taped and insulated to avoid condensation of water. Reactor temperature was controlled with a thermocouple placed directly on the top of the reactor. Pressure was controlled with a pressure controller downstream the reactor.

The effluent of the reactor was analyzed with a gas chromatograph equipped with a TCD detector for quantification of H₂, CO, CO₂ and H₂O in the range of concentrations of interest.

The residence time of the reactants in the reactor was chosen to assure low conversions (less than 2 %), avoiding any significant effect of the forward reaction. Under these conditions, the rate can be modeled with the following power-law expression: $r = k[\text{H}_2]^\alpha[\text{CO}_2]^\beta$. Residence time was typically lower than 3 s. Reaction rates were evaluated from the CO₂ conversion, outlet CO₂ concentration, and residence time by using the CSTR design equation.

Results and discussion

Ambient pressure studies. In order to validate the experimental setup, kinetic experiments were carried out with an empty quartz reactor under the conditions reported in other studies^{3,4,5} (900°C, ambient pressure). Conversions were less than 0.1% in all cases and were in good agreement with the results of Tingey⁴ and Kochubei and Moin⁵. The energy of activation measured for the high-temperature (>875°C), ambient pressure experiments, $E_a = 75 \text{ Kcal/mol}$, was in agreement to the results reported in the literature (76 – 78 Kcal/mol^{4,5}). Kochubei and Moin⁵ had reported a surface effect by quartz at low temperatures (<850°C). Although this surface effect is relatively small, it would suffice to explain the lower value for the energy of activation reported by Graven and Long³ (56 Kcal/mol). In fact, for determining the Arrhenius parameters they used a packed reactor and some of their low temperature points may fall in the transition zone between homogeneous and surface-assisted reaction.

The effect of the walls on the reaction was tested for the Inconel reactor. Inconel is the material of choice for the reactor due to the harsh conditions (high temperature and pressure). For very small residence times (less than 0.5 s), conversions were very high (Figure 1). Moreover, these conversions were two orders of magnitude greater than the conversions observed with the quartz reactor (conversions with the quartz reactor were less than 0.1% under the same experimental conditions, i.e. temperature and residence time, than the Inconel reactor). This result implied that the metal walls of the Inconel reactor catalyzed the reaction. An increase in the Inconel surface area was achieved by packing the reactor with Inconel rings. As shown in Figure 1, the conversions were twice that observed with the empty Inconel reactor (Figure 1). However, the increase in the reaction rate may have been attributed to the enhanced mixing induced by the presence of packing. The replacement of Inconel packing with a similar surface area of quartz packing also induced an increase in the reaction rate. Nevertheless, the conversion was lower than that observed with the Inconel packing (34% for quartz packing versus 41% for Inconel packing). As the quartz surface is considered inert for this reaction^{3,5}, it appears that both catalytic and mixing

effects contributed to the dramatic increase in reaction rate. Figure 1 also illustrates that the reverse water-gas shift reaction was approaching the equilibrium conversion of 55% in the Inconel reactor even though the residence times were less than a second.

The Inconel packing (Inconel is 72% Ni, 17% Cr, 10% Fe) was examined by XPS after reaction. Results showed an increase in the concentration of chromium, and a depletion of nickel on the surface. The surface analysis also revealed a considerable amount of carbon deposits. Formation of carbon structures on Ni-Fe in gas phase reactions involving CO has been reported⁶. Further, chromium-based materials are used as catalysts for the "high-temperature" (400°C) WGS¹. Therefore, it appears that the chromium-rich Inconel surface was an active surface.

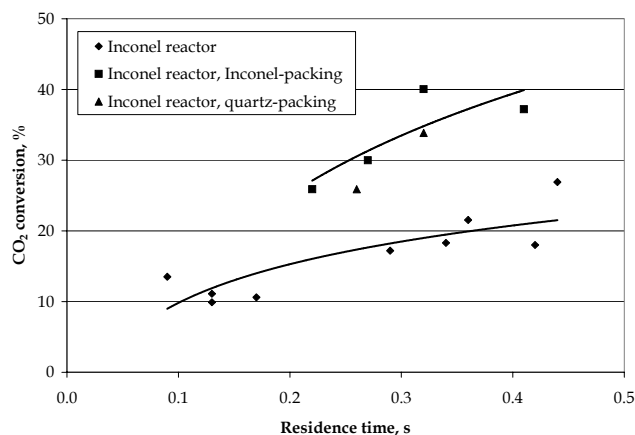


Figure 1. Reverse water gas shift reaction in an Inconel reactor. 900°C, ambient pressure, $[H_2]_0 = [CO_2]_0$. Equilibrium conversion for these conditions is 55%.

High-pressure studies. The behavior of the high-pressure (16 atm), high-temperature (>700°C) was also investigated. An empty quartz reactor was used for the studies. A shift in the mechanism at a temperature around 800°C, consistent with the observations of Tingey⁴, was observed. The values for the rate exponents were very close to those reported previously (0.41 for H_2 , and 1.2 for CO_2 ; low-pressure exponents are 0.5 and 1.0 respectively), leading to the conclusion that the chain reaction mechanism is valid for high-pressure. However, the value for the energy of activation, 51 Kcal/mol, was much lower for the reaction carried out at high-pressure (Figure 2); the value of the pre-exponential factor was $1.8 \times 10^8 \text{ l}^{0.6} \text{ mol}^{-0.6} \text{ s}^{-1}$. An inhibiting effect (i.e. the rate at high pressure was slightly lower than that expected from the power-law model based on low-pressure data) at higher temperatures was also observed.

Even though the rate constant of the gas phase dissociation of hydrogen, which is the first step in the chain reaction mechanism, is pressure-dependent⁷, its effect would not explain the observed results. A surface effect was suspected and studied by adding quartz packing to the reactor. This inhibiting effect appeared to be increased by the presence of packing. Some authors⁸ have suggested a breaking of the chain on the walls under certain circumstances. We are currently exploring this behavior.

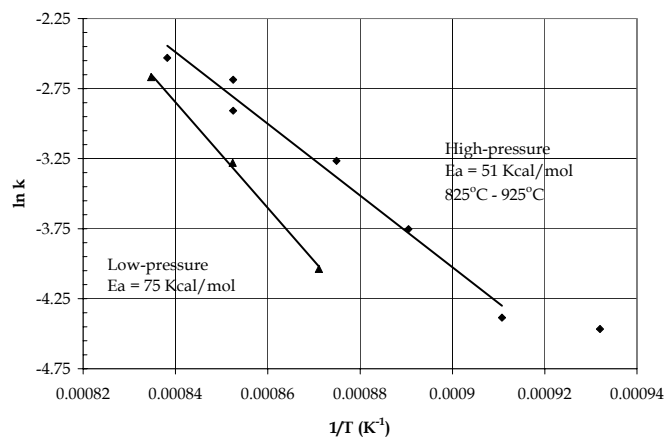


Figure 2. Arrhenius plot for the high-temperature, high-pressure (16 atm) and high-temperature, low-pressure (ambient) reverse water gas shift reaction.

Conclusions

The first experimental study of the high-pressure, high-temperature reverse water gas shift reaction was conducted. The findings of the study may be summarized as:

- Previous hypothesis on the reaction mechanism and homogeneous character of the low-pressure, high-temperature reverse water gas shift reaction were corroborated.
- A strong catalytic wall effect was found by using Inconel, evidenced by an enrichment of chromium and depletion of nickel at the surface.
- A significant reduction in the energy of activation for the high-temperature, high-pressure reverse water gas shift reaction was observed. Current research efforts are underway to explain this phenomenon.

Acknowledgement. This work is supported through the "Gasification Technologies" and "Transportation Fuels and Chemicals" product lines at NETL.

References

- (1) Newsome, D. *Catal. Rev. Sci. Eng.* **1980**, *21*, 275.
- (2) Enick, R.; Morreale, B.; Hill, J.; Rothenberger, K.; Cugini, A.; Siriwardane, R.; Poston, J.; Balachandran, U.; Lee, T.; Dorris, S.; Graham, W.; Howard, B. In: *Advances in Hydrogen*; Kluwer Academic/Plenum Publishers, New York, 2000; pp 93-100.
- (3) Graven, W.; Long, J. *J. Am. Chem. Soc.* **1954**, *76*, 2602, 6421
- (4) Tingey, G. *J. Phys. Chem.* **1966**, *70*, 1406.
- (5) Kochubei, V.; Moin, F. *Kinetika I Kataliz* **1969**, *10*, 1203.
- (6) Trimm, D. *Catal. Rev. Sci. Eng.* **1977**, *16*, 155.
- (7) Warnatz, J. In *Combustion Chemistry*; Gardiner, W, Ed.; Springer Verlag: New York, 1984; pp 197-360.
- (8) Hadman, G.; Thoupson, H.; Hinshelwood, C. *Proc. Roy. Soc. (London)*, **1932**, *A137*, 87.

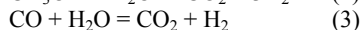
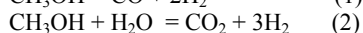
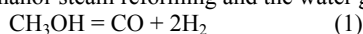
Kinetics of methanol decomposition and water gas shift reaction on a commercial Cu-ZnO/Al₂O₃ catalyst

Yongtaek Choi and Harvey Stenger

Department of Chemical Engineering
Lehigh University
Bethlehem, PA 18015

Introduction

The advantages of high energy density, easy availability and safe handling/storage are now making methanol one of the most promising sources of hydrogen for fuel cell systems. While extensive work has been done for decades on how to synthesize methanol, recent research is now concentrating on how to produce hydrogen efficiently from methanol. The goal of our work is to maximize hydrogen yield while minimizing the size of the reforming unit. Therefore to design a compact and efficient methanol reformer, reaction data and kinetics are needed for methanol decomposition, methanol-steam reforming and the water gas shift reaction (1~3).



There are few published studies addressing the mechanism and kinetics of methanol decomposition on Cu/ZnO/Al₂O₃ catalysts. But several groups have studied the mechanism and rate-expression for methanol-steam reforming. An early hypothesis believed that H₂/CO formation occurred first followed by the water gas shift reaction.¹ A direct reaction to form CO₂ and H₂ from methanol was proposed recently.² Another report showed that the rates for all three reactions (methanol-steam reforming, water-gas shift reaction and methanol decomposition) must be included in the kinetic analysis.³ In those mechanisms the rate determining step is either the dehydrogenation of methoxy groups or methyl formate hydrolysis.^{3,4,5}

In spite of the extensive literature on Cu/Zn/Al₂O₃ catalysts, much remains in dispute concerning the role of the oxidation states of Cu. And also most studies use various x-ray, IR, and TPR/TPD techniques, etc., however, it is hard to find a study which relates the product distribution to the catalyst state. Furthermore, there are few papers, which address the effects of water addition on methanol decomposition. The purpose of our study is to examine the reaction mechanism, by product formation and kinetics of methanol decomposition in the absence and presence of water. Cu oxidation state and its relation to deactivation is also determined through XPS analysis of the catalyst and time-on-stream tests. Rate expressions and kinetic parameters used to fit the experimental data were determined.

Experimental

The Cu/Zn/Al₂O₃ catalyst used in this study is a commercial catalyst manufactured by Sud-Chemie (Catalyst #: EX-2248). The molar Cu: Zn ratio was determined to be 2:1 by XPS analysis and verified by Galbraith Lab (Knoxville, TN). The catalyst was ground and sieved for particle diameter of the catalyst was chosen to eliminate internal diffusion resistance. An effectiveness factor of $\eta > 0.95$ required the size of the catalyst to be below 2 mm. Our studies used a particle size of 200 to 250 microns.

A stainless steel tubular reactor, 1/2 inch in diameter and 12 inches long was used for all reaction tests. To ensure isothermal conditions along the bed length, a split tubular furnace was used and the temperature of catalyst bed was measured directly by a 1/16 inch J-type thermocouple. The reaction tests were performed at temperatures between 110 and 360°C. Two grades of methanol, Laboratory grade (Fisher Scientific, water content ~1 wt%) and

HPLC grade (Aldrich, water content ~0.03 wt%), were used. The methanol feed rate was controlled precisely by a syringe pump, 74900 Series (Cole Palmer), from 0.5 ml/Hr to 8 ml/Hr, giving a volume of vaporized methanol at STP flow of 277~ 4427 cm³/Hr. The catalyst load was between 0.25~1.0 gram and the GHSV at reaction temperature was controlled between 1,000~10,000 Hr⁻¹.

The effluent of the reactor was maintained at 120°C with heating tapes to avoid liquid condensation and connected directly to gas chromatograph. Two columns: Alltech Chemisorb 107(80~100 mesh, 6ft x 1/8 in) and Supelco Carboxen 1000 (60~80 mesh, 15ft x 1/8 in) were connected in series to analyze the condensable and light gas components. Eight components: water, methanol, dimethyl ether, methyl formate, H₂, CO, CH₄, CO₂ were measured during each test run. Material balances on carbon were calculated to verify measurement accuracy.

Results and Discussion

Figure 1 shows a plot of methanol conversion in the absence of water versus reaction temperature at various space velocities. For the lowest space velocity of 280 hr⁻¹(0.5 cm³ of liquid/hr-gcat), the conversion reached 100% at approximately 260 °C. A temperature greater than 330 °C was needed for 100% conversion at the highest space velocity of 4400Hr⁻¹ (8.0 cm³ of liquid/hr-gcat). Careful viewing of the conversion vs. temperature profiles shows two distinct temperature regions. In the lower temperature region, below 230 °C, the rate of decomposition increases slowly with temperature, while at temperatures greater than 230 °C, the decomposition rate increases more rapidly with temperature.

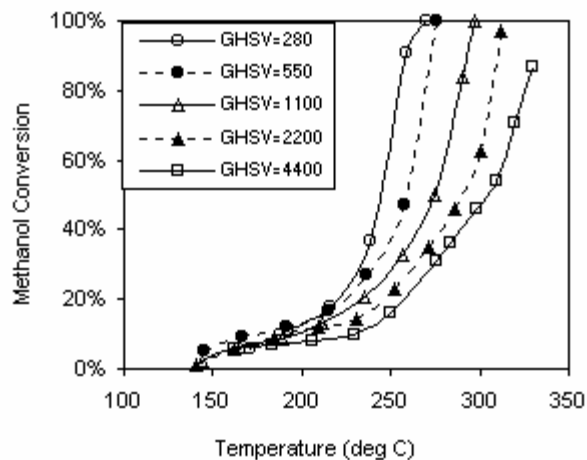


Figure 1 Conversion of methanol with various space velocities in the absence of water as a function of reaction temperature (1.0 gr of Cu/ZnO/Al₂O₃ catalyst, methanol feed: Laboratory Grade, GHSV: 280 ~ 4400 hr⁻¹)

When water is added to the methanol feed, complete methanol conversion occurs at lower temperature. To evaluate the effect of water the temperatures required to achieve 50% conversion of methanol were measured (Figure 2). At equal residence times, this "50% conversion temperature" was 45~60 °C lower for a feed with 30 weight % versus pure methanol.

The most notable effect of water addition is the reduction of all the observed by-products: dimethyl ether, methyl formate and methane. Methyl formate, the main by-product for methanol only decomposition was reduced significantly as water was added. No methyl formate was detected when the feed was 30% by weight or

greater. Also there was no DME or methane formation when the feed had more than 15 wt% water

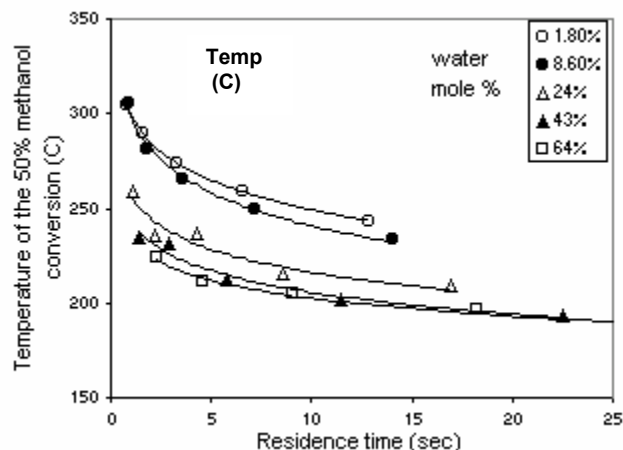


Figure 2 Temperatures to achieve 50% conversion of methanol versus residence time (water content in feed = 1.8, 8.6, 24, 43, 64 mole %, catalyst loading = 1.0 gr, GHSV: 280 ~ 4400 hr⁻¹)

The water gas shift reaction is moderately exothermic ($\Delta H = -41$ kJ mol⁻¹) to the right, thus its equilibrium constant decreases with the temperature, and maximum conversion is attained at low temperatures. Pressure has no significant effect on the equilibrium because there is no change in moles. Equilibrium calculations for the water gas shift reaction have been thoroughly analyzed. **Figure 3** shows the conversion of carbon monoxide with various H₂O/CO ratio in the temperature range of 120°C ~ 250°C. The conversion of CO consistently increases with the H₂O/CO ratio at constant temperature. At the 1:1 equivalent molar feed ratio and 220°C, the typical operation temperature of water gas shift reactor, the conversion reaches about 70% while the equilibrium conversion is calculated as 87%

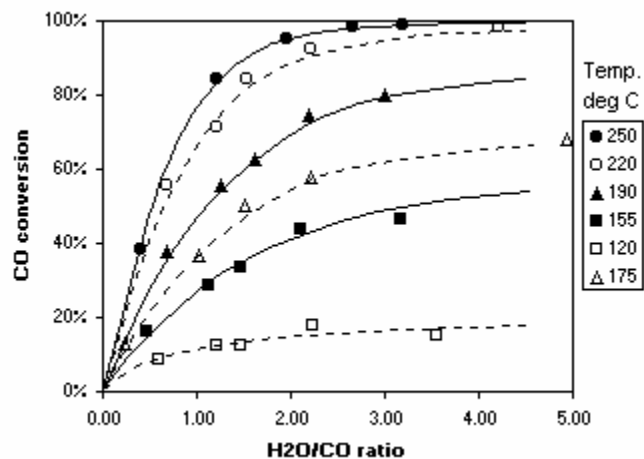
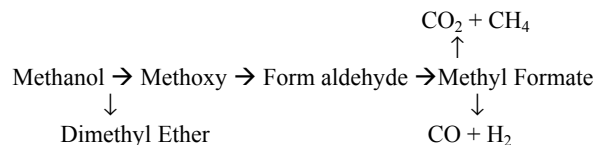


Figure 3 Water gas shift reaction – CO conversion vs. H₂O/CO ratio (reaction temperature = 175 ~ 250°C, catalyst loading = 1.0 gr., pressure : 1 atm, GHSV = 6100 hr⁻¹)

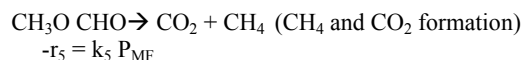
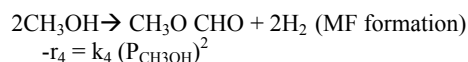
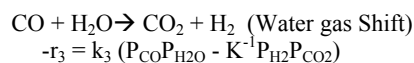
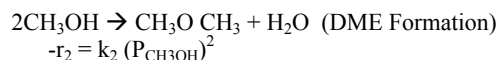
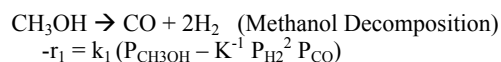
It is difficult to select just one reaction path for methanol decomposition to hydrogen, CO and CO₂ because of the various intermediates formed. However after reviewing several hypotheses

detailed in the literature, we believe they can be simplified to 6 major reactions shown below.



The intermediate compound formed to the largest extent was methyl formate. Therefore we can infer that the rate determining step is decomposition of methyl formate to form H₂, CO or CO₂. For the methanol conversion versus temperature in data shown in Figure1, each profile was seen to have two temperature regions, inferring that two different rate determining steps may exist. In the low temperature region, we observed no dimethyl ether while methyl formate increased significantly with temperature.

Based on the reaction mechanism above, a kinetic model of methanol decomposition can be written as the following 5 reactions. The assumed rate expressions are listed below each reaction.



The rate constants for these 5 reactions are evaluated individually using least squares non-linear regression method for all data points at different temperatures and space velocities. The exit concentration of every component was determined by the numerical integration assuming a one dimensional PFR model. Two parameters, activation energy and frequency factor, in every rate constants are estimated by minimizing the difference between the calculated values and experimental values of each species. For this numerical analysis, MATLAB was used as computing language and subroutine function "ODE23" and "Lsqnonlin" were used for numerical integration and optimization.

References

- (1) J.C. Amphlett, M.J. Evans, R.A. Jones, R.F. Mann and R.D. Weir, Can. J. Chem. Eng., 1981, Vol.59, 720~727
- (2) K. Geissler, E. Newson, F. Vogel, T.-B. Truong, P. Hottinger and A. Wokaun, Phys. Chem. Chem. Phys., 2001, 3, 289
- (3) B A Peppley et al., Applied Catalysis A, 1999, 179, 31~49
- (4) R O Idem and N. N. Bajhshi, Chem. Eng. Sci., 1996, Vol 51 No.14, 3697~3708
- (5) C.J. Jiang, D.L. Trimm and M.S. Wainwright, Appl. Catal. A, 1993, 93, 245~255
- (6) W.H. Cheng, Acc. Chem. Res. 1999, 32, 685~691
- (7) D.S. Newsome, Catal. Rev. – Sci. Eng., 1980, 21(2), 275~318

LOW-COST FIBER OPTIC HYDROGEN SENSORS

R. D. Smith II, Ping Liu, Se-Hee Lee, C. Edwin Tracy and J. Roland Pitts

Basic Sciences Center
National Renewable Energy Laboratory
Golden, CO 80401

Introduction

The ability to detect hydrogen gas leaks economically and with inherent safety is an important technology that could facilitate commercial acceptance of hydrogen fuel in various applications. This paper reports the progress made on the development of a low-cost fiber-optic hydrogen sensor (FOHS) intended to meet the safety requirements of a hydrogen-fueled passenger vehicle.

The FOHS consists of a hydrogen sensitive coating at the end of an optical fiber. When the coating reacts with hydrogen, its optical properties are changed. Light from a central electro-optic control unit is projected down the optical fiber where it is either reflected from the sensor coating back to the central optical detector, or is transmitted to another fiber leading to the central optical detector. A change in the reflected or transmitted intensity indicates the presence of hydrogen. The FOHS offers inherent safety by removing all electrical power from the test sites and reduces signal-processing problems by minimizing electromagnetic interference. Critical detector performance requirements include high selectivity, response speed, and durability as well as potential for low-cost fabrication.

Summary of Prior Work. Initial experiments were conducted using a "simple" sensor configuration, essentially a palladium/metal oxide (Pd/MO_x) reflective fiber optic sensor. The principal material used as the hydrogen sensitive coating was tungsten (VI) oxide or WO₃ (1). A thin over-layer of Pd dissociates the hydrogen molecules into atomic hydrogen, which then readily diffuses into the metal oxide causing the optical change. This sensor design was found to be adequate for hydrogen detection, but too slow for safety applications, with a response time of approximately 30 seconds (2). However, the response time was adequate for the use of the "simple sensor" as a detector of diffusible hydrogen from welded steel (3-5). A surface-plasmon resonance (SPR) sensor was also designed and evaluated. The principle behind SPR is based on light adsorption in a thin metal layer causing oscillation of free electrons, or surface plasmons; hydrogen adsorption by an underlying metal oxide layer causes a change in its refractive index and a subsequent resonant wavelength shift, which is then measured. The response time of the SPR sensors was found to be on the order of 5 seconds. However, the SPR shift was found to be sensitive to changes in relative humidity, causing a false positive signal (2). Alternate materials such as transition metal hydrides were then investigated for their suitability as sensor materials. These materials were subsequently found to be unstable in ambient air. Lattice expansion of the metal hydride during hydrogen absorption also caused delamination of the sensor films at higher concentrations.

Another factor in the unsuitability of these prior sensor designs was degradation of performance, attributable to poisoning of the Pd surface by airborne contaminants. This phenomenon was observed in all types of sensors studied since each design used a thin film of Pd as a hydrogen dissociation catalyst. Research was therefore redirected towards the development of new sensor materials that displayed superior properties in terms of response time and durability.

Experimental

Thin films were fabricated by standard techniques of vacuum deposition. Thermal evaporation was carried out on a Varian Model 3118 evaporator. The working pressure was less than 1×10^{-5} torr and the metal oxide deposition rates were controlled at 0.1 to 0.5 nm/s. The palladium layer was deposited on top of the oxide at a rate of 0.1 nm/s. Plasma enhanced chemical vapor deposition (PECVD) of organic thin films was performed using an RF-powered 13.5 MHz Plasma Technology CVD system. Glass microscope slides were used as substrates to simplify deposition and analysis. The films were deposited at room temperature.

The fiber-optic sensor test station consisted of a gas flow manifold connected to a fiber optic photodiode-array Ocean Optics 2000 Spectrometer. The manifold fed the test gas stream into a test chamber, constructed so that the dead volume was minimal (0.1 cm³). In addition the chamber was constructed so that measurements could be made in either spectral transmittance or reflectance. The data were acquired by a modified LabView software program, which also controlled the alternative switching of gases. Hydrogen/nitrogen mixtures with different concentrations of hydrogen were used to evaluate the response of the sensors and synthetic air (20% oxygen, balance nitrogen) was used for recovery to their initial optical state.

Results and Discussion

Several new types of materials were developed to improve sensor performance. Each has certain advantages as explained below.

Water Doped WO₃. A modification of WO₃ using water vapor as a dopant resulted in a porous sensor material with improved response time. In addition to improving the rate of hydrogen transport due to the higher water content, water doping also produces microstructural changes in the film resulting in increased porosity. Sensors using this material are sensitive down to hydrogen concentrations of approximately 200 parts per million (ppm) and display an extremely rapid initial response to hydrogen as shown in Figure 1.

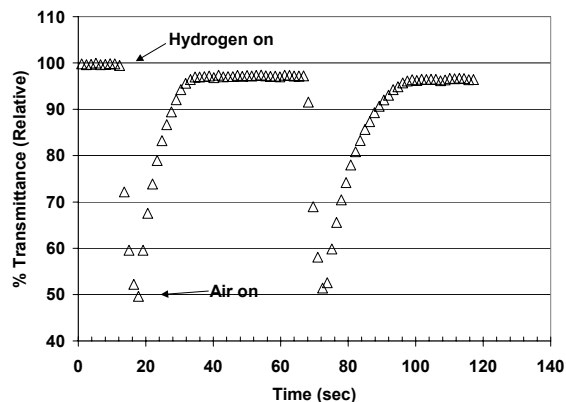


Figure 1. Optical response of Pd/WO₃ sensor to 0.1% hydrogen.

Vanadium Oxide. A new sensor design with vanadium oxide (VO_x) as the sub-layer was also developed. This sensor design utilizes the Pd/PdH_x transition to generate the optical signal, i.e. the optical properties of the Pd itself are changed upon exposure to H₂. The sensor is responsive down to approximately 0.5 percent hydrogen, and is stable even in the presence of pure hydrogen gas, whereas an unprotected Pd thin film will crack and delaminate at hydrogen concentrations above 4 percent. Representative data for the Pd/VO_x sensor is presented in Figure 2.

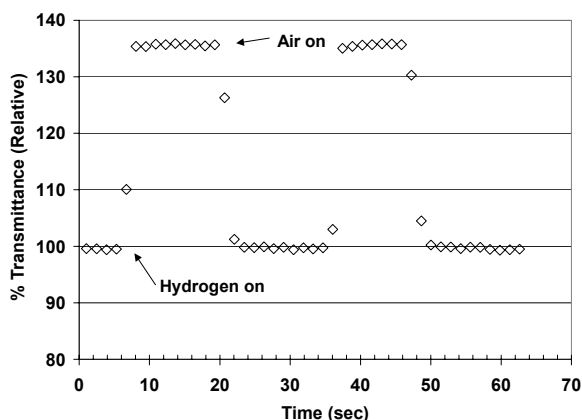


Figure 2. Optical response of Pd/VO_x sensor to 4% hydrogen.

The following mechanism has been established to explain the stability of the Pd/VO_x sensor: hydrogen is dissociated on the surface of palladium and hydrogen atoms diffuse to the interface between palladium and vanadium oxide. Vanadium oxide is reduced with the insertion of protons. During the first exposure, vanadium oxide undergoes an irreversible optical change after which the proton insertion becomes fully reversible while the color remains unchanged. At the same time, the palladium layer gives rise to an optical response due to the formation of the hydride. A high average vanadium oxidation state enhances the absorption of hydrogen in two aspects: a low chemical potential that results in a high thermodynamic driving force, and a large capacity to react with hydrogen due to the great amount of vanadium (V) species that can be reduced. The presence of a vanadium oxide layer that is capable of accepting hydrogen without optical modulation allows the palladium hydride layer to be stable over repeated hydrogen exposures at concentrations higher than 4%.

Materials for Protection of Pd Catalyst. Experiments were conducted with the new sensor materials to determine their susceptibility to selected airborne contaminants. Exposure to CO, CH₄ and H₂S was found to have a detrimental effect on sensor performance. In addition, prolonged exposure to ambient air for periods of longer than 2 days caused similar degradation. It was therefore decided to investigate ways of protecting the Pd surface from these contaminant species.

The main goals were to identify the compounds in ambient air responsible for poisoning of the Pd catalyst. A search of the literature revealed the distinct possibility that airborne hydrocarbons produced from incomplete combustion were forming a Pd-CH₃ complex on the metal surface and deactivating it towards hydrogen dissociation (6). It was decided to attempt the development of surface coatings to protect Pd from these compounds, and if possible to extend the sensor operational lifetime to 6 months. A further priority was to maintain a fast response time for the sensors.

“Dense” Organic Coating. Various coatings were investigated for protection of the Pd catalyst. These included a “dense” organic coating as well as an “active” inorganic coating. The “dense” organic coating consists of a proprietary material that has shown promise for protection of the Pd catalyst layer, essentially acting as a filtration membrane for airborne contaminants. As shown in Figure 3 an unprotected Pd/WO₃ sensor is completely unresponsive after exposure to 10 ppm H₂S, whereas a sensor with the “dense” coating still responds to hydrogen.

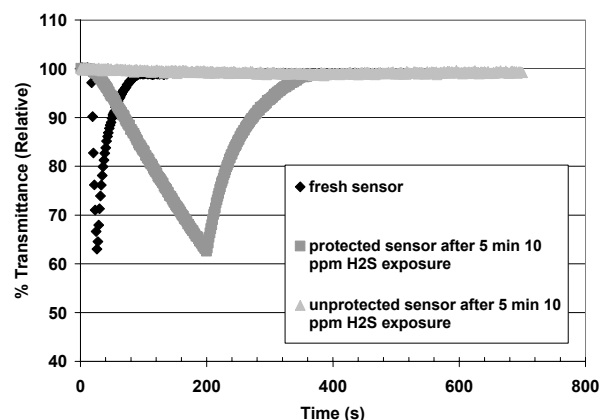


Figure 3. Optical response of Pd/WO₃ sensor with “dense” organic coating exposed to 10 ppm H₂S.

“Active” Inorganic Coating. Of the coatings studied the “active” coating (using a different proprietary material) offered the best protection. Deposition by spin coating produced a thick porous film that did not impede the diffusion of hydrogen or oxygen to the underlying films. Sensors with this “active” coating were protected for approximately two weeks before degrading, whereas unprotected sensors degraded in 1-2 days. Subsequent experiments have shown that the properties of the material in the “active” coating can be used to prevent hydrocarbons from reaching the Pd surface, thus preventing formation of the Pd-CH₃ complex and poisoning of the hydrogen dissociation sites. Sensor operational lifetimes have been extended to over 9 months. In addition, fouled sensors can be partially regenerated by application of the coating.

Figure 4 shows the optical response of a Pd/WO₃ sensor after 10 days ambient air exposure, with and without the coating. The unprotected sensor is totally inert to 0.1 percent hydrogen, but the coated sensor is still active. Figure 5 shows similar data for a Pd/VO_x type sensor after 5 days. The unprotected sensor is compromised but the coated sensor still maintains a fast response. Figure 6 shows a fouled sensor coated then monitored over a period of 65 days. After approximately 9 days the response is approaching that of a fresh sensor.

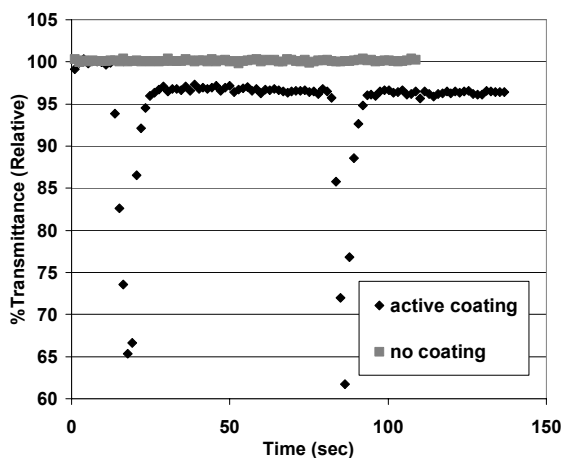


Figure 4. Optical response of Pd/WO₃ sensors tested in 0.1% hydrogen after 10 days ambient air exposure.

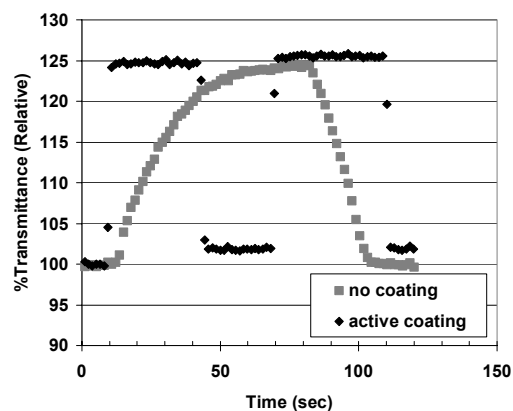


Figure 5.

Optical response of Pd/VO_x sensor tested in 4% hydrogen after 5 days ambient air exposure.

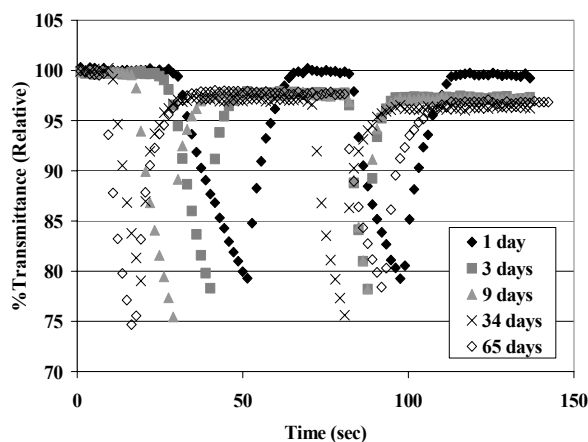


Figure 6. Optical response of fouled Pd/WO₃ sensor with "active" coating, tested in 0.1% hydrogen.

Prototype FOHS. A prototype of the FOHS suitable for field-testing has also been developed. Various designs have been evaluated and the most promising is a sensor that operates in transmittance mode using plastic collimating lenses. One possible design is presented in Figure 7, and optical data generated with a Pd/WO₃ sensor using this design is presented in Figure 8.

Assuming that the prototype sensor will behave similarly to the laboratory samples, the next logical step is to test the sensor under field conditions. Cost management and other factors will of course need to be taken into account if large-scale manufacturing is planned, but the additional elements of collimating lenses are estimated to only raise the cost per sensor to approximately \$25.

Conclusion

New, superior materials have been developed for thin film optical hydrogen sensors. Sensors using these materials display fast response times, high sensitivity and resistance to degradation caused by airborne contaminants. A minimum of further work is needed to bring the prototype sensors to the field-testing stage.

In conclusion, the work described here has taken the FOHS technology to the point where a working sensor is achievable. Further issues will undoubtedly need to be addressed as they arise,

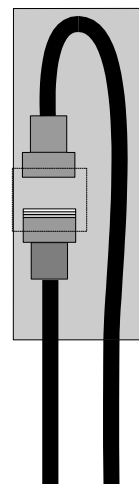


Figure 7. A possible design for the FOHS using collimating lenses.

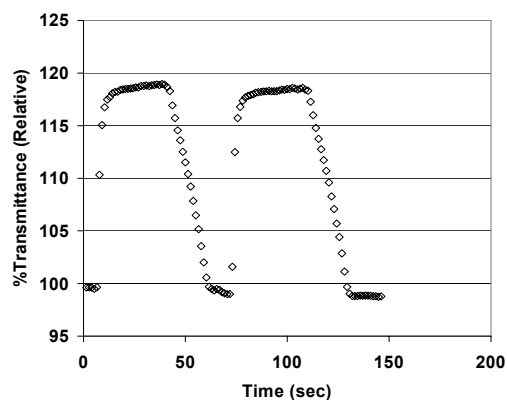


Figure 8. Optical response of prototype Pd/VO_x sensor in 4% hydrogen.

but the research performed at NREL has laid the groundwork for producing a low-cost fiber optic hydrogen sensor ready to meet the safety needs of a growing hydrogen economy.

Acknowledgment. This work was supported by the Hydrogen Program of the U.S. Department of Energy under Contract No. DE-AC-36-99-G010337.

References

1. Ito, K., and Kubo, T. *Proceedings of the 4th Sensor Symposium, Tsukuba, Japan*, **1984**, p. 153-156.
2. Benson, D. K., Tracy, C. E., Hishmeh, G. A., Cizek, P. A., Lee, S. and Haberman, D. P. *Proceedings of the SPIE International Symposium on Industrial and Environmental Monitors and Biosensors*, Boston, MA, **1998**, p. 185-202.
3. Smith II, R.D., Benson, D.K., Olson, D.L. and Wildeman, T.R. *Proceedings from SPIE Photonics West 2000 Conference*, San Jose, CA, **2000**, 3945, p. 174-184.
4. Smith II, R.D., Benson, D.K., Olson, D.L., Pitts, J.R. and Hoffheins, B.S. *Advances in Low Cost Hydrogen Sensor Technology*, *American Chemical Society Review*, Plenum Publishing Co., **2000**.
5. Smith II, R. D., Benson, D. K., Maroef, I., Olson, D. L. and Wildeman T. R. *Welding Journal* **2001**, 80 (5), p. 122s-125s.
6. Albers, P., H. Angert, G. Prescher, K. Seibold and S. F. Parker. *Chem. Commun.* **1999**, p. 1619-1620.

MEMBRANE FUEL PROCESSOR FOR HYDROGEN GENERATION: REACTOR AND PROCESS ISSUES

James R. Lattner, Gregor Kolios, and Michael P. Harold

University of Houston
Department of Chemical Engineering
S225 Engineering Building 1
Houston, TX 77204-4004

Introduction

Hydrogen-fed proton exchange membrane (PEM) fuel cells offer a modular source of power for stationary and mobile applications spanning power stations, remote sensors, soldier-power, and vehicles. Energy density and safety considerations rule out the storage and supply of hydrogen, so the widespread deployment of PEM fuel cells requires efficient, on-demand production of high purity hydrogen from liquid fuels. Technology under development involves a sequence of reaction and purification steps, typically involving fuel reforming, water gas shift conversion, and preferential oxidation.^{1, 2} These steps involve multiple units with different operating conditions and catalysts, adding undesirable complexity, weight, volume, and complexity.

In this study we evaluate the use and feasibility of a catalytic membrane reactor to generate high purity hydrogen for supply to a PEM fuel cell. The use of hydrogen-permselective membranes in fuel processing has been the focus of recent patent activity.³ The basic concept is depicted in **Figure 1**. A liquid fuel is fed to a catalytic reactor wherein the desired chemistry is carried out. The catalyst is in the form of particles or impregnated in the wall of the porous tube. The surface of the tube is coated with a hydrogen permselective membrane such as a Pd-based alloy or a molecular sieving oxide. As hydrogen is generated it is removed through the membrane to the permeate side which is maintained at atmospheric pressure (with or without sweep gas). Elevated pressure reaction provides a trans-membrane driving force for permeation of hydrogen. Removal from the reaction zone of high purity hydrogen through the permselective membrane drives the reforming to high conversion while rejecting CO, a fuel cell poison. We consider several hydrogen producing reaction systems, including:

- Direct methanol decomposition
 $\text{CH}_3\text{OH} \rightarrow 2 \text{H}_2 + \text{CO}$
- Methanol steam reforming
 $\text{CH}_3\text{OH} + \text{H}_2\text{O} \rightleftharpoons 3 \text{H}_2 + \text{CO}_2$
 $\text{CO} + \text{H}_2\text{O} \rightleftharpoons \text{H}_2 + \text{CO}_2$
 $\text{CH}_3\text{OH} \rightleftharpoons 2 \text{H}_2 + \text{CO}$
- Iso-octane steam reforming

We also consider oxidative decomposition and autothermal reforming which involve the co-feed of air with the fuel. Controlled oxidation provides the requisite energy to drive the endothermic reactions, avoiding the need to supply external energy.

Model Framework and Evaluation Strategy

We developed mathematical models of the packed-bed membrane reactor (PBMR) and catalytic membrane reactor (CMR). The PBM model was applied to the methanol decomposition system while the CMR model was applied to the methanol steam reforming. Where possible, we used literature kinetics and transport parameters. Details of the model are discussed elsewhere.⁴ The feasibility of the membrane fuel processor is determined by calculating several performance metrics, including hydrogen utilization and

productivity, device volume and membrane cost. We also developed a process-level model in which we evaluate the complete fuel processor and PEM fuel cell system. Key process issues such as energy integration, water management, and overall efficiency, are evaluated for the conventional fuel processor and membrane fuel processor systems.

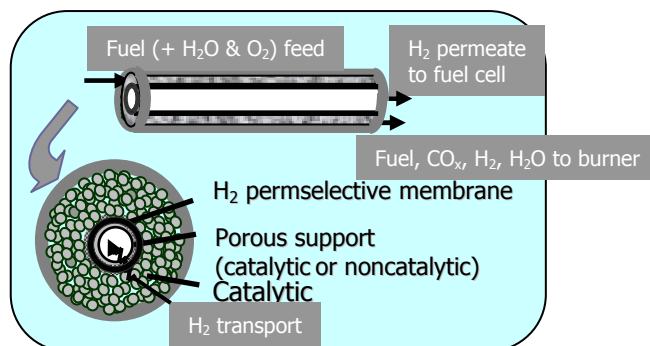


Figure 1. The membrane fuel processor involves feed of fuel to catalytic zone with hydrogen removal to atmospheric pressure stream for direct feed into fuel cell.

Results and Discussion

Methanol Decomposition. The direct decomposition of methanol to hydrogen is attractive for several reasons. Methanol is a liquid at ambient conditions and has a reasonable ratio of hydrogen to carbon. Moreover, the decomposition occurs at relatively low reaction temperature and involves a single reactant. The PBMR model considered a Pd film on the outside surface of macroporous supports (hollow tube or fiber). In the simulations we consider a defect-free Pd film thickness ranging from 1 to 100 μm deposited on commercially available ceramic hollow fibers, which afford high surface to volume. We assume isothermal operation with the permeate hydrogen at 1 atm pressure. Reaction occurs on supported Pd particles and on the Pd membrane surface, following the kinetics provided by Hara et al.⁵ We account for the site coverage by adsorbed product CO which blocks hydrogen dissolution and permeation.

Figure 2 shows the results of a simulation of the PBMR for a 10- μm thick Pd membrane supported on a hollow fiber (outer diameter 1 mm; wall thickness 0.1 mm; length 1 m). At high flow rate (high GHSV) the hydrogen production is limited by low methanol conversion. Since the hydrogen permeate is maintained at 1 atm, hydrogen may back diffuse to the reaction side at the front of the reactor. As the GHSV is decreased, the methanol conversion and hydrogen partial pressure increase. The hydrogen partial pressure exhibits a maximum at an intermediate GHSV, signaling the transition to a second regime of reduced hydrogen generation. A low feed rate limits the hydrogen productivity; here the hydrogen partial pressure approaches that of the permeate (1 atm).

Determination of the production rate of hydrogen provides guidance on determining feasibility of methanol decomposition. **Figure 3** shows the dependence of the PBMR productivity on the hydrogen utilization over a range of reactor temperatures. The productivity exhibits a maximum at an intermediate utilization; the maximum underscores the aforementioned behavior at extremes in the space velocity. Since a 50 kW_e fuel cell requires nominally 0.4 mole H₂/s, these productivities are too low (e.g. 500 liter reactor volume at 80% hydrogen utilization). Our simulations of oxidative

decomposition show that external heating can be avoided but it comes at the expense of hydrogen utilization.

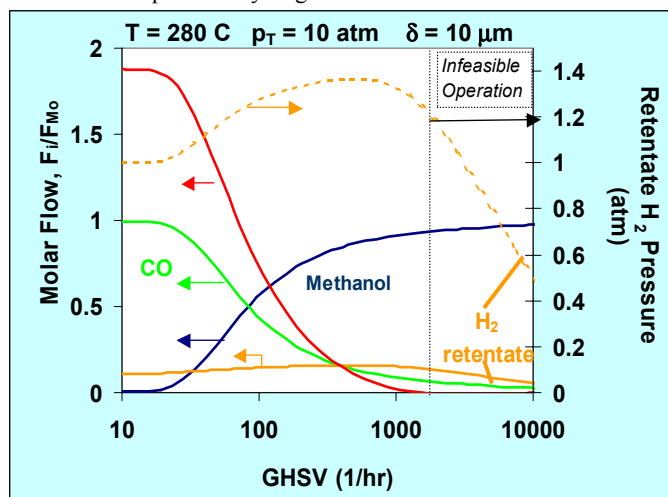


Figure 2. Dependence of the species molar flow rates and retentate hydrogen partial pressure on space velocity (GHSV) for methanol decomposition carried out at 10 atm and 280 C, using a 10 μ m thick, supported Pd membrane.

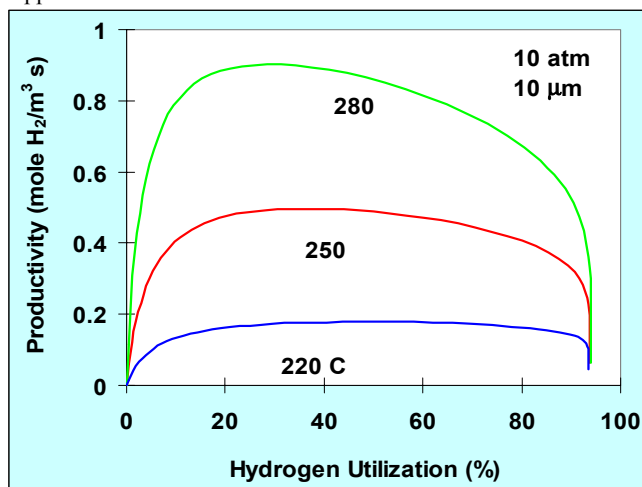


Figure 3. Dependence of the production rate of hydrogen on hydrogen utilization for methanol decomposition.

Methanol Reforming. Steam reforming of methanol is more attractive than decomposition because of the reduced CO production and the higher catalytic rates. We carried out the steam reforming of methanol in a CMR comprised of hollow fiber membranes impregnated with methanol synthesis catalyst (Cu/ZnO) and coated with a Pd-based membrane. We used a comprehensive catalytic kinetic model that accounts for methanol reforming, water gas shift, and methanol decomposition.⁶ The CMR model accounts for multi-component transport and reaction within the catalytically active support as well as site blockage by adsorbed CO. In the first set of simulations we assumed isothermal operation with permeate hydrogen maintained at 1 atm. We are currently evaluating alternative configurations, including coupled autothermal reforming and membrane fuel processing.

Figure 4 shows representative results for reaction carried out at 280 C and 5.2 bar total pressure with a methanol to water feed ratio of 0.93 and a 10 μ m thick Pd membrane. The simulations reveal a

productive membrane processor. The device volume needed for a 50 kW_e PEM exhibits a local minimum at an intermediate space velocity. For example, at a hydrogen utilization of 75% the requisite reactor volume is about 15 liters. While additional volume would be needed for external energy supply, these results are encouraging.

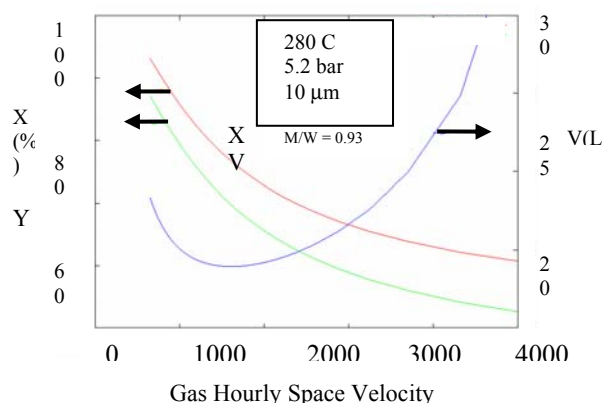


Figure 4. Simulated performance of methanol reforming in membrane processor.

Process Level Issues. We are also evaluating process-level issues of the membrane fuel processor/PEM system, focusing on energy integration, water management, sweep gas use, and overall efficiency. Process simulations of methanol and iso-octane based reforming reveals that complete fuel conversion and hydrogen recovery is unnecessary because the retentate can be combusted to provide the requisite heat for fuel vaporization and endothermic reforming. A comparison of the membrane fuel processor to the conventional system comprising reforming, WGS, and preferential oxidation reveals some notable advantages. For example, the membrane reactor delivers high purity hydrogen to the fuel cell. There are additional process simplifications regards water management and sweep gas utility.

Acknowledgment. This work was supported by the ACS Petroleum Research Fund (ACS-PRF #37053-AC9) and the University of Houston.

References

- (1) Trimm, D.L.; and Onsan, Z.I.; *Catal. Reviews*, **2001**, 43, 31.
- (2) Ogden, J.M.; Steinbugler, M.M.; Kreutz, T.G.; **1999**, *J. Power Sources*, 79, 143.
- (3) Edlund, D.; Pledger, W.A.; US Patent 6,221,117, **2001**.
- (4) Harold, M.P.; Kolios, G.; **2002**, to be submitted.
- (5) Hara, S.; Xu, W.; Sakaki, K.; Itoh, N.; **1999**, *Ind. Eng. Chem. Res.*, 38, 488.
- (6) Peppley, B.A.; Amphlett, J.C.; Kearns, L.M.; Mann, R.F.; *Appl. Catal. A.*, **1999**, 179, 31.

METAL/CERIA WATER-GAS SHIFT CATALYSTS FOR AUTOMOTIVE POLYMER ELECTROLYTE FUEL CELL SYSTEMS

Deborah J. Myers, John F. Krebs, J. David Carter, Romesh Kumar,
and Michael Krumpelt

Chemical Technology Division
Argonne National Laboratory
9700 South Cass Ave.
Argonne, IL 60439

Introduction

Polymer electrolyte fuel cell (PEFC) systems are a leading candidate for replacing the internal combustion engine in light duty vehicles. One method of generating the hydrogen necessary for the PEFC is reforming a liquid fuel, such as methanol or gasoline, via partial oxidation, steam reforming, or autothermal reforming (a combination of partial oxidation and steam reforming). The H₂-rich reformat can contain as much as 10% carbon monoxide. Carbon monoxide has been shown to poison the platinum-based anode catalyst at concentrations as low as 10 ppm,¹ necessitating removal of CO to this level before passing the reformat to the fuel cell stack.

The water-gas shift (WGS) reaction, $\text{CO} + \text{H}_2\text{O} = \text{CO}_2 + \text{H}_2$, is used to convert the bulk of the reformat CO to CO₂. Industrially, the WGS reaction is conducted over two catalysts, which operate in different temperature regimes. One catalyst is a FeCr mixed oxide, which operates at 350–450°C and is termed the high-temperature shift (HTS) catalyst. The second catalyst is a CuZn mixed oxide, which operates at 200–250°C and is termed the low-temperature shift (LTS) catalyst. Although these two catalysts are used industrially in the production of H₂ for ammonia synthesis, they have major drawbacks that make them unsuitable for transportation applications. Both the LTS and the HTS catalysts must first be “activated” before being used. For example, the copper in the copper oxide/zinc oxide LTS catalyst must first be reduced to elemental copper *in situ* before it becomes active for the WGS reaction. This reduction reaction is exothermic and must be carried out under well-controlled conditions using a dilute hydrogen stream (1 vol% H₂) to prevent high catalyst temperatures, which can result in sintering (agglomeration) of the copper particles and loss of active surface area for the WGS reaction. Also, once the catalyst has been activated by reduction, it must be protected from exposure to ambient air to prevent re-oxidation of the copper. The activated catalyst must also be protected from the condensation of liquids, for example, during start-up or transient operation. For these reasons, a more thermally rugged catalyst is needed which has sufficient activity to operate at the low temperatures that are thermodynamically necessary to achieve low CO concentrations.

No single metal, with the exception of copper, has high activity for both the dissociation of H₂O and oxidation of CO, two important elementary reaction steps for the WGS reaction.² Therefore, we are investigating bi-functional catalysts where one component of the catalyst promotes the adsorption and oxidation of CO and the other component dissociates the H₂O. The metals platinum, ruthenium, palladium, and cobalt were chosen as the CO-adsorbing component of the catalyst because they have moderate CO adsorption energies and are less prone to sintering than copper (i.e., higher melting points). The water-dissociating component was chosen to be a material that is readily oxidized and reduced at the oxygen partial pressures and temperatures encountered in the water-gas shift reactor

($p\text{O}_2 < 10^{-30}$, 180–400°C). This ready oxidation-reduction can form labile oxygen adatoms to oxidize co-adsorbed CO and release hydrogen. One such material is ceria doped with species that enhance the formation of oxygen ion vacancies. Dopant cations were chosen that promote the formation of oxygen vacancies in the ceria lattice by virtue of their lower valence state (i.e., trivalent cations) or their ability to cause strain in the ceria lattice (e.g., cations with smaller ionic radii) and promote the formation of Ce³⁺ sites. To test our hypothesis we chose gadolinium, samarium, yttrium, and praseodymium as the trivalent dopants and zirconia as a strain-causing dopant.

Experimental

The ceria and doped cerias tested as water-dissociating catalyst components are listed in Table 1. The ceria powders were either made by the glycine-nitrate process (Ceria, CZY, CZG, CZP) or purchased from Nextech (CSO) or Praxair (CGO). To briefly summarize the glycine-nitrate method, nitrates of cerium and the ceria dopants are dissolved in water and combined with glycine. This mixture is heated to evaporate the water and rapidly oxidize the nitrates. The resulting powder is calcined in air at 800°C for 2 h yielding a homogeneously doped ceria powder with a surface area of 30–60 m²/g. The active metals platinum and cobalt were dispersed on the doped ceria powders by incipient wetness of a metal solution. Platinum loadings ranged from 0.14 wt% to 1 wt%. The catalysts were dried at 80–120°C in air, and then activated by heating in either air or 4% H₂ (in helium) to convert the metal complex to elemental metal particles.

Table 1. Doped ceria compositions tested and BET surface areas before metal addition

Symbol	Composition	BET Surface Area (m ² /g)
Ceria (undoped)	CeO ₂	27.9
CGO	Ce _{0.8} Gd _{0.2} O _{1.9}	36.0
CSO	Ce _{0.85} Sm _{0.15} O _{1.925}	93.4
CZY	Ce _{0.8} Zr _{0.1} Y _{0.1} O _{1.95}	42.2
CZG	Ce _{0.8} Zr _{0.172} Gd _{0.025} O _{1.99}	59.9
CZP	Ce _{0.8} Zr _{0.172} Pr _{0.025} O _{1.99}	52.0

The WGS activity measurements were carried out with two simulated reformat feeds, one with a low CO concentration (1.02% dry) and the other with a high CO concentration (10% dry). For the low CO feed stream, the composition was 0.46% CO, 8.55% CO₂, 21.6% H₂, 55% H₂O, and bal. N₂ (Dry Basis: 1.02% CO, 19.1% CO₂, 48.2% H₂, and bal. N₂). The high CO reactant stream composition was 6.86% CO, 9.12% CO₂, 29.29% H₂, 31.43% H₂O, 1.36% CH₄, and bal. N₂ (Dry Basis: 10% CO, 13.3% CO₂, 42.72% H₂, 1.98% CH₄, and bal. N₂). A small amount of catalyst (0.1–0.3 g) was ground with a mortar and pestle and mixed with alumina powder to achieve a total sample weight of approximately 1 g. Before testing, the catalysts were reduced at 230°C for 1–2 h with 4% H₂ (in helium). To eliminate the effect of mass transfer on the measurements and to get the kinetically-limited activity, the reactor was operated in a differential mode (CO conversions <10%). The flow rate of the simulated reformat was varied to achieve carbon monoxide conversions of less than 10% in general and less than 2% for the majority of the tests. The outlet CO concentration was

determined with either Horiba (0–2 vol%) or ZRH (0–15 vol%) infrared gas analyzers. The outlet CO₂ concentration was determined using the ZRH analyzer. Outlet compositions were also analyzed with an HP 5890 gas chromatograph fitted with two J&W Scientific columns: (1) GS-MolSieve with Ar as the carrier gas for analysis of H₂, CH₄, and CO and (2) GS-Q with He as the carrier gas for analysis of CO₂. The specific surface area of the entire catalyst was determined using nitrogen adsorption BET analysis on a Micromeritics ASAP 2010. Temperature programmed reduction of the catalysts was performed using an Altamira analyzer with 3% H₂ (bal. Ar) and a ramp rate of 30°C/min.

Results and Discussion

The highest WGS activities were observed with platinum as the active metal. Given the high activity of the platinum catalysts relative to the other metals studied, a detailed study of the effect of ceria-dopant and preparation method was undertaken with platinum as the active metal. The dopants did, indeed, significantly improve the WGS activity of the ceria catalyst; the zirconia- and praseodymium-doped catalyst (CZP) showed the greatest improvement, with twice the activity of the undoped ceria catalyst (see Fig. 1). As shown in Fig. 2, the dopant effect is not merely a ceria surface area effect as the highest water-gas shift activity was observed for the CZP support with an intermediate surface area of 52.0 m²/g. The temperature-programmed reduction profiles of the 1 wt% Pt/doped ceria catalysts (Fig. 3) show that the ceria dopants cause both an increase in the extent of reduction of the ceria and a decrease in the reduction peak temperature. Based on these results, we propose that the ceria dopants are improving the water-gas shift activity of the Pt/ceria catalyst by enhancing both the number of Ce³⁺ sites available for the water dissociation reaction and the kinetics for regeneration of these sites.

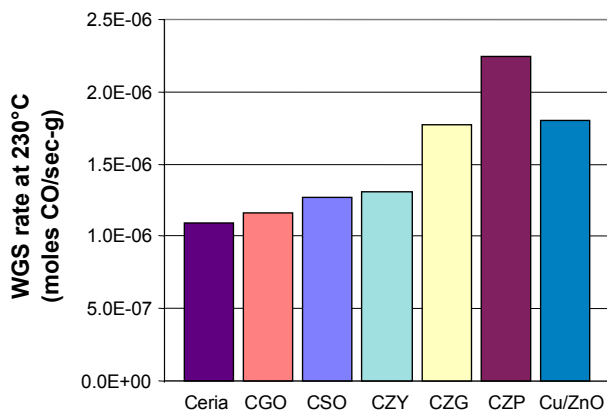


Figure 1. WGS reaction rates at 230°C for 1 wt% Pt/doped ceria catalyst powders. Cu/ZnO is Süd-Chemie Inc.'s C18-7. The reactant gas was "Low CO" reformat (see experimental section).

The WGS reaction rate was found to be independent of CO concentration from 1 to 10 mol% CO on the platinum/doped ceria catalysts. At the lower CO concentration, the 1 wt% platinum/doped ceria catalysts have WGS activities comparable to commercial Cu/ZnO. However, unlike the commercial FeCr and Cu/ZnO catalysts, this catalyst does not have to be activated by *in situ* reduction, does not lose its activity upon exposure to air at 21–550°C, and is active over a wide temperature range (180–400°C) so that it can be used effectively as both the HTS and the LTS catalyst. These

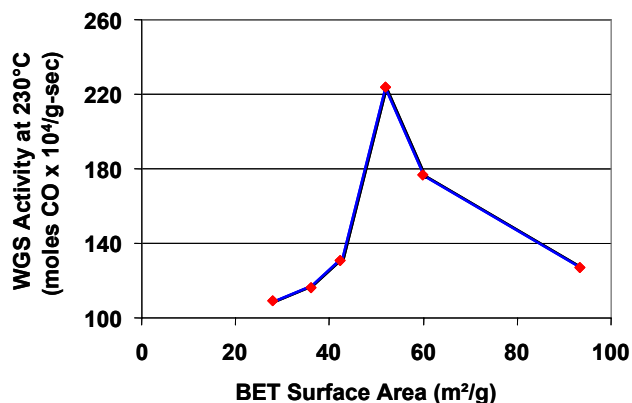


Figure 2. WGS reaction rate at 230°C for 1 wt% Pt/doped ceria catalyst powders vs. their specific surface areas.

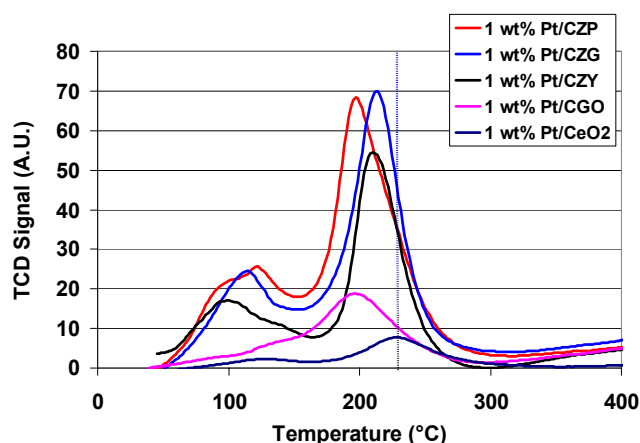


Figure 3. Temperature-programmed reduction of 1 wt% Pt/doped ceria catalyst powders illustrating the effect of the ceria dopant on the reduction behavior of ceria.

properties of the platinum/doped ceria catalysts make them suitable for use in fuel processors for transportation applications. However, the high cost of precious metals, even at loadings as low as the 0.14 wt% achieved in this work, may prohibit the use of these catalysts in light duty vehicles. Our research is now focused on replacing the platinum in these catalysts with less costly metals without sacrificing catalyst activity or durability.

Acknowledgment. This work was supported by the Office of Transportation Technologies, Office of Advanced Automotive Technologies, U.S. Department of Energy. Argonne National Laboratory is owned by the United States government, and operated by the University of Chicago under the provisions of a contract with the Department of Energy under Contract No. W-31-109-ENG-38.

References

1. Gottesfeld, S.; Pafford, J., *J. Electrochem. Soc.*, **1988**, *135*, 2651-2652.
2. Grenoble, D.C.; Estadt, M.M.; Ollis, D.F., *J. Catalysis*, **1981**, *67*, 90-102.

MODELING THE DISCHARGE BEHAVIOR OF A METAL HYDRIDE HYDROGEN STORAGE SYSTEM

Sarang A. Gadre, Armin D. Ebner, Karen D. Daniel, Shaheen A. Al-Muhtaseb, Charles E. Holland and James A. Ritter*

Department of Chemical Engineering
University of South Carolina
Columbia, SC 29208 USA

Introduction

The use of hydrogen as an energy source is receiving increasing attention in the world as the demand for environmentally cleaner fuel is on the rise. Since many metal hydrides have the ability to store hydrogen reversibly in the solid state at relatively low pressures and ambient temperature, they have the potential to serve as a safe and reliable source of hydrogen. Hence, the use of metal hydrides as a hydrogen storage material has been under consideration for many years.^{1,3-7} The Savannah River Technology Center has developed a novel metal hydride bed for transportation applications, e.g., a hybrid electric bus.¹ However, the cylindrical bed containing not only the metal hydride but also an aluminum foam for heat transfer and heat exchanger and feed tubes presents a challenge to the development of a mathematical model that can be used for design and optimization.

Therefore, the objective of this work is to develop a simple mathematical model of this unique bed that still captures the essence of the heat and mass transfer characteristics, which govern the discharge process. This model is calibrated against some preliminary discharge experiments from a hydrogen storage test facility utilizing the SRTC metal hydride bed technology. The performance of the model is evaluated in terms of its ability to predict the pressure and temperature histories during discharge.

Mathematical Model

Due to space constraints, no equations are given here, only the assumptions utilized in the model.² Hydrogenation takes place in a metal hydride when storing hydrogen and dehydrogenation takes place when releasing it. Although this charge/discharge process is classified as a reversible chemical reaction, its behavior mimics that associated with physical adsorption phenomena. Hence, the discharge process is modeled here as a fixed bed adsorption process.

The discharge process starts from a fully charged state at a constant temperature and pressure; and it is carried out at a constant molar flow rate at the discharge end. Hence, the molar flux, which is zero at the closed end, is constant at the outlet. This leads to the assumption that the flux variation inside the bed is linear. All radial gradients are also ignored, and ideal plug flow is assumed. All heat transfer processes between the material and the surroundings are lumped together and accounted for by an overall heat transfer coefficient. The effect of mass transfer/reaction resistance is accounted for by a linear driving force (LDF) approximation.

Experimental

A schematic representation of the metal hydride hydrogen storage test facility is shown in **Figure 1**; design and construction details are given elsewhere.^{1,4} Sixteen surface thermocouples were placed at four angular locations and at four axial positions as shown. Thermocouples were also positioned to measure the temperatures of the water entering and leaving the U-tube heat exchanger, and the hydrogen discharge. A mass flow controller was used to measure and control the hydrogen charge and discharge flow rates. Due to the complexity of the internal design of this bed, these thermocouples helped in assessing the axial temperature gradients, along with the the

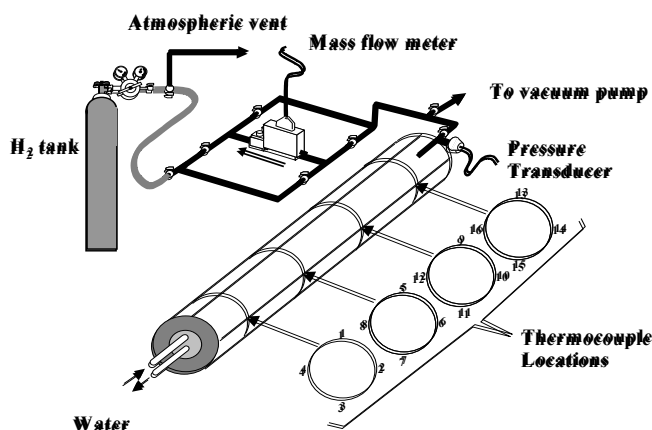


Figure 1. Schematic of the hydrogen storage test facility.

internal distribution of the metal hydride. For the preliminary runs presented here, the water flow rate through the heat exchanger was maintained at 5 gpm. The pressure inside the bed was measured at the bed outlet using a pressure transducer. The temperatures, flow rates and pressures were monitored continuously with a data acquisition system.

The bed was filled initially with hydrogen at around 100 SLPM to the desired pressure. Since this caused the bed to heat up, it was allowed some time to equilibrate at the desired pressure and ambient temperature. The bed was then discharged at a constant molar flow rate (5-40 SLPM) and the pressure and temperatures were recorded continuously, until the desired molar flow rate was no longer sustainable as the bed became depleted of hydrogen. The operating conditions and model parameters are summarized in **Table 1**.

Table 1. Operating Conditions and Parameters	
bed diameter (m)	0.09
bed length (m)	1.52
metal hydride density (kg/m ³)	8700
metal hydride weight (kg)	26.078
porosity	0.69
gas specific heat (kJ/kg/K)	14.42
solid specific heat (kJ/kg/K)	0.419
H ₂ discharge flow rate (SLPM)	5-40
ambient temperature (K)	292-295
initial temperature (K)	292-295
initial pressure (atm)	17-25
mass transfer coefficient	0.08
heat transfer coefficient (W/cm ² /K)	2.609x10 ⁻³

Results and Discussion

One of the key inputs to the mathematical model is the pressure-composition temperature (PCT) relationship. **Figure 2** shows the correlation of a composite Langmuir isotherm model to the hydrogen-Lm_{1.06}Ni_{4.96}Al_{0.04} system in terms of the loading (q) as a function of pressure (P). Clearly, this model correlates very well with the experimental data at both temperatures. Hence, this relationship was used in the model to predict the PCT behavior of this system over a wide range of conditions.

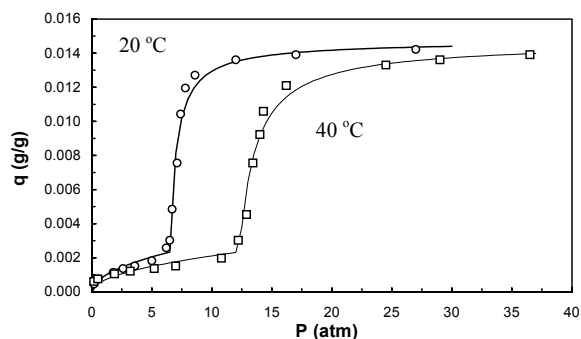


Figure 2. Correlation of a composite Langmuir isotherm model to the hydrogen-Lm_{1.06}Ni_{4.96}Al_{0.04} system.

Six preliminary discharge runs were carried out with the hydrogen storage test facility, with hydrogen demands of 5, 10, 15, 20, 25, and 40 SLPM. The 20 SLPM run was chosen arbitrarily to determine the heat and mass transfer coefficients, the only adjustable parameters in the model, that best fit the experimental pressure history. The results of this fit are presented in **Figure 3**, along with the prediction of the pressure histories for the 5 and 40 SLPM runs. These predictions were made without adjusting the heat and mass transfer coefficients obtained from matching the 20 SLPM run with

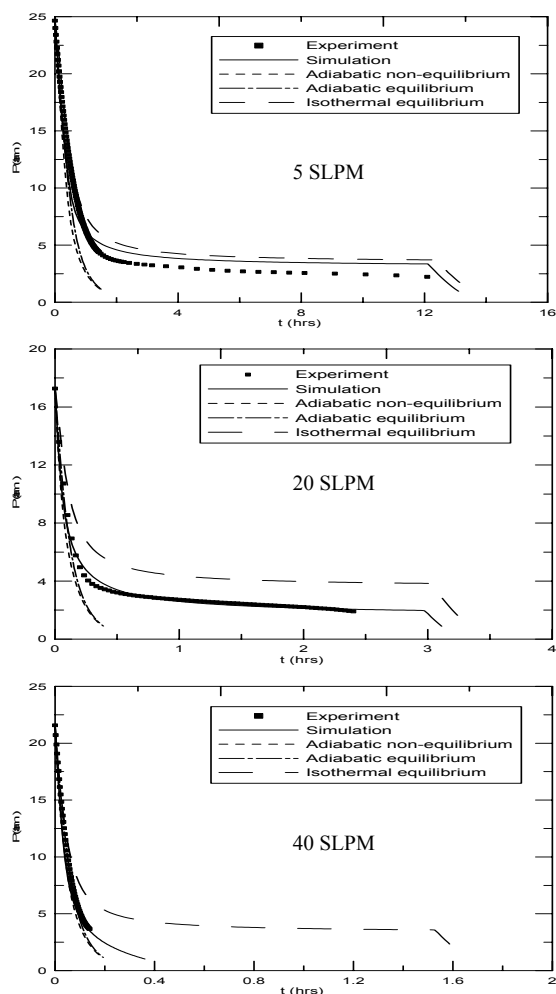


Figure 3. Comparison of the experimental pressures histories with different model predictions during discharge at 5, 20 and 40 SLPM.

the experimental data. The simulation curves correspond to the fitted heat and mass transfer coefficients. The isothermal and adiabatic model predictions used values of infinity and zero for the heat transfer coefficient, respectively; and the equilibrium model predictions used a value of infinity for the mass transfer coefficient, whereas the non-equilibrium cases used the fitted value. The same set of heat and mass transfer coefficients was able to fit the experimental data reasonably well over a wide range of hydrogen flow rate demands. This result was very encouraging. It was also interesting to compare the results with the extreme limits in both parameters. The isothermal-equilibrium model did reasonably well in predicting the pressure discharge curves at low flow rates, but with increasing deviation as the flow rate demand increased. This result suggested that isothermal and equilibrium conditions prevailed at long times during discharge at low flow rates, only. The adiabatic-non-equilibrium and adiabatic-equilibrium curves merge and under predict the experimental data at long times.

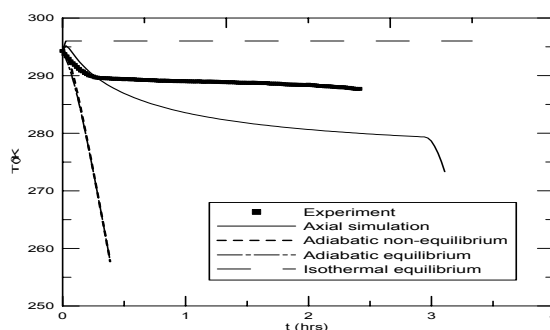


Figure 4. Comparison of the experimental temperature history with different model predictions during discharge at 20 SLPM.

Figure 4 presents the predictions of the temperature histories for the 20 SLPM run. Note that the sixteen thermocouples located on the external surface of the bed revealed that axial gradients did not exist in this system; however, slight differences were noticed at each of the circumferential positions. Hence, the average of all the axial temperatures at a given angular location were plotted along with the simulation. This model was not capable of matching the average experimental temperature history with the same accuracy as the pressure discharge. Similar results were obtained for the other runs. This result suggested the need to develop a model that incorporates a radial temperature distribution inside the bed, which is being done

Acknowledgements

Financial support provided by the National Reconnaissance Office under contract NRO-00-C-0134 is greatly appreciated.

References

1. Heung, L. K. *Hypothesis II conference proceedings*, Norway, **1997**, 1.
2. Lamari, M.; Aoufi, A.; and Malbrunot, P. *AIChE J*, **2000**, 46, 632.
3. Mat, M. D.; and Kaplan, Y. *Int. J. Hydro. Energy*, **2001**, 26, 957.
4. Levesque, S.; Ciureanu, M.; Roberge, R.; and Motyka, T. *Int. J. Hydro. Energy*, **2000**, 25, 1095-1105.
5. Das, L. M. *Int. J. Hydro. Energy*, **1996**, 21, 789-800.
6. Jemni, A.; Nasrallah, S. B.; and Lamloumi, J.; *Int. J. Hydro. Energy*, **1999**, 24, 631-644.
7. Nakagwa, T.; Inomata, A.; Aoki, H.; and Miura, T. *Int. J. Hydro. Energy*, **2000**, 25, 339-350.

Monte Carlo Modeling and Lab Scale Reactor Design of Hydrogen Storage Vessels and Purifiers

James R. Brenner

Florida Tech Chemical Engineering Department, 150 West University Blvd., 210 Olin Engineering Bldg., Melbourne, FL 32901

Abstract

Designs for lab-scale hydrogen storage vessels and hydrogen purification vessels that can be fully mass- and energy-balanced in real time will be presented. The vessels are small enough such that they can be loaded and unloaded safely inside an inert gas-filled glovebox, and can be readily hooked up to liquid nitrogen porosimetry, chemisorption, and temperature-programmed desorption equipment. Because of this, the hydrides can be readily be characterized *in situ*, which is important considering the air- and moisture-sensitivities of metal hydrides.

When a metal foam is inserted into a hydrogen storage vessel as a heat transfer medium, one can see rather marked increases in hydrogen transfer rates. These experimental results are confirmed by Monte Carlo simulations of the process dynamics. Early results from Monte Carlo simulations of the flux of hydrogen through a hydrided palladium membrane suggest a half-order in hydrogen dependence as predicted by Sievert's Law at low hydrogen pressures. At higher pressures, the dependence of flux on hydrogen pressure appears to increase somewhat. In addition, the separation factor for hydrogen isotopes is consistent with experimental data.

Introduction

The storage of H_2 inside metal hydrides and more recently carbon nanofibers has been intensely studied over the years, with extreme emphasis on maximizing hydrogen density, and has been nicely summarized in an article by Dresselhaus [1] and a Department of Energy report by Sandrock [2]. Lowering the weight of environmentally-friendly vehicles is certainly an important consideration, but customers will also be interested in the amount of time that it takes to fuel their vehicle and how fast their vehicle can go. Both of these latter considerations are related to the far less-discussed subject of dynamics of surface hydrogen adsorption and desorption and diffusion-related bulk hydrogen absorption and desorption. Frequently, such properties are strongly affected by heat and mass transfer limitations.

The use of on-board methanol or gasoline reformers is also being considered by several automakers for the next generation of vehicles. One major concern is that hydrogen generated from this reforming will have impurities that severely limit the life of a fuel cell also expected to be part of such vehicles. One way of dealing with such an impure stream would be to filter the H_2 via selective permeation through a membrane. It has long been known that metal hydrides, most notably Pd hydrides, can be used to purify H_2 from gases used in microelectronics manufacturing [3] such as SiH_4 and from other hydrogen isotopes [4]. Metal hydrides represent one of several types of interstitial compounds. Interstitial compounds are defined by their ability to absorb (not adsorb) significant quantities of hydrogen, nitrogen, carbon, boron, and sometimes even oxygen into the bulk of the solid in the forms of hydrides, nitrides, carbides, borides, and hydrates, respectively.

What has not been as well studied is the purification of hydrogen from streams containing CO , CO_2 , H_2O , H_2S , and NO_x using metal hydride membranes. Thus, in theory, any molecule that is a combination of H, C, N, and O could diffuse through the bulk of a metal hydride membrane and be a source of impurities in the "purified" H_2 stream. Even the sulfur-containing molecules are

possible contaminants in the product stream from a metal hydride-based H_2 purifier, when one considers grain boundary diffusion. Furthermore, the binding strength of the sulfur-containing molecules and perhaps others may be high enough that the membrane surface becomes covered with contaminants and is no longer able to perform its hydrogen purification function. Given the complexity of the feed stream, the variety of binding energetics of each of the molecules to the surface, and the variety of diffusion rates through a metal hydride purifier, it is difficult to see which effects are important.

Hydrogen Storage Vessel Design

The lab-scale hydrogen storage vessel shares many features with one pilot-tested by Brenner and Klein at Westinghouse Savannah River Company [5]. As seen in Figure 1 below, the reactor is a stainless steel cylinder that is 7 inches long and 1.90 inches in outer diameter (1 1/2" Schedule 40 pipe). One end of the reactor has a 1-inch VCR plug. This is where the metal hydride powder is loaded and unloaded through. The other end has four 1/4" OD tubes coming out, as well as a custom thermocouple probe and two heater wells. Each of these components will be discussed individually in the following section. All gas lines handling hydrogen are constructed of 316 stainless steel with Cajon VCR fittings. The wiring connectors for pressure transducers and thermocouples and the compressed air for air-actuated Nupro VCR shutoff valves can be disconnected before loading and unloading metal hydride from the hydrogen storage vessel. The fully assembled vessel with accompanying valves, pressure transducers, and rupture disk holder is shown in Figure 2.

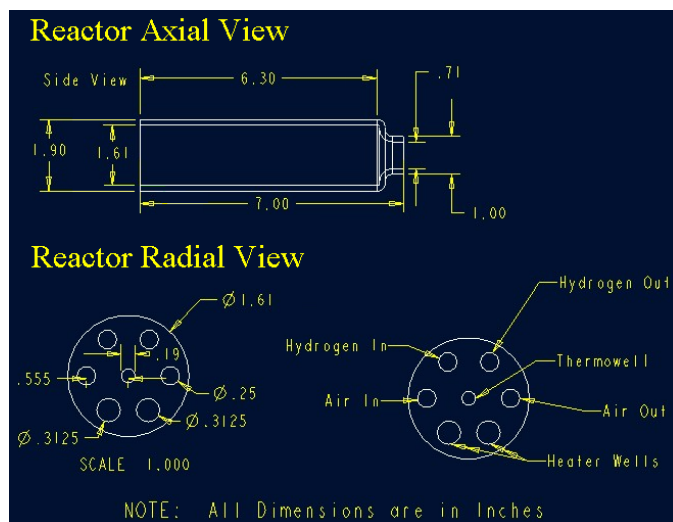


Figure 1. Axial and radial H_2 storage bed profiles

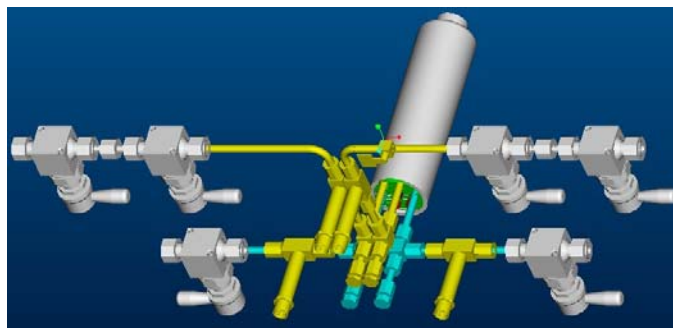


Figure 2. ProEngineer model of a hydrogen storage vessel with accompanying valves, pressure transducers, and thermocouples.

Before the hydrogen stream enters the reactor, it goes through two air-actuated shutoff valves passes through an in-line pressure transducer into a union tee with brazed thermocouple before entering the vessel. Once inside the vessel, the hydrogen flows out of a gas filter tubes into the vapor space above the metal hydride powder. The exiting gas passes through an identical gas filter tube, past a thermocouple and through a pressure transducer before reaching two air-actuated shutoff valves. In a hydrogen purifier, these gas lines replaced with a permeable hydride membrane inlet and a 316 stainless steel 1/4" tube outlet.

A heat exchanger tube goes down the length of the reactor, turns around and comes back out. SWAGELOK components may be used here. There is only a single-valve isolation system on the heat exchange line, since leaking is not a major concern. The heat exchange fluid (typically air, but sometimes LN₂) also goes through the valve, a pressure transducer, and then a union tee with a brazed thermocouple before entering the reactor. When it exits, the heat exchange fluid goes through the same components as it did when it entered the reactor, but in reverse order.

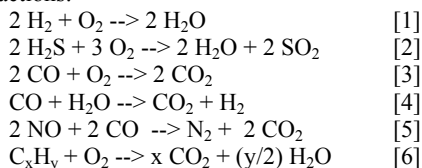
A custom-made 1/8-inch thermocouple probe goes down the center of the reactor for the entire length of the reactor. This thermocouple probe (Omega) consists of three equally spaced temperature measurement sites. This is used to measure the temperature along the length of the reactor. There are also two heater wells along the bottom of the reactor. These heater wells are 5/16-inch OD, $0.247 \pm_{0.000}^{0.005}$ -inch ID tubes that go down the length of the reactor and are reamed to fit a heater inside of it. The cartridge heater inside is nominally 1/4-inch OD, but exactly 0.248-inches.

Also inside the vessel is an aluminum foam made by ERG Aerospace. Insertion of such an aluminum foam resulted in a five-fold increase in hydrogen absorption and desorption rates experimentally. This has been confirmed via simulation as well.

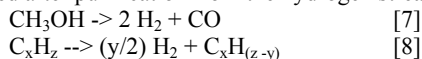
Monte Carlo Simulation Model of a Hydrogen Purifier

The probabilistic simulation consists of comparing a random number against a transition probability, with the transition probability for a first-order reaction being represented by $1 - e^{-kt}$, where t is time and k is a rate constant for a given transition. For second order reactions, the rate constant, k , is replaced by a rate constant and a concentration or pressure.

In order to simulate the lifetime performance of a hydrogen purifier downstream of an on-board catalytic reformer but upstream of a hydrogen fuel cell, it is necessary to account for all of the molecules that the purifier might see. In general, the hydrogen purifier might see any molecule that a current catalytic converter might see. Certain noble metals such as Pt, Rh, and Pd are capable of performing catalytic conversion of automobile exhaust via the following reactions:

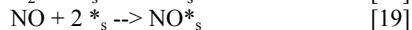
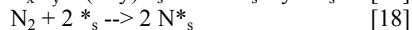
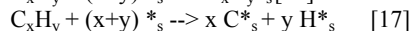
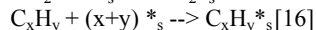
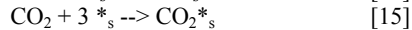
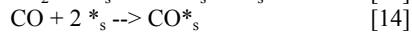
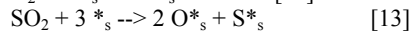
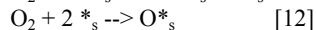
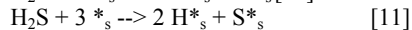
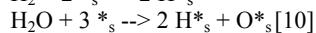
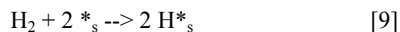


In addition to reactions 1-6, an on-board reformer will have reactions 7 and 8, depending on whether methanol or gasoline is used as a hydrocarbon source, with the hydrocarbon product from reaction 8 getting burned after purification from the hydrogen stream.



During reactions 1-8, it is well known that dissociative adsorption of H₂, H₂O, H₂S, O₂, and SO₂ on the metal surface. Nitride and carbide

formation over numerous transition metals can happen, albeit at very high temperatures, from mixtures of N₂ and H₂ or CH₄ and H₂. Carbide formation with more complicated hydrocarbons than methane must happen at least to a limited extent. Otherwise, there would be no coke overlayer on top of noble metal catalysts used in fluidized catalytic cracker units in petroleum refineries. Thus, in the Monte Carlo model, rate expressions for the dissociation of N₂ and hydrocarbons will be included. Hydrocarbons can also adsorb via molecular adsorption. All other molecules will be assumed to adsorb molecularly in all cases. A further assumption of the Monte Carlo model is that the number of metal surface sites covered by each molecule is one for each atom in the molecule (i.e. CO₂ will occupy three sites, even though it is presumed not to dissociate on the metal surface.). Thus, the surface adsorption model can be summarized as follows.



The surface desorption model presumes that adsorption steps 9-19 are reversible. In addition, it is possible over several late transition metals, most notably Fe and Rh, for surface N and surface H to recombine to form NH₃. Also possible are recombinations of surface C with either surface H to form methane, as observed during regeneration of noble metal catalysts, or with surface O to form either carbon monoxide or carbon dioxide, as observed during combustion. The permeation flux for each species is calculated as the sum of the permeation flux through the bulk of the solid via the interstitial sites, and a flux via grain boundary diffusion.

Hydrogen Purifier Simulation Results and Discussion

Validation of the Monte Carlo hydrogen purifier model has been done by comparing separation factors as a function of reciprocal temperature for the purification of deuterium, D₂, from the protium version of hydrogen, H₂, with data obtained at Westinghouse Savannah River Company [4]. In both cases, the relationship between separation factor and reciprocal temperature is nearly linear. The separation factor is equal to the ratio of the equilibrium constants between each of the gases and the solid hydride, if equilibrium is assumed. What this means is that the difference in Gibbs free energies between hydrogen isotopes is almost independent of temperature, meaning that the entropic term is basically the same for each of the isotopes. Simulation of the hydrogen purifier model with the full reaction chemistry described in reactions 9-19 is in progress.

References

- (1) Dresselhaus, M.S.; Dresselhaus, G. *Adv. Phys.* **1981**, *30*, 139.
- (2) Sandrock, G., "State-of-the-Art Review of Hydrogen Storage in Reversible Metal Hydrides for Military Fuel Cell Applications", US Navy Contract #N00014-97-M-001, July 24, **1997**.
- (3) http://www.purehydrogen.com/home/en/all/papers/white/pe_paper01.html
- (4) Lee, M.W. "Metal Hydrides for Hydrogen Isotope Separation," *Metal Hydrogen System Symposium*, Stuttgart, Germany, Sept. 4-9, **1988**.
- (5) Brenner, J.R.; Klein, J.T. In-Bed Accountability, Cooling Jacket, and Jacket Heat Transfer Analysis of a Passively Cooled Electrically (PACE) Heated Hydrogen Storage Vessel (U). *USDOE Report WSR-TR-98-00220*, Savannah River Site, Aiken, SC, **1998**.

A NEW OXYGEN SENSITIVITY IN PHOTOSYNTHETIC H₂ PRODUCTION

James W. Lee and Elias Greenbaum

Chemical Sciences Division
Oak Ridge National Laboratory
Oak Ridge, TN 37831-6194

We have discovered a new competitive pathway for O₂ sensitivity in algal H₂ production that is distinct from the O₂ sensitivity of hydrogenase per se. This O₂ sensitivity is apparently linked to the photosynthetic H₂ production pathway that is coupled to proton translocation across the thylakoid membrane. Addition of the proton uncoupler FCCP eliminates this mode of O₂ inhibition on H₂ photoevolution. This newly discovered inhibition is most likely due to background O₂ that apparently serves as a terminal electron acceptor in competition with the H₂ production pathway for photosynthetically generated electrons from water splitting. This O₂-sensitive H₂-production electron transport pathway was inhibited by DCMU. Our experiments demonstrated that this new pathway is more sensitive to O₂ than the traditionally known O₂ sensitivity of hydrogenase. This discovery provides new insight into the mechanism of O₂ inactivation of hydrogenase and may contribute to the development of a more-efficient and robust system for photosynthetic H₂ production.

Algal photosynthetic hydrogen (H₂) production by light-activated water splitting is a potentially clean energy resource. However, compared to our knowledge of the pathway of atmospheric carbon dioxide reduction, and in spite of the potential importance of the hydrogen-producing reaction, relatively little is known concerning the mechanistic pathway of electron flow in hydrogen-producing algae. In green algae, such as *Chlamydomonas reinhardtii*, photoevolution of H₂ and O₂ occurs in the same cell, where the photosynthetically produced O₂ can inhibit the production of H₂ (1). Therefore, the application of green algae for H₂ production must address the problem of O₂ sensitivity. Historically, this O₂-sensitive phenomenon was generally interpreted as the direct O₂-inhibition of hydrogenase activity (2). We report here that the classic interpretation of O₂ sensitivity should be revised. In recent experiments that characterized O₂ tolerance in H₂-producing wild-type *Chlamydomonas reinhardtii*, we observed a new O₂ sensitivity that is clearly distinct from that of classical O₂ inhibition of hydrogenase. The O₂ sensitivity indicates there is a competitive electron transport pathway that can redirect electrons from the hydrogenase-catalyzed H₂-production pathway to O₂. That is to say, suppression of H₂ evolution in the presence of low-level background concentrations of O₂ is due to the drain of reducing equivalents away from the hydrogenase pathway and towards the reduction of O₂. Our experiments demonstrated that the competitive pathway mechanism is more sensitive to O₂ than the classic O₂ sensitivity of hydrogenase and can be suppressed by proton uncoupler FCCP.

First evidence of the new O₂ sensitivity was obtained from H₂ production assays in *Chlamydomonas reinhardtii* wild-type strain 137c. The assays were conducted using a laboratory-built dual-reactor flow detection system (3). For each assay, 35 ml of algal sample (3 g Chl/ml) was placed and sealed in each of the two water-jacketed reactors and held at 20°C with a temperature-controlled water bath. The algal sample was purged with a helium flow (50 ml/min) through the liquid reaction medium. The helium flow served two purposes: (1) to remove O₂ from the algal sample

to establish and maintain anaerobic conditions that are necessary for induction of the algal hydrogenase activity and production of H₂ and (2) to carry the photoproduct H₂ gas product to the hydrogen sensors. After induction of hydrogenase and establishment of steady-state photoevolution of H₂ under the helium atmosphere (which requires about 8 h), a primary standard of 1000 ppm O₂ in helium replaced the pure helium at the same flow rate (50 ml/min) to characterize the oxygen sensitivity of photoevolution of H₂. Actinic illumination of 100 :E≡m⁻² ≡s⁻¹ for the H₂ photoevolution assay was provided by an electronically controlled LED light source at wavelength of 670 nm. As illustrated in Fig. 1, introduction of 0.1000% (1000 ppm) O₂ dramatically reduced the rate of algal H₂ photoevolution. The steady-state H₂ production rate in the presence of 0.1000% O₂ was 0.33 :mol H₂ ≡mg Chl¹¹ ≡h¹¹ which is only about 2.8% of the full steady-state rate (12 :mol H₂ ≡mg Chl¹¹ ≡h¹¹) before the introduction of the 0.1000% O₂. In the past, this type of H₂ production decay was commonly interpreted as the inhibition of hydrogenase activity by O₂. Our results prove that this classic interpretation of oxygen sensitivity on algal H₂ production is not consistent with the data. According to the classic interpretation, the decrease in H₂ production after the introduction of 0.1000% O₂ is due to O₂ inhibition of hydrogenase per se: that is, loss of hydrogenase activity is the limiting factor for the rate of H₂ photoevolution. If this interpretation were correct, after a brief dark period in the presence of 0.1000% O₂, one would expect the rate of H₂ photoevolution to be no higher than the inhibited rate (0.33 :mol H₂ ≡mg chl¹¹ ≡h¹¹) preceding the dark interval. However, the data are quite different from the classic expectation. As shown in Fig. 1, there was a surge of H₂ photoevolution after a 2-h dark period in the continuous presence of 0.1000% O₂. The peak rate of H₂ photoevolution was about 15 :mol H₂ ≡mg Chl¹¹ ≡h¹¹, which is about 45 times higher than the classically predicted rate (0.33 :mol H₂ ≡mg Chl¹¹ ≡h¹¹) and well outside the experimental error of the measurement. This assay has now been repeated 6 times and all results were consistent with the observation presented in Fig. 1.

This observation clearly indicated that hydrogenase activity was not the limiting factor for H₂ photoevolution at this level of O₂. There must be an alternative electron transport pathway that takes the photogenerated electrons away from ferredoxin (Fd) to O₂. The observed reduction of H₂ production after the introduction of 0.1000% O₂ can be explained by such a pathway that competes for electrons with the Fd/hydrogenase-catalyzed H₂-production pathway. This is a significant discovery since it fundamentally redefines the meaning of "oxygen tolerance" in algal H₂ production.

Studies with the chemical inhibitor (DCMU) and proton uncoupler (FCCP) yielded additional evidence for the new O₂ sensitivity. FCCP is a proton uncoupler that can dissipate the proton gradient across the thylakoid membrane in algal cells. As illustrated in Fig. 2, in the presence of 1000-ppm O₂ after the induction of the hydrogenase enzyme, the steady-state photoevolution of H₂ around the time of 20:00 hours was slightly less than 1 :mol H₂≡mg Chl¹¹≡h¹¹ (cf. Fig. 1 at ~110 h). After a brief dark period (from 20:20 to 22:20), a burst of H₂ photoevolution appeared, followed by an oscillation in the decay curve. Since both the actinic intensity and the background O₂ concentration (1000 ppm) remained the same, this H₂-production oscillation also indicated that the decay in the rate of H₂ photoevolution resulted not from O₂ inhibition of the hydrogenase enzyme per se but from a competitive kinetic effect of O₂ on

electron transport that is related to the H₂-production process. Addition of 5 :M FCCP produced a dramatic removal of O₂ inhibition on H₂ photoevolution. The rate of H₂ production rose to about 16 :mol≡mg Chl¹¹≡h¹¹. This FCCP-stimulated H₂ production is clearly photo-dependent. As soon as the actinic light was turned off, H₂ production stopped. The data (Fig. 2) also demonstrated that FCCP-enhanced photoevolution of H₂ can last for more than four hours although at a decreasing rate. The decrease in rate of H₂ photoproduction is due to a secondary effect of FCCP known in the photosynthesis research literature as the ADRY effect in which FCCP gradually inhibits PSII activity by deactivation of the photosynthetic water-splitting complex in the S₂ and S₃ states (4). However, FCCP does not have any known effect on hydrogenase per se. Therefore, the observed stimulation of H₂ photoevolution by FCCP in the presence of 1000 ppm O₂ clearly demonstrated that the newly discovered O₂-sensitive electron transport pathway requires the presence of a proton gradient (or ATP) to operate.

DCMU is a chemical inhibitor that binds at the Q_B site of Photosystem II (PSII) and blocks transport of electrons acquired from PSII water splitting to Photosystem I (PSI). The experimental data (not shown) demonstrated that addition of DCMU inhibited the burst of H₂ photoevolution after a dark period in the presence of 1000-ppm background O₂. This result indicated that over 90% of the electrons that are used in the photoproduction of H₂ are derived from PSII water splitting. Therefore, water is the main source of electrons for the H₂ burst after the dark period in the presence of 1000 ppm O₂. Organic reserves such as starch are therefore not the main source of electrons in this mode of H₂ production.

There is an active research effort aimed at isolating H₂-producing, O₂-tolerant mutants of the green alga *Chlamydomonas reinhardtii* (5,6). Using classical chemical mutagenesis and metronidazole-selection techniques, a number of H₂-producing O₂-tolerant mutants of *Chlamydomonas reinhardtii* (e.g., 155G6, 141F2, 76D4, and 104G5) have been recently generated at the National Renewable Energy Laboratory (NREL). According to short-term O₂-tolerance assays, mutants 76D4 and 141F2, respectively, had four and nine times higher O₂ tolerance respectively than did the wild-type parental strain. Mutant strains 104G5 and 155G6 reportedly have an O₂ tolerance 13 times higher than that of the wild-type parental strain (7). However, under continuous steady-state exposure to 0.1% O₂, none of the mutants displayed improved rates of hydrogen production. A typical experimental result is presented in Fig. 3 for mutant strain 155G5 and its wild-type parent 137c. When the carrier gas was shifted from pure helium to 1000-ppm O₂ in helium, H₂ photoevolution decayed at essentially the same rate—from about 13 to 1 :mol H₂ ≡mg Chl¹¹≡h¹¹—in both mutant 155G6 and the wild type 137c. This result indicates that mutant 155G6 does not possess improved O₂-tolerant properties under long-term steady-state conditions. However, the burst (initial rate) of H₂ production immediately following the onset of actinic illumination after a 2-h dark period was occasionally higher in 155G6 than in 137c. The observed higher initial rate in 155G6 compared with that of 137c seems consistent with results of the reported short-term O₂-tolerance assays, which may reflect O₂ tolerance of the hydrogenase per se. The H₂ photoevolution (Fig. 3) showed that the spike was often followed by a quick oscillation (which can be seen on an expanded time scale) and then a steady decay in the rate of H₂ production in both 155G6 and 137c. Also, both strains responded to the addition of 5 :M FCCP and resulted in dramatic relief of O₂ inhibition on H₂ photoevolution. The similarities between 155G6 and 137c in

response to the continuous background (1000-ppm) of O₂ as well as the addition of FCCP suggested that the observed inhibition of steady-state H₂ photoevolution was due to the newly discovered competitive oxygen pathway, not the classical inhibition of hydrogenase per se.

The new O₂ sensitivity was further characterized using a series of O₂ concentrations: 10, 100, 300, 1000, 5000, and 10,000 ppm O₂ in helium. The experimental results showed that introduction of 100-ppm O₂ had no significant effect on the steady-state rate of H₂ photoevolution in 137c. However, addition of 300-ppm O₂ began to show an effect. Figure 4 plots percentage of steady-state H₂-production rate vs. background O₂ concentrations in the mutant 141F2 and the wild-type 137c. These results indicate that compared with wild type, mutant 141F2 does not possess improved O₂-tolerant properties under these steady-state conditions. Therefore, with respect to this newly reported O₂ sensitivity, mutant 141F2 showed no greater tolerance to O₂ than its wild-type parental strain 137c. The O₂ concentration that gave 50% inhibition of H₂ photoevolution was about 500 ppm for both the mutant and the wild type. When the O₂ concentration was raised to 5000 ppm, the inhibition on H₂ production was dramatic and the rate of H₂ photoevolution decreased to nearly zero (Fig 4 and 5). However, the hydrogenase in the algal cells was still active even after the continued presence of 5000 ppm O₂ for more than 10 h. When the actinic was turned on again after hour 198, a small peak of H₂ photoproduction was observed. As illustrated in the expanded scale (inset to Fig. 5), this H₂ photoproduction peak was clearly above the background noise and/or dark-H₂ signal, indicating the presence of active hydrogenase in the algal cells. Therefore, hydrogenase in the wild-type cells can tolerate up to 5000 ppm O₂. The newly discovered O₂ sensitivity is about 10 times more sensitive to O₂ than that of the hydrogenase.

The new O₂ sensitivity is apparently linked to the photosynthetic H₂ production pathway that is coupled with proton translocation across the thylakoid membrane. Addition of the proton uncoupler FCCP can eliminate this mode of O₂ inhibition on H₂ photoevolution. This O₂ inhibition on H₂ production is most likely due to the competitive uptake of reducing equivalents by background O₂, with the H₂ production pathway for photosynthetically generated electrons from water splitting. The O₂-sensitive H₂-production pathway can be inhibited by DCMU. Our experiments demonstrated that the competitive pathway is more sensitive to O₂ than the classic O₂ sensitivity of hydrogenase. These findings redefine the meaning of “oxygen tolerance” in algal H₂ production. As discussed above, this O₂ sensitivity apparently represents a new pathway in the photosynthetic H₂ production that is coupled with proton translocation across the thylakoid membrane. As illustrated in Fig. 6A, the site for the reduction of O₂ could be at the RuBisCo enzyme, that can serve as both a RuDP (also known as RuBP) carboxylase and/or a RuDP oxygenase in the Calvin cycle. Under conditions for H₂ photoevolution where CO₂ is not present and ATP is abundant owing to associated photophosphorylation, the Calvin-cycle enzymes are fully activated and RuBisCo could act as a strong oxygenase. This hypothesis can explain how FCCP mitigates O₂ inhibition of H₂ photoevolution, since operation of the Calvin cycle requires formation of ATP using the proton gradient across the thylakoid membrane. Another possible site for O₂ interaction could be at Ferredoxin (Fd), which, according to the classic Mehler reaction, can serve as electron donor to O₂. Additional experimental studies with different chemical inhibitors and genetic mutants are underway to elucidate this O₂-sensitive H₂-production electron transport pathway.

This discovery also provides a new opportunity to develop a more-efficient and robust system for photosynthetic H_2 production. The experimental data with FCCP (Fig. 2) indicate that use of a polypeptide proton channel that does not deactivate the oxidizing equivalents of Photosystem II could enhance H_2 production by eliminating the problems of both the proton-gradient accumulation (8) and the newly discovered alternative O_2 sensitivity. Therefore, we propose to create a “designer” photosynthetic organism for production of H_2 by genetic insertion of programmable proton channels in thylakoid membranes. The genetic insertion of programmable thylakoid-membrane proton channels can be achieved by transformation of a host alga with a genetic vector that contains a hydrogenase promoter-linked CF_1 suppressor or membrane polypeptide proton-channel gene. The envisioned “super” alga that can be created in this way should be able to perform autotrophic photosynthesis using ambient-air CO_2 as the carbon source and grow normally under aerobic conditions such as in an open pond. When the algal culture is grown and ready for H_2 production, the CF_1 -suppressor or proton-channel gene will then be expressed simultaneously with the induction of the hydrogenase enzyme under anaerobic conditions. The expression of the proton-channel gene should produce polypeptide proton channels in the thylakoid membrane, thus dissipating the proton gradient across the thylakoid membrane without ATP formation (Fig. 6B). The expression of the CF_1 suppressor should create CF_0 , which may act as a free proton channel without the CF_1 cap, thus similarly dissipating the proton gradient across the thylakoid membrane without ATP formation. The free proton-conductive CF_0 or polypeptide proton channels in the thylakoid membrane could provide two advantages for H_2 photoevolution: (1) accumulation of a proton gradient that impedes photosynthetic electron transport from water to ferredoxin (Fd)/hydrogenase could be prevented; and (2) the newly discovered O_2 -sensitive pathway that competes with the H_2 -production pathway for photosynthetically generated electrons could be eliminated.

Therefore, the co-expression of the polypeptide proton channel (or CF_1 suppressor) and hydrogenase genes will make this alga a more-efficient system for production of H_2 by photosynthetic water splitting under anaerobic conditions (Fig. 6B). This organism contains normal mitochondria, which can use reducing power (NADH) from organic reserves (and/or exogenous acetate) to power the cell immediately after returning to aerobic conditions. Therefore, when the algal cell is returned to aerobic conditions after its use under anaerobic conditions for photoevolution of H_2 and O_2 , the cell will stop generating free CF_0 (or polypeptide proton channels) in thylakoid membranes and restore its normal photoautotrophic capability by synthesizing functional thylakoids. Consequently, it should be possible to use this type of genetically transformed organism for repeated cycles of photoautotrophic culture growth under normal aerobic conditions and efficient production of H_2 and O_2 by photosynthetic water splitting under anaerobic conditions.

Acknowledgments

The authors thank C. A. Sanders, B. Forbes, and B. Kusiak for culture media preparation; A. Jones for secretarial support; M. K. Savage for editorial assistance; and C. D. King and V. W. Purdue for technical illustrations. We also thank Drs. M. Seibert and M. L. Ghirardi for their O_2 -tolerant mutants and informative discussions. This research was supported by the U.S. Department of Energy Hydrogen Program, the DOE Office of Science Young Scientist Award (to J. W. Lee), and the Office of Basic Energy Sciences.

Oak Ridge National Laboratory is managed by UT-Battelle, LLC, for the U.S. Department of Energy under contract DE-AC05-00OR22725.

References

1. Greenbaum, E., and J. W. Lee 1998. “Photosynthetic hydrogen and oxygen production by green algae.” In *BioHydrogen*, O. R. Zaborsky ed., pp. 235–241. New York, Plenum Press.
2. Ghirardi, M. L., R. K. Togasaki, and M. Seibert 1997. “Oxygen sensitivity of algal H_2 -production” *Applied Biochemistry and Biotechnology*, 63-65:141–151.
3. Lee, J. W., S. L. Blankinship, and E. Greenbaum 1995. “Temperature effect on production of hydrogen and oxygen by *Chlamydomonas* cold strain CCMP1619 and wild-type 137c” *Applied Biochemistry and Biotechnology*, 51/52:379–385.
4. Samuilov, V. D., E. L. Barsky, and A. V. Kitashov 1995. “ADRY agent-induced cyclic and non-cyclic electron transfer around photosystem II” *Photosynthesis: from Light to Biosphere*, P. Mathis (ed.), Vol. II, 267–270. The Netherlands, Kluwer Academic Publishers.
5. Ghirardi, M. L., S. Markov, and M. Seibert 1996. “Development of an efficient algal H_2 -producing system,” in *Proceeding of the 1996 U.S. Department of Energy Hydrogen Program Review*, vol. I, NREL/CP-21908430, pp. 285–302.
6. Seibert, M., T. Flynn, D. Benson, E. Tracy, and M. Ghirardi 1998. “Development of selection and screening procedures for rapid identification of H_2 -producing algal mutants with increased O_2 tolerance,” In *Biohydrogen*, O. R. Zaborsky, ed., pp. 227-234. New York, Plenum Press.
7. Ghirardi, M. L., Z. Huang, M. Forestier, S. Smolinski, M. Posewitz, and M. Seibert 1999. “Development of an efficient algal H_2 -production,” in *Proceeding of the 1999 U.S. Department of Energy Hydrogen Program Review*.
8. Lee, J. W. and E. Greenbaum 1997. “A new perspective on hydrogen production by photosynthetic water splitting.” ACS Symposium Series 666, *Fuels and Chemicals from Biomass*, B. C. Saha and J. Woodward, eds. Chapter 11, pp. 209–222.

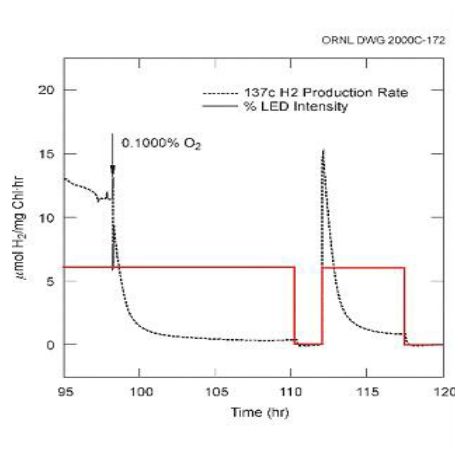


Figure 1. Observation of a new O₂ sensitivity to algal H₂ production in *Chlamydomonas reinhardtii*.

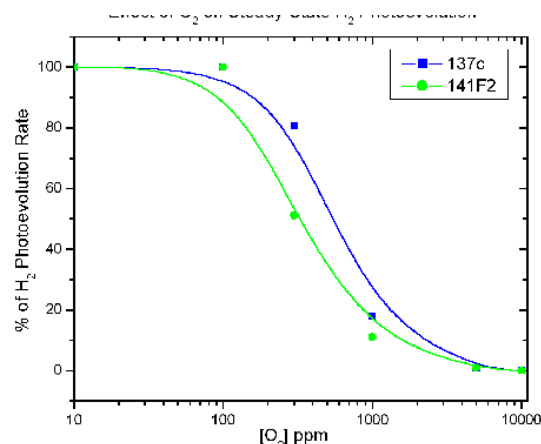


Figure 4. Effect of background O₂ concentrations on steady-state H₂ photoevolution.

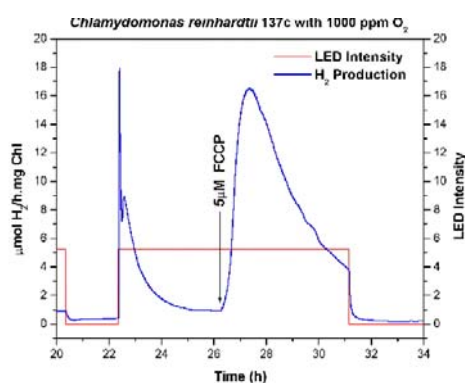


Figure 2. Stimulation of photosynthetic H₂ production in *C. reinhardtii* 137c following addition of the proton uncoupler FCCP in a background atmosphere of 1000-ppm O₂. Addition of 5 μM FCCP produced a dramatic increase in H₂ production, followed by a slow decay. The slow decay is due to a side effect of FCCP known as ADRY, in which FCCP gradually inhibits PSII activity. This experimental result indicates that use of a polypeptide proton channel that does not have the ADRY effect could enhance H₂ production by eliminating the problems of both the proton-gradient accumulation and the newly discovered alternative O₂ sensitivity.

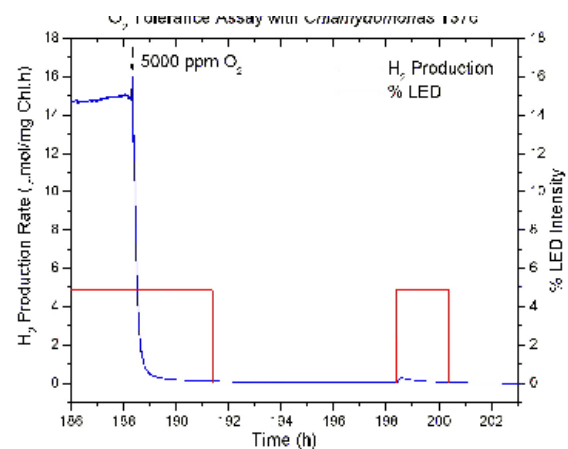


Figure 5. Introduction of 5000-ppm O₂ has dramatic inhibition of H₂ production, but the hydrogenase remains active.

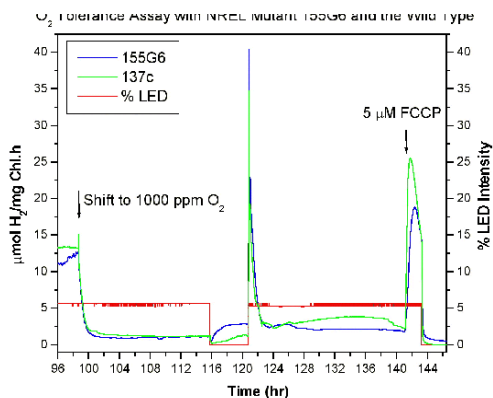
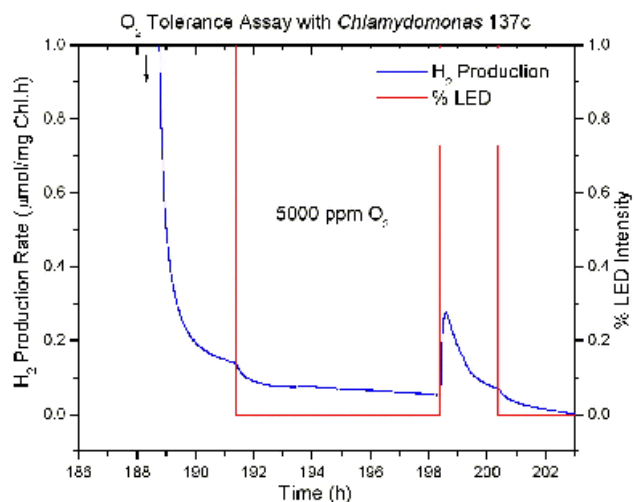


Figure 3. O₂-tolerance assay with NREL mutant 155G6 and the wild-type parental strain 137c.



Inset of Fig. 5. Expanded vertical scale of Fig. 5, showing a clear peak of H₂ photoevolution after 10 h of continued presence of 5000-ppm O₂.

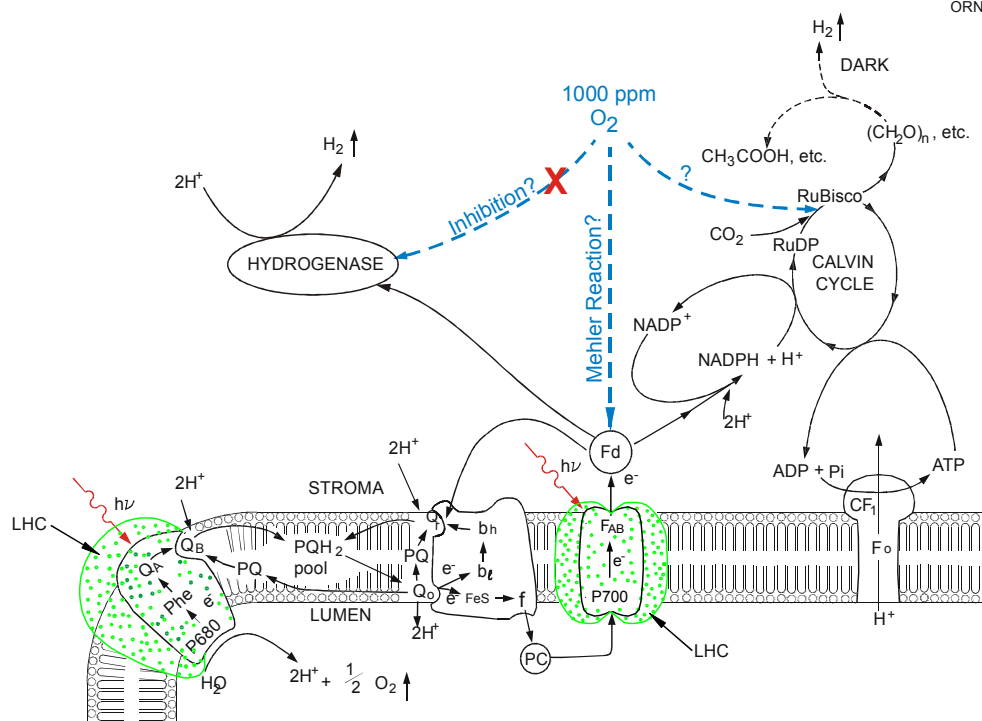
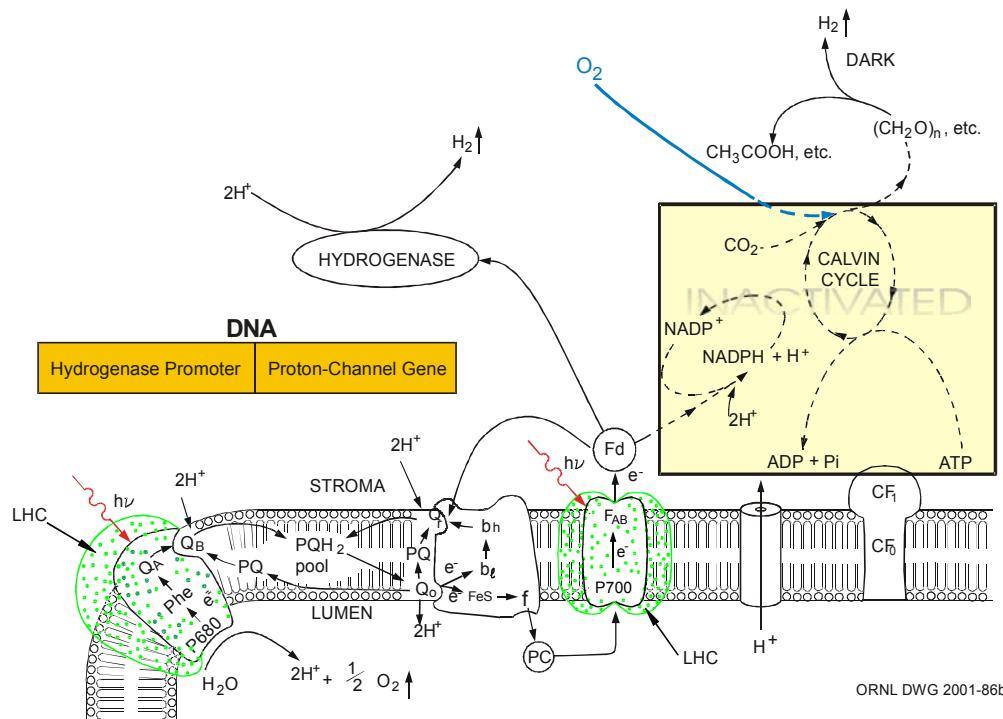


Figure 6A. The newly discovered O_2 sensitivity is likely due to the background O_2 (at about 1000-ppm levels) acting as a terminal sink, in competition with the Fd/hydrogenase H_2 -production pathway, for photosynthetically generated electrons.



ORNL DWG 2001-86b

H_2 Production Under Anaerobic Conditions

Figure 6B. Development of an efficient algal H_2 -production system by construction and transformation of a vector that contains the hydrogenase promoter and a piece of synthetic DNA for a polypeptide proton channel. The transformed alga could grow normally using ambient-air CO_2 under aerobic conditions without the polypeptide proton channel, which could be expressed only with the induction of the hydrogenase under anaerobic conditions when its function is needed for enhanced H_2 production.

PALLADIUM NANOWIRE ARRAYS FOR FAST HYDROGEN SENSORS AND HYDROGEN-ACTUATED SWITCHES

*E.C. Walter, F. Favier, E.J. Menke, R.M. Penner**

Department of Chemistry
University of California, Irvine
Irvine, CA 92697-2025

Introduction

Hydrogen has tremendous potential as an environmentally friendly fuel for vehicles, cell phones, laptop computers, and other mobile devices. But hydrogen-air mixtures are explosive for $[H_2] > 4\%$, and hydrogen leak detection is therefore of considerable importance. Ideally, sensors for leaked hydrogen will be small, power-efficient, inexpensive, and fast in terms of the rate of sensor response.

In this presentation, we describe a new type of H_2 sensor based on an emerging nanotechnology. This sensor consists of a parallel array of 10 to 100 of palladium nanowires, as shown in Figure 1^{1,2}. The resistance of this palladium nanowire array (PNA) was measured by applying a voltage of a few millivolts, and monitoring the current that is of the order of microamps.

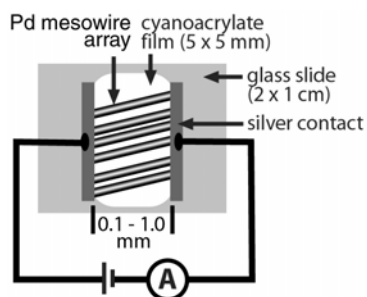


Figure 1. Schematic diagram of a hydrogen sensor based on a palladium nanowire array (PNA).

Although PNAs are an immature technology for H_2 sensing (the first PNA-based H_2 sensor was prepared in April 2001), early versions of these devices exhibit many desirable properties for H_2 leak detection. The preparation of H_2 sensors based on electrodeposited palladium nanowire arrays (PNAs) and the performance of these sensors for detecting hydrogen are both discussed.

Experimental

Electrochemical measurements. All chemicals were reagent grade from Fisher and were used without further purification. Two different Pd plating solutions were used: aqueous 2 mM $PdCl_2$, 0.1 M HCl and 2 mM $Pd(NO_3)_2$, 0.1 M $HClO_4$. Barnstead Nanopure deionized water ($> 17.8 M\Omega$) was employed for all solutions. Pd plating solutions were purged for 10 minutes with pre-humidified N_2 prior to use. Cyclic voltammograms (CVs) and potentiostatic metal plating pulses were applied using an EG&G model 263A potentiostat. All deposition experiments were carried out in a glass electrochemical cell. Highly oriented pyrolytic graphite was freshly cleaved with adhesive tape and held using a Teflon electrode holder. Approximately 0.3 cm^2 of this graphite sample was exposed to the Pd plating solution in the electrochemical cell. A saturated calomel reference electrode (SCE) was employed as the reference electrode.

A platinum foil ($\approx 4\text{ cm}^2$) was employed as the counter electrode in all experiments.

Sensor Fabrication. Briefly, the surface of the graphite electrode onto which Pd nanowires had been deposited was pressed onto a droplet ($\approx 50\text{ }\mu\text{l}$) of cyanoacrylate adhesive ("Special T" super glue, Satellite City) on a degreased glass slide. After this adhesive hardened, the graphite surface was lifted off the cyanoacrylate, and residual carbon layers were removed with a forceps. The vast majority the nanowires initially present on the graphite surface were transferred onto the surface of the cyanoacrylate film using this procedure. Silver contacts (conductive liquid silver, Ted Pella) were manually applied to the two ends of a nanowire array using a thin glass pipette and copper wires were attached to these contacts to facilitate resistance measurements.

Hydrogen Sensing. Most sensor measurements were carried out in a sealed $\approx 50\text{ mL}$ glass jar to which gas inlets and outlets had been attached. A MKS type 647B mass flow and pressure programmer was used in conjunction with an MKS mass flow controller to produce a flow rate of 200 sccm ($\pm 2\text{ sccm}$) in all gas flow measurements. The response time of this controller was $< 100\text{ ms}$. Sensor response times were measured in a % smaller volume cell having a dead volume of $\approx 1\text{ mL}$, using gas flow rates of 200 sccm through a solenoid valve with a switching time of $\approx 10\text{ ms}$. Sensor currents were measured using a potentiostat (EG&G model 263A) which also provided a bias of 5 or 10 mV.

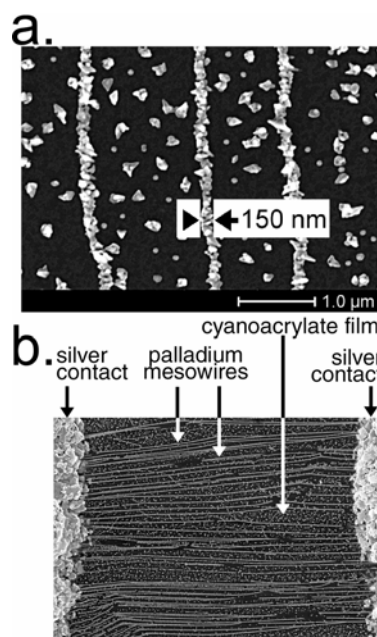


Figure 2. (a) Palladium nanowires prepared by electrodeposition on graphite. (b) A PNA after transfer to a cyanoacrylate film and the application of silver contacts.

Results and Discussion

Palladium nanowires and a PNA are shown in the scanning electron micrographs shown in Figure 2. These nanowires were prepared by electrodepositing palladium metal from a dilute, aqueous plating solution, onto a highly oriented pyrolytic graphite electrode surface. Nanowire growth is obtained by applying three voltage pulses in rapid succession: A $+1.2\text{ V} \times 5\text{ s}$ "conditioning" pulse, a $-0.20\text{ V} \times 10\text{ ms}$ "nucleation" pulse, and a $+0.30\text{ V} \times \approx 10\text{ min}$. "growth" pulse (all voltages vs. SCE). These deposition conditions

produced polycrystalline palladium nanowires with diameters in 200-300 nm range (Fig. 2a). These nanowires, which were 100 μm to 500 μm in length, nucleated and grew at step edges on the graphite surface. Growth at step edges occurs because the energetic barrier to palladium nucleation is somewhat lower at these defect structures as compared with atomically smooth and defect-free terraces. Following the electrodeposition of palladium nanowires, many (i.e., 20 or more) arrays of nanowires are present on the graphite electrode surface. These arrays consist of between 20 and 200 Pd nanowires arranged in parallel.

The response of a PNA sensor to mixtures of H_2 and N_2 are shown in Figure 3a. Most sensors exhibited a large resistance ($> 1.0 \text{ M}\Omega$) in the absence of H_2 (below 0.5%). At a threshold of 2% H_2 , these “mode II” sensors became conductive and the resistance of the PNA decreased by a factor of 1/10 as the H_2 concentration increased from 2% to 10% (Fig. 3b). Some sensors exhibited an appreciable resistance even in the absence of H_2 (data not shown). These “mode I” sensors also exhibited a lower threshold for detecting H_2 of approx. 0.5 % (Fig. 3b).^{1,2}

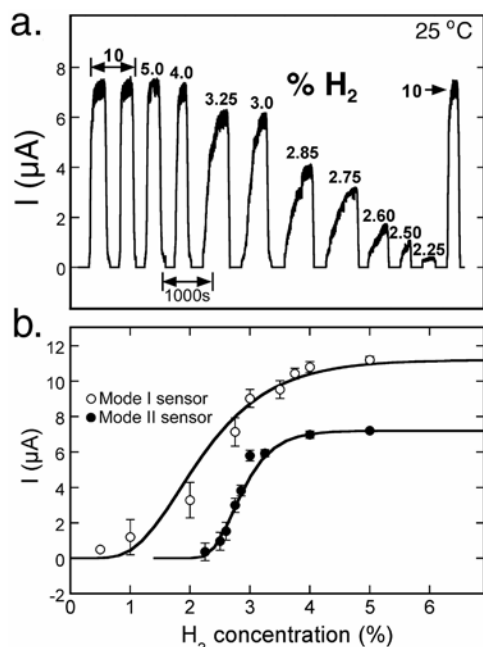


Figure 3. (a) Response of a mode II PNA sensor to hydrogen/ N_2 mixtures as a function of concentration. (b) Calibration plots for typical mode I and mode II PNA sensors.

The response of PNA-based sensors was exactly the opposite expected based on the materials properties of the palladium/hydrogen system.³ Alloys of palladium hydrides have a higher electrical conductivity than pure palladium and H_2 sensors based on palladium resistors respond to hydrogen exposure by becoming more resistive.

The unexpected increased conductance of PNA-based H_2 sensors was caused by the presence of nanoscopic breaks in the nanowires in the PNA.^{1,2} These breaks are visible in SEM images, such as the one shown in Figure 4. These nanoscopic breaks function as “break junctions” that close in the presence of H_2 , and open in its absence, as shown in Figure 5. This surprising behavior is caused by the swelling of the palladium-hydride lattice by 3% as the hydrogen content of the metal increases from pure Pd to $\text{PdH}_{0.7}$.³

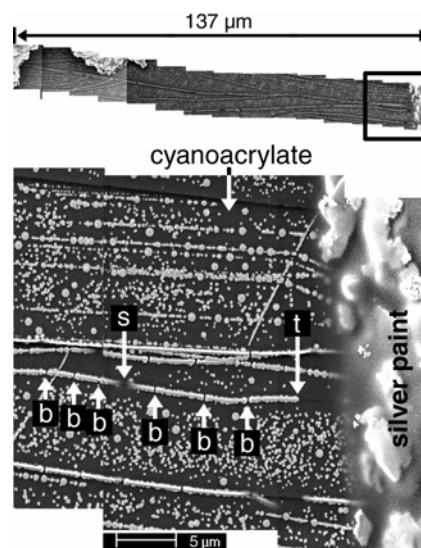


Figure 4. Scanning electron microscopy image of break junctions in the palladium nanowires of a functioning PNA-based H_2 sensor. These break junctions form the basis for sensor function.

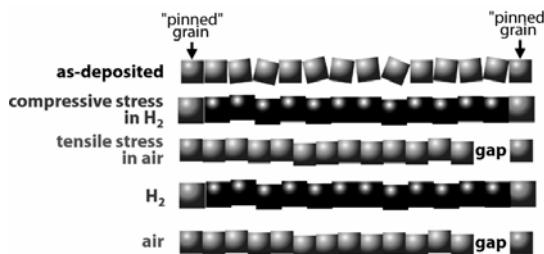


Figure 5. Schematic depiction of the formation of break junctions, and the operation of a break junction in a palladium nanowire.

Summary

Arrays of palladium nanowires, prepared by electrodeposition, can be used to detect H_2 . Individual palladium nanowires in these arrays fracture upon exposure to hydrogen gas, and the resulting nanoscopic gaps function as hydrogen-actuated “break junctions”. Exposure of PNAs to hydrogen causes break junctions in the nanowires to close causing individual nanowires in the array to switch from an insulating to a conducting state. This response to hydrogen is rapid (as fast as 20 ms) and selective.

Acknowledgment. This work was funded by the NSF (grant CHE-0111557) and the UC BioStar Program in conjunction with Nanomix Inc. (Emeryville, CA). F.F. acknowledges funding through NATO. Donations of graphite by Dr. Art Moore of Advanced Ceramics Inc. are gratefully acknowledged.

References

1. Favier, F., Walter, E.C., Penner, R.M., Science **2001**, 293, 2227-31.
2. Walter, E.C., Favier, F., Penner, R.M., Anal. Chem. **2002**, 74, 1546-52.
3. Lewis, F. A. *The Palladium Hydrogen System*; Academic Press: New York, 1967.

RAPID LIGHTOFF OF OCTANE REFORMING

Corey A. Leclerc and Lanny D. Schmidt

Department of Chemical Engineering and Materials Science
University of Minnesota
421 Washington Ave. S. E.
Minneapolis, MN 55455

Introduction

Liquid fuels are gaining increasing attention as a source of hydrogen for several applications. Hydrogen can be added to combustion engines to burn fuels leaner than their air-fuel combustion limits leading to improved engine performance¹, because the lower temperatures of lean combustion suppress NO_x formation, a major pollutant from automobiles.² Hydrogen can also be used in a PEM fuel cell to power an automobile. Liquid fuels have a higher hydrogen density than gaseous alkanes such as methane and they occupy much smaller space than hydrogen gas without the need to cryogenically liquefy or compress. Transferring liquid fuels from distribution stations to automobiles is much easier with liquids and the infrastructure to do so with liquid alkanes (gasoline and diesel) already exists.

The catalytic partial oxidation pathway is a promising route for the production of hydrogen from liquid alkanes. The partial oxidation of liquid alkanes has been shown to attain greater than 95% conversion of fuel with a yield of hydrogen and carbon monoxide around 90% in millisecond contact times.³ In order to make this process practical for applications such as automobiles, it is necessary to be able to start producing hydrogen, on the order of the time for turning a key, i.e. in a few seconds.

This research focuses on using the large amounts of heat from combustion to heat the partial oxidation catalyst to lightoff temperatures in seconds. This is followed by a switch in stoichiometry to partial oxidation stoichiometry in order to produce hydrogen. Iso-octane is a model fuel used as the first step of achieving rapid gasoline lightoff. Although it has been shown that rapid lightoff (~5 seconds) of lower alkanes such as methane is possible⁴, octane will need to be vaporized within the reactor before passing over the catalyst. This research shows how octane can be used to rapidly light off the catalyst, by injecting the fuel into the reactor with a fuel injector. The results are compared to those of methane and butane.

Experimental

The reactor is shown in **Figure 1**. The reactor consists of an 18 mm ID quartz tube with an 80 pores per inch (ppi) α -alumina foam monolith coated with rhodium. The catalyst is prepared by first soaking a 5 mm long monolith in a γ -alumina slurry and drying overnight. The coating of γ -alumina increases the surface area of the monolith.⁵ Then the catalyst is soaked in a Rh(NO₃)₃ salt solution and calcined at 600 °C for 6 hours to give a 5-6% by weight coating of rhodium. The monolith is placed in the reactor wrapped in an alumina/silica paper for a snug fit to prevent gas bypass. A blank monolith is placed immediately downstream of the catalyst to prevent heat losses. Another blank monolith was placed 1 centimeter upstream of the catalyst to act as a flame holder during lightoff of the catalyst. Two nickel leads enter the reactor through a rubber stopper in between the flame holder and the catalyst. The leads are wired to a push button grill sparker for ignition. The back face temperature of the monolith is measured with a 0.01" K-type thermocouple that passes through the downstream heat shield making intimate contact with the catalyst back face. The thermocouple communicates with a PC through a programmable logic controller (PLC) sampling data

once per second. Air flow rate set points are specified on the PC and relayed to a mass flow controller by the PLC with an accuracy of ± 0.1 SLPM. The fuel is introduced at the top of the reactor with an automotive fuel injector. The fuel tank pressure is maintained at 21 psi with nitrogen. The fuel injector is run as a square wave at frequencies from 1.25 Hz and 0.4% open to 19 Hz and 5% open. The fuel is preheated in the first 5 centimeters of the reactor with a heating tape wrapped around the reactor and set to 80 to 100 °C at ignition. The heating tape is turned off at ignition. The heat generated in the system with insulation is able to vaporize the fuel without further heat input from the heating tape. In the area of the catalyst, an inch of high temperature silica/alumina insulation was wrapped around the reactor to prevent radial heat losses.

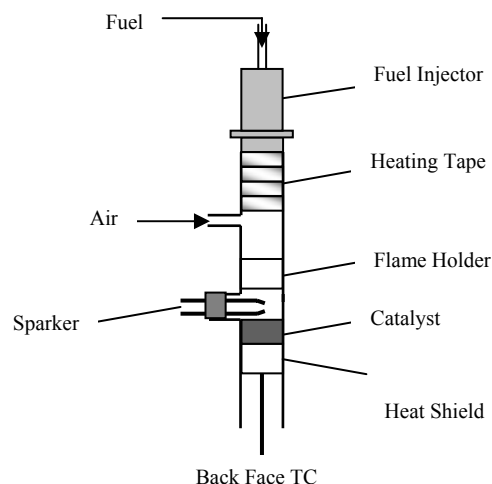
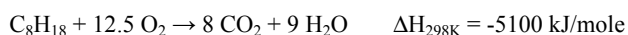


Figure 1. The rapid lightoff reactor

Rapid lightoff of the catalyst is achieved by feeding 2 to 9 liters of air and octane at combustion stoichiometry.



The fuel vaporizes in the heated section. The octane and air mix in the flame holder. The sparker button is pushed causing a spark in the compartment above the catalyst to ignite the air and fuel mixture. A blue flame forms in this compartment rapidly heating the catalyst. Seconds later, the fuel flow rate is increased to partial oxidation stoichiometry.



The flame then extinguishes and the ignited catalyst produces hydrogen. The high flow rates lead to catalyst contact times on the order of milliseconds.

Results and Discussion

Temperature versus time data for octane lightoff is shown in **Figure 2**. Data is shown for varying air flow rates. In this plot, at time zero the combustion stoichiometry is ignited with the spark. The stoichiometry is switched to partial oxidation ($\phi = 3.125$) about 7 seconds after ignition. During the combustion period, the catalyst back face is rising rapidly. After switching to syngas stoichiometry, the temperature levels out to a steady state temperature. For the 9 SLPM air flow rate, the back face temperature rises from room temperature to 1000 °C in about 8 seconds. For the intermediate

flow rates, the heating rate, i.e. the slope of the temperature curve, is slightly smaller due to the lower flow rates. For the low flow rate (2 SLPM), the heating rate is much slower. In this case, the stoichiometry is switched with a back face temperature near 100 °C and the temperature continues to rise to a steady state seconds later. It is important to note that even though the back face temperature is cold, the front face is still ignited. The lightoff temperature for octane on rhodium is only 250 °C,³ so it is expected that some partial oxidation chemistry takes place on the front of the catalyst. The partial oxidation reaction is still exothermic, so heat will be generated to heat the back face.

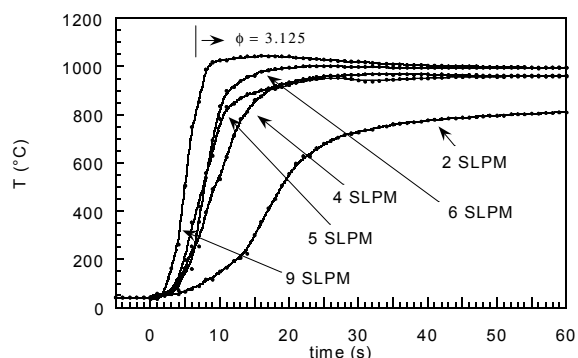


Figure 2. Back face temperatures for octane lightoff (Flow rate label is the air flow rate)

Figures 3 & 4 show similar lightoff data for methane and isobutane respectively.

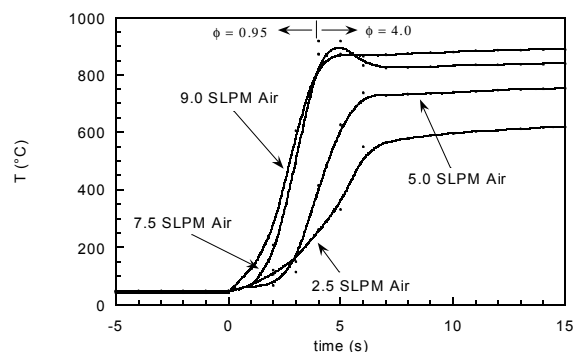


Figure 3. Back face temperature for methane lightoff

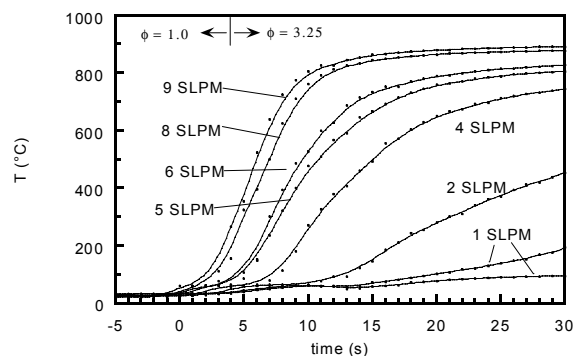


Figure 4. Back face temperature for butane lightoff

Irrespective of the fuel, the back face temperature in all 3 cases rises at approximately the same rate. This is expected, because at 5 SLPM of air, irrespective of the fuel, the heating rate is approximately 1 kW. If the catalyst is treated as a lumped system, then one expects the temperature rise to be found from:

$$dQ/dt = c_p \rho dT/dt$$

If this were true, then since the reactor produces 1 kW of energy and $c_p \rho$ is equal to about 1 J/°C for our catalytic monolith, we should see a temperature rise of 1000 °C per second. However, since our catalyst is a distributed system we would not expect our heating rate of the back face to be this high. One benefit of octane is that it lights off at 250 °C rather than 600 °C which is the lightoff temperature for methane.⁶ Octane lightoff will require less heat than methane.

Conclusions

A rhodium catalyst was ignited in a millisecond reactor in several seconds with heating rates comparable to methane and butane for the partial oxidation of octane. Rapid catalyst heating was attained by feeding the reactants at combustion stoichiometry and igniting the mixture to form a flame directly above the catalyst. The back face temperature rose from room temperature to lightoff (250 °C) in 4 seconds and up to 1000 °C in 8 seconds. The heating rate can be tuned by adjusting the flow rate. As the flow rate increases, so does dQ/dt . This will lead to even higher heating rates of the catalyst.

References

- (1) Cohn, D. R.; Rabinovich, A.; Titus, C. H. *Int. J. of Vehicle Design.*, **1996**, 19, 557.
- (2) Kirwan, J. E.; Greive, M. J.; Quader, A. A. *SAE Paper 012927*. **1999**.
- (3) O'Connor, R. J.; Klein, E. J.; Schmidt, L. D. *Catalysis Letters*. **2000**, 70, 99.
- (4) Leclerc, C. A.; Redenius, J. M.; Schmidt, L. D. *Catalysis Letters*. Accepted.
- (5) Bodke, A. S.; Bharadwaj, S. S.; Schmidt, L. D. *J. Catal.* **1998**, 179, 138.
- (6) Williams, W. R.; Zhao; Schmidt, L. D. *AIChE J.* **1991**, 37 (5), 641.

RECENT ADVANCES IN THE DEVELOPMENT OF DENSE CERAMIC MEMBRANES FOR HYDROGEN SEPARATION

U. (Balu) Balachandran, T. H. Lee, S. Wang, G. Zhang, J. J. Picciolo, J. T. Dusek, and S. E. Dorris

Energy Technology Division
Argonne National Laboratory
9700 S. Cass Ave
Argonne, IL 60439

Introduction

The U.S. Department of Energy's Office of Fossil Energy sponsors a wide variety of research, development, and demonstration programs that aim to maximize the use of vast domestic fossil resources and ensure a fuel-diverse energy sector while responding to global environmental concerns. Development of cost-effective, membrane-based reactor and separation technologies is of significant interest for applications in advanced fossil-based power and fuel technologies. Because concerns over global climate change are driving nations to reduce CO₂ emissions, hydrogen is considered the future fuel of choice for the electric power and transportation industries. Although it is likely that renewable energy sources will ultimately be used to generate hydrogen, technologies based on fossil fuels will supply hydrogen in the interim.

The purpose of this work is to develop dense hydrogen-permeable membranes for separating hydrogen from mixed gases at commercially significant fluxes under industrially relevant operating conditions. Of particular interest is the separation of hydrogen from product streams that are generated during coal gasification, methane partial oxidation, and water-gas shift reactions. Because the membrane will separate hydrogen without using electrodes or an external power supply (i.e., its operation will be nongalvanic), it requires materials that exhibit suitable electronic and protonic conductivities as well as high hydrogen diffusivity and solubility. Good mechanical properties will also be necessary to withstand operating stresses. In addition, the fabricated materials must be thin and dense in order to maximize the hydrogen flux and maintain high hydrogen selectivity.

Membrane development at Argonne National Laboratory (ANL) and the National Energy Technology Laboratory (NETL) focused initially on BaCe_{0.8}Y_{0.2}O_{3-δ} (BCY), because it is a mixed proton/electron conductor with a high total electrical conductivity [1, 2] and may, therefore, yield a high hydrogen flux without using electrodes or electrical circuitry. Despite its high total electrical conductivity, however, its electronic component of conductivity is insufficient to support a high nongalvanic hydrogen flux [3, 4]. To increase the electronic conductivity and thereby increase the hydrogen flux, we have developed various cermet membranes in which a metal powder is dispersed in a ceramic matrix [5, 6]. In these cermets, the metal enhances the hydrogen permeability of the ceramic phase by increasing the electronic conductivity of the composite. A metal with high hydrogen permeability may also provide an additional transport path for the hydrogen.

The cermet membranes in this paper are classified as ANL-1, -2, or -3, based on the hydrogen transport properties of the metal and matrix phases. The first class of membranes, ANL-1, contains a metal with low hydrogen permeability in a hydrogen-permeable matrix, BCY. The hydrogen flux through ANL-1a is higher than that through monolithic BCY because the metal increases the overall electronic conductivity of the membrane. The hydrogen flux was increased with ANL-2a membranes by replacing the metal in ANL-1a with a hydrogen transport metal, i.e., a metal that has a high

hydrogen permeability. Although BCY and the metal phase both contribute to the hydrogen flux through ANL-2 membranes, most of the hydrogen diffuses through the metal [7]. Because BCY contributes relatively little to the overall permeation rate of ANL-2 membranes, exhibits poor mechanical properties, and is chemically unstable under some conditions of interest, ANL-3 membranes were developed. In ANL-3 membranes, the BCY matrix of ANL-1 and -2 membranes is replaced by a ceramic with superior mechanical properties and thermodynamic stability, e.g., Al₂O₃ or ZrO₂. The resulting membrane gives higher hydrogen flux and has higher strength and greater chemical stability. In this paper, we discuss the results from hydrogen permeation tests of the various cermet membranes (ANL-1, -2, and -3).

Experimental

BCY powder was prepared at ANL as previously described [5]. All membranes were prepared to contain 40 vol.% metal phase, except where otherwise noted. BCY and metal powders were mixed together to prepare powders for ANL-1a and -2a membranes. Powders for ANL-3 membranes were prepared by mixing one of two hydrogen transport metals with ceramic powders that are reported to be poor proton conductors [8]. Powders were pressed into disks (≈22 mm in diameter and 2 mm thick) and sintered at temperatures of ≈1400°C. To test permeation, sintered disks were polished and then affixed to an Al₂O₃ tube using a gold ring. During permeation measurements, sweep gas (100 ppm H₂/balance N₂) was passed over one side of the membrane. The sweep gas was analyzed with a Hewlett-Packard 6890 gas chromatograph (GC). Feed gases included 100% H₂, simulated syngas (66% H₂, 33% CO, and 1% CO₂), and "dry" or "wet" 4% H₂/balance He. For wet feed gas, 4% H₂/balance He was bubbled through a water bath at room temperature to give ≈0.03 atm H₂O; for the dry condition, 4% H₂/balance He was introduced directly into the furnace from the gas cylinder.

Results and Discussion

The hydrogen permeation rates for ANL-1a, -2a, and -3b are compared in **Figure 1** for a feed gas of 4% H₂/balance He. Among these membranes, ANL-3b exhibited the highest permeation rate, approximately three times higher than that of ANL-1a over the whole temperature range (600-900°C). ANL-3b gave the highest permeation rate because its metal phase had the highest hydrogen permeability of the various metals tested to date.

Figure 2 shows the temperature and thickness dependence of the hydrogen flux through ANL-3b when wet 100% H₂ was used as the feed gas. With a feed gas of either 100% H₂ (**Figure 3**) or 4% H₂/balance He (**Figure 1**), the hydrogen permeation rate increased with temperature and was proportional to the inverse of membrane thickness over the whole temperature range. The inverse dependence of flux on thickness indicates that the bulk diffusion of hydrogen is rate-limiting for thicknesses >0.1 mm. **Figure 3** shows the temperature dependence of hydrogen flux through an ANL-3a membrane (thickness = 0.04 mm), which contained 50 vol.% hydrogen transport metal. Although this membrane has a different composition and metal concentration than the ANL-3b membranes (**Figure 2**), its significantly higher flux can be attributed primarily to the reduced thickness. This finding indicates that the bulk diffusion of hydrogen is rate-limiting down to 0.04 mm, and that reducing membrane thickness further may increase the permeation flux.

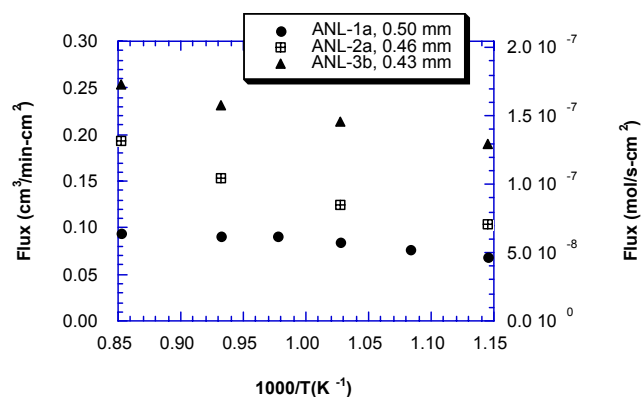


Figure 1. Hydrogen permeation rates through ANL-1a, -2a, and -3b when the feed gas is wet 4% H₂/balance He. Thickness of each membrane shown on inset.

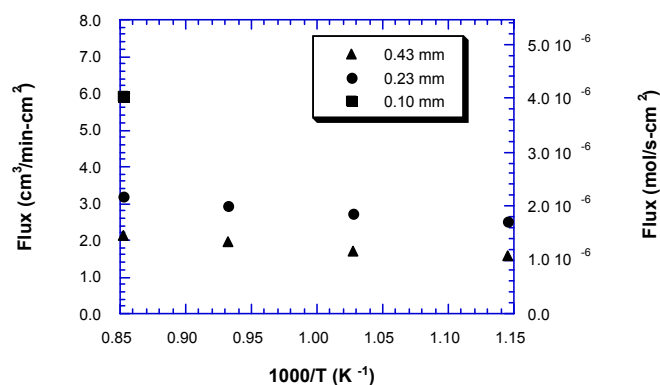


Figure 2. Hydrogen permeation rates through 0.10-, 0.23-, and 0.43-mm-thick ANL-3b when the feed gas is wet 100% H₂

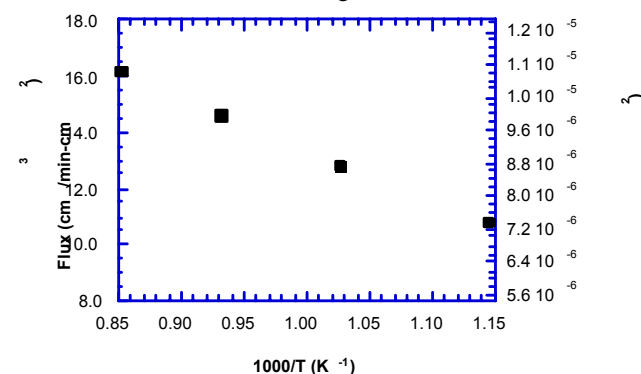


Figure 3. Hydrogen permeation rates through ANL-3a membrane (thickness = 0.04 mm) with 50 vol.% hydrogen transport metal. Feed gas is 100% H₂.

The chemical stability of ANL-3b in simulated syngas (66% H₂, 33% CO, and 1% CO₂) was tested by measuring its hydrogen flux at several temperatures for times up to 190 h. The results obtained from a 0.43-mm-thick membrane are shown in **Figure 4**. Feed gas of 4% H₂/balance He was flowed before and after exposure to syngas at each temperature in order to measure the leakage rate of hydrogen by measuring the helium concentration in the sweep gas. No helium leakage was measured at any of the temperatures. **Figure 4** shows no noticeable decrease in flux during up to 190 h of operation. Similar tests with 0.23-mm-thick ANL-3b showed no decrease in the hydrogen flux during 120 h of exposure to syngas at 900°C.

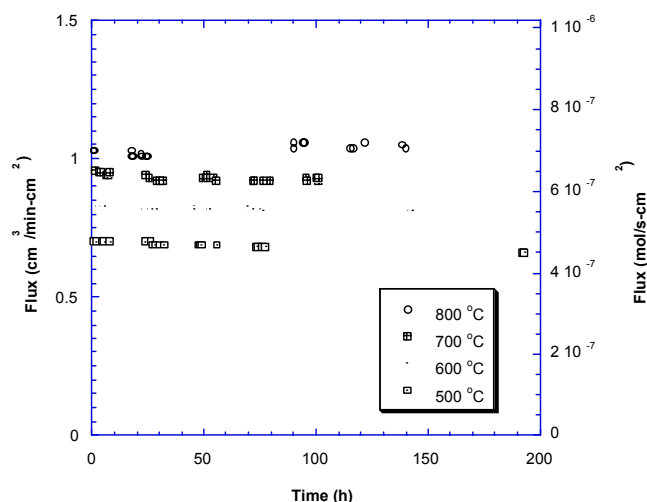


Figure 4. Hydrogen permeation rates through ANL-3b (0.43-mm thick) vs. time in simulated syngas (66% H₂, 33% CO, and 1% CO₂) at various temperatures.

Conclusions

We have developed cermet membranes that nongalvanically separate hydrogen from gas mixtures. The highest measured hydrogen flux was 16.2 cm³ (STP)/min-cm² for an ANL-3a membrane at 900°C. For ANL-3 membranes with thickness of 0.04–0.5 mm, the permeation rate is limited by the bulk diffusion of hydrogen through the metal phase. Permeation rates may be increased by decreasing the membrane thickness. The permeation rates in a syngas atmosphere for times up to 190 h showed no degradation in performance, indicating that ANL-3 membranes may be suitable for long-term, practical hydrogen separation.

Acknowledgement. This work is supported by the U.S. Department of Energy, National Energy Technology Laboratory, under Contract W-31-109-Eng-38.

References

- (1) H. Iwahara, T. Yajima, and H. Uchida, *Solid State Ionics*, **1994**, 70/71, 267.
- (2) H. Iwahara, *Solid State Ionics*, **1995**, 77, 289.
- (3) J. Guan, S. E. Dorris, U. Balachandran, and M. Liu, *Solid State Ionics*, **1997**, 100, 45.
- (4) J. Guan, S. E. Dorris, U. Balachandran, and M. Liu, *J. Electrochem. Soc.*, **1998**, 145, 1780.
- (5) J. Guan, S. E. Dorris, U. Balachandran, and M. Liu, *Ceram. Trans.*, **1998**, 92, 1.
- (6) U. Balachandran, T. H. Lee and S. E. Dorris, in *Proc. 16th Annual International Pittsburgh Coal Conf.*, Pittsburgh, PA, Oct. 11–15, **1999**, Pittsburgh Coal Conf. Pittsburgh, PA.
- (7) U. Balachandran, T. H. Lee, G. Zhang, S. E. Dorris, K. S. Rothenberger, B. H. Howard, B. Morreale, A. V. Cugini, R. V. Siriwardane, J. A. Poston Jr., and E. P. Fisher, in *Proc. 26th Intl. Technical Conf. on Coal Utilization and Fuel Systems*, Clearwater, FL, Mar. 5–8, **2001**, Coal Technical Association, Gaithersburg, MD. pp. 751–761.
- (8) K.-D. Kreuer, *Chem. Mater.*, **1996**, 8, 610.

RENEWABLE HYDROGEN PRODUCTION BY CATALYTIC STEAM REFORMING OF PEANUT SHELLS PYROLYSIS PRODUCTS

Robert J. Evans¹, Esteban Chornet¹, Stefan Czernik¹, Calvin Feik¹, Richard French¹, Steven Phillips¹, Jalal Abedi², Yaw D. Yeboah², Danny Day³, Jan Howard³, Dennis McGee⁴, and Matthew J. Realff⁵

¹Chemistry for Bioenergy Systems
National Renewable Energy Laboratory,
1617 Cole Blvd, Golden, CO 80401

²Department of Engineering
Clark Atlanta University
Atlanta GA 30314

³Scientific Carbons Inc
Blakely GA 31723

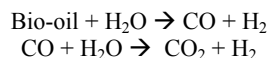
⁴Enviro-Tech Enterprises Inc
Matthews NC 28105

⁵School of Chemical Engineering
Georgia Institute of Technology
Atlanta GA 30332

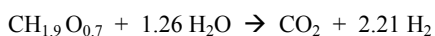
Introduction

The goal of this work is the production of renewable hydrogen from agricultural residues, in the near-term time frame and at a comparable cost to existing methane-reforming technologies. Near term production of renewable hydrogen from biomass requires a co-product strategy to compete with conventional production of hydrogen from the steam reforming of natural gas.^{1,2} The production of hydrogen by the processing of pyrolysis products that are produced as a by-product of activated carbon is one path that is possible to demonstrate the co-product strategy.

NREL began the development of a biomass to hydrogen process in 1993.¹ The original concept was that the pyrolysis oil could be fractionated into two fractions based on water solubility. The water-soluble fraction is to be used for hydrogen production and the water insoluble fraction could be used in adhesive formulations.³ The bio-oil can be stored and shipped to a centralized facility where it is converted to hydrogen via catalytic steam reforming and shift conversion. Catalytic steam reforming of Bio-oil at 750-850°C over a nickel-based catalyst is a two-step process that includes the shift reaction:



The overall stoichiometry gives a maximum yield of 17.2 g H/100 g bio-oil (a 40-50% energy yield is expected in practice):



The process has been demonstrated at the bench scale using model compounds and the carbohydrate-derived fraction of bio-oil.^{1,4} Regional networks of pyrolysis plants could be established to provide oil to a central steam reforming facility. The process is adaptable to other organic waste streams such as aqueous-steam fractionation processes used for ethanol production and trap grease. Recent laboratory work has demonstrated the feedstock flexibility with the processing of pyrolysis oil fractions from different feedstocks as well as other biomass-derived streams such as glycerine from biodiesel production, trap grease, and wood hydrolysis effluents.⁵

Although the adhesive byproduct option remains viable, commercial deployment opportunities are still not near term. Hence, other opportunities had to be developed based on the co-product strategy. The conversion of biomass to activated carbon is an alternative route to hydrogen with a valuable co-product as outlined in Figure 1. Slow pyrolysis is used in the first step of the activated carbon process to maximize the yield of charcoal and organic vapors are produced as a by-product in 25% yield. Southwest Georgia was identified as an excellent opportunity because of the importance of agriculture, the forest product industry and the need for zero emission transportation fuels in the Atlanta area. Scientific Carbons Inc. in Blakely GA uses pelletized peanut shells as the feed material for the production of activated carbon. They feed up to 1000 kg/hour of the densified peanut shells to a two-stage process producing activated carbon. The vapor by-products from the first stage, pyrolysis, are currently used as fuel for steam generator.

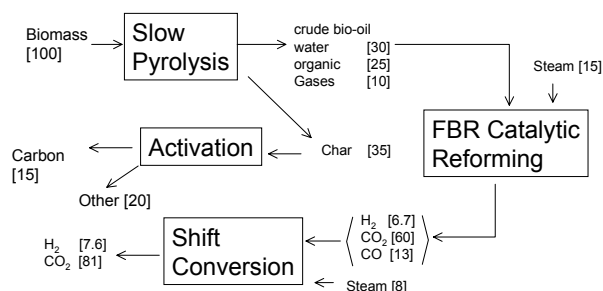


Figure 1. Mass Balance and Unit Operations in the Slow Pyrolysis of Biomass to Activated Carbon and Hydrogen

Catalyst performance is promising with run times in a two-inch fluid bed reactor of over 100 hours. Systematic studies of variation in catalyst composition have shown that commercial steam reforming catalysts perform well for the conversion.⁶ However, physical attrition is a problem since these catalysts are not manufactured for fluid bed operation.⁴

This paper reports on the design, set up, and shake-down of the scaled-up catalytic steam reforming reactor and on the initial tests for conversion of whole biomass pyrolysis vapors to hydrogen.

Experimental

Pelletized peanut shells obtained from the Birdsong peanut processing plant in Blakely, GA, were fed to a 20 cm fluid bed pyrolysis reactor. An in-line grinder was used to reduce the particle size to that required for fluid bed operation. Superheated steam at a mass ratio of 1.5:1 was used as a carrier gas and also as a reactant in the reformer. 10 kg/hour of pelletized peanut shells were fed into a bed of 300-400 μm sand at 500 °C. Char is separated in two cyclones. The steam/vapor stream then enters a preheater that raises its temperature to 650-700°C.

The catalytic fluid bed reformer can process 7-10 kg/h of pyrolysis vapor. The maximum allowable operating temperature and pressure are 900 °C and 140 kPa, respectively. The reformer is equipped with fluid bed reactor, vapor and liquid injection, steam and O₂ injection, internal and external cyclones for disengaging catalyst particles, instrumentation, data acquisition, and safety features (alarms, etc.). Commercial nickel-based catalyst ground to a particle size of 300-500 μ is being used in the reactor. The catalyst is fluidized using superheated steam, which is also a reactant in the reforming process. The cyclones capture both fine catalyst particles and solid carbon generated by gas phase pyrolysis of the vapors that may occur in competition with the catalytic steam reforming. The Inconel reactor with a porous distribution plate is placed inside a

three zone electric furnace to maintain the reactor at the desired temperature during the endothermic steam reforming operation. The reformed products flow through the spray scrubbers and a cold wall condenser before passing through a coalescing filter to remove aerosols.

Results and Discussion

In the initial tests the pilot-scale fluid-bed pyrolysis reactor was used to produce pyrolysis products from which a slipstream of the product vapors was sent to a 5 cm steam-reforming reactor.^{4,5} The purposes of the run were:

- Shake down the pyrolysis operation in the fluid bed, with emphasis on recent system modifications, demonstrate long duration operation in the pyrolysis mode, and perform online analysis of the product vapors.
- Reform the whole pyrolysis vapors (for the first time) in the 5 cm catalytic steam reforming fluid bed reactor.

The latter was the key objective, since the more chemically stable, lignin-derived phenolics may be more likely to coke on the nickel catalyst. Prior runs in the 5 cm reformer have used only the aqueous carbohydrate-derived fraction of pyrolysis oil. Reforming in the large-scale unit is planned to begin in March 2002 and will be reported at the symposium in June.

The composition of the pyrolysis products from the fluid bed system was unexpected. The char yield for this run was very high (~40%) and is due to multiple reasons: the high ash content, which catalyzes char formation from carbohydrates; and high lignin (32%) and protein (8%) content, both of which produce char yields greater than 30%. Studies in the laboratory showed that, even with small particle size and high temperature, the char yields from peanut shells were a minimum of 25% under conditions where wood char yields would be 12%.

The reforming test proceeded very smoothly. Gas composition at the outlet of the reformer was monitored during the operation and is shown in Figure 2. The composition of the gas indicates that the yield of hydrogen from this agricultural residue feedstock is approximately 90% of maximum. Additional optimization of process conditions should result in somewhat higher yields (note that, in a commercial operation, the remaining CO would be converted to additional hydrogen using conventional water-gas shift processing). In these tests, the gas product stream was flared. No breakthrough of pyrolysis products was noted and the methane level, which is a sensitive indicator of catalyst activity, did not increase. The significant finding here is that the lignin-derived pyrolysis products are reformed completely.

Summary

The steam reforming of biomass pyrolysis oil, when integrated with the production of high value products, is a promising near-term approach to the production of renewable hydrogen. Based on bench-scale work at NREL, a team from Georgia is utilizing the NREL Thermochemical Users Facility and its staff to develop a 10-20 kg/hr scale reactor that will be operated at NREL this year before being run at the production site in Georgia on densified peanut shells. The application in Georgia is at a plant that makes activated carbon from peanut shells and has pyrolysis by-products available for conversion. The key technical goals for the shakedown at NREL are to ensure the safety of the reactor and obtain preliminary performance data on the catalyst, especially physical attrition and deactivation.

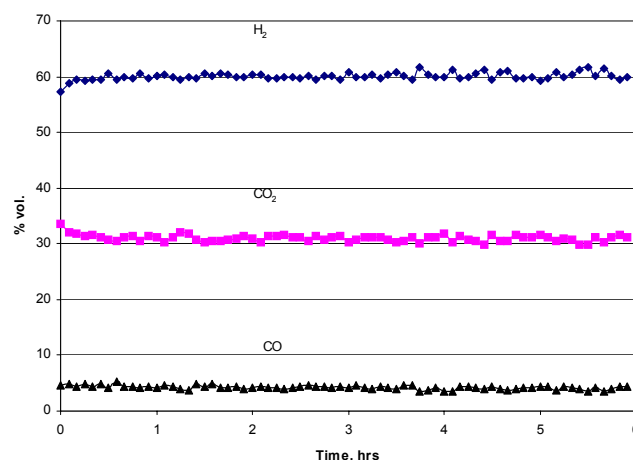


Figure 2. Gas composition from reforming peanut-shell pyrolysis vapors.

In phase two, the reactor will be tested on the pyrolysis vapors produced in the first step of the activated carbon process. An interface system is being designed this year for construction and operation in phase 2. In phase three the hydrogen produced will be purified by converting residual CO to H₂ over a shift catalyst and separating hydrogen from CO₂ using pressure swing adsorption. The purified hydrogen will be mixed with natural gas and used in a transportation demo. Working with the team from Georgia, other agricultural residues and deployment logistics are being evaluated for cost and co-product potential.^{7,8}

The scaled-up reactor will be shipped to the industrial site in Georgia for phase 2 testing in 2002. The hydrogen produced in the third phase of the project will be blended with CNG and used to power a bus in the nearby city of Albany, GA in Phase 3 of this project. This integrated strategy will demonstrate the potential impact of hydrogen and bioenergy on the economic development and diversification of rural areas.

Acknowledgement. The authors gratefully acknowledge the support of the DOE Hydrogen Program

References

1. Chornet, E.; Czernik, S.; Wang, D.; Gregoire, C.; Mann, M., In *Proceedings of the 1994 DOE/NREL Hydrogen Program Review*, Livermore, California, NREL/CP-470-6431; CONF-9404194, **1994**, pp. 407-432.
2. Spath, P.L.; Mann, M.K., In *Hydrogen Energy Progress XII. Proceedings of the 12th World Hydrogen Energy Conference*, Buenos Aires, Argentina, Bolcich, J. C. and Veziroglu, T. N., Eds. Vol. 3, **1998**, pp. 2057-2067.
3. Kelley, S.S.; Wang, X.-M.; Myers, M. D.; Johnson, D. K.; Scahill, J. W., In *Developments in Thermochemical Biomass Conversion*, Bridgwater, A. V. and Boocock, D. G. B., Eds., London: Blackie Academic & Professional, **1997**, pp. 557-572.
4. Chornet, E.; Czernik, S.; Feik, C.; French, R., In *Proceedings of the 2001 DOE/NREL Hydrogen Program Review*, Baltimore, MD., **2001**.
5. Czernik, S., French, R.; Feik, C.; Chornet, E., In *Progress in Thermochemical Biomass Conversion*, Bridgwater, A. V., Ed. London: Blackwell Science Ltd., **2001**, pp. 1577-1585.
6. Garcia, L., French, R.; Czernik, S.; Chornet, E., *Applied Catalysis A: General*, **2000**, 201, 225-239.
7. Abedi, J.; Yeboah, Y. D.; Realff, M.; McGee, D.; Howard, J.; Bota, K.B. In *Proceedings of the 2001 DOE/NREL Hydrogen Program Review*, Baltimore, MD., **2001**.
8. Ozyurt, B. D.; Realff, M. J., In *AIChE National Meeting Special Symposium*, Dallas, TX., **1999**.

SELECTIVE CATALYTIC OXIDATION OF CO IN H₂ OVER Au/ γ -Al₂O₃

C.K. Costello¹, H.-S. Oh^{1,2}, J.H. Yang¹, Y.M. Wang³, S.R. Bare⁴, H.H. Kung¹, M.C. Kung¹

¹Department of Chemical Engineering, Northwestern University, Evanston, IL 60208-3120, USA; ²Current Address: Hyundai Motor Company & Kia Motors Co., South Korea; ³Department of Materials Science, Northwestern University, Evanston, IL 60208-3120, USA; ⁴UOP Research Center, 50E Algonquin Road, Box 5016 Des Plaines, IL 60017-5016, USA

Introduction

Gold has historically been considered one of the most inert elements, and, consequently, its potential catalytic properties have long been ignored. However, since Haruta's report¹ of the exceptionally high catalytic activity of supported gold for low temperature CO oxidation, these catalysts have been subject to intense investigation.

Supported gold catalysts have great potential for use in fuel cell applications. The H₂ feed to a proton exchange membrane fuel cell contains approximately 1–2% CO, which poisons the Pt anode, severely decreasing the fuel cell power output. For practical applications, the CO concentration must be reduced to less than 10 ppm². One method to achieve this low CO concentration is to selectively oxidize the CO in the H₂ stream, and it is desirable to carry out this reaction at the fuel cell operating temperature (80–100°C) or at the methanol reformer unit temperature (250–300°C). The catalysts currently used include Pt, Ru, and Rh, which need temperatures of at least 150–200°C to operate efficiently, but experience a significant loss of selectivity at higher temperatures³. Supported gold catalysts can selectively oxidize CO at the fuel cell operating temperature, making them an attractive candidate for this application.

Despite the increasing number of published work on supported gold catalysts, the origin of their remarkable catalytic activity remains unknown. It is generally agreed that the activity is highly dependent upon the preparation procedure. These catalysts are typically prepared from chloride-containing precursors, and any residual chloride severely decreases catalyst activity. Highly active catalysts typically contain small (3–5 nm) Au particles, and it is well known that the presence of chloride facilitates Au particle agglomeration. However, chloride may also act to poison the catalytic active sites, which have been proposed to consist of an ensemble of Au⁺–OH[–] and metallic Au⁰ atoms^{4,5}.

Supported gold catalysts may be affected by the addition of other ions, such as phosphate or cesium. The addition of phosphate anions to the catalysts significantly inhibits the activity for CO oxidation, while the addition of Cs has been observed to suppress H₂ oxidation⁶. This report examines the effects of chloride, phosphate, and cesium ions on Au/ γ -Al₂O₃ for selective CO oxidation in H₂ (SCO) and discusses the results of further investigation into the nature of the active sites for this reaction.

Experimental

Catalyst Preparation. The γ -Al₂O₃ used as the support material was prepared by hydrolysis of aluminum isopropoxide in the presence of 2-methyl-2,4-pentanediol⁷. Three different procedures were used to prepare the catalysts described in this study. A preparation at low pH and low temperature was used to examine the

effects of residual chloride on the catalysts. 50 ml of an 8.4 mM solution of H₂AuCl₄ (Aldrich 99.999%) was added to 2.5 g of Al₂O₃ suspended in 50 ml of de-ionized H₂O at 0°C. After 1 hr, the sample was suction filtered, re-suspended in 50 ml room temperature de-ionized water and then suction filtered again. This procedure was repeated with room temperature water, followed by 50°C water. The catalyst was dried at room temperature overnight and calcined at 350°C for 4 hr in air. A fraction of this catalyst was treated with magnesium citrate to remove chloride either before or after calcination. The dried or calcined catalyst was re-suspended in a Mg-citrate solution (Mg-citrate/Au=1.6), stirred for 1 hr, then suction filtered. It was washed twice with doubly distilled water, dried, and calcined at 350°C for 4 hr. Catalysts were prepared with Au acetate precursor to examine the effects of adding chloride to the catalysts. An aqueous solution of Au acetate containing the appropriate weight of Au was introduced to the Al₂O₃ support by incipient wetness. The catalysts used in the remainder of the studies were prepared from a H₂AuCl₄ precursor using a method similar to that described above, but the preparation was carried out at 70°C, and the pH of the H₂AuCl₄ solution was adjusted to 7 with NaOH.

Catalyst Characterization. The amount of Au in the catalysts was determined by ICP, and the particle size was found by averaging the diameters of over 200 particles using TEM. Analysis of the residual chloride in the catalysts was done using H₂ TPR coupled with FTIR spectroscopy.

Reaction Conditions. In the chloride experiments, 20–80 mg of catalyst was mixed with 0.5 g SiC and placed in a quartz microreactor. The feed was 1% CO, 0.5% O₂, 48% H₂, and balance He. The reactions were carried out at 100°C with a flow rate of 90 ml/min, and the reaction products were analyzed by gas chromatography using two columns: a molecular sieve 13X column for H₂, CO, and O₂ and a Haysep Q column for H₂O and CO₂. The remainder of the SCO reactions were carried out at room temperature using 40 mg of catalyst with no diluent. The feed was 1% CO, 0.5% O₂, 40.55% H₂, and balance He at a flow rate of 200 ml/min. The products were analyzed with GC using the two columns described above and by FTIR for CO and CO₂ using a 75 ml gas phase cell.

Results and Discussion.

Effect of Chloride on Particle Size. When no attempt was made to remove residual Cl[–] from the catalyst after the preparation with no pH adjustment (pH ~ 4), the catalyst had an average Au particle diameter of 44.6 nm and contained 0.37 wt% Cl[–] after calcination. It had a SCO activity of 0.05±0.03 mol CO mol Au^{–1} min^{–1}. If Mg-citrate was added to this catalyst prior to calcination, the particle size was much smaller, 16.7 nm, with only 0.01 wt% Cl[–] remaining after calcination, resulting in a catalyst with a much higher SCO activity of 1.2±0.1 mol CO mol Au^{–1} min^{–1}. If Mg-citrate was added to the catalyst after calcination, the amount of Cl[–] in the catalyst was less than 0.01 wt%, but the average particle size was 49.6 nm. This catalyst had a SCO activity of 0.96±0.1 mol CO mol Au^{–1} min^{–1} despite its large particle size.

These data confirm that the presence of Cl[–] causes Au particle agglomeration. The catalysts not treated with Mg-citrate prior to calcination, which had high residual amounts of Cl[–], had much larger Au particles than the catalyst calcined in the absence of Cl[–]. The high activity of the catalyst treated with Mg-citrate after calcination is surprising, as the majority of published works suggest that very small Au particles are needed to affect CO oxidation. The difference in activity between this catalyst and the catalyst not treated with Mg-citrate suggests that small Au particle size cannot be the necessary requirement for high activity and that Cl[–] has a direct inhibitive effect

on the catalyst. It is possible that Cl^- replaces the hydroxyl group in the active site to form Au^+-Cl^- , poisoning the sites active for CO oxidation.

Chloride Addition to Calcined Catalysts without Cl^- . In order to further examine the potential of Cl^- as a poison for the catalytic active site, Cl^- was added to a catalyst prepared with an Au acetate precursor. The catalyst was first impregnated with phosphate anions to a phosphate/Au ratio of approximately 4. The phosphate anions suppress uptake of Cl^- by the Al_2O_3 surface, so that the Cl^- can be added directly to the Au. The addition of phosphate decreased the catalyst activity for SCO by one-third, indicating that some phosphate is associated with the gold particles.

Cl^- was added to this catalyst with a Cl^-/Au ratio of 0.01. This suppressed the initial activity of the catalyst almost completely, though the activity did increase with time on stream before reaching a steady state (Figure 2). In fact, the activity could be suppressed at a Cl^-/Au ratio as low as 0.0006, indicating that only a small fraction of Au is associated with the active sites.

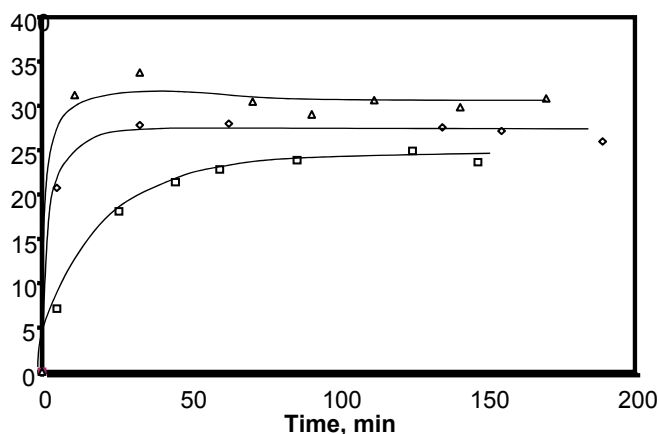


Figure 2. CO conversion (%) over 1.1 wt% $\text{Au}/\gamma\text{-Al}_2\text{O}_3$ during SCO at 100°C with 90 ml/min of 1% CO , 0.5% O_2 , 48% H_2 , and balance He. Δ : $\text{Cl}^-/\text{Au} = 0$, \circ : $\text{Cl}^-/\text{Au} = 0.0006$, \square : $\text{Cl}^-/\text{Au} = 0.01$.

The transient behavior of the catalysts to which Cl^- was added support the proposal that Cl^- acts to poison the active site by replacing the Au^+-OH^- with Au^+-Cl^- . Initially, most of the active sites are poisoned, so the initial activity is very low. During the SCO reaction, the H_2O produced by H_2 oxidation hydrolyses the Au^+-Cl^- and restores the Au^+-OH^- , gradually increasing the catalytic activity.

Effect of Phosphate Addition. Phosphate anions were added to the catalysts prepared at pH 7 to a phosphate/Au ratio of approximately 4 by impregnation followed by drying at room temperature. Prior to phosphate addition, the activity for SCO at room temperature was $4.12 \pm 0.26 \times 10^{-4}$ mol CO g-cat $^{-1}$ min $^{-1}$. After phosphate addition, this catalyst had no activity at room temperature. When the catalyst was heated to 100°C in the SCO feed, the activity increased to reach a steady state value of $5.06 \pm 0.44 \times 10^{-4}$ mol CO g-cat $^{-1}$ min $^{-1}$. Upon cooling back to room temperature, the activity dropped to the steady state value of $1.8 \pm 0.62 \times 10^{-4}$ mol CO g-cat $^{-1}$ min $^{-1}$. This behavior suggests that the phosphate anions initially block the active sites for CO oxidation, preventing the reaction from occurring, since it is unlikely that the Au particles would sinter at room temperature as a result of the presence of the phosphate anions. H_2O generated during the SCO reaction at 100°C can displace part of the phosphate from the gold, restoring some of the original activity. This behavior is similar to that of chloride poisoning.

Effect of Cesium Addition. Cesium was added to the catalysts prepared at pH 7 by impregnation with CsNO_3 followed by drying at 100°C. Preliminary results suggest that the addition of Cs does suppress H_2 oxidation, thereby increasing CO conversion in an O_2 -limiting reaction (Figure 3). This implies that H_2 oxidation and CO oxidation occur at different active sites on the $\text{Au}/\gamma\text{-Al}_2\text{O}_3$ catalyst. The active sites for H_2 oxidation are blocked by the Cs ions, but those for CO oxidation are seemingly unaffected.

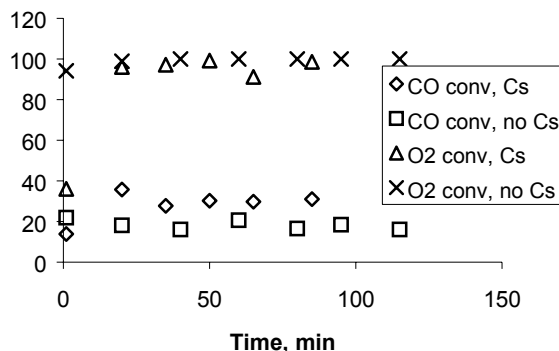


Figure 3. Effect of Cs addition on 1 wt% $\text{Au}/\gamma\text{-Al}_2\text{O}_3$ activity in SCO at room temperature, 200 ml/min of 1% CO , 0.5% O_2 , 40.55% H_2 , balance He.

Isotope Effects in SCO. A deuterium kinetic isotope effect ($r_{\text{H}}/r_{\text{D}}$) of 1.4 ± 0.2 was observed when H_2 was replaced with D_2 in the SCO feed. The CO conversion during the reaction is 30% less in the presence of D_2 , and the selectivity toward CO_2 formation relative to H_2O (D_2O) formation increased from 77% with H_2 to 87% with D_2 present in the feed.

Conclusions

The effect of Cl^- on $\text{Au}/\gamma\text{-Al}_2\text{O}_3$ catalysts is two-fold. Cl^- acts both to agglomerate Au particles and to poison the active sites by replacing the Au^+-OH^- with Au^+-Cl^- . Phosphate anions also act to block the active sites for CO oxidation, while Cs ions appear to adversely affect H_2 oxidation. The suppression of activity by the addition of chloride, phosphate, and cesium ions and the suppression of activity that occurs in the presence of D_2 are phenomena that can be used to generate a better understanding of the active sites and mechanisms involved in selective CO oxidation.

Acknowledgement. This work was supported by the EMSI program of the NSF and Department of Energy Office of Science (CHE-9810378) at the Northwestern University Institute for Environmental Catalysis.

References

- (1) Haruta, M.; Kobayashi, T.; Sano, H.; Yamada, N.; *Chem. Lett.*, **1987**, 405.
- (2) Bethke, G.K.; Kung, H.H. *Appl. Catal. A: Gen.* **2000**, 194-195, 43.
- (3) Kahlich, M.; Gasteiger, H.; Behm, R. *J. Catal.* **1999**, 182, 430.
- (4) Oh, H.-S.; Costello, C.K.; Cheung, C.; Kung, H.H.; Kung, M.C. *Stud. Surf. Sci. Catal.* **2001**, 139, 375.
- (5) Bond, G.C.; Thompson, J.N. *Gold Bull.* **2000**, 33, 41.
- (6) Uphade, B.; Okumura, M.; Tsubota, S.; Haruta, M. *Appl. Catal. A: Gen.* **2000**, 190, 43.
- (7) Yan, J.-Y.; Kung, M.C.; Sachtler, W.M.H.; Kung, H.H. *J. Catal.* **1997**, 172, 178.

Use of discharge plasma for environmentally benign production of hydrogen

Franz-Josef Spiess¹, Steven L. Suib¹, Kanji Irie², Yuji Hayashi³, and Hiroshige Matsumoto⁴

(1) Department of Chemistry, University of Connecticut, 55 N.Eagleville Rd., U-3060, Storrs, CT 06269, Fax: 860-486-2981, (2) Daido Steel Co., Ltd, Daido Steel, (3) Nagasaki University, (4) Fujitsu Laboratories Ltd

Introduction

Fuel cells are considered the future of transportation. In a fuel cell, hydrogen and oxygen are consumed and produce just water as an exhaust gas. In order for the fuel cells to become more competitive, the cost of hydrogen production has to be much lower. There are several ways hydrogen can be produced today. Electrolysis, water splitting via solar energy or thermochemical water splitting can be used as described in a review by Czuppon et al (1).

Licht et al. report the possibility of over 18 % conversion of water by solar energy to hydrogen fuel based on calculations and experiments with RuS₂ being one of the candidates (2,3). Other materials like oxide semiconductor photocatalysts like doped InTaO₄ or TiO₂ (modified or in conjunction with sonication) were investigated as well (4-6). Mechano-catalytic methods and biological hydrogen from fuel gases and water are promising concepts, as well (7,8).

Our research group previously worked on water splitting with discharge plasmas (9-11). In two cases (8,9) argon was the diluant gas, in the other (10), it was helium. In this work, methane was used as the diluant with admixtures of nitrogen or argon.

Experimental

A simple setup was used as shown in Figure 1. The tubular reactor consists of a porous, hollow copper as an inner electrode in a quartz tube (12 mm outer diameter), which is wrapped with aluminum foil as an outer electrode.

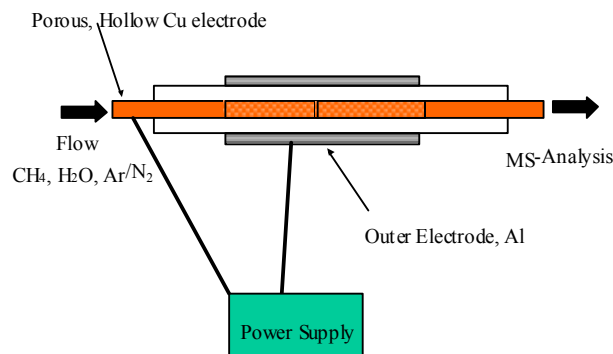


Figure 1. Reaction setup showing a tubular reactor and the connections to the power supply

The feed is a mixture of water (introduced by a bubbler), and methane with admixtures of argon or nitrogen as needed. The content of the feed gas is 3 % water and balance methane at flow rates of 5 to 250 mL/min. The reaction mixture was continuously monitored with a MKS-UTI PPT quadrupole residual gas analyzer mass spectrometer with a Faraday cup detector and a variable high-pressure sampling manifold. The system was equilibrated at the beginning and then the voltage was turned on to the desired level and continued until an equilibrium value was achieved. The electrodes used were provided by Dr. Hayashi of Nagasaki University or designed and assembled in

your lab. Gases used were obtained from commercial vendors like Airgas.

Results and Discussion

Initial studies using air and nitrogen as balance gases in tubular and fan PACT reactors showed a hydrogen yield of up to 23 % (relative %) based on the water put in. Ways to improve the conversion to hydrogen were sought. Several modifications in the gas composition were tried. Preliminary tests with methane were done and showed promise.

The tests in this area were intensified. A more thorough calibration curve for the methane/hydrogen mixture was established than the one used in the preliminary experiments with a mass spectrometer as the online analysis device.

The experimental conditions are similar to the ones used in earlier experiments. The peak-to-peak voltage used was 1.0 to 1.1 kV and currents around 200 mAmps yielding a power of about 5 Watt. The gases used were argon, nitrogen, methane and water vapor. The gases were mixed online as needed. The electrode was the porous hollow copper electrode in all these experiments.

In the first set of experiments, water (3.1 %) was mixed with balance nitrogen. The reaction was observed at various flow rates ranging from 5-250 mL/min, and the voltage (peak-to-peak) was kept at a constant 1.022 kV. The calibration was carried out before and after the experiment and yielded the same values.

The hydrogen production (here as volume %) is shown in the Figure 2. It follows an exponential decline with respect to the applied flow rate. It might be that there is a maximum conversion in the range around 5 mL/min, but the lowest achievable flow rate was 5 mL/min below that it is difficult to achieve flow because of the rotameter used in the setup. The highest hydrogen production achieved is about 15 % (total volume percent of the mixture). This is not the conversion of water or methane to hydrogen. The input concentration of water is 3.1 % (by volume).

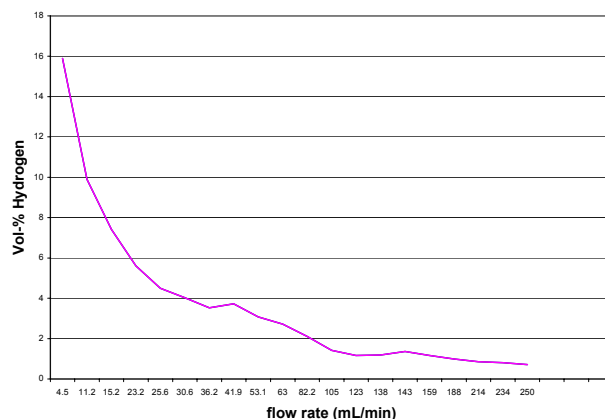


Figure 2. Hydrogen production in volume-% in relation to the applied flow rate.

The decomposition of methane follows the same trend as the hydrogen yield as seen in Figure 3 (solid line). It is highest at low flow rates at about 35 %. The decomposition rate of methane is lower than the hydrogen yield calculated from methane as seen in figure 3 (dotted line). Therefore it is believed that water contributes to this number significantly.

In the second set of experiments, the flow rate was set at 20 mL/min. This time, argon, was mixed in at different ratios to methane. A significant effect is seen on the conversion in this case as seen in Figure 4. The conversion drops and is almost independent

from the methane content in the range from 25 to 75 % by volume argon at the set flow rate.

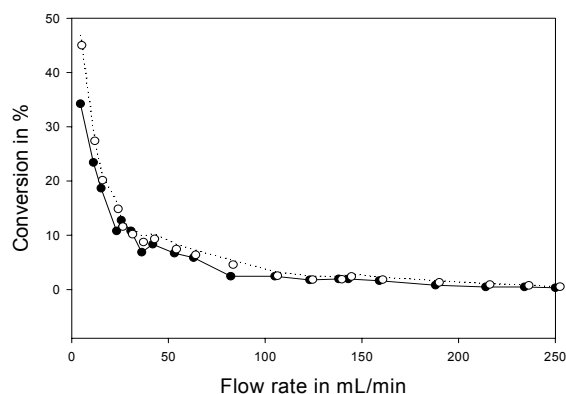


Figure 3. Decomposition of methane in relation to flow rate (solid line) and conversion of water and methane to hydrogen in relation to flow rate (dotted line).

The same experiment was carried out, at the exact flow rate. In this case nitrogen was mixed with methane at different ratios. The results are comparable to the ones obtained in the argon case, but the conversion is slightly lower in the nitrogen case. The conversion in pure nitrogen is significantly lower than in the case of methane alone, in the case of argon it is slightly higher.

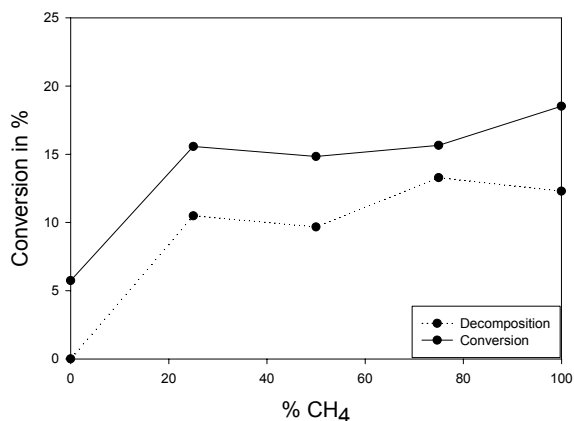


Figure 4. Decomposition of methane in relation to methane content (dotted line) and conversion of water and methane to hydrogen in relation to methane content (solid line).

Furthermore, it was observed that carbon deposits form on the copper electrode. These deposits have been collected and sent in for analysis, but the results weren't received yet. It is hard to get these deposits off the electrode, especially due to the brittle character of the electrode.

It was tried to determine, the conversion of methane alone to hydrogen, but it was impossible to get water totally out of the system. Even after purging the setup with nitrogen over an entire weekend, water was not removed.

Other electrodes will be tried in the future; maybe different metal hollow electrode could be tried. Other ideas to increase the conversion are to introduce a higher level of water vapor by different means.

Carbon monoxide and carbon dioxide are also detected as product in the mass spectrometric analysis. It is believed that the oxygen of the water reacts with the carbon of methane to form these

oxides and hydrogen is formed thereby. The other important reaction is the decomposition of methane to coke (as evident in the deposits on the electrode) and hydrogen. These products might react further to higher saturated or unsaturated hydrocarbons. This aspect will be investigated further.

Conclusions

The decomposition of a combination of methane and water by discharge plasma represents a promising way to produce hydrogen. Hydrogen production of up to 16 % is shown. Furthermore, the effects of admixtures of nitrogen and argon are demonstrated. The main products are hydrogen, coke and carbon monoxide and dioxide. Several aspects of the reaction can be optimized like the applied voltage. A preliminary reaction scheme is suggested and will be refined by complementary experiments.

Acknowledgement. The authors thank JFCC and Daido Steel Co. for support of this research. We also thank Dr. Guanguang Xia and Dr. William Willis for assistance in the power measurements and reactor setup.

References

- (1) Czuppon, T. A.; Knez, S.A.; Newsome, D.S. in *Encyclopedia of Chemical Technology*; Kirk-Ohmer, 4th ed.; Wiley: New York, NY, 1991; Vol. 13, p. 867.
- (2) Licht, S.; Wang, B.; Mukerji, S.; Soga, T.; Umeno, M.; Tributsch, H.; *Int. J. Hydrogen Energy* **26** (2001), 653, 659.
- (3) Licht, S.; Ghosh, S.; Tributsch, H.; Fiechter, S. *Sol. Energy Mater. Sol. Cells* **70** (2002), 471-480.
- (4) Zou, Z.; Ye, J.; Sayama, K.; Arakawa, H. *Nature* **414** (2001), 625-627
- (5) Abe, R.; Sayama, K.; Domen, K.; Arakawa, H. *Chem. Phys. Lett.* **344** (2001), 339-344.
- (6) Harada, H.; Hosoki, C.; Kudo, A. *J. Photochem. Photobiol., A* **141** (2001), 219-224.
- (7) Hitoki, G.; Takata, T.; Ikeda, S.; Hara, M.; Kondo, J. N.; Kakihana, M.; Domen, K. *Catal. Today* **63** (2000), 175-181.
- (8) Chen, X.; Marquez, M.; Rozak, J.; Marun, C.; Luo, J.; Suib, S. L.; Hayashi, Y.; Matsumoto, H. *J. Catal.* **178** (1998), 372-377.
- (9) Chen, X.; Suib, S. L.; Hayashi, Y.; Matsumoto, H. *J. Catal.* **201** (2001), 198-205.
- (10) Luo, J.; Suib, S. L.; Hayashi, Y.; Matsumoto, H. *J. Res. Chem. Intermed.* **26** (2000), 849-874.

VISION 21: ENERGY PLANTS FOR THE 21ST CENTURY

Lawrence A. Ruth

U.S. Department of Energy
National Energy Technology Laboratory
626 Cochran's Mill Road
P.O. Box 10940
Pittsburgh, PA 15236-0940

Introduction

Vision 21 is the U.S. Department of Energy's initiative to develop the technology for new generations of ultra-clean 21st century energy plants. The goal of Vision 21 is to effectively remove, at affordable costs, environmental concerns associated with the use of fossil fuels for producing electricity and other valuable energy products. The environmental concerns include "traditional" air pollutants such as sulfur and nitrogen oxides, and particulate matter; liquid and solid discharges; and gases associated with global climate change. In order to achieve this ambitious goal, DOE's National Energy Technology Laboratory (NETL) has implemented an intensive, long-range research and development collaboration among industry, academia, and government aimed at providing substantial advances in fossil energy-related technologies.

The approach is to stress innovation and revolutionary technologies. A suite of technology subsystems, or "modules," is being developed to become the building blocks of future Vision 21 plants. These modules will be interconnected in different configurations to utilize fossil fuels and "opportunity" feedstocks, such as petroleum coke and biomass, and produce market-driven products. The selection of feedstocks, products, plant configurations and sizes, and environmental controls will be site specific and determined by prevailing market conditions.

To achieve Vision 21's ambitious objectives (Table 1), an R&D roadmap (www.netl.doe.gov/coalpower/v21rdmp.pdf) was developed jointly by government and industry. For each technology that will play a key role in Vision 21 energy plants, the roadmap defines performance objectives and outlines strategies for achieving these objectives. These key technologies include gasification, combustion and high-temperature heat exchange, gas purification and separation, turbines, fuel cells, environmental controls, process controls and sensors, synthesis gas conversion to fuels and chemicals, materials, and computational modeling and virtual simulation.

Coal, of course plays a major role in our energy supply, particularly in electricity generation, because it is widely distributed and low in cost. The U.S. has the largest coal reserves of any country, about a 250-year supply at current use rates. In terms of energy value, coal constitutes approximately 95% of U.S. fossil energy reserves, with an energy equivalent of about one trillion barrels of crude oil – comparable to the entire world's known oil reserves. We need to rely on our abundant and secure coal reserves to meet the growing demand for electricity, maintain competitive energy prices, and sustain economic growth. However, coal must meet increasingly stringent environmental standards – a requirement that can be met through better technology. Although Vision 21 is a fossil fuel rather than a coal only initiative, the formidable environmental challenges associated with coal use means that coal technology needs particular attention.

Table 1. Vision 21 Energy Plant Performance Targets

Efficiency-Electricity Generation ¹	60% for coal-based systems (HHV) 75% for natural gas-based systems (LHV)
Emissions	Atmospheric release of: <4.3 g/GJ (0.01 lb/10 ⁶ Btu) S and N oxides <2.2 g/GJ (0.005 lb/10 ⁶ Btu) particulate matter <1/2 emission rates for organic compounds listed in "Utility HAPS Report" ² <0.4 mg/GJ (1 lb/10 ¹² Btu) Hg 40-50% reduction in CO ₂ emissions by efficiency improvement, 100% reduction with sequestration
Costs	Products of Vision 21 plants competitive with other energy systems with comparable environmental performance, including specific carbon emissions
Timing	Vision 21 subsystem/module designs by 2012, commercial plant designs by 2015, technology "spinoffs" by 2005

1. based on fuel higher (HHV) and lower (LHV) heating values
2. "Study of Hazardous Air Pollutant Emissions from Electric Utility Steam Generation Units – Final Report to Congress, Volume 2," EPA-453/R-98-004b, 1998

The Vision 21 Energy Plant

Figure 1 shows an artist's rendition of a Vision 21 energy plant. It is important to emphasize, however, that a Vision 21 plant would not be an "energyplex." In most cases, electricity would be the primary or only product. When it makes sense economically, other products such as hydrogen or clean liquid transportation fuels, could be co-produced. The gasifier produces a fuel gas (syngas) that is cleaned and used to produce power with gas turbines and fuel cells as well as clean transportation fuels and chemicals. The plant features modular design and makes a market-driven product slate. Coal and "opportunity" feedstocks are gasified using oxygen produced with a low-cost air separation membrane. The syngas is cleaned and a second membrane is used to separate hydrogen. Carbon monoxide in the syngas may be shifted to CO₂ and the CO₂ sequestered if necessary. Electricity is generated with a fuel cell using the hydrogen and a gas turbine using the energy in the fuel cell exhaust. Heat remaining in the gas turbine exhaust is used to generate steam for process heating. A portion of the syngas is diverted for the production of clean liquid fuels and high-value chemicals.

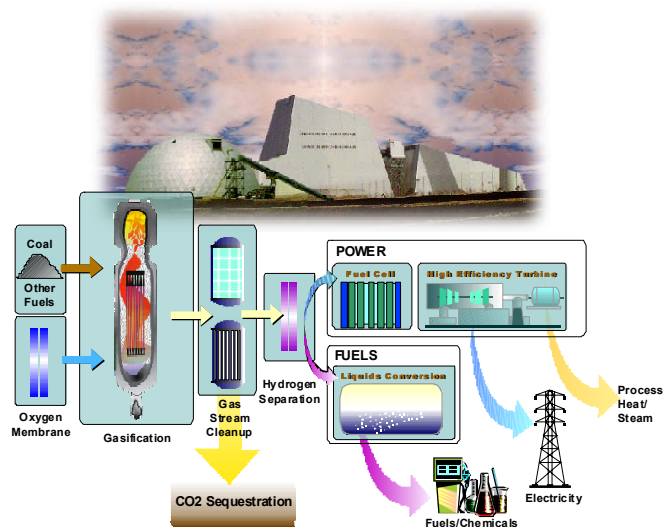


Figure 1. Example Configuration of a Vision 21 Energy Plant

Vision 21 Technologies

Descriptions of several Vision 21 key technologies are given below along with examples of current activities.

Combustion and High-Temperature Heat Exchange. Vision 21 addresses a range of combustion issues, including ultra-low NO_x combustion; fuel-flexible combustion, i.e., use of alternative feedstocks in combination with coal or natural gas; syngas combustion external to a turbine; char combustion; high-temperature heat exchange; and “sequestration-ready” combustion systems.

The goal of Vision 21 is to achieve NO_x emission of 4.3 g/GJ (0.01 lb/million Btu), or about one order of magnitude below today’s most stringent regulatory requirements, at an installed cost of \$25/kW. The strategy will be to drive emissions to the lowest levels practicable using combustion technology.

Fuel-flexible combustion is needed to accommodate opportunity feedstocks that could lower the cost of electricity. The objective is to fire up to 30 percent alternative fuel with coal without adverse impacts on system performance and availability. The barriers to overcome include feed preparation and injection, corrosion and erosion, emissions, and the effect of altered ash properties on fouling and slagging.

High-temperature heat exchange is needed in applications ranging from syngas coolers associated with integrated gasification combined cycle (IGCC) plants to high-efficiency power cycles using ultra-supercritical boilers and indirectly fired cycles.

Sequestration-ready combustion systems would produce a concentrated CO₂ product gas that would be available for sequestration. Separation of CO₂ from the exhaust of such systems will be less costly and more efficient than separating CO₂ from gas streams in which the CO₂ was diluted with other gases, i.e., nitrogen. One approach is nitrogen-free combustion, burning fuels in mixtures of oxygen and CO₂. The products of combustion are then CO₂ and water, which can be readily separated. Rocket engine combustion technology is being applied to a steam generator that would power an advanced turbine, emitting only water and a stream of CO₂ ready for sequestration. The size of the steam generator is dramatically smaller than boilers used today; a unit of several hundred megawatts capacity would be about the size of an office desk, opening up possibilities for portability and reduced cost.

Gasification. Gasifiers with improved feedstock flexibility, better availability, and increased cold gas efficiency are needed for Vision 21. Improvements being sought include gasifiers with the capability to process up to 30 percent opportunity feedstocks (e.g., biomass, petcoke) along with coal, availability greater than 95 percent (compared with <85 percent today), and cold gas efficiencies exceeding 82 percent (~72 percent today). The cost target for the gasifier, including syngas cooling and auxiliaries but not air separation, slag handling, and feed system, is \$150/kW (\$200-250/kW today). The syngas cost target is \$2.50/GJ (\$2.50/million Btu) compared to ~\$4/GJ (\$4/million Btu) today.

Two types of advanced gasifiers are being studied at DOE’s Power Systems Development Facility located in Wilsonville, AL. These are the transport gasifier, which has the potential to process coals with a wide range of properties at high throughput and reduced cost, and the partial gasifier, which produces syngas and char products and integrates well with high-efficiency combined cycles. The partial gasifier operates at lower temperatures (~870°C) than conventional gasifiers and may mitigate operational and reliability concerns associated with higher temperature operation.

Gas Separation. More energy efficient, lower cost gas separation technology is needed, especially for O₂, H₂, and CO₂. Ion-electron conducting membranes that separate oxygen from air are

under development for applications including IGCC and oxygen-enriched combustion, and also for integration with high-temperature solid oxide fuel cells. In the latter, the system exhaust consists only of steam and CO₂ for sequestration. Hydrogen separation from coal-derived syngas would create opportunities in fuel cell power and in clean transportation fuels, including hydrogen and synthesized liquid fuels. Proton-electron conducting membranes comprising non-porous ceramic composites have produced pure H₂ in laboratory-scale equipment. The main development issues are achieving commercially viable H₂ fluxes and membrane stability in corrosive environments, and designing effective seals and manufacturing procedures. Technologies for CO₂ separation include CO₂ hydrates which, in order to be successful, must have the ability to capture and release CO₂ in an energy-efficient manner and avoid problems with trace contaminants, which may interfere with hydrate formation.

Fuel Cells. Achieving the efficiency target for Vision 21 energy plants will likely require the use of fuel cells. Solid oxide and molten carbonate fuel cells are leading candidates for Vision 21 applications because their high operating temperatures allow ready integration with Vision 21 plants based on coal gasification. However, substantial improvements will be required, including scale up to sizes larger than 30 MW, lower capital costs, increased power density, higher fuel conversion efficiency, and higher sulfur tolerance. Both types of high-temperature fuel cells are being developed, as is a “hybrid” power system that combines a fuel cell and gas turbine to generate electricity at unprecedented efficiency. An experimental hybrid system based on a 250 kW fuel cell and 30 kW microturbine has been operated for nearly 4000 hours.

Materials. Realizing the performance targets of Vision 21 energy plants will require advanced materials with capabilities beyond those now available. New alloys are being developed that can withstand severe environmental conditions, including high temperatures, corrosive and/or erosive atmospheres, and elevated pressures. Ultra-high performance materials, including intermetallics and ceramic composites, are being developed for applications at temperatures (1000-1700°C) above those possible with conventional materials. Coatings are used to provide corrosion protection to underlying structural components, and may be either metallic materials, such as the intermetallic iron aluminide, or ceramics. Finally, functional materials include alloys and ceramics for gas filters, e.g., to remove particulate from syngas to levels required for gas turbines, catalysts for synthesis of transportation fuels, fuel cell electrodes, and gas separation membranes.

Computational Modeling and Virtual Simulation. Computer modeling and simulation presents a major opportunity for Vision 21 plants because simulations can be used to describe the interactions among tightly integrated configurations of technology modules. The goal is to unify all module and component codes, and all computer-related plant design activities, into an integrated suite of codes that can exchange information easily and accurately and transfer to the user information that provides a realistic visual simulation of plant layout and operation. Activities are underway to accomplish this goal.

Note on References

Information on the activities mentioned can be found in the Proceedings of the 2001 Vision 21 Program Review Meeting, Morgantown, WV, Nov. 6-7, 2001, available at www.netl.doe.gov under Publications, Conferences, Proceedings.